

**Exclusive Measurements**  
**of the  $pp \rightarrow pp\pi^+\pi^-$  Reaction**  
**Close to Threshold**



Dissertation der Fakultät für Physik  
der Eberhard-Karls-Universität zu Tübingen  
zur Erlangung des Grades eines Doktors  
der Naturwissenschaften

vorgelegt von

Jens Pätzold

aus Ebingen

2002

Tag der mündlichen Prüfung: 19. Juli 2002

Dekan: Prof. Dr. Herbert Müther

1. Berichterstatter: Prof. Dr. Heinz Clement

2. Berichterstatter: Prof. Dr. Gerhard Wagner

## Abstract

Two-pion production in elementary nucleon-nucleon ( $NN$ ) collisions offers a variety of aspects concerning the dynamics of the total system as well as that of its subsystems  $\pi\pi$ ,  $NN$ ,  $\pi N$ ,  $\pi\pi N$  and  $\pi NN$ .

All existing data on this reaction below a proton beam energy of  $T_p = 900$  MeV were taken in inclusive and/or low-statistics measurements, which allow only limited access to the reaction mechanisms. Therefore exclusive high-statistics measurements of the  $pp \rightarrow pp\pi^+\pi^-$  reaction have been carried out at the CELSIUS storage ring using the PROMICE/WASA detector setup with the cluster-jet  $H_2$  target.

The obtained values for integral cross sections have turned out to be an order of magnitude lower than expected from previous bubble-chamber measurements. Differential cross sections at  $T_p = 750$  MeV and 775 MeV offer a new opportunity for studying the mechanisms of this reaction. Close to threshold this reaction is expected to be dominated by the excitation of the  $N^*(1440)$  resonance in one of the participating nucleons, since single  $\Delta$  excitation leads to the emission of a single pion only. Indeed, for the first time the measured differential cross sections show clear signs of the  $N^*(1440)$  excitation as well as of the interference of its decay channels into the  $N\pi\pi$  system. The data also demonstrate that  $\sigma$ -exchange between the colliding nucleons is the dominant interaction process.

In recent years the CELSIUS/WASA detector in Uppsala has been upgraded. As part of the work presented here, a thin trigger hodoscope (FWC) was developed. Its purpose is to have cleaner trigger conditions in the experiments. First test measurements were taken under simple conditions to check the performance of the sensitive detector components and of the new trigger electronics. This upgrade was done in order to measure rare decays of the light neutral mesons ( $\pi^0$ ,  $\eta$ ). In the future it will be also used again for exclusive measurements of charged two-pion production. In addition it will create the opportunity to exclusively measure the neutral reaction channels e.g.  $pp \rightarrow pp\pi^0\pi^0$ .

## Zusammenfassung

Zweipionproduktion in elementarem Nukleon-Nukleon- ( $NN$ -)Stoß bietet eine Vielzahl von Aspekten bezüglich der Dynamik sowohl des ganzen Systems als auch seiner Subsysteme  $\pi\pi$ ,  $NN$ ,  $\pi N$ ,  $\pi\pi N$  und  $\pi NN$ .

Alle existierenden Daten dieser Reaktion unterhalb einer Protonenstrahlenergie von  $T_p = 900$  MeV wurden in inklusiven Messungen und/oder Messungen mit geringer Statistik genommen, welche nur einen begrenzten Zugang zu den Reaktionsmechanismen erlauben. Deswegen wurden exklusive Messungen der Reaktion  $pp \rightarrow pp\pi^+\pi^-$  mit hoher Statistik am CELSIUS Speicherring mit dem PROMICE/WASA Detektor und dem Clusterjet  $H_2$  Target durchgeführt.

Die erhaltenen Werte für die integralen Wirkungsquerschnitte erweisen sich um eine Größenordnung niedriger als frühere Blaskammermessungen erwarten ließen. Differentielle Wirkungsquerschnitte bei  $T_p = 750$  MeV und  $775$  MeV bieten neue Möglichkeiten die Reaktionsmechanismen dieser Reaktion zu untersuchen. Nahe der Schwelle erwartet man, daß die Reaktion durch die Anregung der  $N^*(1440)$  Resonanz in einem der beiden Nukleonen beherrscht wird, da einfache  $\Delta$  Anregung nur zur Erzeugung von einem Pion führt. Tatsächlich zeigen die gemessenen differentiellen Wirkungsquerschnitte zum ersten Mal klare Anzeichen für die  $N^*(1440)$  Anregung als auch für die Interferenz seiner Zerfallskanäle in den  $N\pi\pi$ -Kanal. Die Daten zeigen auch, dass der  $\sigma$ -Austausch zwischen den stoßenden Nukleonen der dominante Wechselwirkungsprozess ist.

Während der letzten Jahre wurde der CELSIUS/WASA Detektor in Uppsala erweitert. Als Teil der hier präsentierten Arbeit wurde ein dünnes Triggerhodoskop (FWC) für diesen Detektor entwickelt. Es dient dazu sauberere Triggerbedingungen in den Experimenten zu haben. Erste Testmessungen wurden unter einfachen Bedingungen durchgeführt, um das Verhalten der sensitiven Detektorkomponenten und der neuen Triggerelektronik zu überprüfen. Diese Erweiterung wurde durchgeführt, um die seltenen Zerfälle der leichten neutralen Mesonen ( $\pi^0$ ,  $\eta$ ) zu messen. In Zukunft soll der Detektor auch wieder dazu benutzt werden exklusive Messungen der geladenen Zweipionproduktion durchzuführen. Zusätzlich wird er neue Möglichkeiten für die exklusive Messung der neutralen Reaktionskanäle eröffnen z.B.:  $pp \rightarrow pp\pi^0\pi^0$ .

# Contents

<b>Abstract</b>	<b>i</b>
<b>Zusammenfassung</b>	<b>ii</b>
<b>Contents</b>	<b>iii</b>
<b>List of Figures</b>	<b>vii</b>
<b>List of Tables</b>	<b>xi</b>
<b>1 Introduction</b>	<b>1</b>
1.1 Mesons as exchange particles of the nuclear force . . . . .	1
1.2 Pion production . . . . .	2
1.3 Two-pion production in $pp$ collision . . . . .	2
1.4 Reaction subsystems . . . . .	3
1.5 Theoretical and experimental situation . . . . .	4
<b>2 Experimental Setup</b>	<b>6</b>
2.1 The Theodor Svedberg Laboratory (TSL) . . . . .	6
2.2 The CELSIUS accelerator and storage ring . . . . .	6
2.3 The PROMICE/WASA detector setup . . . . .	8
2.4 The trigger and data acquisition system . . . . .	12
2.5 The measurements . . . . .	14
<b>3 Analysis</b>	<b>15</b>
3.1 Analysis tools . . . . .	15
3.2 Event generator . . . . .	16
3.3 Detector simulation . . . . .	17
3.4 Data analysis . . . . .	18
3.4.1 Decoding . . . . .	18
3.4.2 Pedestal subtraction . . . . .	18

---

3.4.3	TDC zero-point . . . . .	19
3.4.4	Light pulser correction . . . . .	19
3.4.5	Trigger selection . . . . .	19
3.4.6	Energy calibration . . . . .	19
3.4.7	Track reconstruction . . . . .	21
3.4.8	Non-uniformity correction . . . . .	22
3.4.9	Particle identification . . . . .	23
3.4.10	Energy reconstruction . . . . .	23
3.4.11	Event reconstruction . . . . .	25
3.4.12	Physical cuts . . . . .	25
3.4.13	Kinematical fit . . . . .	28
3.4.14	Energy threshold simulation . . . . .	29
3.4.15	Trigger simulation . . . . .	30
3.5	Normalisation . . . . .	30
3.5.1	$pp$ elastic scattering . . . . .	30
3.5.2	Trigger inefficiency . . . . .	31
3.5.3	Data acquisition life time . . . . .	31
3.6	Efficiency and acceptance correction . . . . .	32
3.7	Future improvements of the analysis . . . . .	35
<b>4</b>	<b>Results</b>	<b>36</b>
4.1	Definition and calculation of observables . . . . .	36
4.1.1	Invariant mass . . . . .	36
4.1.2	Missing mass . . . . .	37
4.1.3	Scattering angles, planarity and opening angles . . . . .	37
4.1.4	Subsystem scattering angles . . . . .	38
4.2	Integral cross sections . . . . .	38
4.2.1	The calculation of integral cross sections . . . . .	38
4.2.2	Results for integral cross sections . . . . .	40
4.3	Comparison with phase space distributions . . . . .	42
4.4	Reaction mechanisms in detail . . . . .	43
4.4.1	Final state interaction (FSI) . . . . .	43
4.4.2	Meson exchange . . . . .	44
4.4.3	$N^*$ excitation and decay . . . . .	46

4.4.4	$\Delta$ propagators . . . . .	48
4.4.5	$\Delta\Delta$ excitation . . . . .	50
4.5	Differential cross sections at 750 and 775 MeV . . . . .	51
4.5.1	Invariant masses . . . . .	52
4.5.2	Angular distributions . . . . .	56
4.5.3	Kinetic energy distributions . . . . .	72
4.6	Search for a narrow dibaryon resonance $d'$ . . . . .	76
4.7	Summary . . . . .	78
<b>5</b>	<b>Outlook</b>	<b>79</b>
5.1	CELSIUS/WASA detector . . . . .	79
5.1.1	Pellet target . . . . .	80
5.1.2	CELSIUS/WASA detector setup . . . . .	80
5.1.3	The new forward window counter (FWC) . . . . .	82
5.2	Two-pion production with CELSIUS/WASA . . . . .	84
5.3	Chiral Restoration . . . . .	85
<b>A</b>	<b>Uncorrected differential cross sections</b>	<b>87</b>
A.1	Invariant masses . . . . .	88
A.2	Angular distributions . . . . .	92
A.3	Kinetic energy distributions . . . . .	108
<b>B</b>	<b>Acceptance and efficiency</b>	<b>112</b>
B.1	Invariant masses . . . . .	113
B.2	Angular distributions . . . . .	114
B.3	Kinetic energy distributions . . . . .	118
<b>C</b>	<b>Acronyms</b>	<b>119</b>
<b>D</b>	<b>Nomenclature</b>	<b>121</b>
<b>E</b>	<b>Software</b>	<b>122</b>
E.1	Programs . . . . .	122
E.1.1	cvs . . . . .	122
E.1.2	gmake . . . . .	122
E.1.3	root . . . . .	122

---

E.1.4	clhep & GEANT4 . . . . .	123
E.1.5	gcc . . . . .	123
E.2	GIN format . . . . .	123
E.3	Analysis abstraction . . . . .	124
<b>Acknowledgments</b>		<b>125</b>
<b>List of Publications</b>		<b>127</b>
	Journals . . . . .	127
	Conference proceedings . . . . .	128
	Conference contributions . . . . .	129
	Shortcuts for conference names . . . . .	129
<b>Bibliography</b>		<b>130</b>
<b>Lebens- und Bildungsgang</b>		<b>134</b>



## List of Figures

1.1	Theoretical and experimental situation . . . . .	5
2.1	Theodor Svedberg Laboratory (cross section) . . . . .	7
2.2	Theodor Svedberg Laboratory (top view) . . . . .	8
2.3	CELSIUS accelerator ring . . . . .	9
2.4	PROMICE/WASA setup . . . . .	10
2.5	PROMICE/WASA setup (3d view) . . . . .	10
2.6	Forward hodoscope (FHD) . . . . .	11
2.7	Trigger unit . . . . .	12
2.8	DAQ setup . . . . .	14
3.1	Flow chart of the analysis procedure . . . . .	16
3.2	Example of the light pulser correction (one) . . . . .	20
3.3	Example of the light pulser correction (two) . . . . .	21
3.4	Non-uniformity correction for some elements . . . . .	22
3.5	Particle identification with $\Delta E$ -E-plots . . . . .	24
3.6	Time distribution of delayed hits . . . . .	25
3.7	Dead material & quenching correction for protons . . . . .	26
3.8	Dead material & quenching correction for pions . . . . .	27
3.9	Missing mass of the two proton system . . . . .	28
3.10	Missing mass of the three measured particles . . . . .	29
3.11	$pp$ elastic scattering cross section from SAID . . . . .	30
3.12	Scheme for acceptance and efficiency correction . . . . .	32
3.13	Uncertainty of acceptance and efficiency correction of $M_{pp}$ . . . . .	33
3.14	Uncertainty of acceptance and efficiency correction of $\theta_{\pi^-}$ . . . . .	34
4.1	Definition of subsystem scattering angles . . . . .	38
4.2	Integral cross section of $pp \rightarrow pp\pi^+\pi^-$ . . . . .	41
4.3	Effect of proton proton FSI . . . . .	43
4.4	Effect of meson exchange . . . . .	45

4.5	Feynman diagram of inelastic meson exchange . . . . .	46
4.6	Effect of the interference of $N^*$ decay channels . . . . .	47
4.7	Illustration of the analogy to $\pi N$ scattering . . . . .	48
4.8	Effect of the $\Delta$ propagators . . . . .	49
4.9	Effect of the $\Delta\Delta$ excitation . . . . .	50
4.10	Invariant masses for two particles, with models, $T_p = 750$ MeV .	52
4.11	Invariant masses for two particles, with models, $T_p = 775$ MeV .	53
4.12	Invariant masses for three particles, with models, $T_p = 750$ MeV .	54
4.13	Invariant masses for three particles, with models, $T_p = 775$ MeV .	55
4.14	Scattering angles in c.m. system, with models, $T_p = 750$ MeV . . .	56
4.15	Scattering angles in c.m. system, with models, $T_p = 775$ MeV . . .	57
4.16	Scattering angles in lab. system, with models, $T_p = 750$ MeV . . .	58
4.17	Scattering angles in lab. system, with models, $T_p = 775$ MeV . . .	59
4.18	Opening angles in c.m. system, with models, $T_p = 750$ MeV . . .	60
4.19	Opening angles in c.m. system, with models, $T_p = 775$ MeV . . .	61
4.20	Planarity angles, with models, $T_p = 750$ MeV . . . . .	62
4.21	Planarity angles, with models, $T_p = 775$ MeV . . . . .	63
4.22	Two particle scattering angles, with models, $T_p = 750$ MeV . . . .	64
4.23	$pp$ subsystem scattering angles, with models, $T_p = 750$ MeV . . .	64
4.24	Two particle scattering angles, with models, $T_p = 775$ MeV . . . .	65
4.25	$pp$ subsystem scattering angles, with models, $T_p = 775$ MeV . . .	65
4.26	$\pi^+\pi^-$ subsystem scattering angles, with models, $T_p = 750$ MeV .	66
4.27	$p\pi$ subsystem scattering angles, with models, $T_p = 750$ MeV . . .	66
4.28	$\pi^+\pi^-$ subsystem scattering angles, with models, $T_p = 775$ MeV .	67
4.29	$p\pi$ subsystem scattering angles, with models, $T_p = 775$ MeV . . .	67
4.30	$p\pi\pi$ subsystem scattering angles, with models, $T_p = 750$ MeV . .	68
4.31	$p\pi\pi$ subsystem scattering angles, with models, $T_p = 775$ MeV . .	69
4.32	$pp\pi$ subsystem scattering angles, with models, $T_p = 750$ MeV . .	70
4.33	$pp\pi$ subsystem scattering angles, with models, $T_p = 775$ MeV . .	71
4.34	Kinetic energies in c.m. system, with models, $T_p = 750$ MeV . . .	72
4.35	Kinetic energies in c.m. system, with models, $T_p = 775$ MeV . . .	73
4.36	Kinetic energies in lab. system, with models, $T_p = 750$ MeV . . .	74
4.37	Kinetic energies in lab. system, with models, $T_p = 775$ MeV . . .	75
4.38	Search for a narrow structure of a dibaryon resonance $d'$ . . . . .	76

5.1	The CELSIUS/WASA detector setup (schematic) . . . . .	80
5.2	Side view of the CELSIUS/WASA detector (picture) . . . . .	81
5.3	CELSIUS/WASA detector, one half of the yoke removed (picture) . . . . .	82
5.4	FWC construction plans . . . . .	83
5.5	FWC performance . . . . .	84
5.6	Sample event in the detector simulation . . . . .	85
A.1	Invariant masses for two particles, uncorrected, $T_p = 750$ MeV . . . . .	88
A.2	Invariant masses for two particles, uncorrected, $T_p = 775$ MeV . . . . .	89
A.3	Invariant masses for three particles, uncorrected, $T_p = 750$ MeV . . . . .	90
A.4	Invariant masses for three particles, uncorrected, $T_p = 775$ MeV . . . . .	91
A.5	Scattering angles in c.m. system, uncorrected, $T_p = 750$ MeV . . . . .	92
A.6	Scattering angles in c.m. system, uncorrected, $T_p = 775$ MeV . . . . .	93
A.7	Scattering angles in lab. system, uncorrected, $T_p = 750$ MeV . . . . .	94
A.8	Scattering angles in lab. system, uncorrected, $T_p = 775$ MeV . . . . .	95
A.9	Opening angles in c.m. system, uncorrected, $T_p = 750$ MeV . . . . .	96
A.10	Opening angles in c.m. system, uncorrected, $T_p = 775$ MeV . . . . .	97
A.11	Planarity angles, uncorrected, $T_p = 750$ MeV . . . . .	98
A.12	Planarity angles, uncorrected, $T_p = 775$ MeV . . . . .	99
A.13	Two particle scattering angles, uncorrected, $T_p = 750$ MeV . . . . .	100
A.14	$pp$ subsystem scattering angles, uncorrected, $T_p = 750$ MeV . . . . .	100
A.15	Two particle scattering angles, uncorrected, $T_p = 775$ MeV . . . . .	101
A.16	$pp$ subsystem scattering angles, uncorrected, $T_p = 775$ MeV . . . . .	101
A.17	$\pi^+\pi^-$ subsystem scattering angles, uncorrected, $T_p = 750$ MeV . . . . .	102
A.18	$p\pi$ subsystem scattering angles, uncorrected, $T_p = 750$ MeV . . . . .	102
A.19	$\pi^+\pi^-$ subsystem scattering angles, uncorrected, $T_p = 775$ MeV . . . . .	103
A.20	$p\pi$ subsystem scattering angles, uncorrected, $T_p = 775$ MeV . . . . .	103
A.21	$p\pi\pi$ subsystem scattering angles, uncorrected, $T_p = 750$ MeV . . . . .	104
A.22	$p\pi\pi$ subsystem scattering angles, uncorrected, $T_p = 775$ MeV . . . . .	105
A.23	$pp\pi$ subsystem scattering angles, uncorrected, $T_p = 750$ MeV . . . . .	106
A.24	$pp\pi$ subsystem scattering angles, uncorrected, $T_p = 775$ MeV . . . . .	107
A.25	Kinetic energies in c.m. system, uncorrected, $T_p = 750$ MeV . . . . .	108
A.26	Kinetic energies in c.m. system, uncorrected, $T_p = 775$ MeV . . . . .	109
A.27	Kinetic energies in lab. system, uncorrected, $T_p = 750$ MeV . . . . .	110

---

A.28 Kinetic energies in lab. system, uncorrected, $T_p = 775 \text{ MeV}$ . . . .	111
B.1 Invariant masses for two particles, acceptance and efficiency . . .	113
B.2 Invariant masses for three particles, acceptance and efficiency . .	113
B.3 Scattering angles in c.m. system, acceptance and efficiency . . . .	114
B.4 Scattering angles in lab. system, acceptance and efficiency . . . .	114
B.5 Opening angles in c.m. system, acceptance and efficiency . . . . .	115
B.6 Planarity angles, acceptance and efficiency . . . . .	115
B.7 Two particle scattering angles, acceptance and efficiency . . . . .	116
B.8 $pp$ subsystem scattering angles, acceptance and efficiency . . . . .	116
B.9 $\pi^+\pi^-$ subsystem scattering angles, acceptance and efficiency . .	116
B.10 $p\pi$ subsystem scattering angles, acceptance and efficiency . . . .	116
B.11 $p\pi\pi$ subsystem scattering angles, acceptance and efficiency . . .	117
B.12 $pp\pi$ subsystem scattering angles, acceptance and efficiency . . . .	117
B.13 Kinetic energies in c.m. system, acceptance and efficiency . . . . .	118
B.14 Kinetic energies in lab. system, acceptance and efficiency . . . . .	118

## List of Tables

1.1	Channels of two-pion production . . . . .	2
1.2	Subsystems in two-pion production . . . . .	3
2.1	Primary triggers . . . . .	12
2.2	Secondary triggers . . . . .	13
3.1	Quenching parameters . . . . .	17
3.2	FPC wire to element mapping . . . . .	18
3.3	Trigger inefficiency . . . . .	31
4.1	Determination of the integrated luminosities . . . . .	39
4.2	Values for calculating the integral cross sections . . . . .	39
4.3	Compilation of errors . . . . .	40
4.4	Integral cross sections . . . . .	42
4.5	Parameters for FSI . . . . .	44



# 1

## Introduction

Two-pion production is a tool which allows us to examine the characteristics of the interaction of the most fundamental hadronic systems, which are formed by nucleons and pions. This chapter gives an introduction to two-pion production and its connection to the theory of the interaction of nucleons. The theoretical and experimental situation of this reaction prior to our measurements will be shown.

### 1.1 Mesons as exchange particles of the nuclear force

The meson theory describes the nuclear forces by the exchange of scalar, pseudo-scalar and vector mesons. The nuclear forces can be divided into three regimes: an attractive long-range and medium-range part ( $r \gtrsim 0.5$  fm) and a repulsive short-range part ( $r \lesssim 0.5$  fm). The meson theory effectively describes the characteristics of the nuclear forces. This model is quite successful for the description on the nucleon level. In 1935, led by theoretical considerations Yukawa has already proposed the existence of an exchange meson for the long-range part. Later (1946) it was experimentally found by Powell and called pion or  $\pi$ -meson ( $\pi$ ). The until now hypothetical  $\sigma$ -meson was introduced to describe the medium-range part of the nuclear forces. The  $\rho$  and  $\omega$ -mesons are considered to be responsible for the repulsive short-range part.

The meson theory has proven to be very successful, but Quantum-Chromodynamics (QCD) is commonly believed to be the underlying fundamental theory of hadronic interaction dealing with different degrees of freedom. QCD calculations succeed in the perturbative region, i.e. at high energies, where the coupling constant  $\alpha_s$  of the strong interaction is small enough to allow perturbative calculations. Massless bosons, the gluons, are the exchange particles between “coloured” quarks in this theory. Quarks and gluons build the substructure of nucleons and mesons. It is difficult to perform QCD calculations for nuclei and for hadrons (confined quarks), because the coupling constant  $\alpha_s$  is growing strongly towards lower energies. This makes perturbative calculations impossi-

ble. Until now it was not clear how the successful meson exchange model could be justified within the more fundamental framework of QCD.

Chiral perturbation theory ( $\chi$ PT) is another possibility for perturbative calculations. The fundamental symmetry used here is the helicity or chirality of the quarks. But this symmetry is broken explicitly, because even the masses of the light quarks are not zero:  $m_d \neq m_u \neq 0$ . Then for each hadron a parity partner should exist. However, this symmetry is not observed in nature. So the mechanism of spontaneous symmetry breaking of the QCD ground-state has been introduced. The QCD with quarks and gluons as the degrees of freedom is rewritten in terms of pion fields. This is used for new perturbative calculations in the framework of  $\chi$ PT.

## 1.2 Pion production

Pion production reactions are one possibility to examine the properties of the  $\pi N$  system. Apart from  $\pi N$  and  $\gamma N$  collisions,  $NN$  collisions are one of the simplest experimentally accessible systems for this reaction. In recent years single-pion production reactions have been studied extensively. Close to threshold only a few partial waves contribute to the reaction, which makes the description easier.

## 1.3 Two-pion production in $pp$ collision

Experimental data for two-pion production are rare. From 1995 to 1998 new experiments were carried out with the PROMICE/WASA detector setup to measure this reaction close to threshold.

In proton-proton collisions five different two-pion production reactions are accessible, as shown in Tab. 1.1.

reaction channels
$pp \rightarrow pp\pi^+\pi^-$
$pp \rightarrow pp\pi^0\pi^0$
$pp \rightarrow nn\pi^+\pi^+$
$pp \rightarrow pn\pi^+\pi^0$
$pp \rightarrow d\pi^+\pi^0$

**Table 1.1:** Table of two-pion production channels in proton-proton collision

This work focuses on the charged two-pion production reaction  $pp \rightarrow pp\pi^+\pi^-$ , especially on the measurements at 750 and 775 MeV proton beam energy, where we performed runs of high statistics to record enough events necessary for getting differential cross section spectra. In Wolfram Brodowski's PhD thesis [Bro01] part of the results at 750 MeV have already been presented.

The reactions  $pp \rightarrow pp\pi^0\pi^0$  and  $pp \rightarrow pn\pi^+\pi^0$  have been measured between 650 and 775 MeV proton beam energy. The results are presented in Jan Johanson's PhD thesis [Joh00], together with those for  $pp \rightarrow pp\pi^+\pi^-$  at 650 and 680 MeV.



The total production cross section of the different channels can be decomposed into different isospin amplitudes  $M_{I_f I_{2\pi} I_i}$  [Dak83, Bys87, Joh02]. Here  $I_f$  denotes the isospin of the final nucleon pair,  $I_{2\pi}$  the isospin of the two pions and  $I_i$  the isospin of the initial nucleon pair.

$$(1.1) \quad \sigma(pp\pi^+\pi^-) = \frac{1}{6}|M_{101}|^2 + \frac{1}{120}|M_{121}|^2 + \frac{1}{8}|M_{111}|^2 + \sqrt{\frac{1}{180}}|M_{101}||M_{121}|\cos\phi$$

$$(1.2) \quad \sigma(pp\pi^0\pi^0) = \frac{1}{12}|M_{101}|^2 + \frac{1}{60}|M_{121}|^2 - \sqrt{\frac{1}{180}}|M_{101}||M_{121}|\cos\phi$$

$$(1.3) \quad \sigma(nn\pi^+\pi^+) = \frac{3}{20}|M_{121}|^2$$

$$(1.4) \quad \sigma(pn\pi^+\pi^0) = \frac{3}{40}|M_{121}|^2 + \frac{1}{8}|M_{111}|^2 + \frac{1}{4}|M_{110}|^2$$

Properties of the individual isospin components may be deduced from a comparison of the integral cross sections of the individual reaction channels.

## 1.4 Reaction subsystems

Having differential cross section spectra we are able to investigate the different subsystems of the reaction. Tab. 1.2 shows the subsystems with keywords that characterise each system.

subsystem	keyword
NN	FSI [Brü69, Sch98]
$\pi\pi$	$\sigma$ meson, ABC [Aba60, Aba61], “Anti-ABC” effect [Bel99]
$\pi N$	$\Delta$ system
$\pi\pi N$	$N^*(1440)$ system
$\pi NN$	exotic resonances ( $d'$ ) [Bro96, Bro01]

**Table 1.2:** Table of subsystems in the two-pion production reaction

Final state interaction (FSI) between the two nucleons is a common effect of pion production close to threshold. High momentum transfer is needed to produce pions, so the nucleons come close to each other. The necessary energy to produce the pions is taken from the kinetic energy of the nucleons. Now rather slow and tight together the nucleons experience the attractive nuclear forces.

The scalar, iso-scalar  $\pi\pi$ -channel corresponds to the still hypothetical  $\sigma$  meson, which was originally introduced to describe the medium-range part of the nucleon-nucleon forces. The ABC effect [Aba60, Aba61] has been observed in the  $(\pi\pi)_{I=I=0}$  channel. In the ABC effect the invariant mass spectrum of the  $\pi^+\pi^-$ -system shows an enhancement at low masses compared to phase space. However, with the MOMO detector setup at COSY an enhancement in the  $\pi^+\pi^-$ -system to higher masses has been observed [Bel99] (the “Anti-ABC-effect”).

The  $\Delta$  and the  $N^*(1440)$  are the first excited states of the nucleon. They play an important role for pion production close to threshold. The presumably involved production mechanisms go mainly via the excitation of one or both excited states, which explains the relative high cross sections near threshold.

In nature two groups of quark configurations exist: mesons consisting of two valence quarks (a quark and an anti-quark) and baryons built of three valence quarks. Apart from these two existing quark configurations, states of six bound quarks are allowed in QCD, too. For a long time the search for those states, referred to as dibaryons, has been performed. The search for the dibaryon  $d'$ , a proposed six quark state coupled to the  $\pi NN$  system and decoupled from the NN system, was also the starting point for this experiment [Bro96, Bro01].

## 1.5 Theoretical and experimental situation

In all recently discussed models, the two-pion production reaction mechanisms include an excitation of the  $\Delta$  and the  $N^*(1440)$  in either one or both of the participating nucleons. There is also a contribution of non-resonant terms. Fig. 1.1 shows the results of the calculation from [Alv98]. It shows the contribution of different reaction mechanisms to the integral cross section of the  $pp \rightarrow pp\pi^+\pi^-$  reaction. According to this model, the excitation of  $N^*$  with its subsequent decay  $N^* \rightarrow p(\pi\pi)_{l=0}$  gives the main contribution close to threshold. At intermediate energies within the range shown in the figure the other decay channel  $N^* \rightarrow \Delta\pi$  is getting stronger and stronger, as it is the main contribution there. Finally, at even higher energies, the simultaneous  $\Delta$  excitation of both nucleons is the leading reaction mechanism. This is understandable, because more energy is needed to excite twice the  $\Delta$  than is needed for one  $N^*(1440)$ . Single  $\Delta$  excitation leads only to the emission of a single  $\pi$  and does not contribute to two-pion production. The contribution of non-resonant terms is negligible in this calculation.

If these calculations are realistic, we expect to examine selectively the  $N^*(1440)$  at small and intermediate energies in this reaction. At present its properties are not well known, in particular concerning decay branching ratios [PDG00]. (See section 4.4.3, where the details are discussed.)

In addition Fig. 1.1 shows previously measured data of this reaction. The data mainly come from bubble-chamber measurements on hydrogen or on deuterium both with low statistics. New facilities with storage rings providing circulating proton beams and thin internal targets have created the possibility for new threshold experiments. They provide the necessary combination of high luminosity and low background. Together with new detector setups, a new generation of microprocessors as well as new storage media, the experimental situation has improved greatly. This makes it possible to take a large amount of data and process them quickly for analysis.

The measurements presented in this thesis as well as in recent analyses [Joh00, Bro01] were taken at CELSIUS<sup>1</sup> with the PROMICE/WASA detector setup, which was well suited for measuring charged particles and decay photons of neutral pions. The same reaction has been examined at COSY<sup>2</sup> with the COSY-11 setup [Gro97] and with COSY-TOF [Kre02, Ehr03]. Those very recent measurements are still in the process of analysis. Another possibility for probing the  $\pi\pi$ -

<sup>1</sup>Theodor Svedberg Laboratory, Uppsala, Sweden

<sup>2</sup>Forschungszentrum Jülich, Germany

*L. Alvarez-Ruso et al./Nuclear Physics A 633 (1998) 519–543*

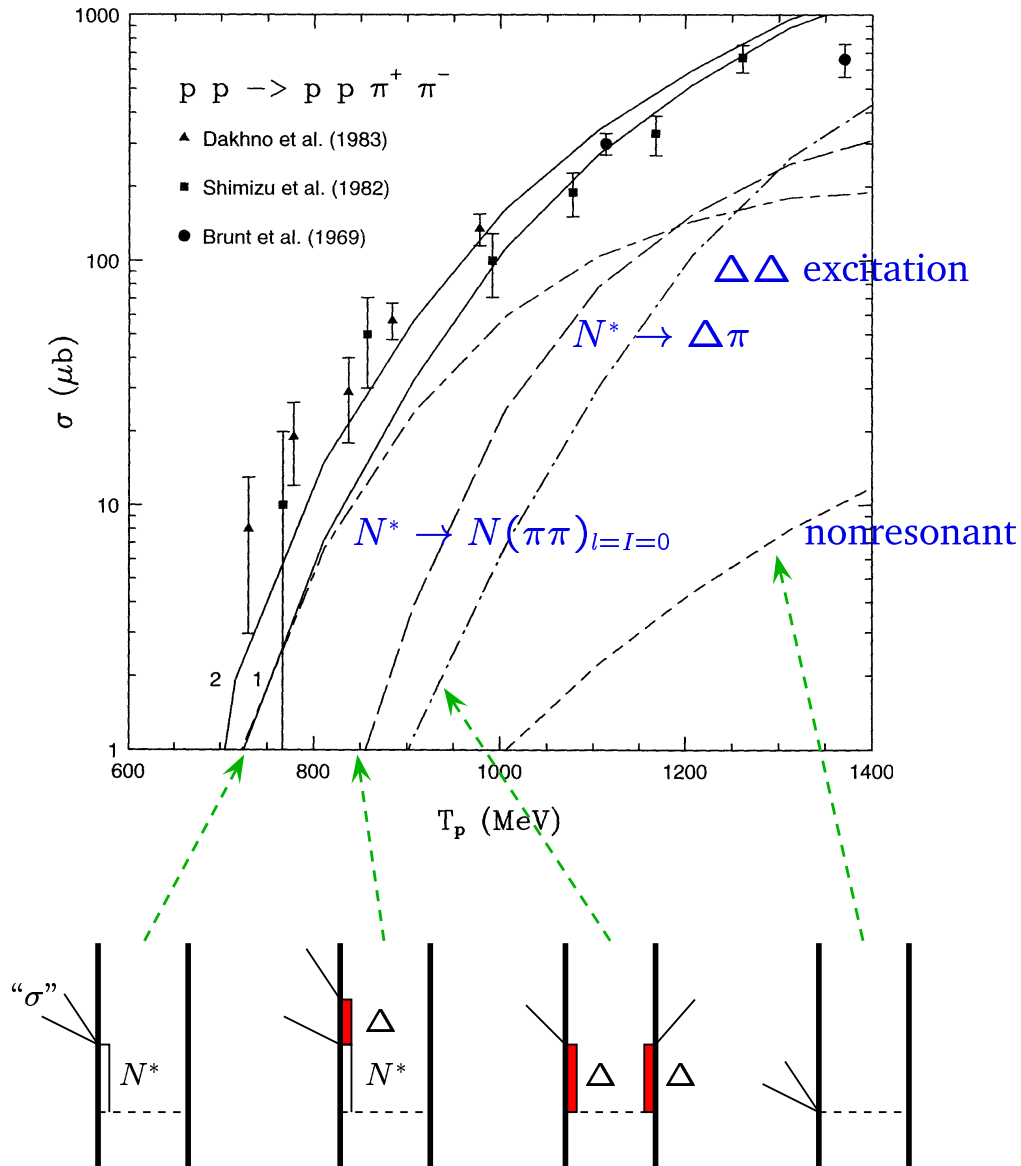


**Figure 1.1:** Known cross sections prior to our measurements. The existing data of integral cross sections on charged two-pion production are compared to calculations from [Alv98]. The leading order Feynman diagrams are shown to illustrate the figure.

system is pion induced pion production on nuclei ( $\pi A \rightarrow \pi\pi A$ ) which has been measured for the charged channels at TRIUMF<sup>3</sup> [Bon96, Bon97, Bon98, Bon99, Bon00] — one of the “meson factories” — and for the neutral channels with Crystal Ball [Nef00]. First test measurements of photon induced two-pion production have recently been carried out with the TAPS detector setup at MAMI<sup>4</sup> [Jan01]. The implications of these results will be covered in the last chapter (section 5.3) in the context with the question of chiral restoration.

<sup>3</sup>TRI University Meson Facility, Vancouver, Canada

<sup>4</sup>MAInz MIcrotron, Johannes Gutenberg-Universität Mainz, Germany

# 2

## Experimental Setup

This chapter gives a general view of the site where the experiment has been performed. It shows how the necessary beam is produced and gives a short note on the technique used for the target. It describes the components of the detector and gives a simplified explanation of the trigger and data acquisition system.

### 2.1 The Theodor Svedberg Laboratory (TSL)

The experiment that is presented in this thesis was performed at the national Swedish facility for accelerator based research, the Theodor Svedberg Laboratory (TSL) [TSL00] in Uppsala. Figures 2.1 and 2.2 show a side view and a top view of the buildings with the accelerators and beam lines. The Gustaf Werner cyclotron delivers accelerated ions ranging from proton beams up to xenon beams. It is used to feed the CELSIUS ring with ions.

### 2.2 The CELSIUS accelerator and storage ring

CELSIUS stands for Cooling with Electrons and Storing of Ions from the Uppsala Synchro-cyclotron. Light ion beams from protons up to  $^{40}\text{Ar}$  can be stored, cooled and accelerated in the ring. The maximum kinetic energy for protons is 1360 MeV, however, cooling can only be used up to an energy of 550 MeV. Fig. 2.3 shows a view of the ring. The ring has four  $90^\circ$  bends each consisting of 10 magnets sharing a common coil and four straight sections. One straight section is used for injection and another one at the opposite side is used for electron cooling. It also contains the RF cavity, used for accelerating the ions. Each of the remaining two sections has a target station: one with the hydrogen pellet target [Eks96] used with the new WASA  $4\pi$  detector (see chapter 5), the other with the cluster gas-jet target [Eks97] where the PROMICE/WASA detector setup, used by the experiment presented in this thesis, was located. The CELSIUS ring is operated in cycles of typically 5 to 15 minutes. First, ions from the cyclotron

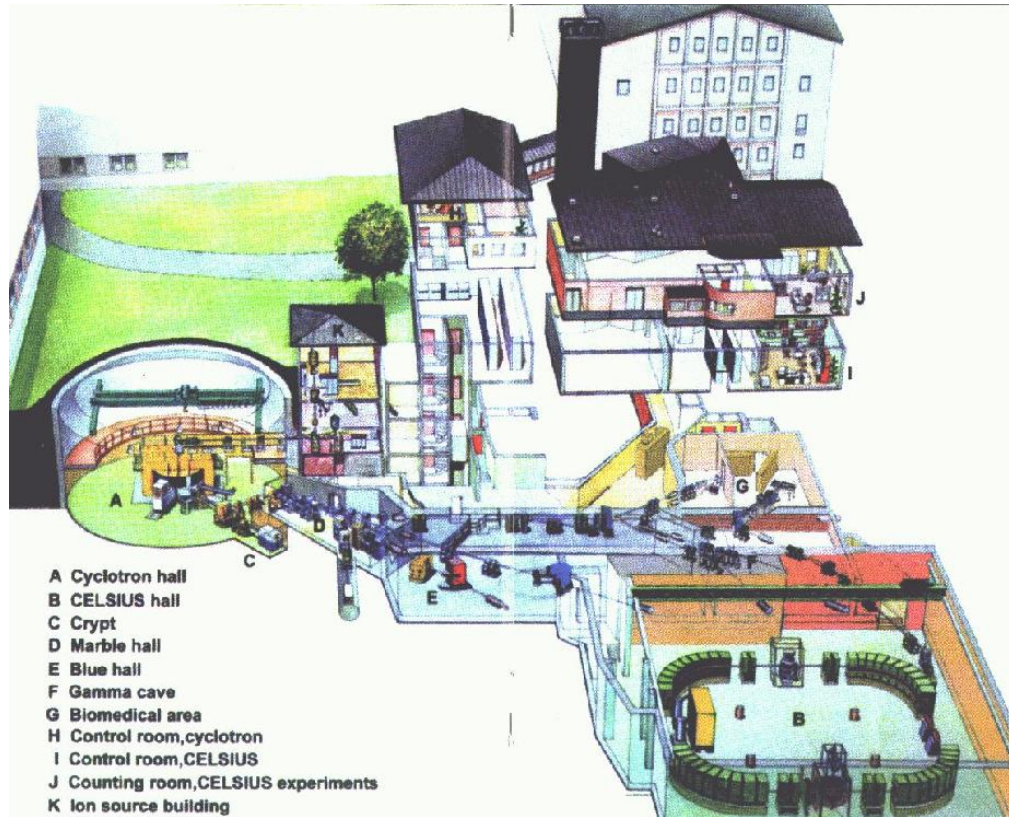


**Figure 2.1:** Cross section of the Theodor Svedberg Laboratory. The office building is visible at the top of the figure. In the lower part the accelerator laboratories are visible, located below the surface level. [TSL99]

are injected into the ring. The preferred method is stripping injection, in which  $H_2^+$ -ions are stripped off their electrons by using a carbon foil mounted at the entrance to the ring. The ions then break up into single protons. About  $1.1 \times 10^{11}$  protons can be stored in the ring with this technique. Next in the cycle, the ions are accelerated using the RF cavity. It provides an electric field that oscillates with the frequency of the revolution frequency of the ions stored in the ring. The magnetic field in the bending sections and the frequency of the RF cavity are slowly increased to accelerate the particles. When the desired energy is reached, the magnetic field is kept constant (flat top). During this time the data are usually collected. At the end of each cycle the beam is dumped by returning the magnetic field to the initial values used during injection. For the used 5 minute cycle the flat top lasts about 4 minutes. So we had a duty factor of about 80%.

The cluster gas-jet target provides a higher density and thus a higher luminosity than a gas-jet target. It is thin enough and, more importantly, windowless to reduce background. The clusters are formed by pressing gas through a cooled nozzle at temperature and pressure conditions close to phase transition conditions between gas and liquid. This gives a target thickness in the order of  $10^{14}$  atoms/cm<sup>2</sup>. With about  $10^{10}$  protons in the ring after acceleration, a luminosity of about  $5 \times 10^{30}$  cm<sup>-2</sup>s<sup>-1</sup> can be reached. After passing the beam the target is collected by a cryogenic dump, which must be occasionally regenerated during the experiment. To keep the pressure in the ring within the required region ( $10^{-9}$  mbar) a lot of high vacuum pumps are specially located in the area of

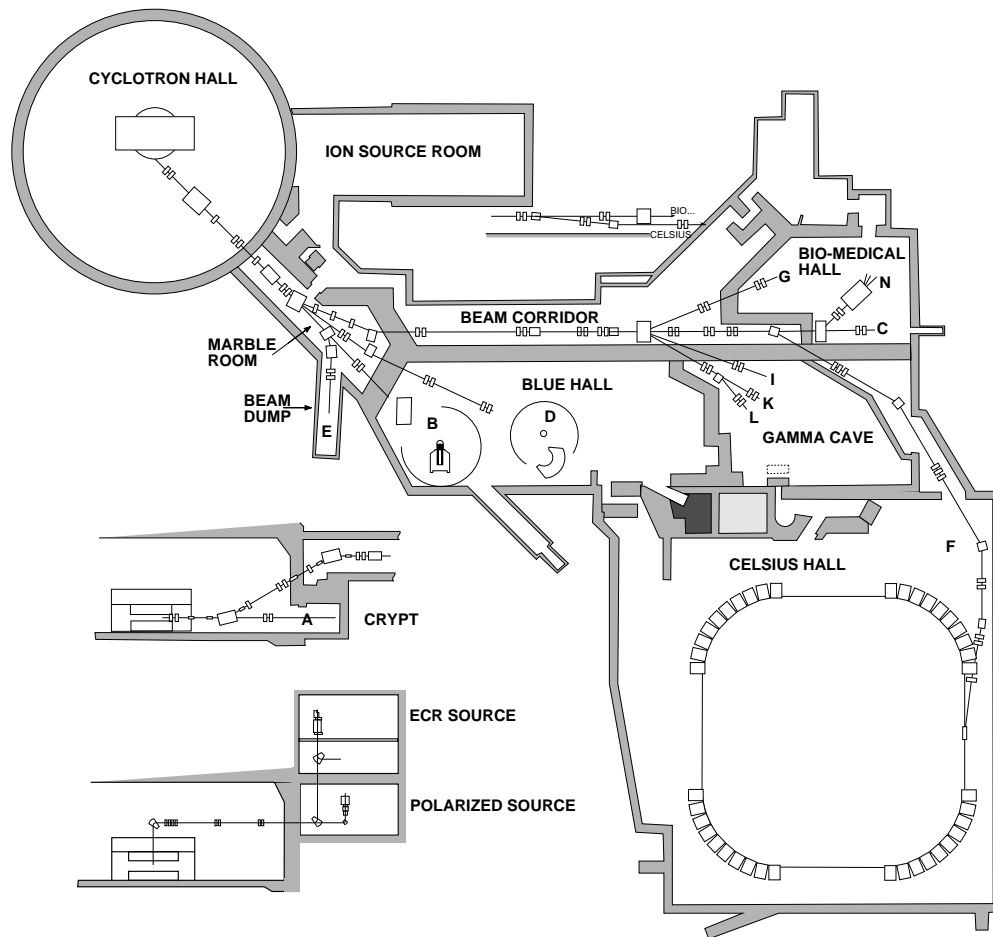


**Figure 2.2:** Top view of the Theodor Svedberg Laboratory. The long beam line from the cyclotron to the CELSIUS ring is clearly visible. [TSL92]

the targets.

## 2.3 The PROMICE/WASA detector setup

The PROMICE/WASA<sup>1</sup> detector setup [Cal96] was designed to measure meson production in the near threshold energy region.

A top view of the longitudinal section of the detector is shown in Fig. 2.4 as well as a side view in Fig. 2.5. The detector consists of two parts: the forward detector (FD) to measure the emitted charged particles, which tend to have small scattering angles close to threshold. The FD covers in principle an angular range from  $3^\circ$  to  $24^\circ$ . However the analysis should be restricted to angles from  $3^\circ$  to  $21^\circ$  to prevent particles from hitting the surrounding material, which does not allow full energy reconstruction. The central detector (CD) was designed to measure neutral mesons by their two decay photons.

The detector closest to the target in the FD and right behind the scattering chamber is the forward window counter (FWC) and has 4 elements, one in each quad-

<sup>1</sup>PRoduction Of Mesons In CElsius/Wide Angle Shower Apparatus

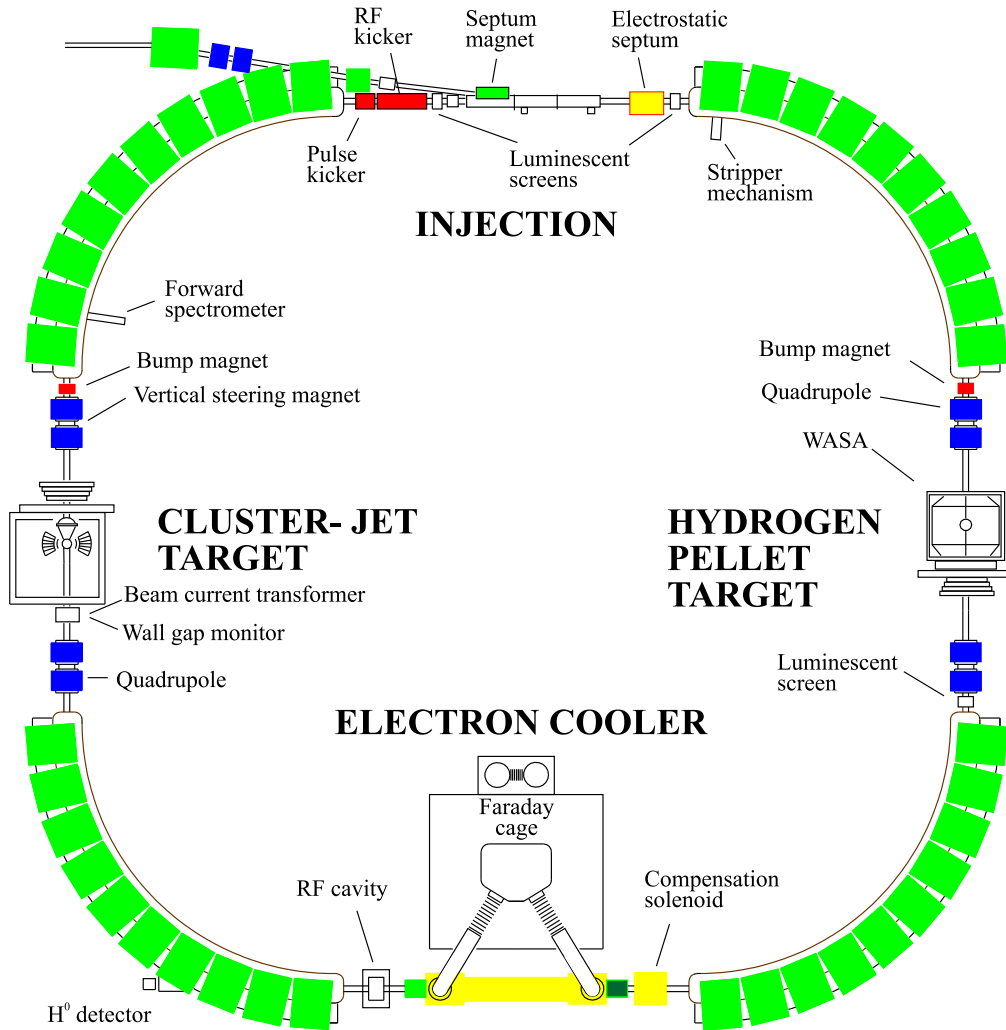


**Figure 2.3:** Setup of the CELSIUS accelerator ring: four bending sections with their magnets and four straight sections with installations for special purposes. [TSL96]

rant. Between each of the elements is a gap, which is just behind a supporting structure inside the scattering chamber.

Next is the tracker (FPC, forward proportional counter). It consists of parallel layers of thin walled individual drift tubes operated in the proportional region. Each module for measuring one coordinate has four layers of drift tubes. Four of those modules exist, each rotated by 45 degrees to each other [Dyr97]. However, in this experiment only the modules for  $x$  and  $y$  were connected and used.

The forward hodoscope (FHD) consists of three layers of 5 mm thick plastic scintillators. The first and the second layer are made of 24 spirally shaped (Archimedesian spirals) elements, twisted in opposite directions. The third layer has 48 straight elements. The structure of this detector makes it possible to reconstruct polar and azimuthal angle of particle tracks from the overlapping hits in the three layers. Fig. 2.6 shows example hits from two tracks in the FHD. For more tracks more and more ambiguities can be produced. They are resolved as soon as matching hits in the FPC are required.

The forward range hodoscope (FRH) consists of four layers of 11 cm thick plastic scintillators. Each layer has 24 elements which are divided like pieces of a cake.

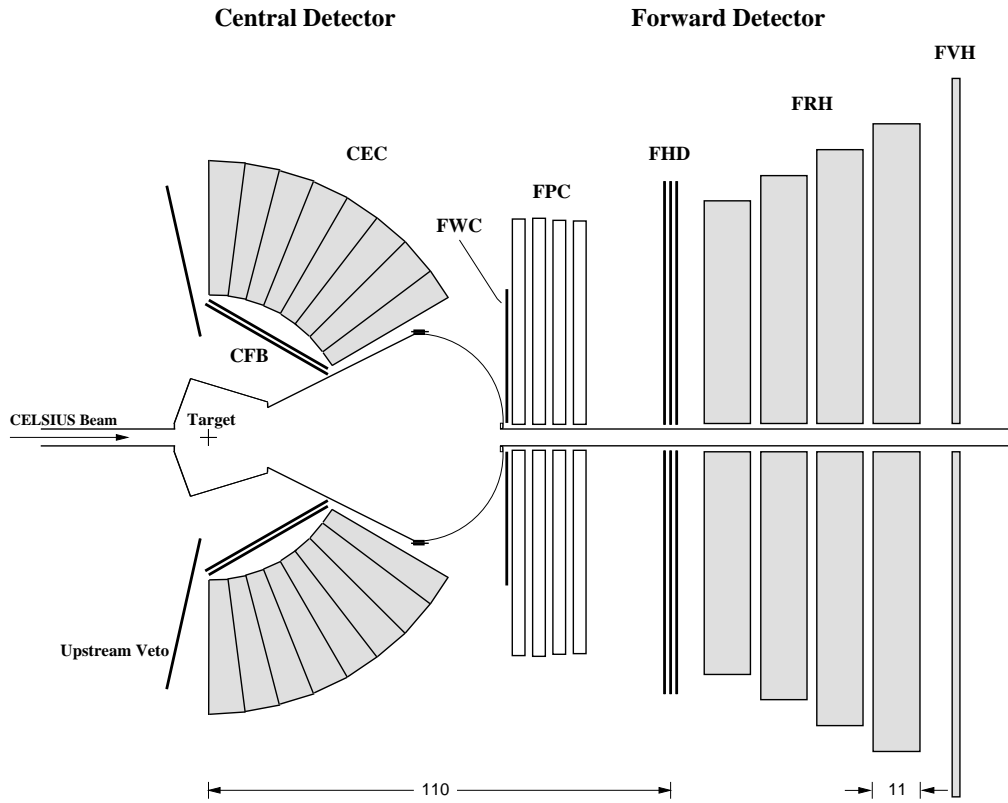


**Figure 2.4:** Top view of the longitudinal section of the PROMICE/WASA setup. The two main parts and the detector parts are indicated by their names, for details see text. [Bro01]

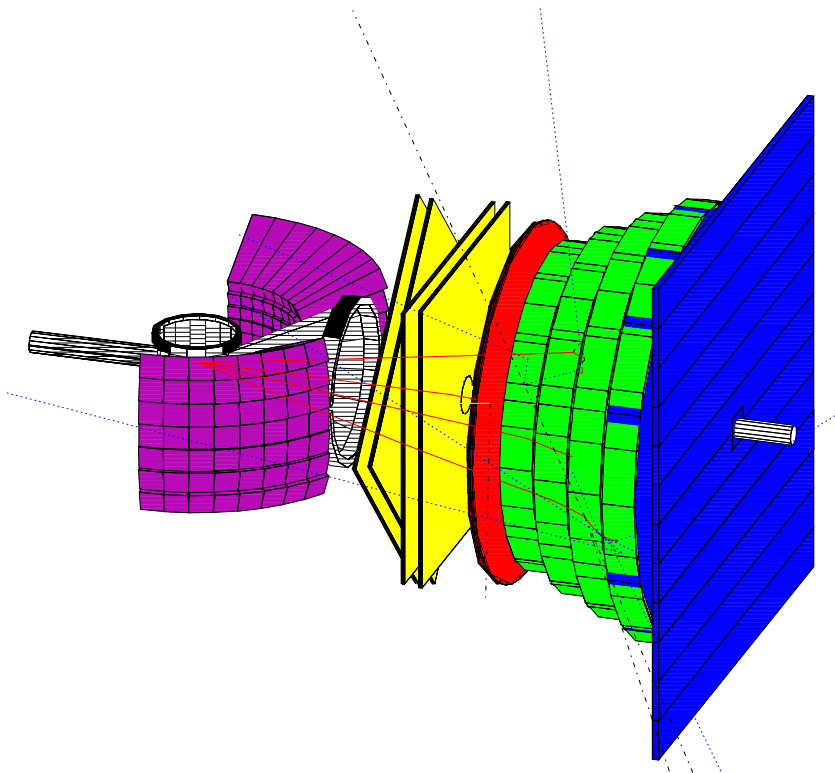


**Figure 2.5:** Three dimensional view of the PROMICE/WASA setup. It gives a more realistic impression of the appearance of the detector. [Sio96]



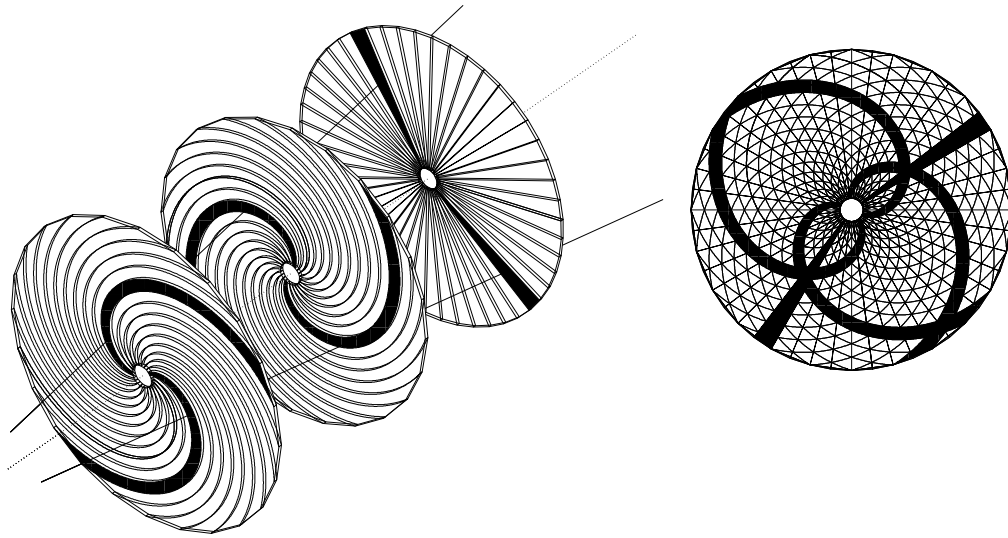


**Figure 2.6:** Design of the forward hodoscope. Two tracks pass the detector, each hitting one element in each plane. Due to their different shapes (left Archimedean, right Archimedean spirals and straight elements), it is possible to reconstruct the exact hit position by the intersection of all layers. [Wat94]

Two elements of the third plane of FHD always cover one element of FRH. FRH is used to measure the total kinetic energy of the particles by stopping them in the elements of this detector. Furthermore, by connecting the detector elements of the FRH and the third plane of FHD to a multi hit TDC (time to digital converter) positively charged pions can be identified by the delayed pulse technique, explained in section 3.4.9.

For particles having too much energy to be stopped in FRH, the forward veto hodoscope (FVH) is used to distinguish their tracks from slower particles. This detector consists of 12 horizontally arranged plastic scintillator bars, each 20 mm thick and with a width of 12 cm. Photo-multipliers are connected to both ends of the bars, which makes it possible to obtain horizontal hit information from time differences with a hit resolution of about 12 cm [Bro95].

The CD consists of two arrays of  $7 \times 8$  CsI crystals (CEC, Central Electromagnetic Calorimeter). Each crystal is 30 cm long. Each array covers the scattering angle from  $30^\circ$  to  $90^\circ$  and an azimuthal angle of  $\pm 25^\circ$ .

In front of each array the central fibre detector (CFB) was mounted. It consists of 20 horizontal plastic scintillator elements and of 28 vertical elements, each element with a thickness of 4.5 mm. It is used to discriminate charged particles from neutrals since a plastic scintillator has a low probability of interaction with neutral particles.

For the exact reconstruction of the energy of the particles it is essential to be sure about the stability of the gain of the photo-multipliers. A light pulser system [Zab94] is connected to all photo-multipliers which allows correction of the gain in the offline analysis (see section 3.4.4).

For more details of the detector setup see [Cal96].

## 2.4 The trigger and data acquisition system

The total signal rate of some detectors in this experiment is in the order of  $10^5$  per second. The trigger system is used to decrease this rate and reduce the interesting events to about 350 events per second, which is the rate the data acquisition system (DAQ) can cope with.

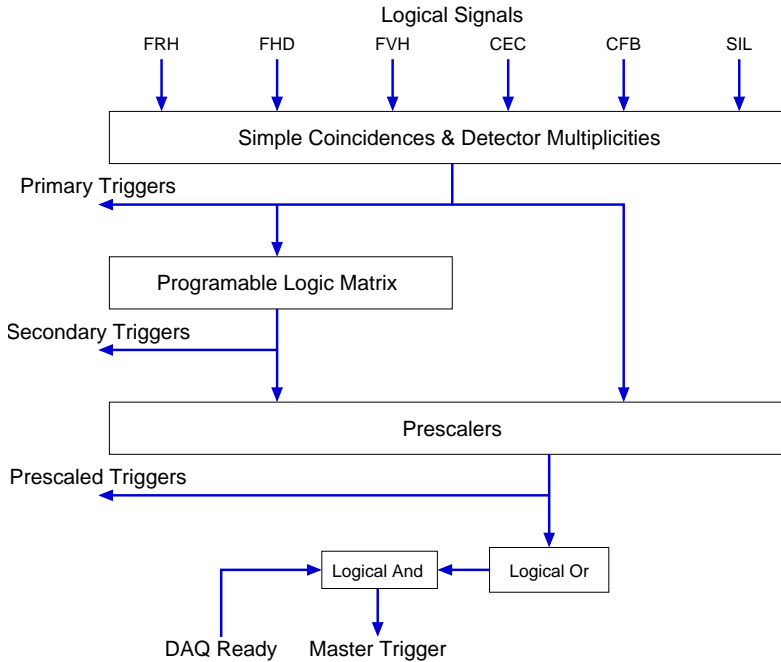


**Figure 2.7:** Schematic view of the trigger unit, excluding level adapters and delays for clarity. See next figure for the connection of the trigger unit in the DAQ system.

Trigger	Description	DAQ	factor
T1	FHD: at least one element in two planes	×	$2^{12}$
T2	T1*(FHD: at least two elements in any plane)		
W2	two FWC hits		
T5	two CFB planes hit in right or left side		
W1	one FWC hit		
T6	two CFB planes hit in right and left side		
T9	at least one $\gamma$ in CD		
T8	CEC left and right		
T7	one CEC hit		
T3	one FRH-1 plane hit	×	$2^8$
FVH	inverted FVH hit		
TR4	four hits in FRH-1		
TR3	three hits in FRH-1	×	$2^8$
T10	two $\gamma$ in CD	×	$2^0$
SIL	Silicium luminosity detector		
TJ3	three hits in FHD-3	×	$2^6$

**Table 2.1:** List of primary triggers used in the experiment. It shows the triggers that are connected to the DAQ and the pre-scaling factors used at one time in the experiment.

Trigger	Description	DAQ	factor
TWR32	TR3*TJ3*W2	×	2 <sup>0</sup>
TWJ32	TJ3*W2*FVH	×	2 <sup>2</sup>
SIL2	SIL*W1	×	2 <sup>2</sup>
TW42	TR4*W2		
TW2	T2*W2		
TW29	T2*W2*T9*FVH	×	2 <sup>3</sup>
TW1	T1*W1		
TW25	T2*W2*T5	×	2 <sup>1</sup>
TW15	T1*W1*T5	×	2 <sup>9</sup>
TW27	T2*W2*T7		
T14	(not active)		
THE3	(not active)		
TS	(not active)		
TPD	(not active)		
TW21	T2*W1	×	2 <sup>9</sup>
TLP	Light pulser event trigger	×	

**Table 2.2:** List of secondary triggers used in the experiment. It shows the triggers that are connected to the DAQ and the pre-scaling factors used at one time in the experiment. (The trigger TLP was specially connected: an inhibit on the other trigger was set shortly before the pulse. This provided this trigger without any dead-time, so that each light pulser event was recorded.)

All signals of the detector are connected to discriminators. With these logical signals and simple logical conditions the primary triggers are formed, such as particle multiplicities in one detector plane. The secondary triggers are made by connecting the primary triggers with a programmable matrix to more complicated conditions. From these two sets of triggers one can connect a subset to the pre-scalers, which in turn are connected with a “big OR” as master trigger to the DAQ, see Fig. 2.7. For a list of triggers used in the experiment see Tab. 2.1 and 2.2.

Each time a master trigger occurs and the DAQ is ready to handle the next event, all signals from the detectors are digitised. To do this the detector signals are connected to ADCs (amplitude to digital converter, in fact QDCs are used to convert the accumulated charge to digital) and to TDCs or LRTDC (the used multi hit TDCs also have a long range of about 8  $\mu$ s, this is why they are also referenced as LR for long range). The triggers are connected to TDCs, to act as a “better” pattern unit for the trigger condition of an event. They are also connected to a scaler (one should rather refer to this device as a counter), which counts the free rates of the trigger signals and which serves, via a clock on one channel, as a time stamp for an event. Each event is recorded on a tape. Each tape can be filled with about 4 Gbyte of data or 4 – 5 million events. In fact the CAMAC crate, which is shown in Fig. 2.8, was not used in the experiment.

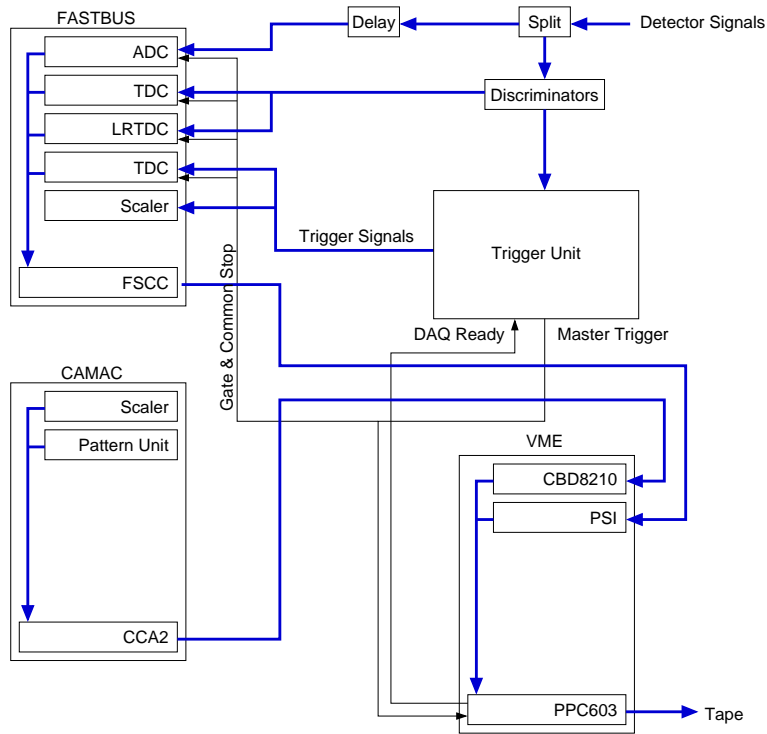


**Figure 2.8:** Schematic view of the DAQ (data acquisition) system, excluding level adapters and some delays for clarity. For the details of the trigger unit see previous figure.

## 2.5 The measurements

The data have been taken during two beam times. The measurement times are usually distributed in shifts of 8 hours. In April 1996 the data at the beam energy  $T_p = 750$  MeV (27 tapes in 23 shifts) and two thirds of the data at  $T_p = 775$  MeV (11 tapes in 10 shifts) were recorded. The last third of the data at 775 MeV was taken in March 1998 (4 tapes in 5 shifts). The data on the tapes are split into different runs (files). Each time when the conditions were changed or when about 1 million events had been recorded a new run was started. Usually the first run on a tape is a pedestal run, used for adjusting the position of no charge collection in the ADCs (see section 3.4.2). The values obtained from this run are used for the following data runs as zero position for the ADC values.

Two-pion production events have been selected throughout all tapes. However, only one single tape per energy and beam time period has been used for calibration and normalisation. For 750 MeV tape number WS0350 was used as reference tape for normalisation and energy calibration. For 775 MeV the tape with the number WS0383 was used for normalisation. For the energy calibration at this beam energy the calibration parameters of tape WS0350 were again applied at this energy. For the runs that were taken two years later in March 1998 the tape WS0535 was used for obtaining calibration parameters.

The main trigger in this experiment was the trigger TWR32, requiring three tracks in the FD. Due to energy and momentum conservation and the known beam momentum the reaction is fully determined by measuring three out of the four particles of the reaction  $pp \rightarrow pp\pi^+\pi^-$ . Since the  $\pi^-$  cannot be clearly identified, the two protons and the  $\pi^+$  are selected in the analysis.

# 3

## Analysis

The purpose of the offline data analysis is to extract differential cross sections of different observables. To perform this task the events on tape must be analysed to select the desired two-pion production events and to reconstruct their energy and scattering angles for each particle. To calculate cross sections the data are normalised by comparing two-pion production with proton-proton elastic scattering.

This chapter shows how the recorded events were reconstructed, how the task of normalisation was performed and how the data was corrected for acceptance and efficiency in order to compare them with different models.

### 3.1 Analysis tools

The tasks of the data analysis are carried out using computer programs for the reconstruction of the recorded events, for the simulation of the detector performance and for the calculation of simulated events.

The programming language Fortran is traditionally used in high energy physics as it is used for programming the CERNLIB [cern] and GEANT3 [geant3]. These packages are used together with the code written by our collaboration to make detector response simulations [Ca197]. A more modern language is C++ [Lip98, Str99] which can be used together with the package for histogramming and graphical representation called “root” [root]. This language and this package have been used throughout the work for this thesis. New applications for the event reconstruction and the simulation of events have been written. By using a object-oriented design [Boc94] these programs are much more readable and maintainable in comparison with old-fashioned procedural programs, especially if they use a lot of short named and global variables as the CERN package does. A new development at CERN is the package GEANT4 [geant4], also entirely written in C++, but it is presently not used for the simulation of our detectors. Only core parts like random number generators, three vectors and the “System of Units” are included in the new development presented here.

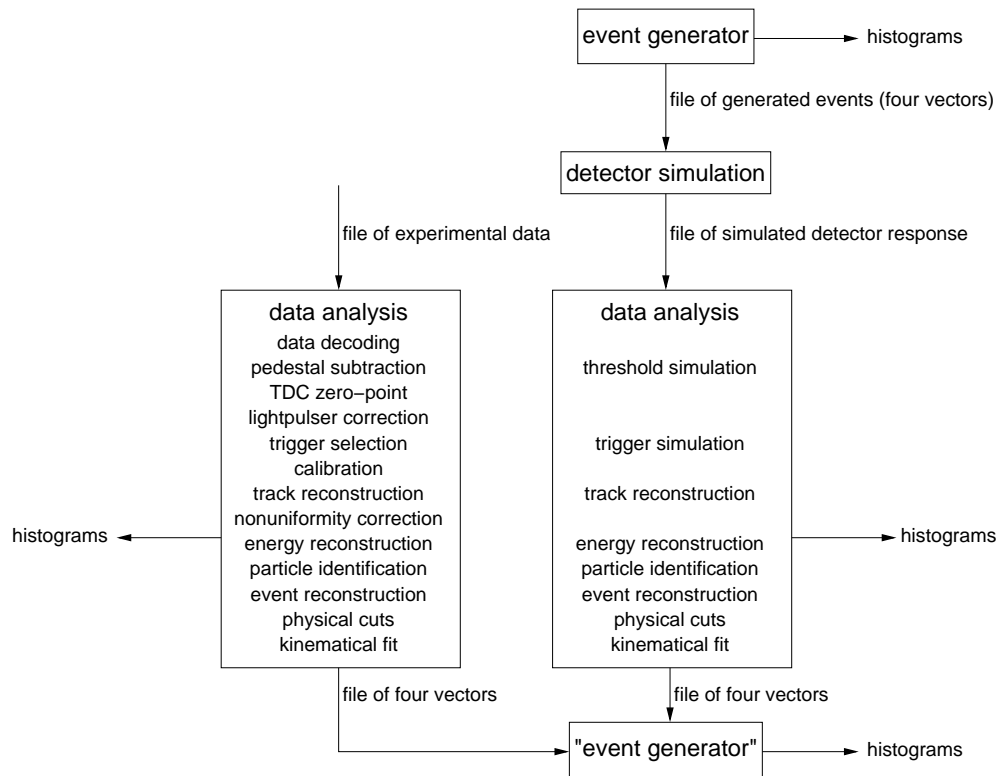


**Figure 3.1:** Flow chart of the analysis procedure. It shows where the different programs take action. Note that the data analyses for real data and simulated detector response are slightly different. For more details see text. The event generator in quotation marks at the bottom is used to histogram four-vector files coming out of the analysis chain, to fill the same histograms in all analysis steps (see section 3.6 later in this chapter).

## 3.2 Event generator

An object-oriented design was used for the event generators. The event generators are implemented in the code as classes derived from a virtual base class defining the interface for all event generators. By specialisation the generators are made more and more complex. Usually all generators are specialisations of a phase space generator. After defining the masses and momentum of the beam, the mass of the target as well as the masses of the outgoing reaction particles, it produces events with probabilities corresponding to the available phase space volume. The same algorithm is implemented as the one which is used in GENBOD, which is a subroutine in the CERNLIB. Then, model calculations are implemented by modifying the weight of events, by multiplying a weight at each calculation step with the previous weight.

A special generator can be used to generate events for all models with the same weight and still distributed according to their primary weights. To work correctly it has to be initialised with the maximum weight  $w_{\max}$ , that can occur in the corresponding model. This procedure may be used for all models, because it is implemented as a wrapper around the event generators' base class, translating weights to distributions according to the following scheme: Produce an event with the weight  $w$ . Take a random number from a flat distribution with  $0 \leq p \leq w_{\max}$ . If  $w \geq p$  use the event, otherwise start again.

The event generator can also handle four-vector input files. This allows the recording of identically defined histograms for the model in full acceptance, for simulated events and for real data as well as for the output of other sources (with L. Alvarez-Ruso model calculations were exchanged on an event basis). This is heavily used during the process of acceptance and efficiency correction and for the comparison of different reaction models.

### 3.3 Detector simulation

The aim of the detector simulation is to perform a simulation of the detector response as close as possible to the real detector. This was done using the program GEANT3. In user subroutines one defines the detector setup, the starting point and direction of the reaction particles; how to translate the deposited energy to detector response in ADC and TDC devices and also which processes should be included in the tracking of particles through the different materials. It is also possible to do special tasks during the tracking of particles after each simulation step. At each step the particle has travelled a small pathway ( $\Delta x$ ) through the virtual detector and has deposited a small amount of energy ( $\Delta E$ ). These values are used for the simulation of the quenching effects of plastic scintillator material. Quenching is a saturation effect by recombination of ionised atoms without producing light, becoming stronger if there is a higher ionisation density. The simulation of this effect is implemented according to the following formula [Leo94, Bir51] and a factor is given at each tracking step by which the apparent energy has to be reduced.

$$(3.1) \quad F\left(\frac{dE}{dx}\right) = \frac{1}{1 + kB\frac{dE}{dx} + C\left(\frac{dE}{dx}\right)^2}$$

At each step a quotient  $\Delta E/\Delta x$  is supplied, which is a good approximation of the

particle	$kB$ [cm/GeV]	$C[(\text{cm/GeV})^2]$
p	12.6	0
$\pi$	11.4	0
$\mu$	11.4	0

**Table 3.1:** Table of quenching parameters for plastic scintillator used in the detector simulation

differential quotient  $dE/dx$ . Tab. 3.1 gives the parameters used for the different particle types [Roz88].

This application reads in four-vector files from the event generator and delivers a special output-format with the hits of the detector elements, which can be entered into the analysis program, as with real data from the experiment.

## 3.4 Data analysis

This section describes the data analysis and how it is done for both real and simulated data. Fig. 3.1 shows a schematic flow chart of the analysis process. Please note the differences between the chain for real data and for simulated data.

### 3.4.1 Decoding

The data from the experiment are written on tape or disk in a special format. The first step is to extract each individual event from this file. The information of ADCs and TDCs are connected to a channel in a certain device (“Fastbus” module) that is mounted into a certain slot in a certain crate, where the individual signals were connected to with cables. The scheme: crate, slot, channel and device must be translated to a detector, plane, element and kind of information (time or energy) scheme. This referencing of the information is called decoding. (See also E.3.)

For most detectors this is straight forward to do. For the FPC, however, more decoding must be done. Inside the electronics the individual channels are fed to the cables which are not in their natural order along their measuring axis. So a group of 16 cable numbers must be always mapped to their position in the detector, see Tab. 3.2. In addition one channel of the measuring device is used

cable number	0	1	2	3	4	5	6	7	8	9	10	11	12	13	14	15
element/position	4	1	6	3	0	5	2	7	8	13	10	15	12	9	14	11

**Table 3.2:** FPC wire to element mapping. This table shows how a group of 16 wires is mapped to the position in the detector coded in the element number.

for two elements using a time sharing method. Half of the signals of the FPC are delayed and added electronically to the other ones. These two possible hits in one channel must be separated from each other.

### 3.4.2 Pedestal subtraction

The ADCs (actually QDCs) collect the charge of the detector signal during a given gate defined by the main trigger. Usually the devices are not adjusted to deliver a zero value, when there is no signal on a cable during the gate. This non-zero value is called pedestal. The adjustment of shifting the pedestal to zero must be done as the first step in the offline analysis. For each channel a value is acquired from special pedestal runs, when all detector channels are recorded to tape. Usually a suppression of pedestal values is turned on for the production runs. The pedestal itself has a distribution around a mean value depending on the noise on the cable. So this noise must also be suppressed by applying a small threshold.



### 3.4.3 TDC zero-point

For the time measurement it is necessary to define a zero point for each detector channel. Differences for the zero point in different detectors arise from the fact that the different detector elements have different cable lengths and internal signal travelling times in different devices. Only hits within a certain time around the reference time interval are considered as immediate hits, belonging to a given event.

### 3.4.4 Light pulser correction

All photo-multipliers are monitored with a light pulser system. This signal can be used to control and correct the gain for each element. A light pulser signal is released with a frequency of 1.5 Hz. A reference value is defined for each element. When a light pulser event is going to be analysed, the reference value is compared with the actual signal in this event. A correction value for following events is calculated to shift this light pulser signal to the reference value. Each time the average of the last 10 light pulser values is taken to obtain a smoother correction in the analysis. For an unknown reason light pulser events occasionally occur which are completely out of range. These events are left out, if there is a single deviation of more than 20% (see Fig. 3.2 and 3.3). The FHD photo-multipliers show a dependence of the response to the light pulser that is correlated to the cycle time of the CELSIUS beam (see also [Bro01]). This correlation is not visible in case of FRH. The element of FRH shown in Fig. 3.3 shows a spontaneous fluctuation in the gain of the PM tube.

### 3.4.5 Trigger selection

The electronics of the trigger unit provides signals of a large number of trigger conditions. When a certain trigger condition is set, it is indicated by a hit in the TDC channel belonging to that trigger. However, during the offline analysis to select events, that are collected under a certain trigger condition, only events with those trigger conditions that are actually connected as triggers to the data acquisition should be selected (see Tab. 2.1 and 2.2, triggers with indicated pre-scaling factors are connected to the DAQ). Otherwise a biased sample of events due to the overall trigger selection setting during the data taking will be obtained.

Trigger T1 and T3 are used for selecting  $pp$  elastic scattering. Trigger TWR32 was the trigger for collecting charged two-pion production events. (See section 2.4 for the available triggers.)

### 3.4.6 Energy calibration

At this stage of the analysis an initial estimation of the translation from ADC value to energy is done. In the case of the FRH a second order translation (quadratic) and in the case of the FHD a first order (linear) parameterisation was used. This value will be modified later throughout the analysis by the non-uniformity correction. The calibration parameters have been taken from [Bro01].

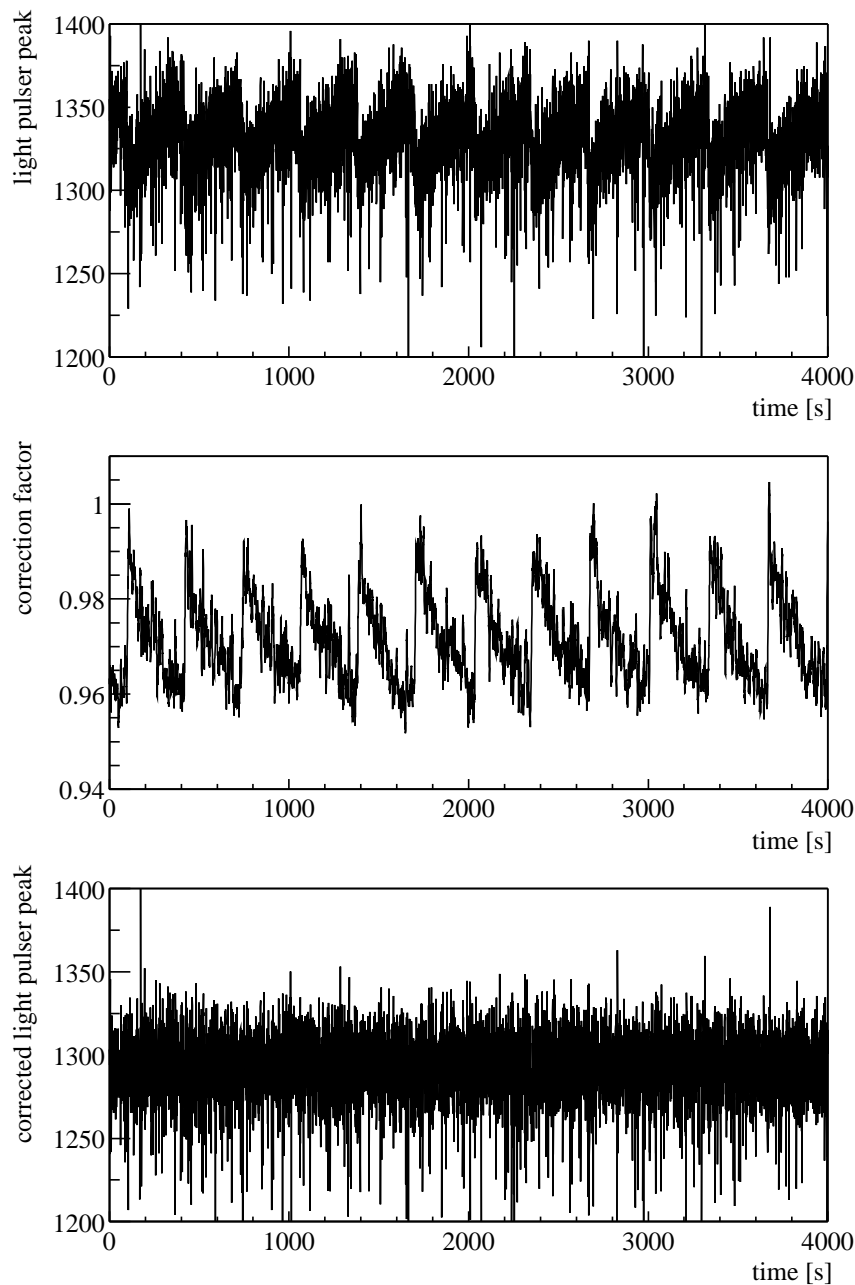


**Figure 3.2:** Light pulser correction for one element of the straight FHD plane. Top: light pulser peak position, middle: correction value, bottom: corrected light pulser peak position. The correction factor for this tape is generally shifted to round about 98%, compared to the reference tape, where it is around 100% by definition. For this element a regular short term change in the gain is visible, which could be connected to the accelerator cycle of 5 minutes

In his work he gives a detailed description of how the parameters have been obtained:  $pp$  elastic scattering was used for adjusting the low energetic part in the energy spectra. These particles have high energy and break through all the layers and are nearly minimum ionising. The reaction  $pp \rightarrow pp\pi^0$  was used for the high energetic part. This reaction delivers a continuous energy spectrum for the protons. There are particles with just the right amount of energy to stop at the end of a specific layer and thus deposit as much energy as possible in this layer.

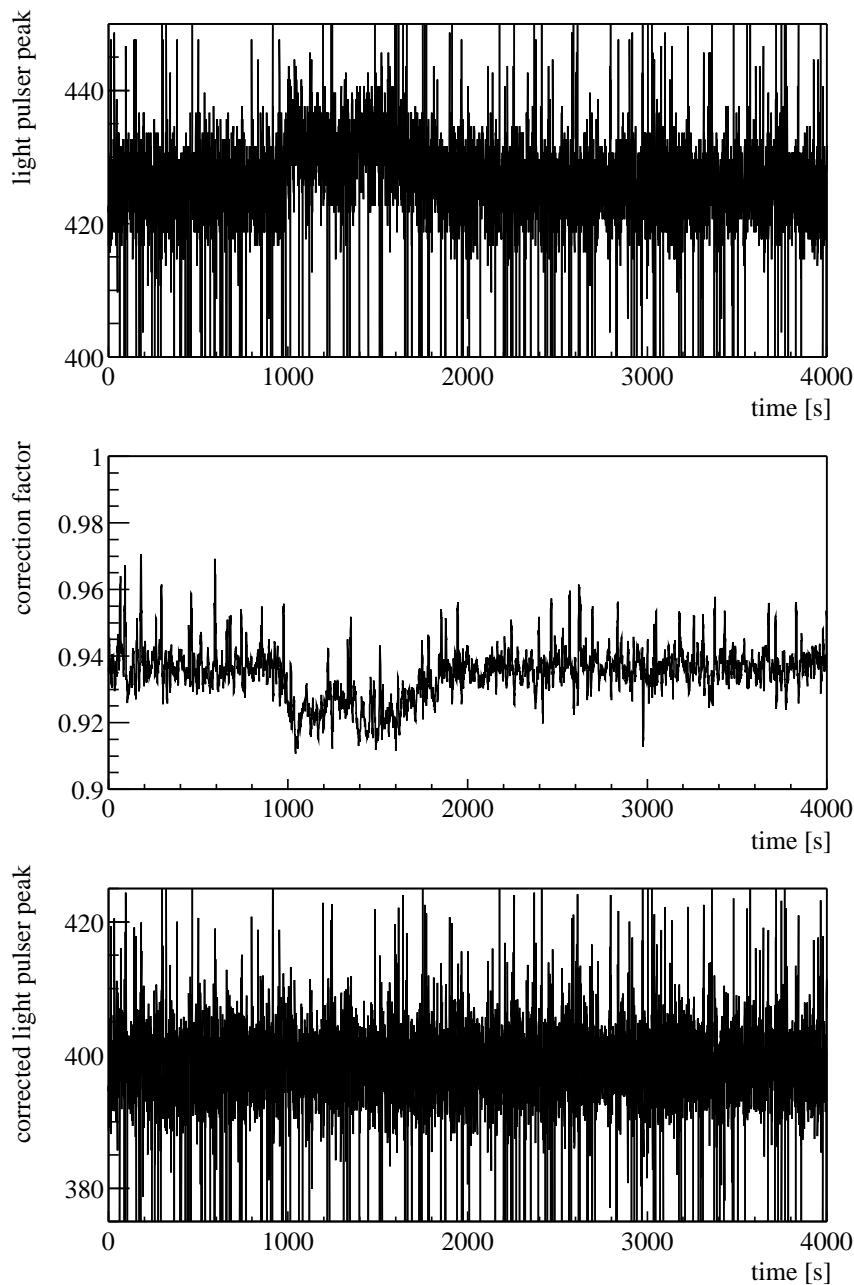


**Figure 3.3:** Light pulser correction for one element of the FRH. Top: light pulser peak position, middle: correction value, bottom: corrected light pulser peak position. The correction factor for this tape is generally shifted to round about 94%, compared to the reference tape, where it is around 100% by definition. In this element a spontaneous fluctuation of the gain is visible.

### 3.4.7 Track reconstruction

The algorithm for the track reconstruction is a completely new development, so it differs from that used in [Bro01, Joh00]. First the detectors shaped like pieces of cake are connected to tracks, starting with the FHD detector's straight layer and continuing with the FRH planes. Then a loop over all combinations of left and right spirally shaped elements of the FHD detector is performed. If a matching intersection from these two layers to an already existing track in the straight

elements is found, it is connected to one single track. Similarly all possible combinations of FPC hits are generated and the matching ones are connected to the already existing tracks. By connecting the FPC coordinate with the beam-target vertex, the scattering and azimuthal angle are calculated.

For the cleanup of the track buffer the following conditions must be fulfilled: The scattering angle should be between  $3^\circ$  and  $21^\circ$ . The track should have hits in the FPC. The condition of having no missing element is already fulfilled from the algorithm of connecting the hits.

Later on in the analysis chain, tracks are removed with elements belonging to two tracks.

### 3.4.8 Non-uniformity correction

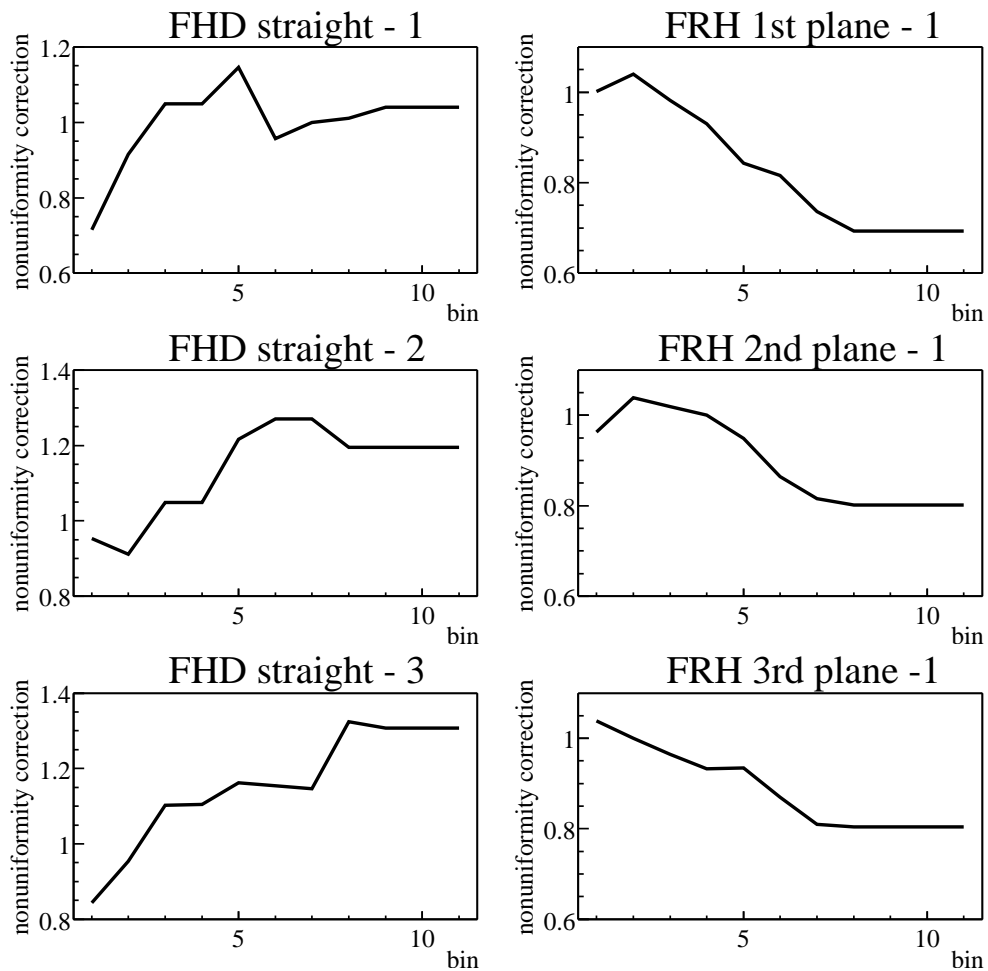


**Figure 3.4:** Graphs of the non-uniformity correction for some detector elements. Note that the four outer bins in case of FRH and the three outer bins in case of FHD are set to the same values.

The detector elements of FRH and FHD do not have the same light output efficiency at different positions of the detector. This effect is corrected by applying a correction dependent on the radial position of the hit. 11 radial bins are defined and between the bins a linear interpolation is applied. Outer bins, where the

correction factor could not be determined because of lack of statistics, are set to the value of the most outer bin which has a valid factor. Experimental data of elastic scattered protons are compared to simulated data. The non-uniformity parameters are adjusted, so that the spectra of experimental data of elastic scattered protons peak at the same position as simulated data do. Fig. 3.4 shows the non-uniformity values for some elements of the detector.

### 3.4.9 Particle identification

For the identification of protons a cut in the  $\Delta E$  over  $E$  plot is used, see Fig. 3.5. This method uses the fact that different particles have different characteristic energy losses ( $\Delta E$ ) in a thin detector ( $\Delta x$ ) compared to their total kinetic energy. Or in other words they have different characteristic  $\frac{dE}{dx}(E)$ .

For identifying the positively charged pions the method referred to as delayed pulse technique is used. In matter positive and negative pions behave differently. Negative pions are captured by a nucleus forming a pionic atom and are absorbed very fast. Positive pions behave as if in vacuum and decay with a mean life time of  $\tau = 26$  ns into muons. This decay is too fast to be measured by our electronics, so the subsequent decay of the muon to the positron with  $\tau = 2.2$   $\mu$ s is used and this is the reason for using multi-hit TDCs for measuring hit times in this experiment.

So tracks are considered to be a  $\pi^+$  if there is a delayed hit in the detector element where the particle has stopped or in one of the neighbouring elements. The efficiency for this identification is about 69% [Bro01] with a substantial systematical uncertainty (see 4.2.1). For further cleanup the pion is expected to be in the characteristic  $\Delta E$ - $E$ -region. Fig. 3.6 shows a histogram of the considered delayed hits with a fit of an exponential function giving the mean life time.

As said before,  $\pi^-$  is not identified and reconstructed in the analysis.

### 3.4.10 Energy reconstruction

The energy actually measured in the plastic scintillators is less than the particle had originally when it started. This comes from dead material in front of the detectors where the particles already loose energy. In addition there is quenching in the plastic scintillator material. This is the already mentioned effect from saturation in the material if there is a high ionisation density leading to direct recombination without producing light. Both effects are adjusted together by applying a correction. This correction is naturally dependent on the particle type, because both effects are different for different particles. Fig. 3.7 and 3.8 show how the correction is obtained both for protons and pions in detector simulations by comparing the “measured” energy with the true one, which is known in simulations. The “measured” energy is the one obtained from the detector simulation by the propagation of the generated event through the virtual detector.

The scatterplots show on the  $x$ -axis the “measured” (or deposit) energy and on the  $y$ -axis the ratio true energy divided through “measured” (or deposit) energy.

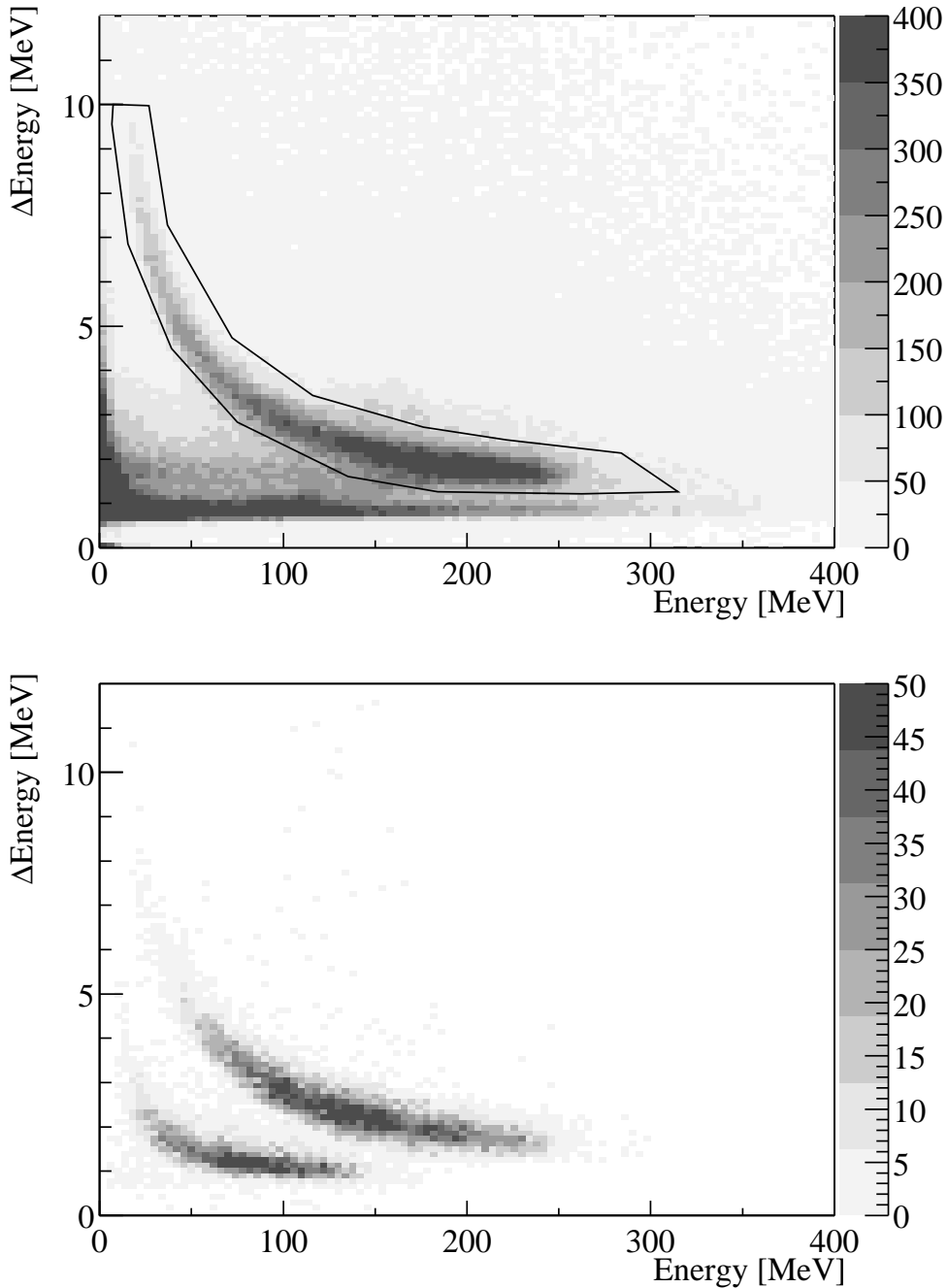


**Figure 3.5:** The upper scatterplot shows the  $\Delta E$ - $E$ -plot for the selection of protons.  $\Delta E$  is the information from the straight element in FHD.  $E$  is the information from all FRH elements with a hit from this track. The line in the scatterplot indicates the cut used for proton track selection. The lower part shows the  $\Delta E$ - $E$ -plot for the finally selected two-pion production events, now also the pion “band” (lower “band”) is clear of background.

The simulated particles are distributed over the whole FD detector with a kinetic energy from 0 to 400 MeV. So the correction is obtained by fitting a correction curve into the upper histograms to the band that encloses the distribution in the lower left, where most of the particles are located. The band right in the middle of the distribution comes from punch-through particles not depositing the whole kinetic energy in the detector. Those events are rejected in the analysis

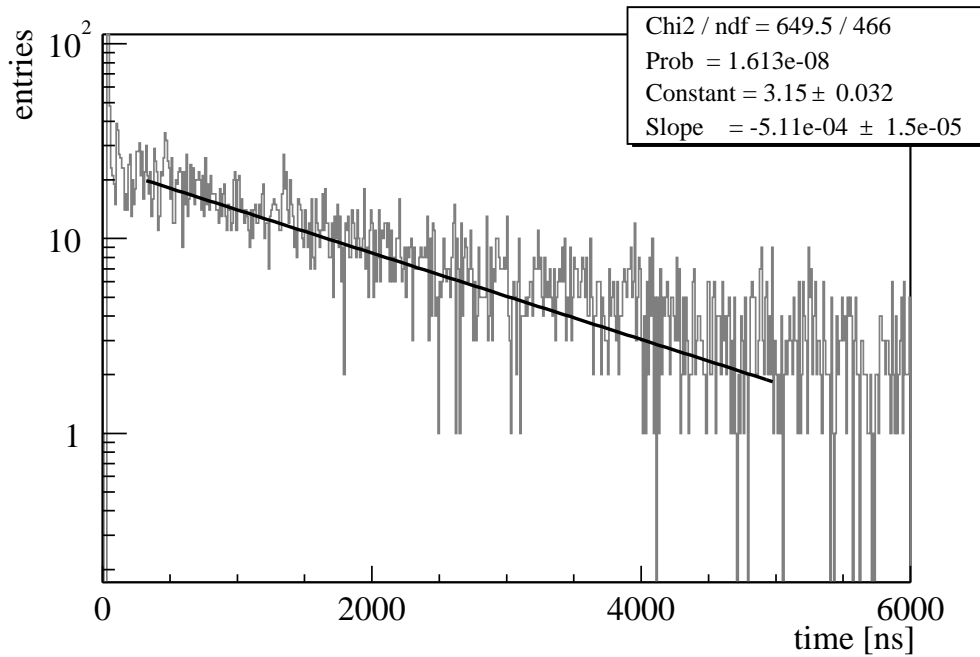


**Figure 3.6:** Spectrum of the distribution of the delayed signals from  $\pi^+$  tracks. An exponential function is fitted to the spectrum. The slope translates to  $1.96 \mu\text{s}$ , which fits reasonably well to the mean life time of  $2.2 \mu\text{s}$  of a muon.

by testing if there is a hit in the FVH. The rest of the distribution comes from nuclear reactions where a part of the kinetic energy is carried away by neutral particles. The lower histograms illustrate how the correction works, showing the factor on the  $y$ -axis after applying the correction.

### 3.4.11 Event reconstruction

If the desired number of tracks is found in a recorded event and if they are from the desired particle type, then this event is selected and the tracks are put together to form one event.

The four-vectors of these particles are calculated from the reconstructed information. As is the case for  $pp\pi^+\pi^-$ , tracks that are not measured (here the  $\pi^-$ ) are reconstructed from the existing ones by applying energy and momentum conservation.

### 3.4.12 Physical cuts

Having now fully reconstructed events, there is still a lot of background from other reactions in the selected events, coming mainly from  $pp \rightarrow pp\pi^0$  and the subsequent Dalitz decay of the  $\pi^0 \rightarrow \gamma e^+ e^-$ , which can lead to at least three charged particles hitting the FD, thus fulfilling the main triggers' hit condition. So these events contribute as the main background of the trigger. From a rough calculation it is already clear, that only about one out of 50 events is from two-pion production: The  $pp \rightarrow pp\pi^0$  cross section at  $T_p = 750 \text{ MeV}$  is around  $\sigma = 3.8 \text{ mb}$ ; the Dalitz decay has a branching ratio of about 1.2% giving a cross

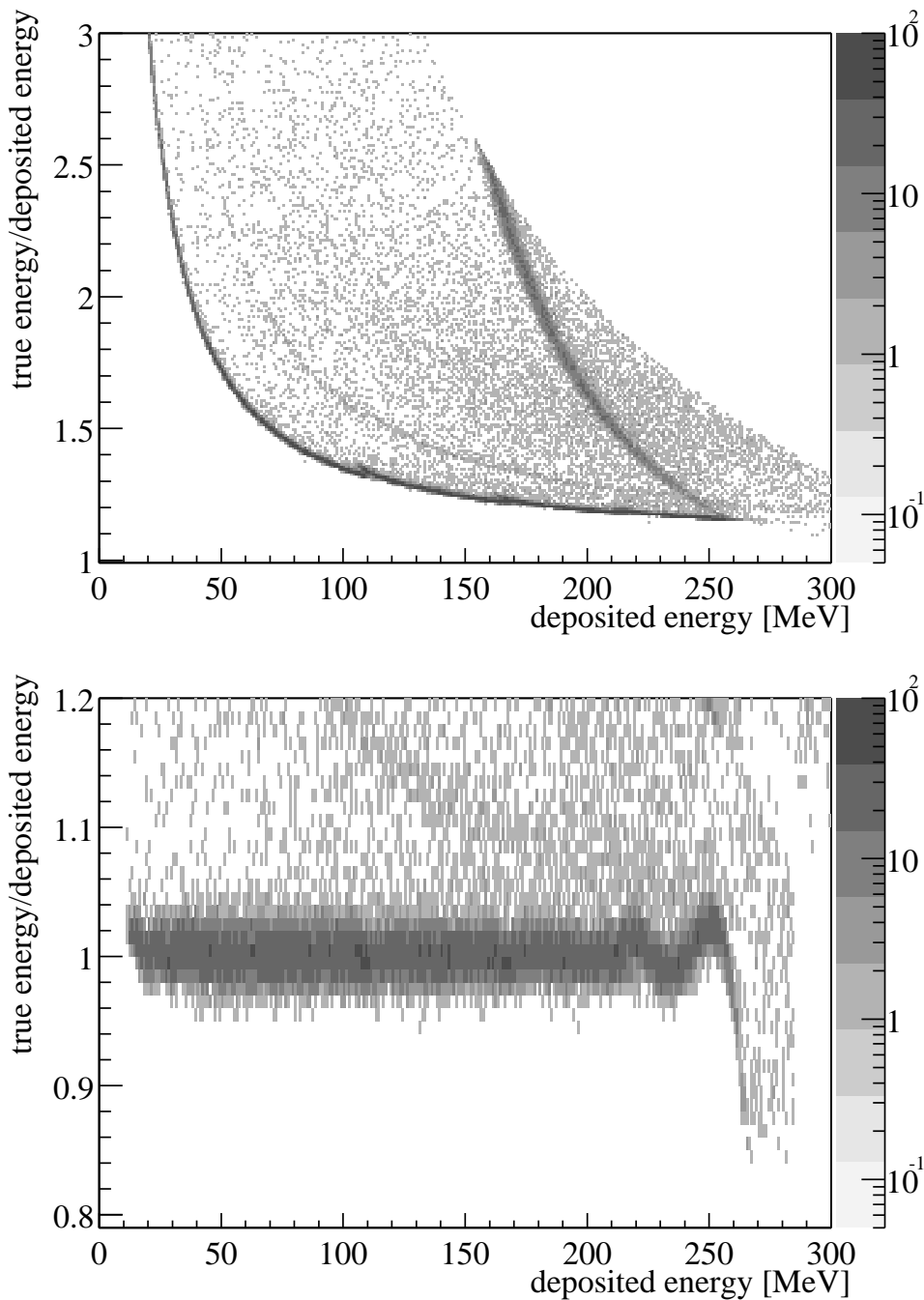


**Figure 3.7:** The upper scatterplot shows the combined effect from dead material and quenching for protons in the plastic scintillators. This plot is generated from the detector simulation, where the incident particle energy is known. The simulated protons are distributed over the whole FD detector with a kinetic energy from 0 to 400 MeV. Most particles are lying in the small band that is enclosing the distribution in the lower left part. The back-bending part is from punch-through particles not depositing the whole kinetic energy in the detector. The rest of the distribution comes from nuclear reactions where a part of the kinetic energy is carried away by neutral particles. The lower scatterplot shows the effect after including the correction for quenching and dead material.



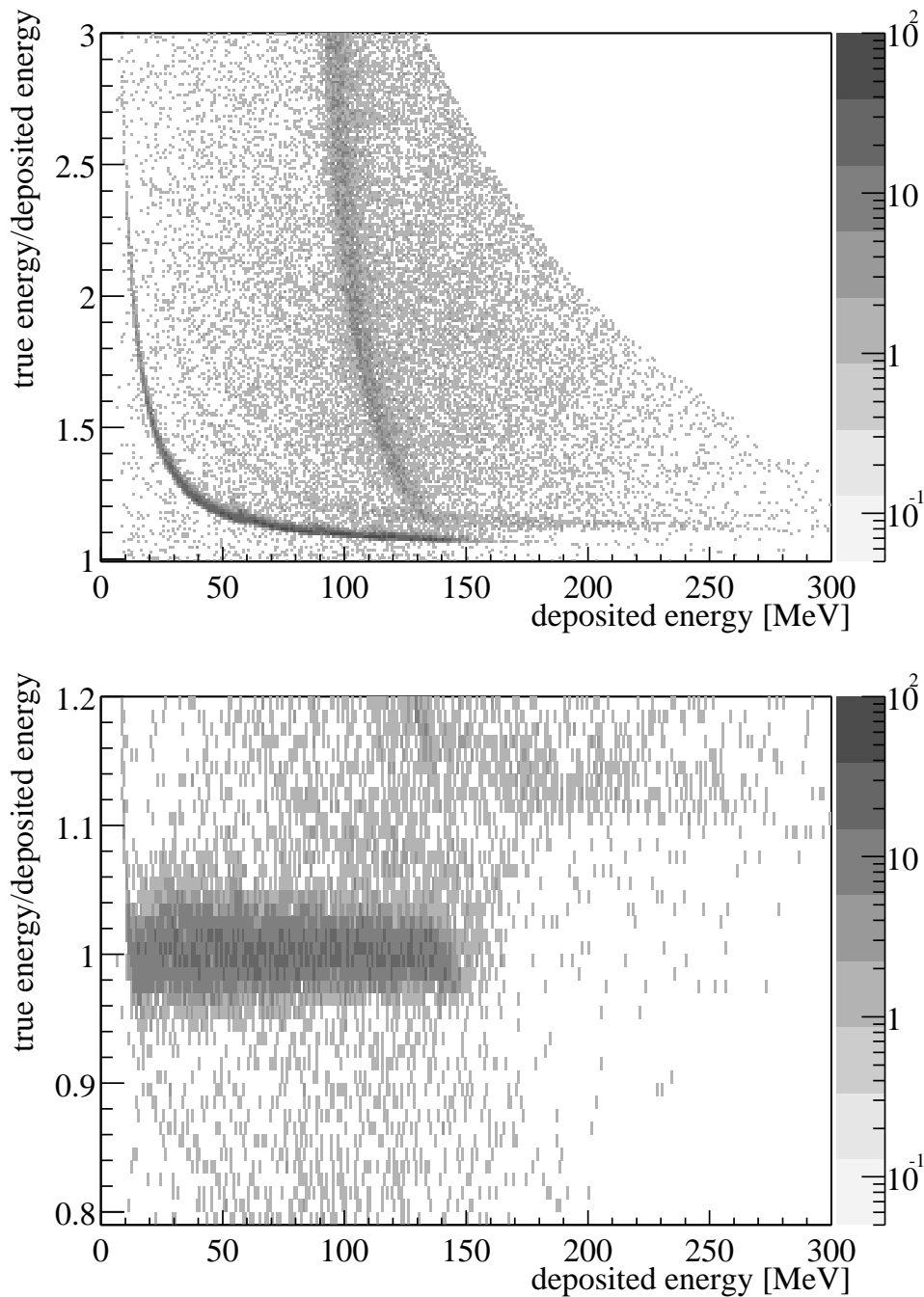


**Figure 3.8:** The upper scatterplot shows the combined effect from dead material and quenching for pions in the plastic scintillators. This plot is generated from the detector simulation, where the incident particle energy is known. The simulated pions are distributed over the whole FD detector with a kinetic energy from 0 to 400 MeV. Most particles are lying in the small band that is enclosing the distribution in the lower left part. The back-bending part is from punch-through particles not depositing the whole kinetic energy in the detector. The rest of the distribution comes from nuclear reactions where a part of the kinetic energy is carried away by neutral particles. The lower scatterplot shows the effect after including the correction for quenching and dead material.

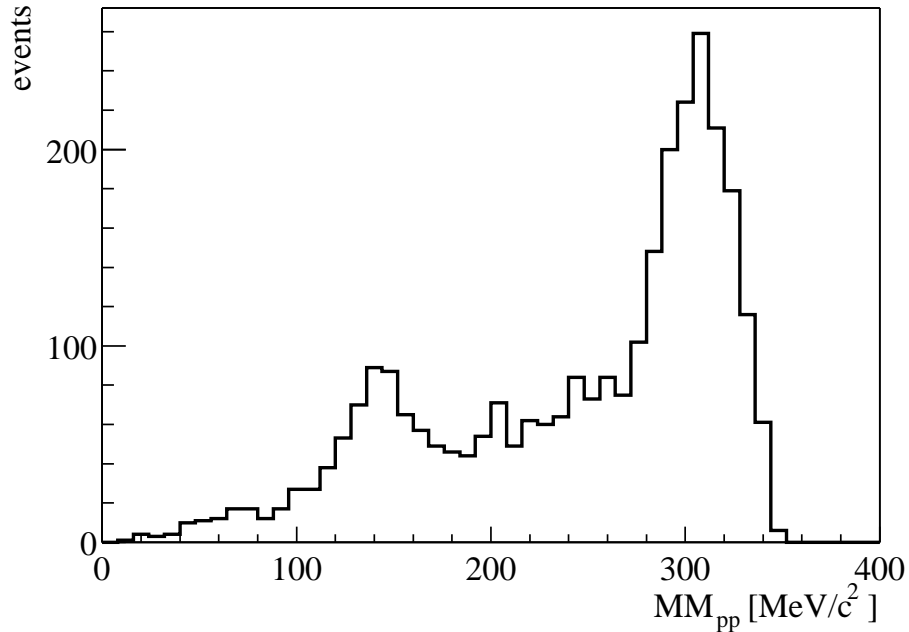


**Figure 3.9:** Missing mass of the two-proton system with contributions from single and two-pion production of the measurements at  $T_p = 775 \text{ MeV}$ . With a cut selecting events above  $260 \text{ MeV}/c^2$  two-pion production is selected.

section of about  $46 \mu\text{b}$ , compared to about  $1 \mu\text{b}$  for two-pion production.

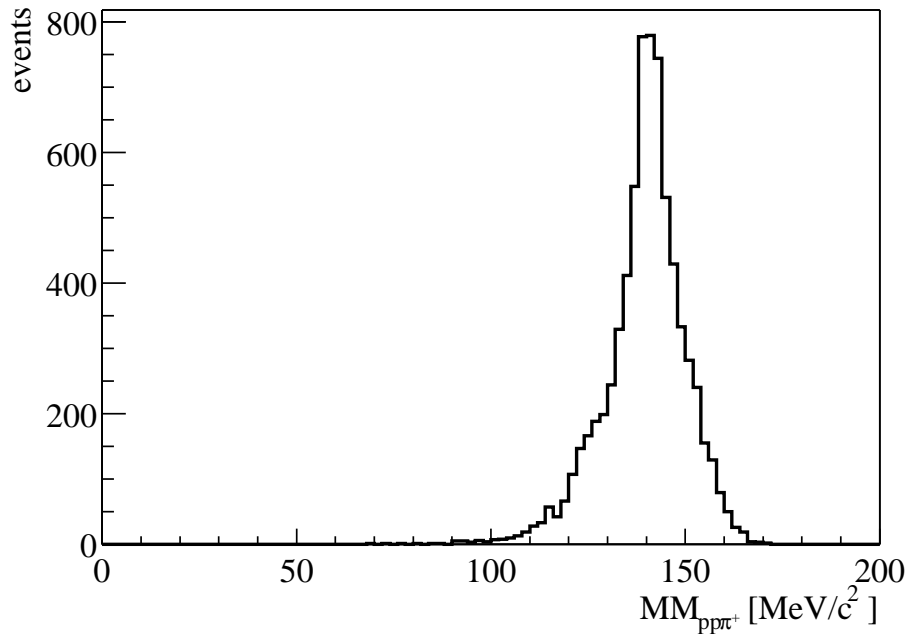
Fig. 3.9 shows the missing mass (see section 4.1.2 for its definition) of the two protons. Around the one pion mass the contribution of  $\pi^0$  production is seen. Starting at the two-pion threshold the contribution of two-pion production is visible. With a cut of  $MM_{pp} \geq 260 \text{ MeV}/c^2$  two-pion production events are selected.

Fig. 3.10 shows the missing mass of the three measured particles, the two protons and the  $\pi^+$ , only for those events selected according to the condition explained in the previous paragraph ( $MM_{pp} \geq 260 \text{ MeV}/c^2$ ).

### 3.4.13 Kinematical fit

As the last step before having four-vectors for all particles of the event, a kinematical fit is applied. In our case 3 out of 4 particles are measured. The beam momentum, the beam particle mass and the target mass are known, so a 1C (one constraint) fit is made. Since the measurement is overdetermined by one constraint, different combinations of measured observables could be taken to calculate the momentum of the not measured  $\pi^-$ . This may lead to different solutions depending on the set of observables used. So the main advantage of the kinematical fit is to obtain a consistent set of values for all the four-vectors, that fulfil both momentum and energy conservation.

All measured properties of the measured particles have an experimental uncertainty. By adjusting the measured values considering these uncertainties under the constraints of energy and momentum conservation a fit is applied [Kup95]



**Figure 3.10:** Missing mass of the three measured particles, the two protons and the  $\pi^+$ , for events with  $MM_{pp} \geq 260 \text{ MeV}/c^2$  of the measurements at  $T_p = 775 \text{ MeV}$ . It corresponds to the invariant mass of the not measured  $\pi^-$ . Its mean mass is around  $140 \text{ MeV}/c^2$  and its FWHM (full width at half maximum) is about  $14 \text{ MeV}/c^2$ .

(minimisation under constraints [Fis90]). The version from A. Kupsc has been translated from Fortran to C++.

Because of some differences between real data and simulated detector response the following tasks must be done in the data analysis procedure with simulated data (compare in Fig. 3.1).

#### 3.4.14 Energy threshold simulation

The deposited energy in a detector element gives an electrical signal via the photo multipliers. This signal has to rise higher than a certain threshold to be registered by the electronics. So the real data have a lower limit on ADC values due to pedestal suppression during acquisition. Very low signals are not taken into account. This threshold is rather small: Below  $1 \text{ MeV}$  ( $0.8 \text{ MeV}$ ) for the FRH and about  $0.1 \text{ MeV}$  for FHD. The threshold for signals to be taken into account by the TDC is somewhat higher. Here the signal is transformed by a discriminator into a logical signal. The signal threshold in the discriminator for signals taken into account corresponds to a certain energy (about  $6 \text{ MeV}$  for FRH and  $0.3 \text{ MeV}$  for FHD). The simulation of those two features is done by removing ADC hits if they are below the ADC threshold and by removing TDC hits if the deposited energy is below the TDC threshold. The same applies for the delayed hit where the deposited energy of the positron was used to test the threshold.

### 3.4.15 Trigger simulation

Real data are recorded if the appropriate trigger is set. Trigger conditions do not affect simulated data. So in the analysis of simulated data the trigger condition should be tested manually. This means there must be at least the number of TDC hits (after threshold simulation) in the different detectors, that we obtained in the real data due to the trigger conditions. For the TWR32 this test requires three hits in FRH first plane (TR3) and three hits in FHD with straight elements (TJ3) with TDC entries.

## 3.5 Normalisation

### 3.5.1 $pp$ elastic scattering

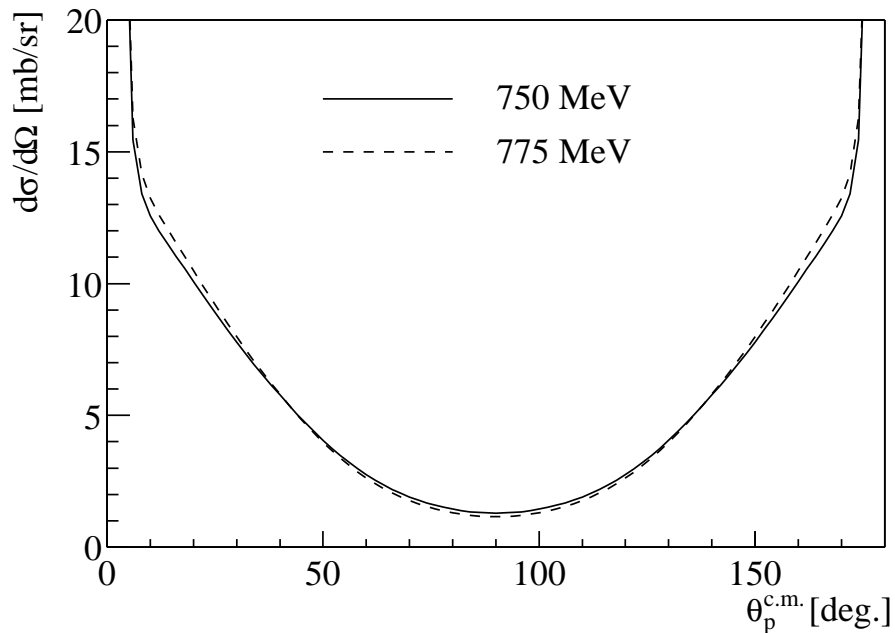


**Figure 3.11:** Angular distribution of  $pp$  elastic scattering for  $T_p = 750$  MeV (solid) and  $T_p = 775$  MeV (dashed) from the phase shift analysis SAID.

The integral cross sections are determined by calculating the integral experimental luminosities from proton-proton elastic scattering. The “known” differential cross sections are from the SAID data base [SAID] and are included into the event generator. Fig. 3.11 shows the angular distribution used for both energies.

The data are selected with the trigger T1 or T3. The opening angle for the two protons in elastic scattering is a little bit larger than  $80^\circ$ . So a coincident hit between the FD and CD is required. Both tracks must be coplanar ( $\Delta\phi \geq 165^\circ$ ) and a cut on the opening angle ( $70^\circ \leq \delta \leq 90^\circ$ ) is applied. To be able to do this a simple track reconstruction for the central detector was implemented.

The event generator was providing  $pp$  elastic scattering events with one proton

in the interval from 2 – 26 degrees. So for the calculation of the luminosity the cross section for  $pp$  elastic scattering integrated from 2 – 26 degree has to be used, not the total angular integral of the elastic cross section. (for the calculation of luminosities, see next chapter section 4.2)

Note, a coincidence between the left CD array and the right CD array cannot be used, because no appropriate trigger was connected to the DAQ, so cross checks with this condition cannot be made.

### 3.5.2 Trigger inefficiency

The trigger inefficiency for the trigger TWR32 was studied:

TWR32 is a secondary trigger, so as a first step the coincidence of the primary triggers W2, TJ3 and TR3 was checked. This coincidence does not work in less than one case out of  $10^4$ . The next step was to check the inefficiency for each primary trigger. TR3 requires at least three TDC hits in FRH first plane and TJ3 at least three TDC hits in the straight element plane of FHD. W2 requires two hits in the four FWC elements. The results are shown in Tab. 3.3. The values are

reference tape	WS0350	WS0383
beam energy [MeV]	750	775
W2 inefficiency	1.4%	1.4%
TJ3 inefficiency	0%	0%
TR3 inefficiency	3.5%	2.6%
TWR32 inefficiency	4.9%	4.0%

**Table 3.3:** Trigger inefficiencies of the single primary triggers and the result for the secondary trigger, that is build from these triggers.

obtained by selecting events with the triggers TR3 and TJ3, that are connected to the DAQ. Then the pattern in the detector was tested if it matched to the trigger conditions. If this was fulfilled, the trigger condition should have also been set. If the trigger condition was not set, there would be an inefficiency. Note that only those trigger conditions that have not started the data acquisition can be tested, therefore always the “other” trigger was tested in each event.

### 3.5.3 Data acquisition life time

The life time of the data acquisition system (DAQ) is determined with the entries of the scalers. The life time is the time of the whole measurement, when the DAQ was actually ready to take events. It should be taken into account that events occurring during readout processing will be dropped, thus reducing the number of recorded events compared to those actually happening. The free scaler rates deals with this, they record the free rate of the triggers. Additionally the number of events with this trigger condition that are actually written to tape can be counted. The ratio of both numbers gives the DAQ life time correction factor:

$$(3.2) \quad \epsilon_{\text{DAQ}} = \frac{\text{number of events written to tape}}{\text{freely accumulated rate}}$$

## 3.6 Efficiency and acceptance correction

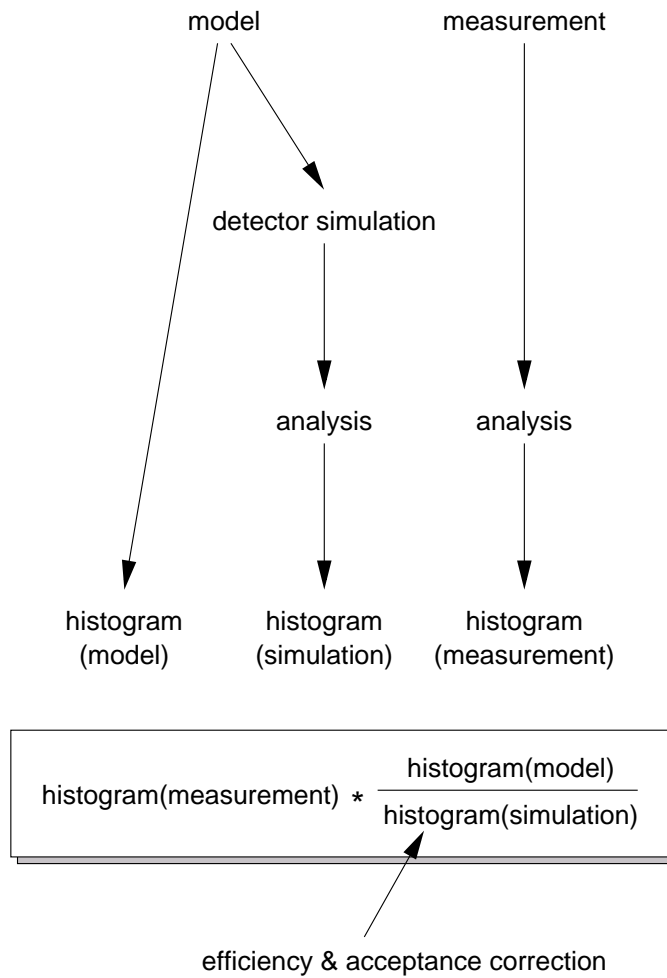


**Figure 3.12:** Scheme that is used for acceptance and efficiency correction. Three histograms defined identically for all interesting observables are needed: the model calculation for the full  $4\pi$  acceptance, the same spectrum after detector simulation and analysis and the real data after analysis. The calculation shown in the box is performed on the three histograms. The fraction in the formula denotes the acceptance and efficiency correction histogram that is used to correct the data.

Finally the data are efficiency and acceptance corrected. The chart in Fig. 3.12 shows the principle of the procedure used to gain those spectra.

Three histograms of the same observable are needed: one with the model calculation for the full  $4\pi$  acceptance, the second with the result after detector simulation and analysis and the third with real data after the analysis. By dividing the first and the second histogram a correction histogram is produced. The histogram from real data is multiplied with this correction and gives the final result.

Fig. 3.13 and 3.14 show the effect and model dependency of this method of two different observables at 750 MeV. The first figure shows the invariant mass of the  $pp$  system ( $M_{pp}$ ). Here the two model calculations already show a significant difference. But since there is nearly full phase space coverage for the protons in the experiment, this does not significantly change the corrected spectra. Only at

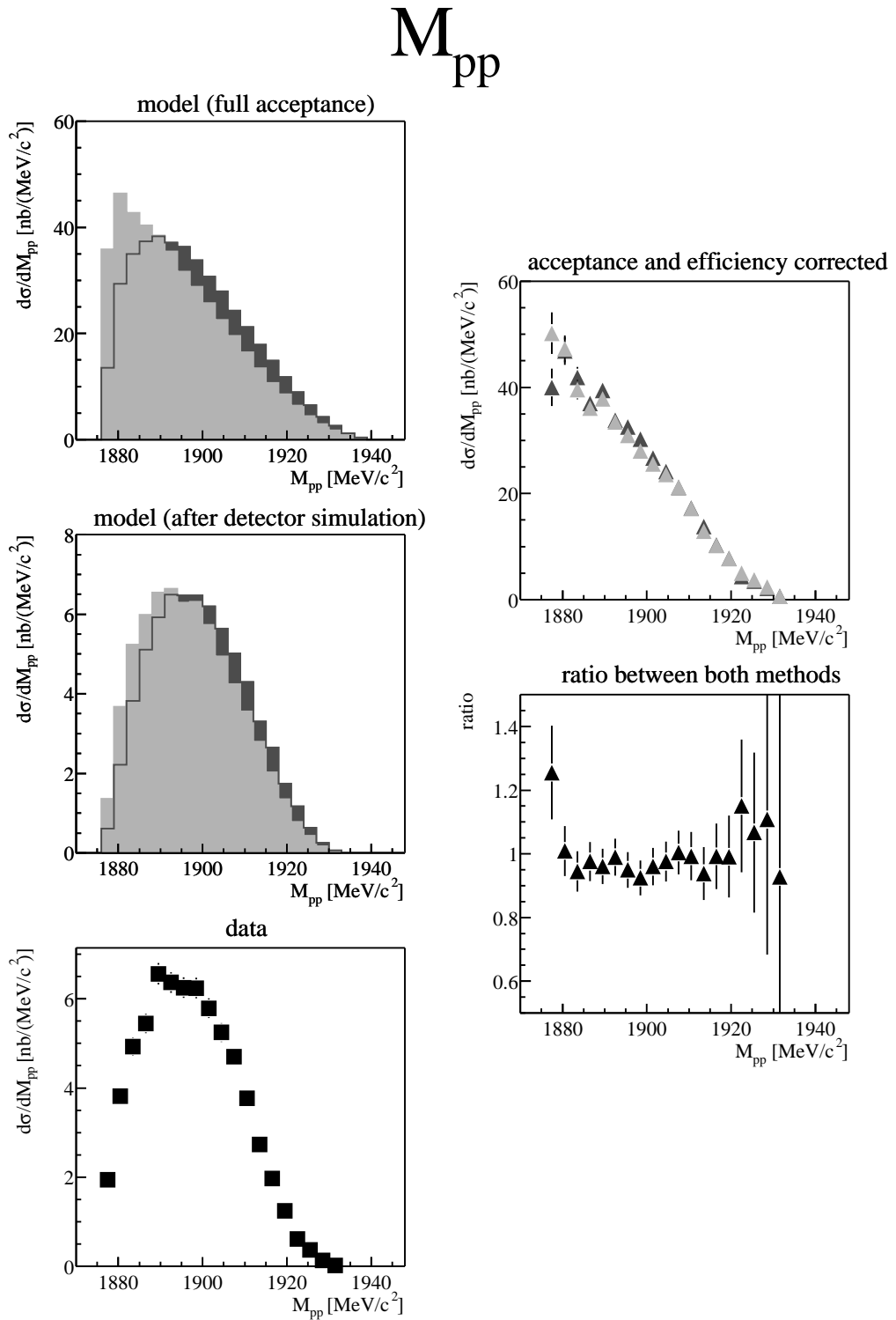


**Figure 3.13:** Acceptance and efficiency correction of the observable  $M_{pp}$ . The correction is dependent upon different models (dark gray: pure phase space, light gray: full model). The left column shows from the top: the model calculations for the full  $4\pi$  acceptance, then the spectra after the detector simulation and analysis and finally the spectrum from real data. On the right the top figure shows the acceptance and efficiency corrected real data using corrections from both models and at the bottom the ratio between them. This characterises the uncertainty of this method.

Although the models have a different distribution, they give quite similar results for the correction. This is because all the protons are nearly covered by the acceptance of the detector.

$$\theta_{\pi^-}^{\text{c.m.}}$$

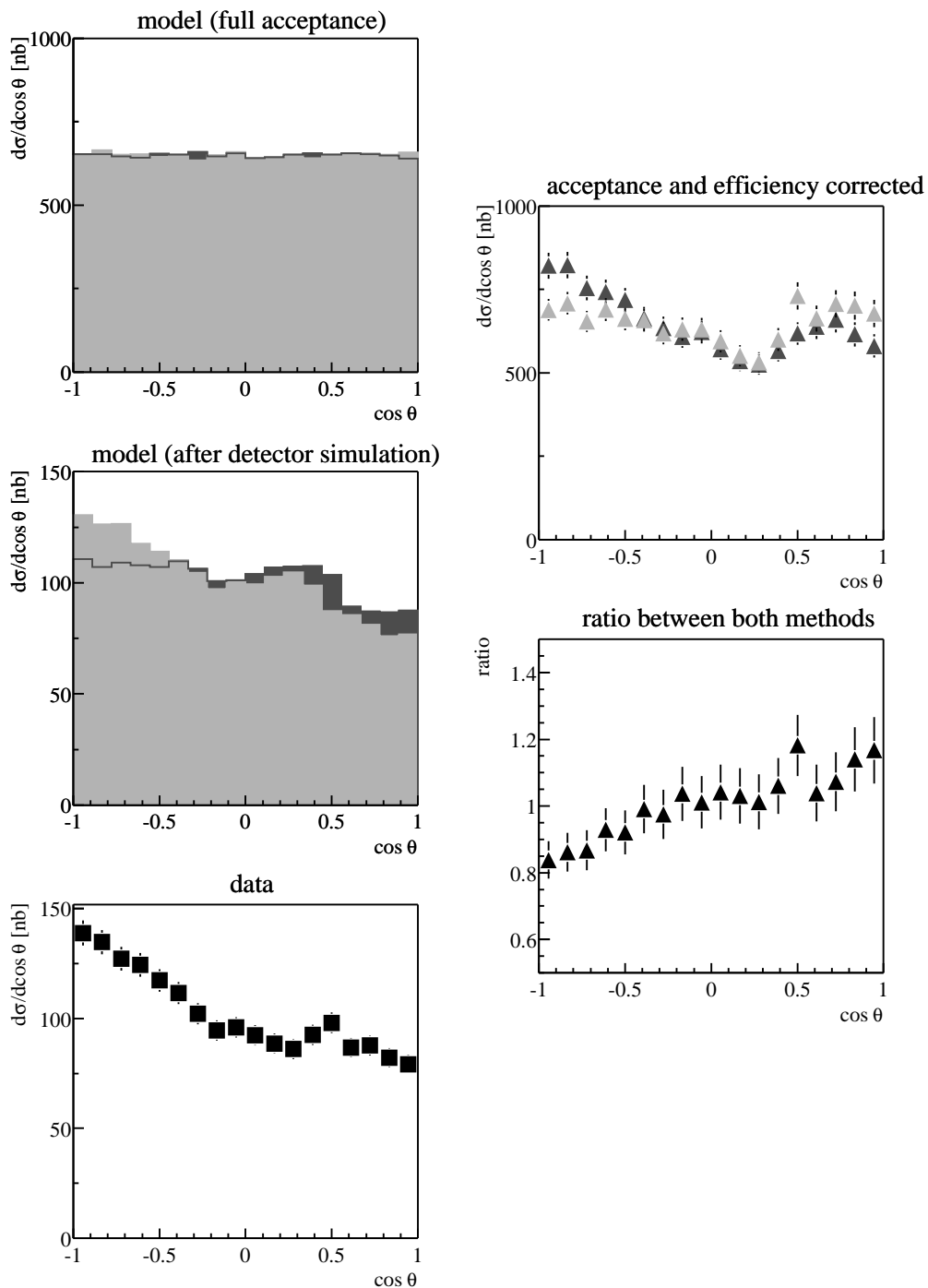


**Figure 3.14:** Acceptance and efficiency correction of the distribution of the observable  $\theta_{\pi^-}$  in the overall c.m. system. The correction is dependent upon different models (dark gray: pure phase space, light gray: full model). The left column shows from the top: the model calculations for the full  $4\pi$  acceptance, then the spectra after the detector simulation and analysis and finally the spectrum from real data. On the right the top figure shows the acceptance and efficiency corrected real data using corrections from both models and at the bottom the ratio between them. This characterises the uncertainty of this method. Although the models have the same flat distribution, they have different results after detector simulation. This is because the reconstruction of the unmeasured  $\pi^-$  is greatly affected by the angular distribution of the  $\pi^+$ . Only about 30% of the positive pions are covered by the detector acceptance.



the edge some effect can be seen.

In contrast the second figure shows the effect of the scattering angle of the  $\pi^-$ . Here the model calculations show nearly the same distribution. But since the reconstruction of the unmeasured  $\pi^-$  is greatly affected by the geometrically limited acceptance of the detector for the  $\pi^+$ , the results from both models after simulation and analysis are different and give different acceptance and efficiency corrections in the final spectra. The results differ from each other by about 20%. Since we have identical particles in the incident channel, the angular distributions for all particles in the overall c.m. system have to be symmetric around  $90^\circ$ . This gives us a possibility to select the correct extrapolated angular distribution of the  $\pi^-$ .

It is clearly visible that this method raises a systematical uncertainty in the results. We have done our best to describe the data as well as possible in all observables with our full model (see section 4.4.4, the full model according to eq. 4.20). But we cannot fully exclude that different model calculations that equally well describe the data in the measured range may lead to a different correction.

The spectra that are shown in the next chapter (especially the complete set of spectra in section 4.5) are corrected for acceptance and efficiency as described here. In appendix A the basic results from the analysis are shown. They do not show any dependence on the reaction mechanisms assumed. In appendix B the results from the detector simulation to obtain the acceptance and efficiency are displayed.

## 3.7 Future improvements of the analysis

The angular distribution in the overall centre of mass system of each individual particle has to be symmetric around  $90^\circ$ , because identical particles are in the incident channel. This means 0 and 180 degrees can not be distinguished. In the measured angular distribution of the protons a slight deviation from this symmetry is visible. The distribution can be shifted by assuming another energy as the nominal one. For 750 MeV one would expect a shift to a lower energy, shifting the distribution to more forward angles. For 775 MeV nominal energy, a shift to a higher beam energy would shift the distribution to more backward angles. From a rough test one would estimate this shift to be below 5 MeV, which is about the order of uncertainty you would expect for this accelerator [Bro01].

In the analysis all three reconstructed tracks are required to stop in the FRH. Events with particles that punch through the detector and hit the FVH have not been used. At 775 MeV this is already cutting to some extent into the acceptance, which can be seen in the invariant mass spectra. This situation may be improved by also taking those particles into account, however, with a worse energy resolution. (See in section 3.4.10 about the energy reconstruction. The method used there for the quenching correction may in principle also be applied to the particles that are not stopped. The more scattered energy distribution is immediately visible in the figures shown in that section.)

# 4

## Results

In this chapter the results of the measurements of charged two-pion production are shown. The integral cross sections and a multitude of differential cross section spectra at 750 and 775 MeV proton beam energy are presented. The possible reaction mechanisms to describe the data will be discussed in detail. The following spectra show data corrected to full  $4\pi$  acceptance in comparison with model calculations. Raw (uncorrected) data spectra with the direct results from the analysis are given in appendix A. The event selection and reconstruction of the data at 750 MeV are from [Bro01]. The analysis of the data at 775 MeV was carried out as part of the work for this thesis. The analysis for obtaining the experimental luminosities to calculate total cross sections for both energies are also performed in this work.

### 4.1 Definition and calculation of observables

At this position I am going to give some definitions of some frequently used observables. The notation is as follows:  $E$  denotes the total energy of a particle,  $\mathbf{p}$  its three-momentum vector. If several particles are involved, then  $i$  is chosen as index for each individual particle. In the case of observables between exactly two particles  $i$  and  $j$  are the indices for the particles.

#### 4.1.1 Invariant mass

The invariant mass is the Lorentz-invariant mass of the sum of the four-momentum vectors ( $E$  total energy,  $\mathbf{p}$  three-momentum vector) of a particle ensemble:

$$(4.1) \quad M = \sqrt{\left(\sum_i \frac{E_i}{c^2}\right)^2 - \left(\sum_i \frac{\mathbf{p}_i}{c}\right)^2}$$

The invariant mass of one particle is trivial and gives the rest mass of the particle itself. But for two or more particles the invariant mass gives information about

the reaction dynamics. The invariant mass is distributed between the sum of the rest masses of the considered particles and this sum plus the mass equivalent of the free energy available in the reaction. The distribution follows phase space, if no special dynamics is involved in the reaction. But if a particle is generated in an intermediate state, the invariant mass of the particles that have formed this intermediate state gives the mass of this intermediate particle. (e.g. neutral pions are reconstructed with this method from their two decay gammas.) Similarly the width of very unstable states (like  $\Delta$  and  $N^*$ ) may be seen in the invariant mass spectra of their decay products. If their pole position is outside of the dynamic range of the reaction (as it is the case here), the effect is seen in a shift of the invariant mass distribution towards the pole compared to phase space.

#### 4.1.2 Missing mass

The missing mass is similar to the invariant mass, but here the invariant mass of the unobserved particles is calculated. Energy and momentum conservation are used for the calculation. The initial conditions of the target ( $m_t$ ) and the beam ( $E_b, \mathbf{p}_b$ ) have to be taken into account:

$$(4.2) \quad MM = \sqrt{\left(m_t + \frac{E_b}{c^2} - \sum_i \frac{E_i}{c^2}\right)^2 - \left(\frac{\mathbf{p}_b}{c} - \sum_i \frac{\mathbf{p}_i}{c}\right)^2}$$

The missing mass of the measured particles may help to identify the missing particles, e.g. for one missing particle the result for the missing mass of the measured particles should be equal to the rest mass of the missing particle. (see the application in section 3.4.12.)

#### 4.1.3 Scattering angles, planarity and opening angles

$\theta$  is the scattering angle measured with respect to the beam direction, this direction is usually taken as  $z$ -axis. With the  $x$ -axis lying horizontally and using the right hand rule,  $x$  points to the left and  $y$  points up as seen by looking along the beam direction.  $\phi$  is the angle between the  $x$ -axis and the projection of the particle track into the  $x$ - $y$ -plane

These angles are calculated as:

$$(4.3) \quad \theta = \arctan \frac{\sqrt{p_x^2 + p_y^2}}{p_z}, \quad \phi = \arctan \frac{p_y}{p_x}$$

The opening angle ( $\delta$ ) between two particles is defined as the following:

$$(4.4) \quad \delta_{ij} = \frac{\mathbf{p}_i \cdot \mathbf{p}_j}{|\mathbf{p}_i| |\mathbf{p}_j|}$$

Planarity ( $\Delta\phi$ ) is the difference in  $\phi$  for two particle tracks and is calculated according to:

$$(4.5) \quad \Delta\phi_{ij} = \frac{p_{i_x} p_{j_x} + p_{i_y} p_{j_y}}{\sqrt{p_{i_x}^2 + p_{i_y}^2} \sqrt{p_{j_x}^2 + p_{j_y}^2}}$$

### 4.1.4 Subsystem scattering angles

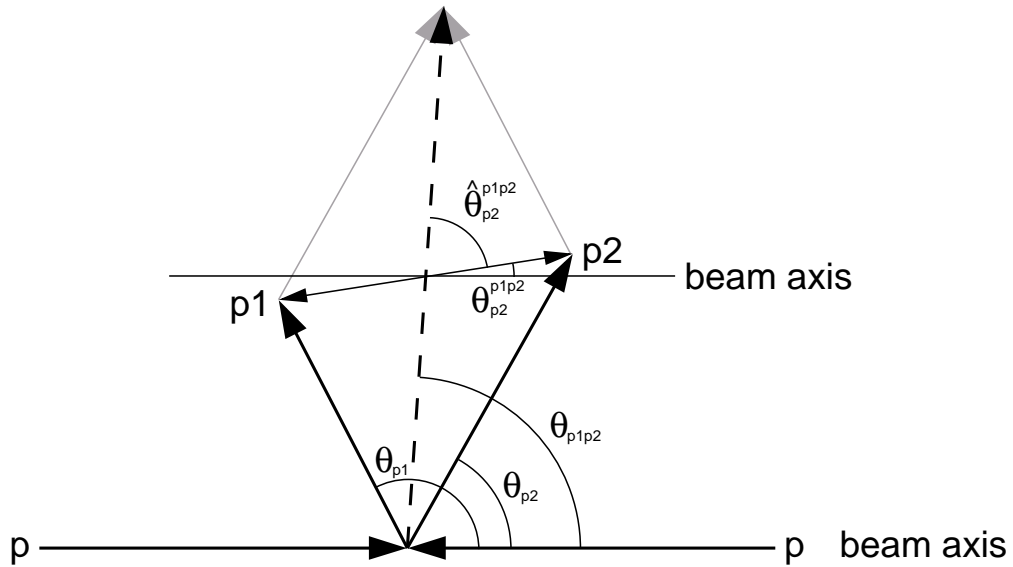


**Figure 4.1:** Definition of the different scattering angles in the subsystem of particles, here for the case of two particles ( $p_1, p_2$ ) resulting from the reaction in the overall centre of mass system. For simplification, the figure shows a non-relativistic construction. The other particles are not shown. For details see text.

In Fig. 4.1 the definition of the different scattering angles in the subsystem of particles is given. There are the scattering angles in the overall centre of mass system for particle  $p_1$  and  $p_2$ :  $\theta_{p_1}$  and  $\theta_{p_2}$ . The scattering angle of the centre of mass motion of both particles  $p_1$  and  $p_2$  in the overall c.m. system is called  $\theta_{p_1p_2}$ . When going into the rest frame of the two particles, two angles are defined:  $\theta_{p_2}^{p_1p_2}$  is the scattering angle of  $p_2$  in the rest frame of  $p_1$  and  $p_2$  with respect to the beam axis;  $\hat{\theta}_{p_2}^{p_1p_2}$  is the scattering angle of  $p_2$  in the rest frame of particle  $p_1$  and  $p_2$  with respect to the sum momentum of both particles in the overall c.m. system.

## 4.2 Integral cross sections

### 4.2.1 The calculation of integral cross sections

The number of events for a reaction ( $N_{ex}$ ) with the integral cross section ( $\sigma$ ), a given integrated luminosity ( $\int Ldt$ ), the detector acceptance ( $\epsilon_{acc}$ ) and the data acquisition life time ( $\epsilon_{DAQ}$ ) is written as:

$$(4.6) \quad \text{pre-scaling factor} \cdot N_{ex} = \sigma \cdot \int Ldt \cdot \epsilon_{acc} \cdot \epsilon_{DAQ}$$

The actually measured number is reduced by the pre-scaling factor of the trigger with which the reaction was recorded.

Tab. 4.1 shows the values for obtaining the integral luminosities during the measurements recorded on the reference tapes. With these values the integral cross

energy [MeV]	750		775	
reference tape	WS0350		WS0383	
$\sigma_{pp}(2 - 26^\circ)$ [mbarn]	19.3		19.65	
$\epsilon_{\text{DAQ}}$	60%		65%	
$\epsilon_{\text{acc}}$ (for $pp$ )	$\frac{46394}{381616} = 0.122$		$\frac{48373}{390089} = 0.124$	
measurement time [s]	13863		16228.5	
Trigger	PT1	PT3	PT1	PT3
pre-scaling-factor	$2^{13} = 8192$	$2^{12} = 4096$	$2^{12} = 4096$	$2^{12} = 4096$
$N_{pp}$	4479	8958	9186	9589
integrated luminosity $\int L dt$ [mbarn $^{-1}$ ]	$2.61 \cdot 10^7$	$2.61 \cdot 10^7$	$2.38 \cdot 10^7$	$2.48 \cdot 10^7$
luminosity $L$ [cm $^{-2}$ s $^{-1}$ ]	$1.9 \cdot 10^{30}$	$1.9 \cdot 10^{30}$	$1.5 \cdot 10^{30}$	$1.5 \cdot 10^{30}$

**Table 4.1:** Numbers needed for obtaining the integrated luminosities as well as the integrated luminosity itself both for 750 and 775 MeV. For convenience the mean luminosities during the data taking of this tape are also shown.

energy [MeV]	750	775
reference tape	WS0350	WS0383
$\text{acc}_{pp\pi^+\pi^-}$	$\frac{47781}{2000000} = 0.024$	$\frac{40295}{2000000} = 0.020$
$N_{pp\pi^+\pi^-}$ (reference tape)	466	664
$N_{pp\pi^+\pi^-}$ (all tapes)	8016	9603
$\sigma_{pp\pi^+\pi^-}$ [nbarn]	1240	2100
trigger inefficiency	4.9%	4%
corrected $\sigma_{pp\pi^+\pi^-}$ [nbarn]	1300	2190
error (statistical/systematical)	5%/18%	5%/18%
error [nbarn]	80/220	130/370

**Table 4.2:** Values used for calculating the integral cross sections and the results from these calculations.

section of the examined reaction  $pp \rightarrow pp\pi^+\pi^-$  were calculated. In Tab. 4.2 the used values are presented.

The errors for the integral cross section are divided into statistical and systematic errors. The different examined error sources (see also Tab. 4.3) are the following:

The statistical error for  $pp$  elastic scattered protons for about 10000 events is about 1%. For roughly 450 events of two-pion production it is 5%. This gives a sum of about 5% statistical error for the results.

When analysing  $pp$  elastic scattering the ratio of good events in the simulated data and in the real data changes (thus changing the acceptance) with different cut conditions on the scattering angle. The different cuts on the scattering angle were used to check the sensitivity of the analysis of protons that are scattered under large angles. These protons have very low kinetic energy, which makes

error	value
$pp$ elastic (statistical)	1%
$pp\pi^+\pi^-$ (statistical)	5%
statistical $\Sigma$	5%
$pp$ elastic (analysis)	8%
$pp\pi^+\pi^-$ (analysis)	12%
DAQ lifetime uncertainty	8%
model uncertainty	6%
systematical $\Sigma$	18%

**Table 4.3:** List of the different examined error sources for the values of integral cross section for the reaction  $pp \rightarrow pp\pi^+\pi^-$  for both energies 750 and 775 MeV. The different systematical errors are added quadratically. Also included in the analysis are error of uncertainties when treating the delayed pulse technique and the different behaviour of results in detector simulation and real data when changing cuts.

it difficult to simulate them correctly and calculate whether they will hit the detector or not. This uncertainty is estimated to be about 8%.

It is similar for the analysis of  $pp \rightarrow pp\pi^+\pi^-$  events. Here the main contribution to the error comes from the delayed pulse technique. This technique behaves very differently in real data and simulated events, when changing some selection criteria. Altogether this error is estimated to be 12%, see also [Bro01].

There are inconsistent scaler values in the data. The DAQ lifetime is different for different triggers, varying by about 8% around the used mean value.

The number of events that are not covered by the detector acceptance is dependent on the model used. By comparing a pure phase space distribution with the full model the difference in the number of events that are not covered by the detector acceptance is 6%.

When adding the different systematical errors quadratically, an overall systematical error of 18% is obtained.

## 4.2.2 Results for integral cross sections

Fig. 4.2 shows the energy excitation function of the integral cross section of the reaction  $pp \rightarrow pp\pi^+\pi^-$ . Our full set of new data (black points) are compared to previous published data (open symbols) and to calculations from [Alv98]. The figure shows calculations with two different parameter sets (dashed and solid line) and with and without  $pp$ FSI (upper and lower line respectively). The improvement in the quality of the data is obvious. For our data the error bars denote both statistical and systematical uncertainty. The new data are now much closer to the threshold of the reaction. In the overlap region with existing data, our new data are an order of magnitude smaller. The former data were taken mainly in bubble chamber measurements partly on deuterium (here not corrected for Fermi motion) not on hydrogen. Only the data point from [Cve81] corresponds in general with our data.

The model calculations with the parameter set indicated by the dashed lines

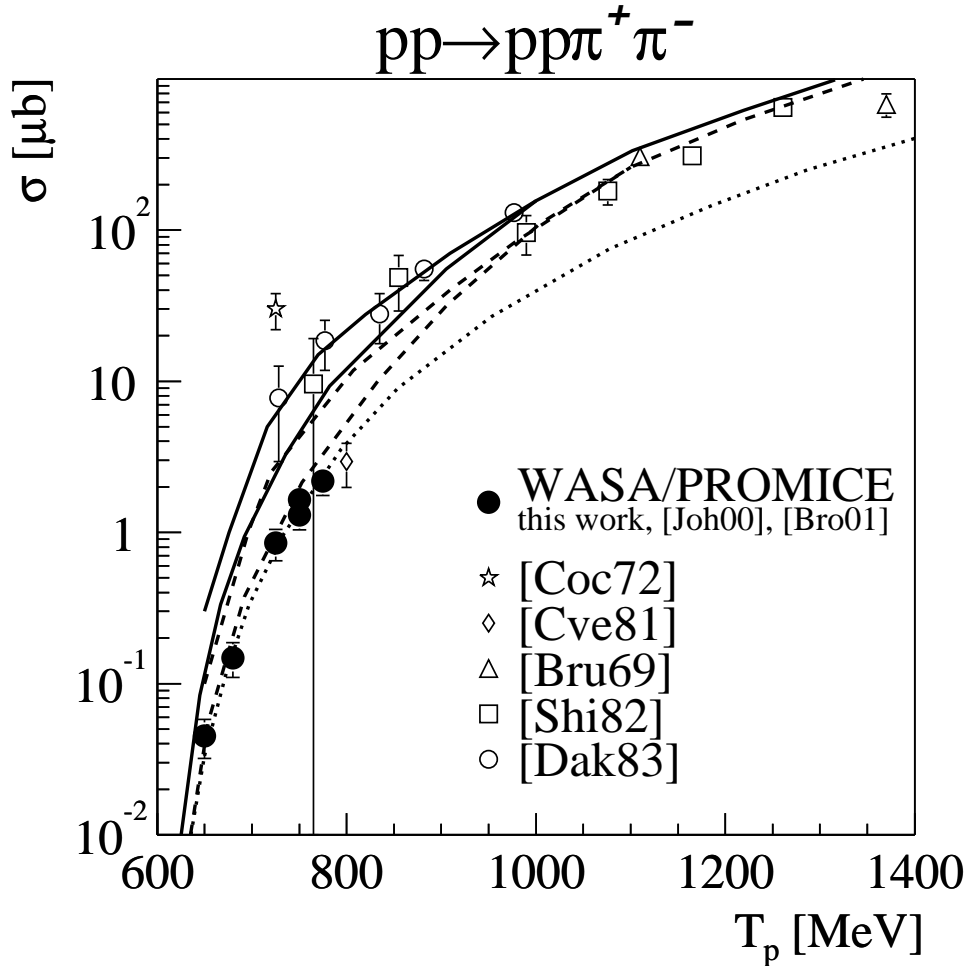


**Figure 4.2:** Energy excitation function of the integral cross section of the reaction  $pp \rightarrow pp\pi^+\pi^-$ . Our new data (black points) are compared with old data (open symbols) and predictions with two different parameter sets from [Alv98] (solid and dashed line), with and without  $pp$ FSI (upper and lower lines respectively) and a phase space fit to our data (dotted line).

describes the data better than the calculation shown by the solid lines. In the next sections (see 4.4.1) we will find that  $pp$ FSI (final state interaction) is needed to describe the data. Including this in the calculation, the predicted values again appear too high (upper dashed line, the calculation with FSI). But strictly the  $pp$ FSI that was included into the calculations here had not taken the Coulomb repulsion into account. Including the correct calculation for  $pp$ FSI, the curve would increase the integral cross section of the calculations by only a factor of 1.5 [Alv01] in the energy region around 750 MeV.

Tab. 4.4 shows all results from the measurements with the PROMICE/WASA detector. The slight difference in the two independent analysis on the same data sample at 750 MeV between [Bro01] and my work could not yet be solved. One part is a different trigger inefficiency that was used: 12% compared to 4.9% here. The rest is probably due to the reconstruction procedure of the analysis.

Energy [MeV]	Cross section [nbarn]	Reference
650	45(13)	[Joh00]
680	148(38)	[Joh00]
725	850(150)	[Bi198]
750	1650(250)	this work & [Bro01]
750	1300(300)	this work
775	2190(500)	this work

**Table 4.4:** Table of integral cross sections of the reaction  $pp \rightarrow pp\pi^+\pi^-$ .

### 4.3 Comparison with phase space distributions

Fig. 4.10 – 4.37 show differential cross section spectra corrected for acceptance and efficiency of the data at  $T_p = 750$  and  $775$  MeV. Corrected data (black points) are compared to phase space distributions (shaded area). At this stage please ignore the different displayed model calculations of different reaction mechanisms indicated with different line types. They will be introduced and explained in the next section.

The presentation of differential cross sections is divided into invariant masses, angular and energy distributions. The seven possible invariant masses of two and three particle systems are shown. The angular distribution of all particles are shown in the overall centre of mass (c.m.) system and in the laboratory (lab.) system. Also distributions of opening and planarity angles between two particles and the scattering angles of the centre of mass motion of two particles are shown. The spectra of  $\theta_{\pi^+\pi^-}$  and  $\theta_{p\pi^+}$  are equivalent to the spectra of  $\theta_{pp}$  and  $\theta_{p\pi^-}$  respectively but with a reversed sign on the  $x$ -axis. The different subsystem angular distributions give an indication of the involved partial waves in the different subsystems.

There are significant deviations in the distributions between phase space and data.  $M_{pp}$  is shifted to low invariant masses.  $M_{\pi^+\pi^-}$  is shifted to high invariant masses.  $M_{p\pi^+}$  and  $M_{p\pi^-}$  do not look the same: The  $p\pi^+$  system is shifted to higher invariant masses (Figs. 4.10 and 4.11). Reflections of the same effects could also be found in the invariant masses of the three-particle systems (Figs. 4.12 and 4.13).

The angular distributions of the protons in the overall centre of mass system are pronounced in the forward and backward direction (Figs. 4.14 and 4.15). The angular distributions of the protons in the laboratory system show a shift to lower angles compared to phase space distributions (Figs. 4.16 and 4.17).

The distributions of the opening angles between the two pions show a huge difference between phase space and data (Figs. 4.20 and 4.21).

In the  $\pi\pi$  subsystem the distributions of the scattering angle  $\hat{\theta}_{\pi^+\pi^-}$  show a possible contribution from a p-wave, i.e. a dependency proportional to  $\cos \theta$  (Figs. 4.26 and 4.28).

In the next section, we will go through the mechanisms that affect the different distributions step by step.



## 4.4 Reaction mechanisms in detail

As shown in the previous section, the data show significant deviations from phase space distributions. On the next pages the attempt is made to explain these deviations by various reaction mechanisms.

Fortunately, it appears that the contribution of each reaction mechanism mainly affects specific observables. The next subsections describe the different reaction mechanisms that are included into the final model calculation. The typical observables that are affected are shown in the description of the respective effects. Section 4.5 contains all the spectra of all calculated observables in which phase space distributions are compared to our model and to the data for both beam energies 750 and 775 MeV.

The usual way of including different mechanisms into a model simulation is the following: One takes the phase space event, which already has some weight due to the algorithm that calculates phase space. This weight is then multiplied by factors that come from the calculation of each effect.

### 4.4.1 Final state interaction (FSI)

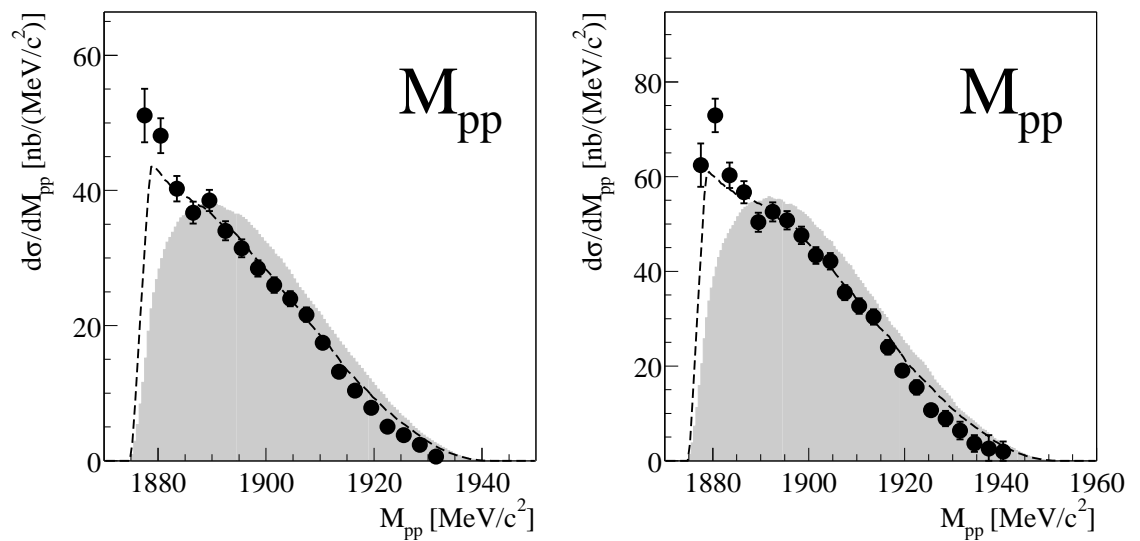


**Figure 4.3:** Spectra of invariant masses of the proton-proton system. They show the effect of proton-proton final-state interaction (FSI), on the left for 750 MeV and on the right for 775 MeV. The shaded area shows phase space, the dashed lines include  $pp$ FSI in comparison with the data (black dots).

Figure 4.3 shows the invariant mass spectra of the proton proton system at 750 and 775 MeV beam energy. The data are strongly enhanced towards low invariant masses. This can be explained by strong proton-proton final-state interactions (FSI). The figure shows the result of including FSI into the model according to a phenomenological approach with effective range approximation using parameters from elastic scattering.

With the following formulae [Sch98] the FSI effect can be approximated. As-

suming s-waves and omitting spin and isospin for simplicity the  $NN$  scattering amplitude  $f(k)$  can be written as:

$$(4.7) \quad f(k) = \frac{1}{k} e^{i\delta_0} \sin \delta_0 = \frac{1}{k} \frac{1}{\cot \delta_0 - i}$$

where  $k$  denotes half of the relative momentum of the two protons, i.e. the proton momentum in the  $pp$  system. For a short range potential and small energies the so-called effective range approximation can be applied where  $r_0$  is the effective range and  $a_s$  the scattering length:

$$(4.8) \quad \cot \delta_0 = \frac{1}{2} r_0 k - \frac{1}{ka_s}$$

This leads to a cross section corrected by FSI

$$(4.9) \quad \sigma(k) \sim |1 + R^{-1} f(k)|^2 \approx 1 + \left| \frac{R^{-1}}{\frac{1}{2} r_0 k^2 - a_s^{-1} - ik} \right|^2$$

where a parameter  $R$  has been introduced, which can be understood to describe the size of the reaction zone of the FSI and as a measure of the s-wave probability of the two nucleons. For the proton-proton case a correction  $F_c$  for the Coulomb repulsion has to be included into the formula, because this part of the potential is not correctly described in terms of scattering length and effective range only (see also [Brü69]). Finally the factor for  $pp$ FSI is computed as:

$$(4.10) \quad \sigma(k) \sim \left( 1 + \frac{R^{-2}}{\left(-a_s^{-1} + \frac{1}{2} r_0 k^2\right)^2 + k^2 F_c^2(a_c k)} \right) F_c(a_c k)$$

$$(4.11) \quad F_c(a_c k) = \frac{2\pi}{a_c k \left( e^{\frac{2\pi}{a_c k}} - 1 \right)}$$

In Tab. 4.5 the parameters used in the calculations of  $pp$ FSI are given.

Variable	Value	Comment
$a_s$	-7.82 fm	scattering length
$r_0$	2.79 fm	effective range
$R$	2.75 fm	size parameter
$a_c$	57.5 fm	Bohr radius

**Table 4.5:** Table of the parameters used for calculation of the effect of  $pp$ FSI.

#### 4.4.2 Meson exchange

The proton angular distributions (Fig. 4.4) show a significant deviation from a flat distribution. This may originate from meson exchange. In the calculation for meson exchange from [Sch00] the meson propagator is taken into account in terms of a phenomenological Feynman graph (Fig. 4.5).

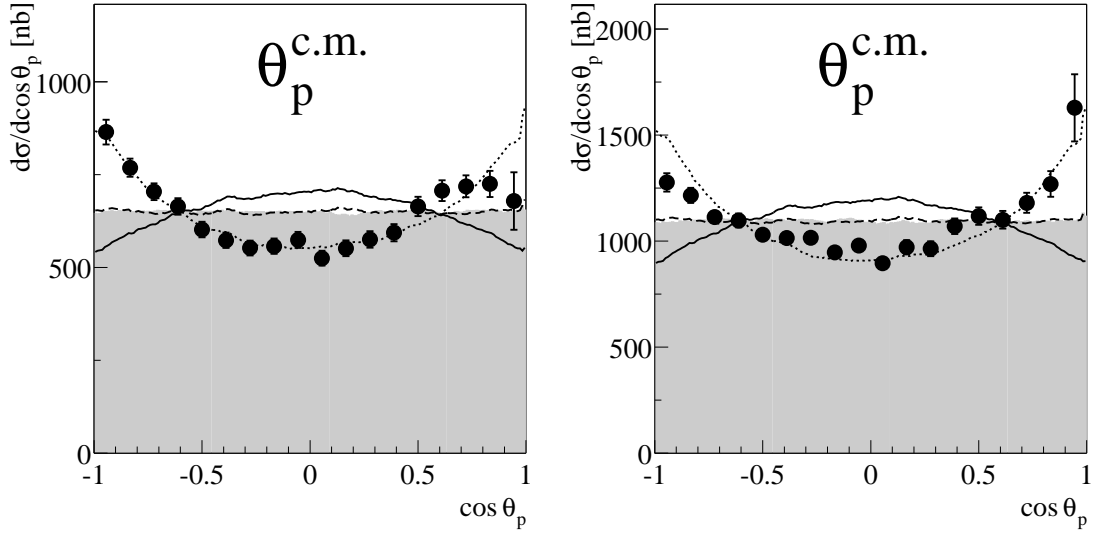


**Figure 4.4:** Effect of meson exchange. The angular distribution of the protons for 750 (left) and 775 MeV (right) beam energy shows the effects of  $\sigma$  (dotted line) and  $\pi$  exchange (solid line), that is added to the model so far (FSI). The dashed line still shows the model including only FSI. The data exclude  $\pi$  exchange and favour  $\sigma$  exchange, for details see text.

The amplitude for  $\sigma$  exchange is written in a Lorentz-invariant form as ( $\psi_i$  denotes the wave function of the incoming and outgoing protons):

$$(4.12) \quad A_\sigma \sim (\bar{\psi}_4 \psi_2) \frac{1}{q^2 - m_\sigma} (\bar{\psi}_3 \psi_1)$$

The amplitude for  $\pi$  exchange is written as:

$$(4.13) \quad A_\pi \sim (\bar{\psi}_4 \gamma_5 \psi_2) \frac{1}{q^2 - m_\pi} (\bar{\psi}_3 \gamma_5 \psi_1)$$

Antisymmetrisation for the identical nucleons is performed. Taking the squared absolute value leads to the following formulae for  $\sigma$  (upper signs) and  $\pi$  exchange (lower signs):

$$(4.14) \quad |A(p_1, p_2, p_3, p_4)|^2 = 4(p_1 p_3 \pm m^2)(p_2 p_4 \pm m^2)[D_{24} + D_{23}]^2 + \\ + 4(p_1 p_4 \pm m^2)(p_2 p_3 \pm m^2)[D_{23} + D_{14}]^2 - \\ - 2[(p_1 p_3)(p_2 p_4) + (p_2 p_3)(p_1 p_4) - (p_1 p_2)(p_3 p_4) + m^4 \\ + m^2(p_1 p_2 + p_3 p_4 \pm p_1 p_4 \pm p_2 p_3 \pm p_2 p_4 \pm p_1 p_3)] \\ [D_{24} + D_{13}][D_{23} + D_{14}]$$

$$(4.15) \quad D_{ij} = \frac{1}{2m^2 - m_{meson} - 2(p_i p_j)}$$

An assumed mass of  $m_\sigma \approx 400 \text{ MeV}/c^2$  for the  $\sigma$ -meson has been taken.  $p_1$  and  $p_2$  are the four-momentum vectors of the incoming protons,  $p_3$  and  $p_4$  are the four-momentum vectors of the protons after the reaction. The momentum

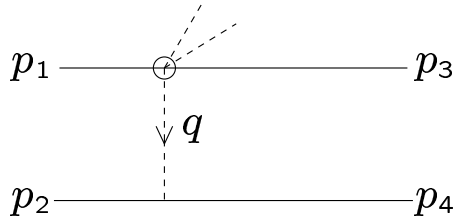


**Figure 4.5:** Feynman diagram for meson exchange in inelastic proton-proton collisions leading to the production of two mesons.

transfer  $q$  is calculated as  $q = p_4 - p_2$ , see Fig. 4.5. For the calculation the inelastic characteristic of the reaction is important. For elastic scattering, where  $|p_1| = |p_2| = |p_3| = |p_4|$ , the formulae produce no effect on the angular distribution of the protons.

The data (Fig. 4.4) disagree with  $\pi$  exchange and favour  $\sigma$  exchange.

#### 4.4.3 $N^*$ excitation and decay

The  $N^*$  excitation in one of the participating nucleons should be the main reaction path. This is visible in the shift towards high invariant masses in the  $M_{p\pi^+\pi^-}$  spectrum, the  $N^*$  system (Fig. 4.6 top).

The  $\pi\pi$  invariant mass is strongly shifted to higher masses (Fig. 4.6 middle) and in the opening angle of the two pions a large difference between phase space distributions and the data is visible (Fig. 4.6 bottom). Both these effects can be understood by the interference of two decay channels of the  $N^*(1440)$  excitation. The decay of the  $N^*$  into the  $N\pi$  system does not contribute to the two-pion production, whereas the decays to the  $N\pi\pi$  system do. The interference between the two decay channels  $N^* \rightarrow p(\pi\pi)_{l=I=0}$  (the  $\pi\pi$  system with relative angular momentum  $l = 0$  and isospin  $I = 0$  is also referred to as the scalar, iso-scalar channel or  $\sigma$  channel) and  $N^* \rightarrow \Delta\pi$  gives following leading order terms in the reaction amplitude [Alv99]:

$$(4.16) \quad A \sim 1 + c(\mathbf{k}_1 \cdot \mathbf{k}_2) = 1 + c|k_1||k_2| \cos \delta_{\pi\pi}$$

where  $k_i$  denotes the momentum of the two pions in the overall c.m. system. The 1 is for the route  $N^* \rightarrow p(\pi\pi)_{l=I=0}$ . The term  $\mathbf{k}_1 \cdot \mathbf{k}_2$  represents the decay route  $N^* \rightarrow \Delta\pi$ . The latter can be explained with an analogy to  $\pi N$  scattering.

$\pi N$  scattering is calculated as  $(\sigma \cdot \mathbf{k}_1)(\sigma \cdot \mathbf{k}_2) = \mathbf{k}_1 \cdot \mathbf{k}_2 + i\sigma(\mathbf{k}_1 \times \mathbf{k}_2)$ , where  $\sigma$  denotes the vector of the spin matrixes (Fig. 4.7 left side). For the  $N^*$  decay via the  $\Delta$  resonance the graph looks similar (Fig. 4.7 right side). From spin considerations this results in  $4(\mathbf{k}_1 \cdot \mathbf{k}_2) + i\sigma(\mathbf{k}_1 \times \mathbf{k}_2)$ . This factor of 4 in amplitude translates into a factor of 16 in cross section so that the vector product can be neglected.

For the best description of the data, the constant  $c$  has to be chosen, such that the mean of  $c|k_1||k_2|$  is about  $-0.25$ . This is equivalent to an admixture of 25% of the decay amplitude  $N^* \rightarrow \Delta\pi$  to the dominant  $N^* \rightarrow p(\pi\pi)_{l=I=0}$  amplitude. There is a destructive interference for pions emerging parallel to each other (low invariant masses, small opening angles) and a constructive interference for par-

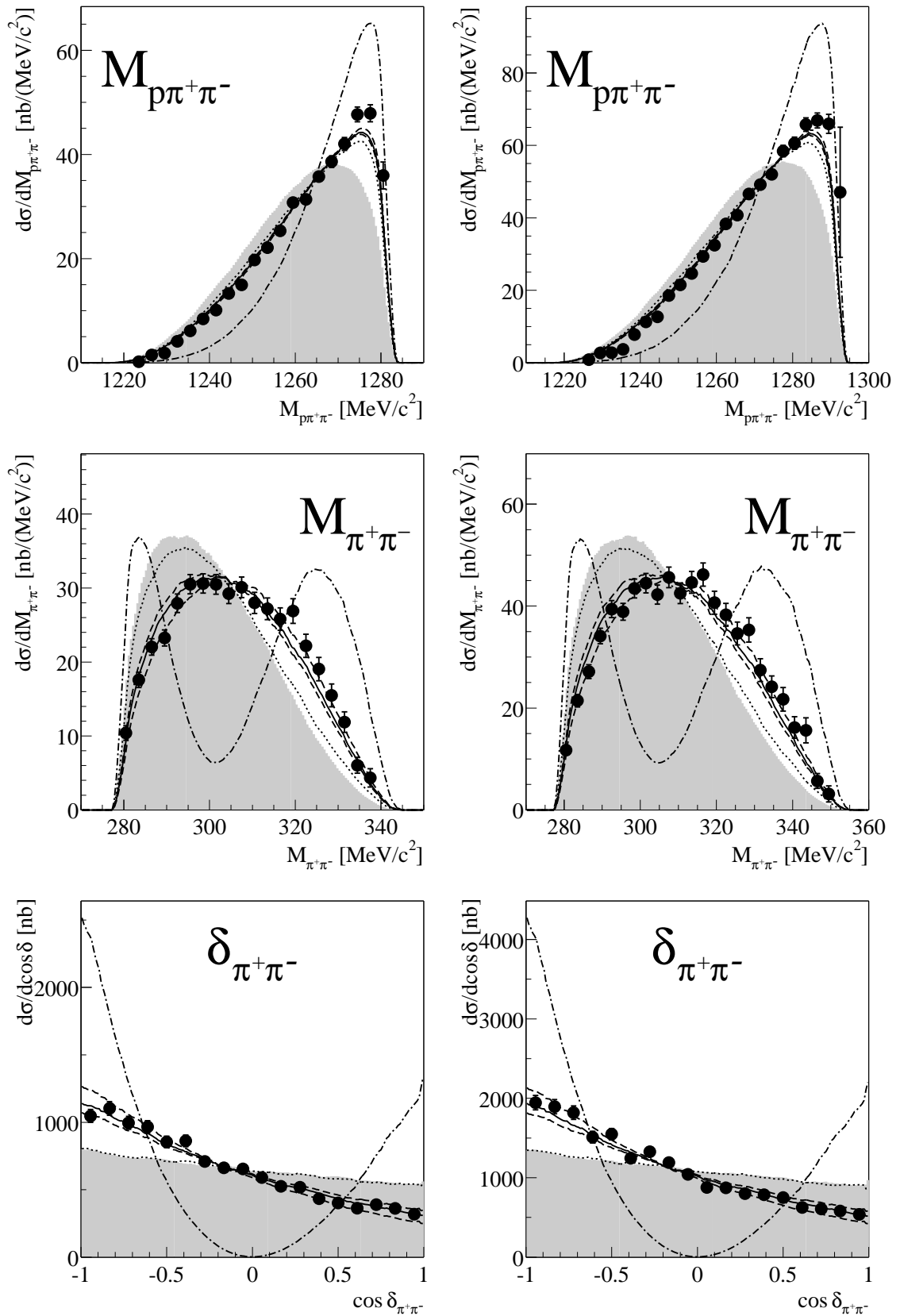


**Figure 4.6:** Effect of the  $N^*$  excitation. The invariant mass of the  $N^*$  system ( $M_{p\pi^+\pi^-}$ ) is shown at the top. The invariant mass of the  $\pi\pi$  system as well as its opening angle for both 750 (left) and 775 MeV (right) beam energies are displayed in the middle and at the bottom respectively. Phase space (shaded area) is shown in comparison with FSI &  $\sigma$  exchange and the decay  $N^* \rightarrow p(\pi\pi)_{i=0}$  (dotted), the decay  $N^* \rightarrow \Delta\pi$  (dashed dotted) and interference between both those decays with different mixing ratios of the decay  $N^* \rightarrow \Delta\pi$ . (25% solid, 20% and 33% dashed), for details see text.

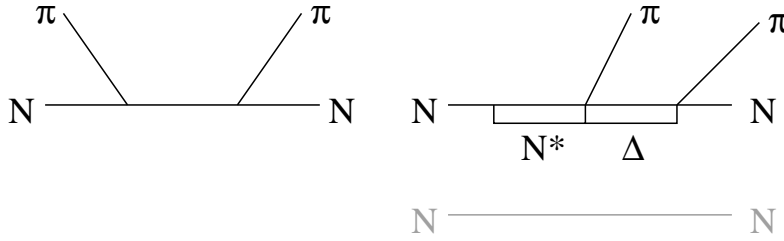


**Figure 4.7:** Illustration of the analogy between the  $N^*$  decay  $N^* \rightarrow \Delta\pi$  and  $\pi N$  scattering.

ticles coming out in a opposite direction (high invariant mass, high opening angles). See Fig. 4.6, where different mixing ratios are shown in comparison: pure  $N^* \rightarrow p(\pi\pi)_{l=I=0}$  decay, pure  $N^* \rightarrow \Delta\pi$  decay and different mixing ratios of these decay channels (20%, 25%, 33% admixture of the  $N^* \rightarrow \Delta\pi$  decay).

For about 25% admixture of the  $N^* \rightarrow \Delta\pi$  decay in the amplitude, the results of the squared amplitude can be simplified according to

$$(4.17) \quad |1 + c|\mathbf{k}_1||\mathbf{k}_2| \cos \delta_{\pi\pi}|^2 = 1 + \underbrace{2c|\mathbf{k}_1||\mathbf{k}_2| \cos \delta_{\pi\pi}}_{50\%} + \underbrace{c^2|\mathbf{k}_1|^2|\mathbf{k}_2|^2 \cos^2 \delta_{\pi\pi}}_{\approx 6\%}$$

The last term contributes to only about 6%. In the spectrum of the opening angle of the two pions the contribution of the 50% in  $\cos \delta_{\pi^+\pi^-}$  is directly visible.

This approach implies a dependence of the mixing ratio of the two  $N^*$  decays on the energy, because of the factor of  $\mathbf{k}_1 \cdot \mathbf{k}_2$  in the decay via  $\Delta$ . With increasing energy the decay via the  $\Delta$  route should increase according to this factor. There may exist a small effect in the data of the opening angle, implying an energy dependence in the right direction, but it is too small to be clearly discriminated in the data for the two neighbouring energies measured.

Our results for the mixture ratio coincides with results from [Alv98], where the coupling for the different decay branches is calculated from branching ratios of the  $N^*$  into the  $N\pi\pi$  channels. He took the values of the particle data booklet [PDG00]: 5% – 10% (7.5%) for  $N^* \rightarrow N(\pi\pi)_{l=I=0}$  and 20% – 30% (25%) for  $N^* \rightarrow \Delta\pi$  (The number in brackets are the mean values that are taken in the calculation).

#### 4.4.4 $\Delta$ propagators

So far the model is still incomplete, because the  $\Delta$  propagators for the  $N^* \rightarrow \Delta\pi$  route are still missing in the calculation above. These propagators are represented in the calculation by the appropriate Breit-Wigner term:

$$(4.18) \quad D_\Delta = \frac{1}{M_{p\pi} - M_\Delta + \frac{i}{2}\Gamma_\Delta}$$

We obtain the following expression for the reaction amplitude:

$$(4.19) \quad A \sim 1 + c(\mathbf{k}_1 \cdot \mathbf{k}_2)[3D_{\Delta^{++}} + D_{\Delta^0}]$$

the factors in front of  $D_{\Delta^{++}}$  and  $D_{\Delta^0}$  simply derive from isospin coupling. These calculations are displayed by the dashed lines in Fig. 4.8.

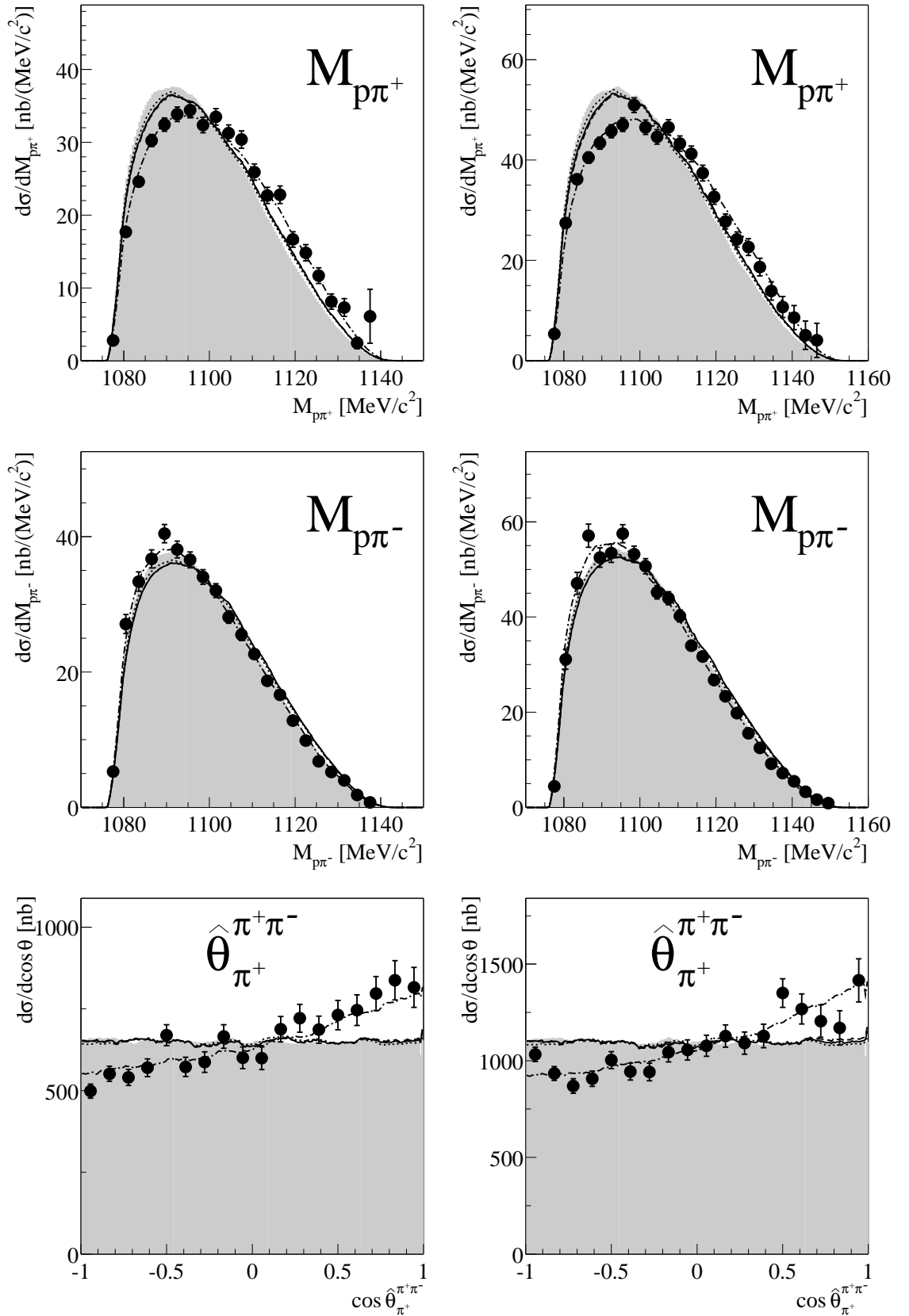


**Figure 4.8:** Invariant masses of the  $p\pi^+$  and of the  $p\pi^-$  system (top and middle) and scattering angle of the pion in the  $\pi\pi$ -system with respect to the pions' summary momentum (bottom). The left side shows the results for 750 MeV and the right one for 775 MeV. The dotted and solid lines are as before FSI &  $\sigma$ -exchange and FSI &  $\sigma$ -exchange &  $N^*$  decays (eq. 4.16). The dashed and the dashed-dotted lines now also include the  $\Delta$ -propagators according to eq. 4.19 and eq. 4.20 respectively (see text).

Although this approach already gives a very reasonable description, the asymmetry observed in the  $\hat{\theta}_{\pi^+}^{\pi^+\pi^-}$  angular distribution is not yet described in the calculations so far. The isospin dependence observed in the  $p\pi$  system, most notably in  $M_{p\pi^+}$  and  $M_{p\pi^-}$  is also not accounted for. An excellent description of all observables (dashed-dotted lines in Fig. 4.8) is obtained, if we also tentatively multiply the first term with the  $\Delta$  propagators in the following way:

$$(4.20) \quad A \sim \left(1 + c(\mathbf{k}_1 \cdot \mathbf{k}_2)\right) \sqrt{9|D_{\Delta^{++}}|^2 + |D_{\Delta^0}|^2}$$

We do not only need to multiply both the  $N^* \rightarrow \Delta\pi$  and the  $N^* \rightarrow N(\pi\pi)_{l=I=0}$  amplitude with the  $\Delta$  propagators, but in addition these  $\Delta$  propagators have to be added incoherently, which best describes the data for all observables. This is a phenomenological approach, which is still awaiting its theoretical justification. Another possible explanation of the observed effect could be a Coulomb effect in the  $p\pi$  FSI. One expects Coulomb repulsion in the  $p\pi^+$  case which would lead to a shift to higher invariant masses. For the  $p\pi^-$  case, Coulomb attraction should lead to a shift to lower invariant masses, just like the observed effect in the data. No calculations have been done yet to support this suggestion quantitatively.

#### 4.4.5 $\Delta\Delta$ excitation

The  $\Delta\Delta$  excitation might also be a candidate to the reaction mechanisms. However, more energy is needed to excite two  $\Delta$ s compared to the excitation of one nucleon to one  $N^*(1440)$ . So this process is expected to play a role at higher energies only (see section 1.5). This is consistent with the following observation. This process is the only process so far, that may produce a non-uniform angular distribution of the pions. The  $\pi^-$  angular distribution is shown in Fig. 4.9, it includes the prediction from [Alv00] for the  $\Delta\Delta$  process. From this a maximum contribution of this process to the reaction can be estimated, which must be on the level of a few percent only at the measured energy.

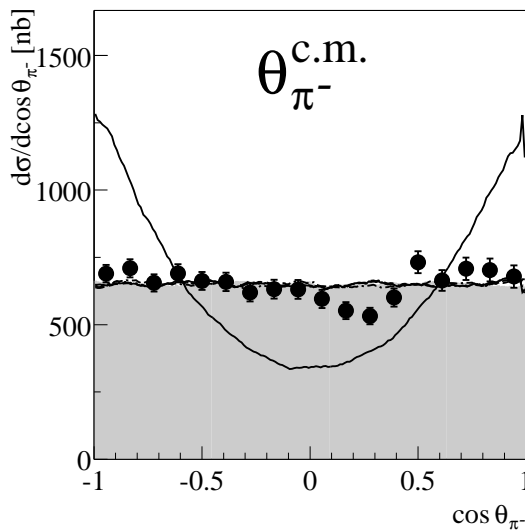


**Figure 4.9:** Effect of the  $\Delta\Delta$  process on the  $\pi^-$  angular distribution. It displays the data at 750 MeV in comparison to calculations of the  $\Delta\Delta$  process from [Alv00]. No significant deviation from a uniform distribution is observed in the data, for details see text.



## 4.5 Differential cross sections at 750 and 775 MeV

In this section the data measured at  $T_p = 750$  and  $775$  MeV are presented.

The event selection and reconstruction at  $750$  MeV are from [Bro01]. Whereas in [Bro01] a satisfactory description of all data was not achieved, our calculation including the  $\Delta$  propagators according to eq. 4.20 is now able to describe the data very well in all observables. So new calculations for the correction of acceptance and efficiencies have been carried out using this model. All spectra corrected for acceptance and efficiency shown in this and the previous section are treated with this model. The full description of the observed distributions leads to a reduction of systematic uncertainties for the corrected spectra, because some observables are rather dependent on the correct description of the reaction dynamics (see section 3.6).

The event selection and the reconstruction at  $775$  MeV are part of this thesis. Since the relative distribution of the differential cross sections at  $775$  MeV are very close to those obtained at  $750$  MeV, the theoretical description at  $750$  MeV also describe the effects seen in the data at  $775$  MeV.

The data show a significant deviation from phase space, as was already denoted in section 4.3. In the following pages the data are additionally compared to the effects on the distributions in the differential cross section spectra that come from: FSI, FSI &  $\sigma$ -exchange, FSI &  $\sigma$ -exchange &  $N^*$  decays according to eq. 4.19 and the latter mechanisms now also including  $\Delta$  propagators according to eq. 4.20, multiplied to both decay routes. The  $\Delta\Delta$  excitation does not play a significant role and is not shown here.

The caption below the figures is divided into two parts. First the difference to phase space distributions is mentioned, then the effects describing the data are discussed. On each double page on the left the results of  $750$  MeV beam energy are shown and on the right side those of  $775$  MeV.

## 4.5.1 Invariant masses

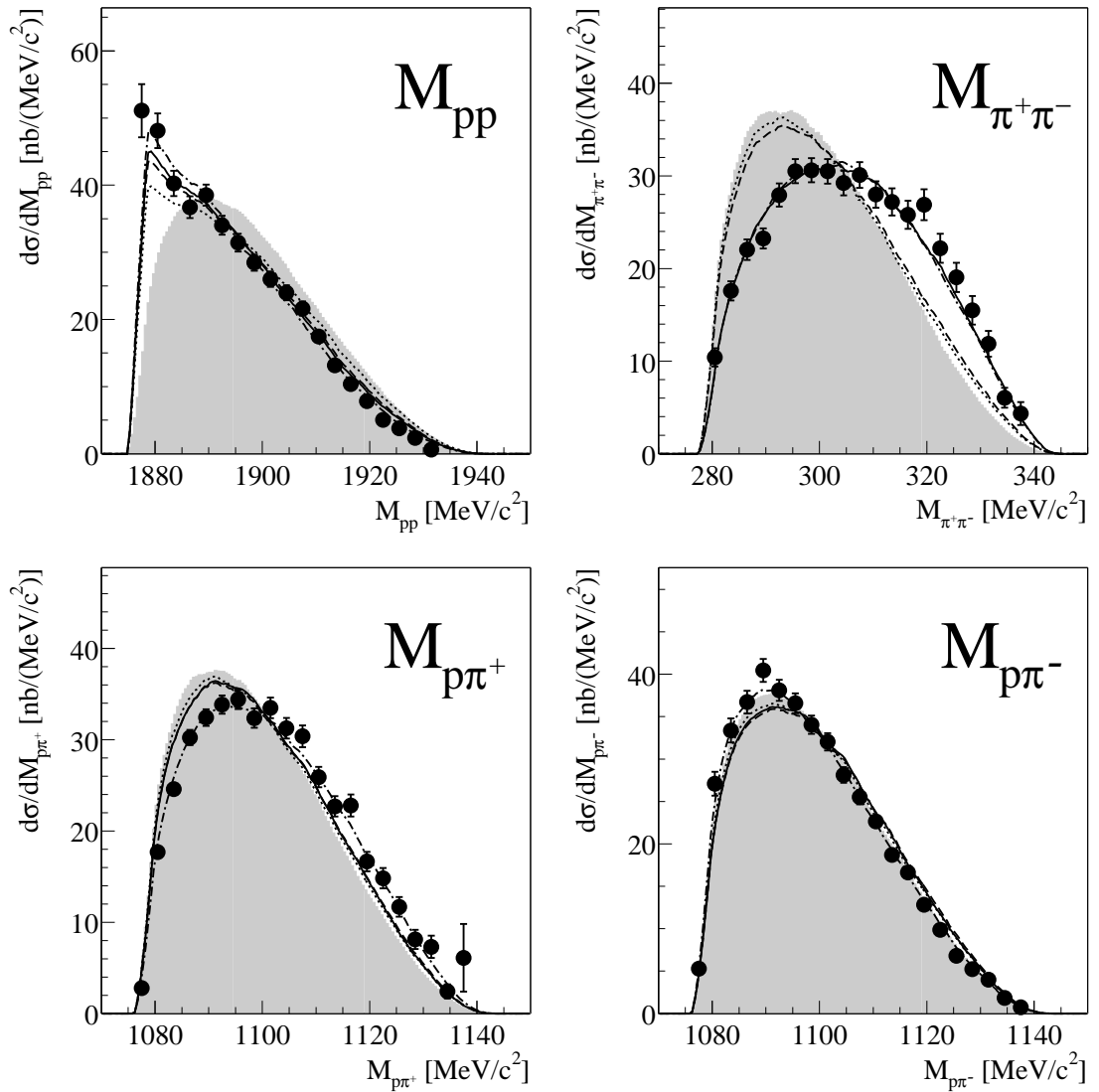


**Figure 4.10:** Invariant masses of two particle systems at  $T_p = 750$  MeV.

Corrected data (black points) are compared to phase space distributions (shaded area).  $M_{pp}$  shows an enhancement to low invariant masses compared to phase space, whereas  $M_{\pi^+\pi^-}$  shows a shift to higher invariant masses. The two  $M_{p\pi}$  spectra look different,  $M_{p\pi^+}$  is shifted to higher invariant masses,  $M_{p\pi^-}$  is described quite well by phase space. Different lines show the effects from FSI (dashed), FSI &  $\sigma$ -exchange (dotted), FSI &  $\sigma$ -exchange &  $N^*$  decays according to eq. 4.19 (solid) and the latter mechanisms now including  $\Delta$  propagators according to eq. 4.20 (dashed-dotted), which best describes the data for all observables.

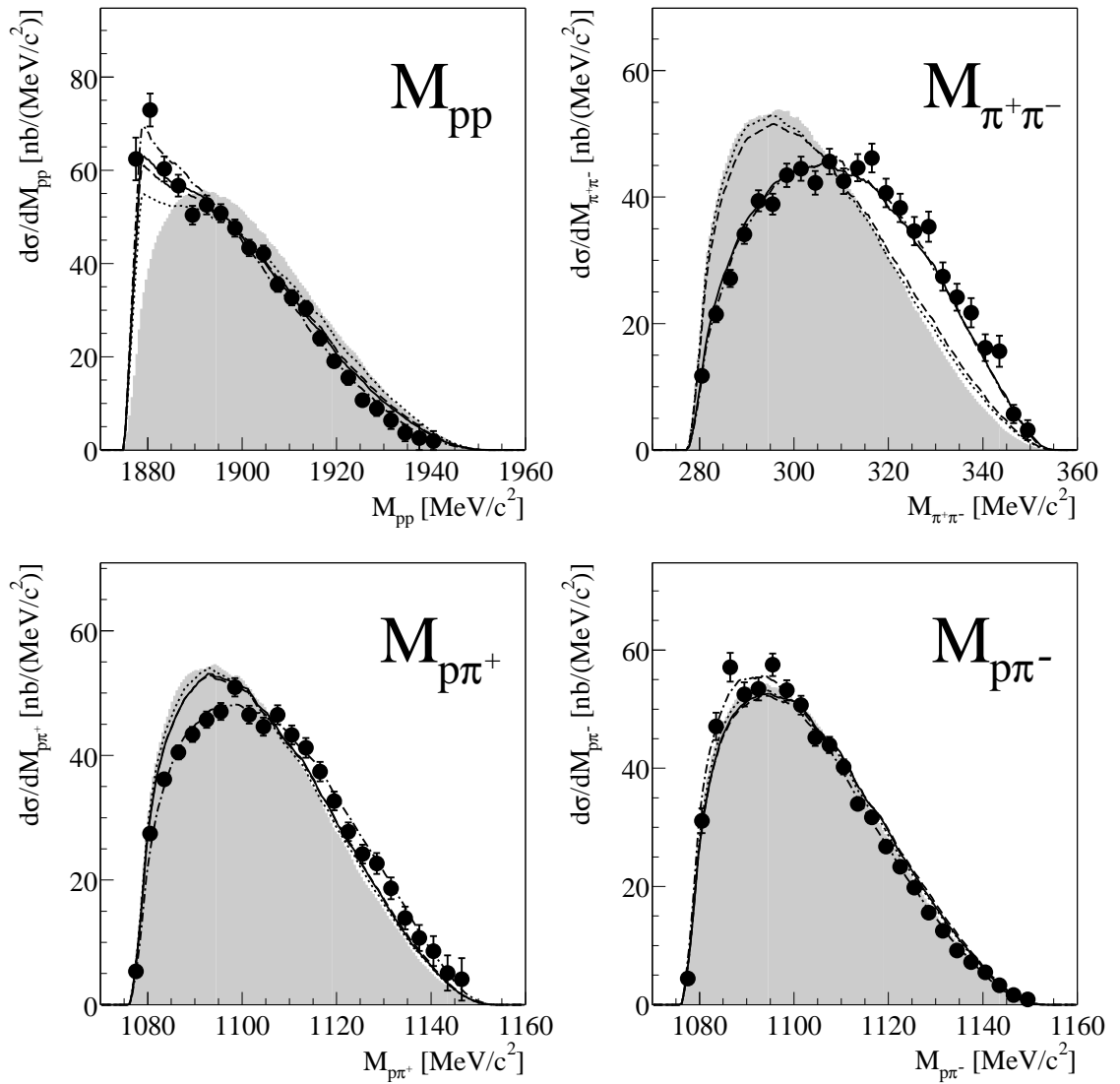


**Figure 4.11:** Invariant masses of two particle systems at  $T_p = 775$  MeV.

Corrected data (black points) are compared to phase space distributions (shaded area).  $M_{pp}$  shows an enhancement to low invariant masses compared to phase space, whereas  $M_{\pi^+\pi^-}$  shows a shift to higher invariant masses. The two  $M_{p\pi}$  spectra look different,  $M_{p\pi^+}$  is shifted to higher invariant masses,  $M_{p\pi^-}$  is described quite well by phase space. Different lines show the effects from FSI (dashed), FSI &  $\sigma$ -exchange (dotted), FSI &  $\sigma$ -exchange &  $N^*$  decays according to eq. 4.19 (solid) and the latter mechanisms now including  $\Delta$  propagators according to eq. 4.20 (dashed-dotted), which best describes the data for all observables.

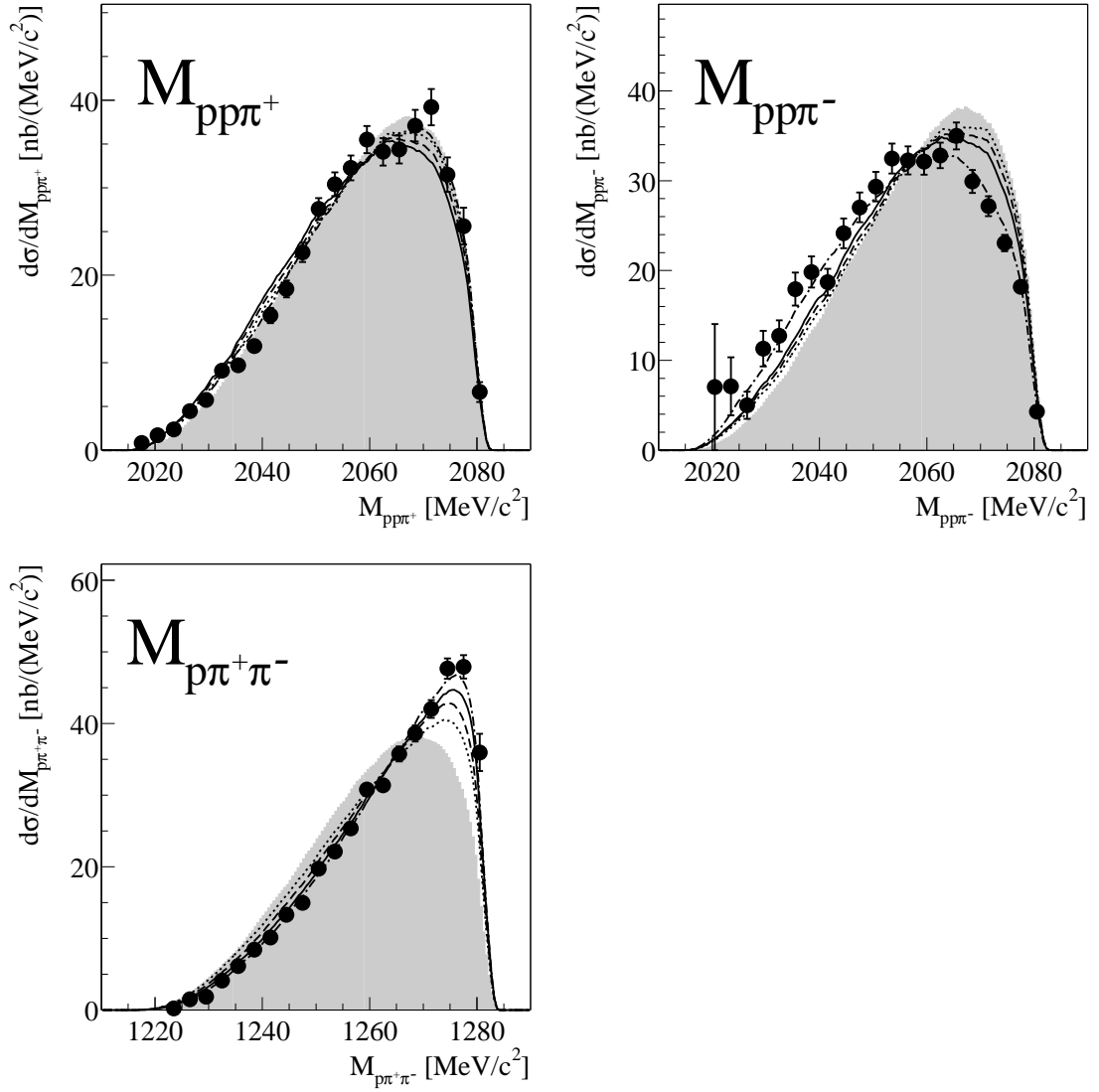


**Figure 4.12:** Invariant masses of three particle systems at  $T_p = 750$  MeV.

Corrected data (black points) are compared to phase space distributions (shaded area). The  $M_{pp\pi}$  spectra show the reflection of the effect in the  $M_{p\pi}$  spectra in the previous figure.  $M_{p\pi^+\pi^-}$ , the  $N^*$  system, shows a strong tendency to high invariant masses compared to phase space.

Different lines show the effects from FSI (dashed), FSI &  $\sigma$ -exchange (dotted), FSI &  $\sigma$ -exchange &  $N^*$  decays according to eq. 4.19 (solid) and the latter mechanisms now including  $\Delta$  propagators according to eq. 4.20 (dashed-dotted), which best describes the data for all observables. The strong enhancement in the  $M_{p\pi^+\pi^-}$  spectrum is due to the  $N^*$  excitation in the reaction and a part is due to the  $\Delta$  propagators.

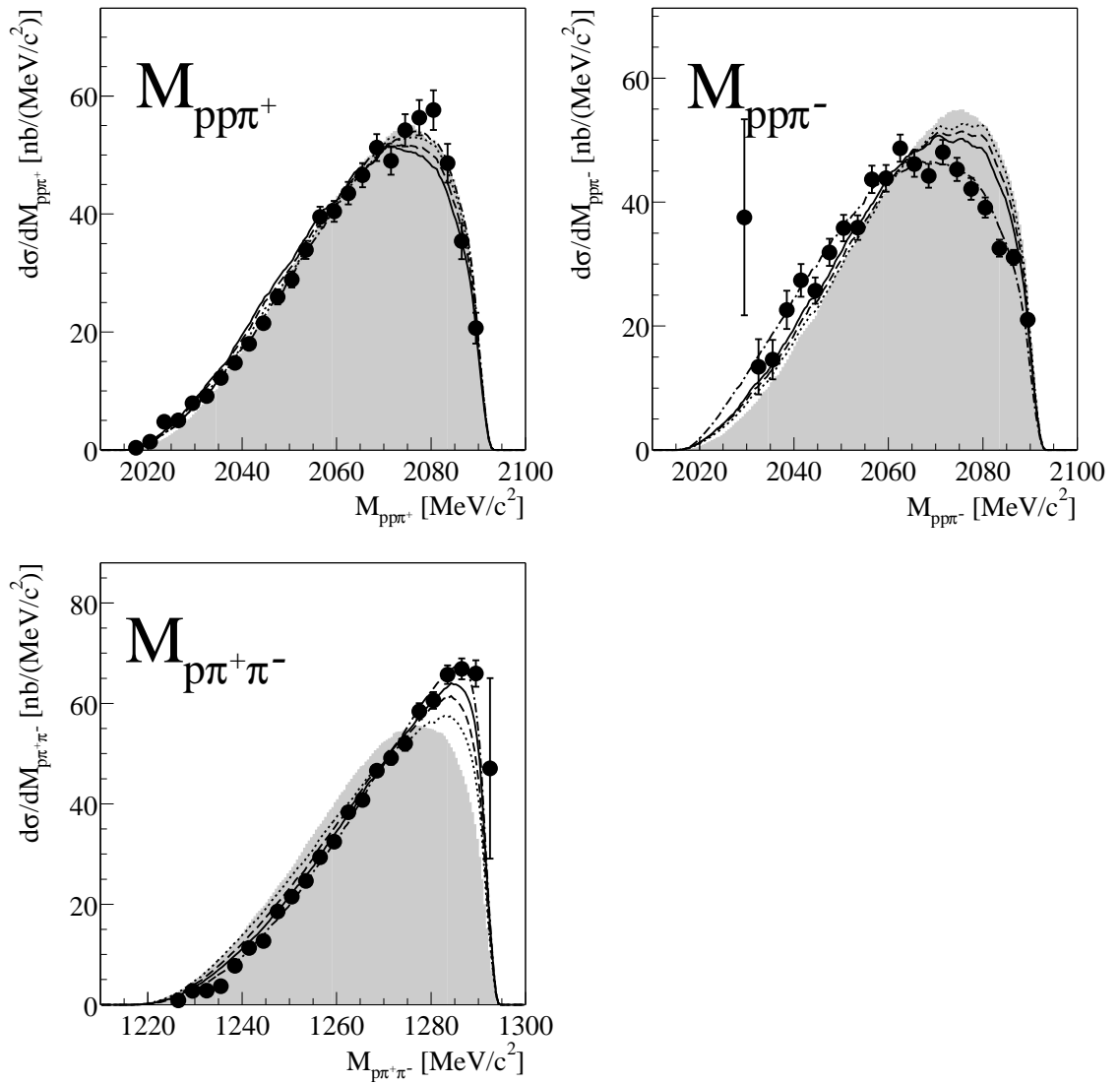


**Figure 4.13:** Invariant masses of three particle systems at  $T_p = 775$  MeV.

Corrected data (black points) are compared to phase space distributions (shaded area). The  $M_{pp\pi}$  spectra show the reflection of the effect in the  $M_{p\pi}$  spectra in the previous figure.  $M_{p\pi^+\pi^-}$ , the  $N^*$  system, shows a strong tendency to high invariant masses compared to phase space.

Different lines show the effects from FSI (dashed), FSI &  $\sigma$ -exchange (dotted), FSI &  $\sigma$ -exchange &  $N^*$  decays according to eq. 4.19 (solid) and the latter mechanisms now including  $\Delta$  propagators according to eq. 4.20 (dashed-dotted), which best describes the data for all observables. The strong enhancement in the  $M_{p\pi^+\pi^-}$  spectrum is due to the  $N^*$  excitation in the reaction and a part is due to the  $\Delta$  propagators.

## 4.5.2 Angular distributions

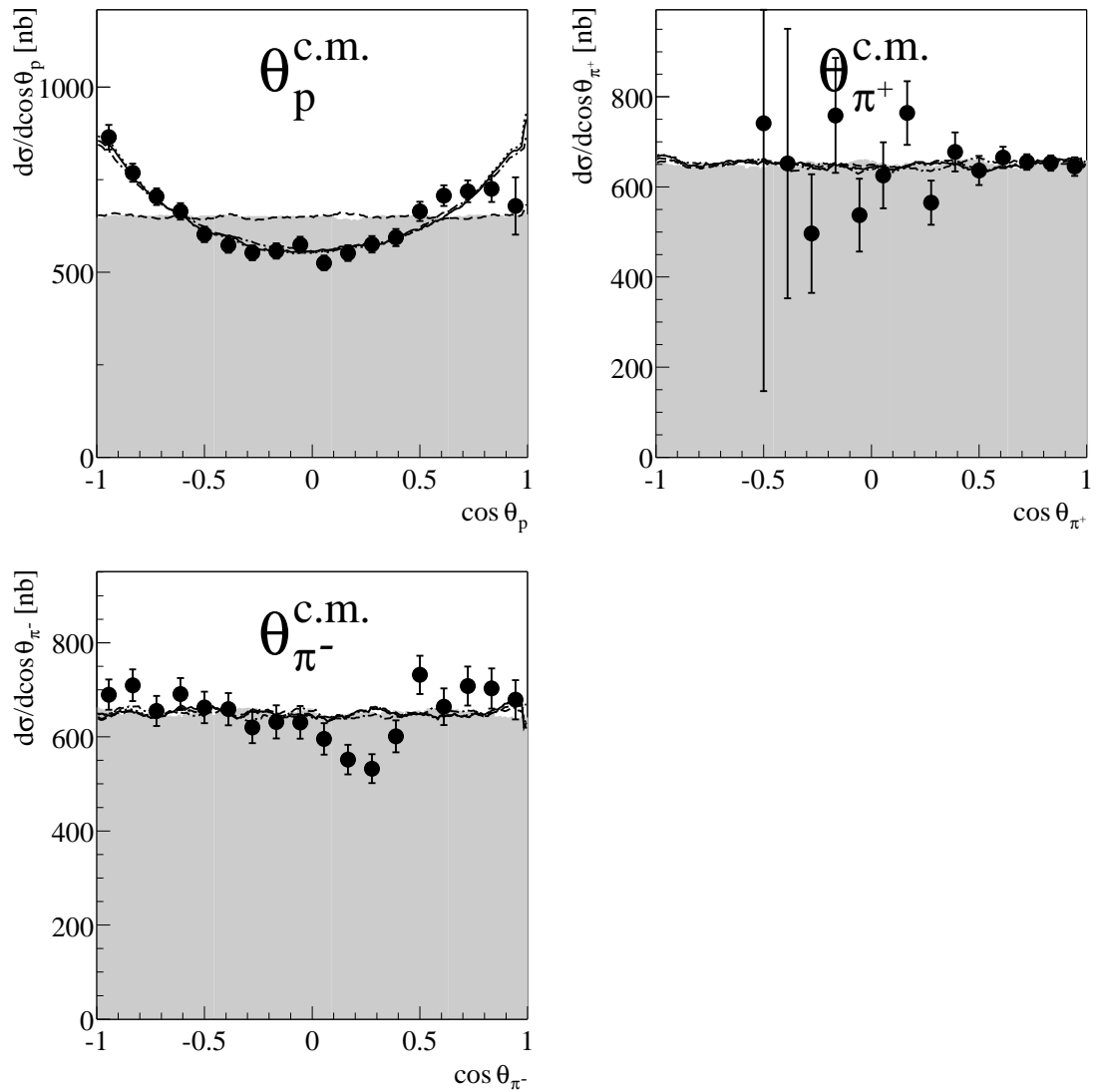


**Figure 4.14:** Scattering angles in c.m. system at  $T_p = 750$  MeV.

Corrected data (black points) are compared to phase space distributions (shaded area). The angular distributions of the pions, within statistical fluctuations, are comparable with a uniform distribution.  $\theta_p^{c.m.}$  shows more events in the forward and backward angles.

Different lines show the effects from FSI (dashed), FSI &  $\sigma$ -exchange (dotted), FSI &  $\sigma$ -exchange &  $N^*$  decays according to eq. 4.19 (solid) and the latter mechanisms now including  $\Delta$  propagators according to eq. 4.20 (dashed-dotted). No mechanism shows an effect on the angular distribution of the pions. The effect in the scattering angle of the proton is described through the  $\sigma$ -exchange.

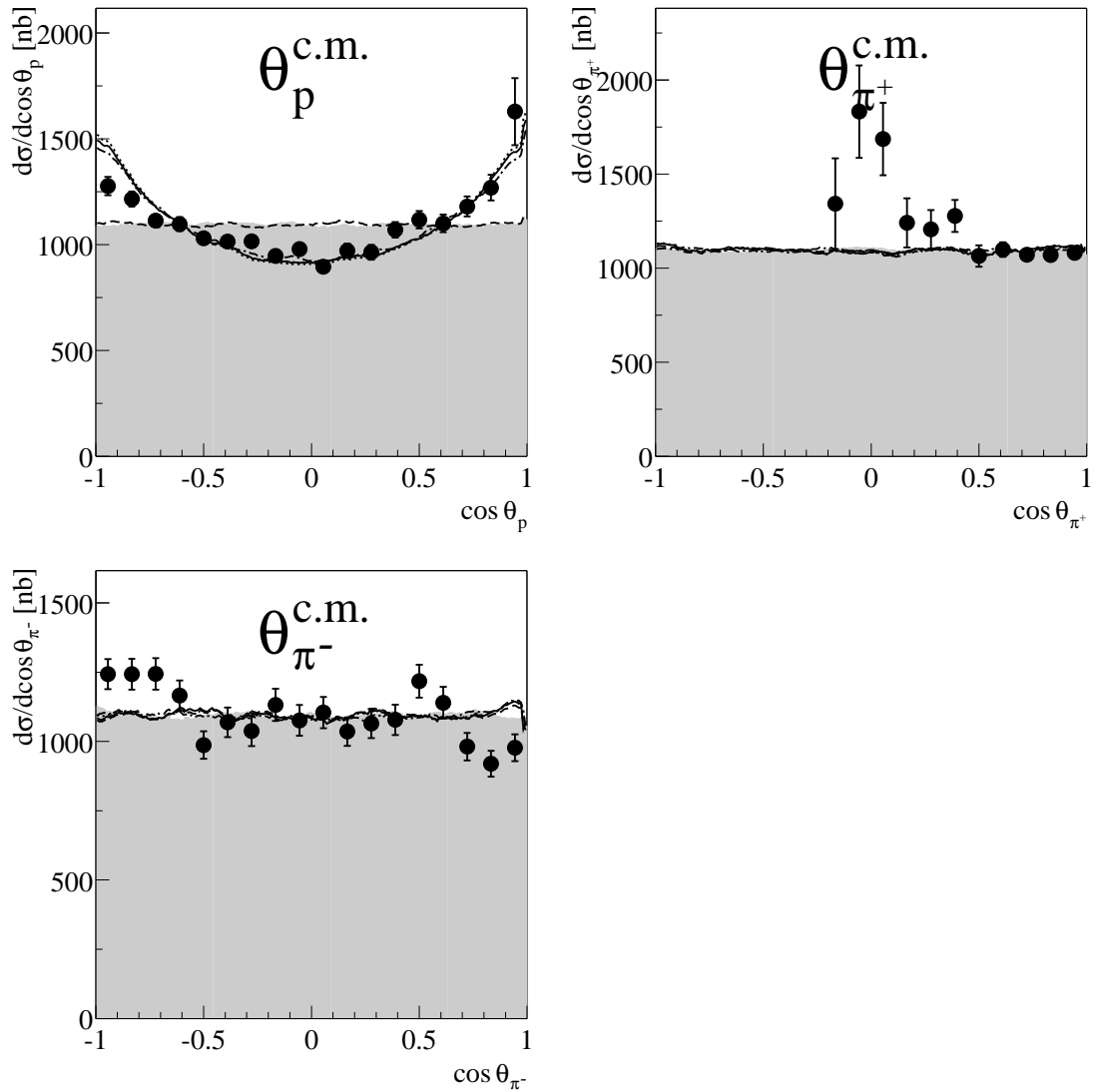


**Figure 4.15:** Scattering angles in c.m. system at  $T_p = 775$  MeV.

Corrected data (black points) are compared to phase space distributions (shaded area). The angular distributions of the pions, within statistical fluctuations, are comparable with a uniform distribution.  $\theta_p^{c.m.}$  shows more events in the forward and backward angles.

Different lines show the effects from FSI (dashed), FSI &  $\sigma$ -exchange (dotted), FSI &  $\sigma$ -exchange &  $N^*$  decays according to eq. 4.19 (solid) and the latter mechanisms now including  $\Delta$  propagators according to eq. 4.20 (dashed-dotted). No mechanism shows an effect on the angular distribution of the pions. The effect in the scattering angle of the proton is described through the  $\sigma$ -exchange.

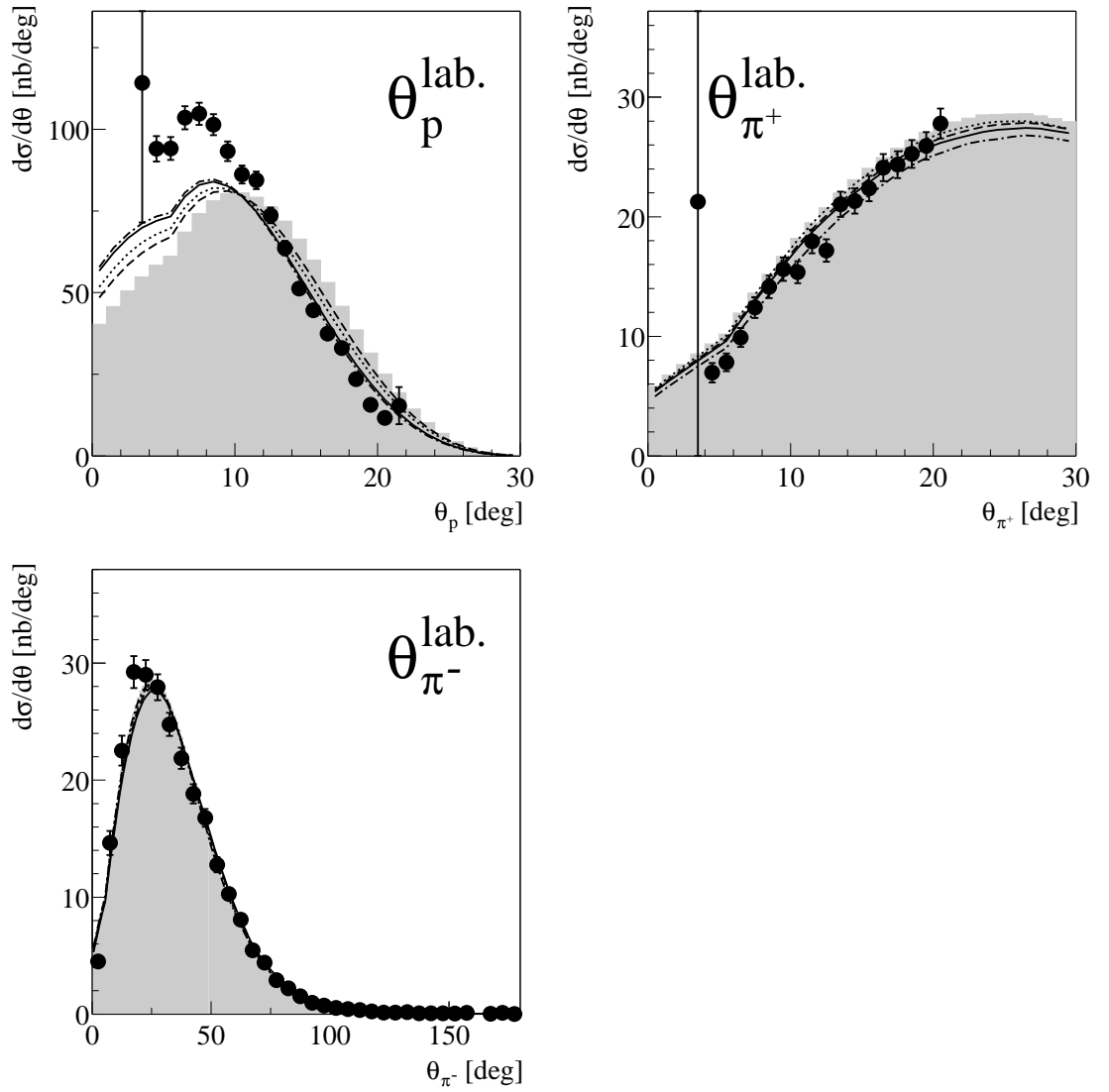


**Figure 4.16:** Scattering angles in lab. system at  $T_p = 750$  MeV.

Corrected data (black points) are compared to phase space distributions (shaded area). The scattering angles of the pions more or less follow phase space. Apart from a problem with the correction (see uncorrected spectra) the data show a shift to smaller scattering angles.

Different lines show the effects from FSI (dashed), FSI &  $\sigma$ -exchange (dotted), FSI &  $\sigma$ -exchange &  $N^*$  decays according to eq. 4.19 (solid) and the latter mechanisms now including  $\Delta$  propagators according to eq. 4.20 (dashed-dotted). The shift to smaller angles in  $\theta_p^{lab.}$  is explained by the effect of  $pp$ FSI.



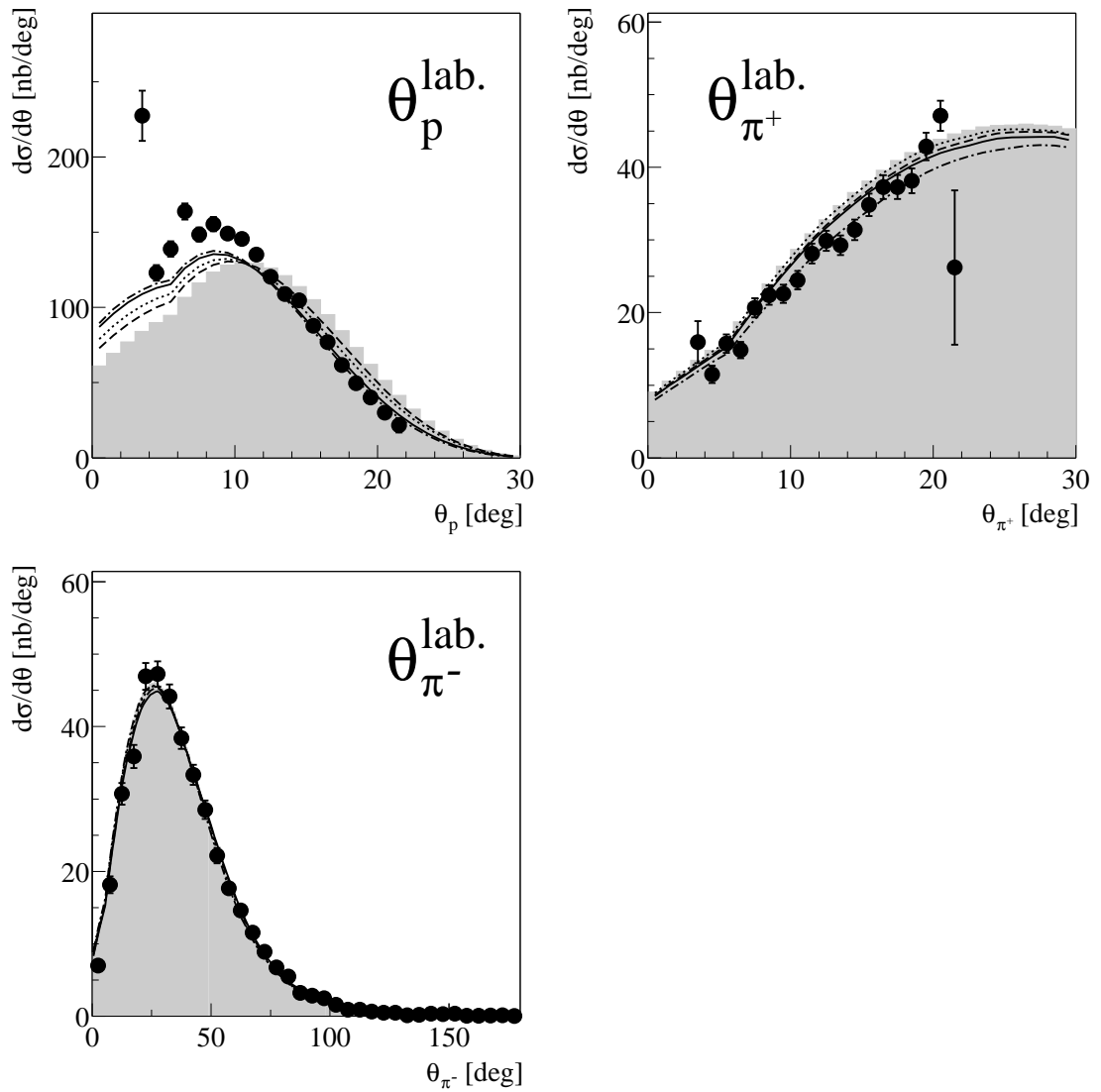


**Figure 4.17:** Scattering angles in lab. system at  $T_p = 775$  MeV.

Corrected data (black points) are compared to phase space distributions (shaded area). The scattering angles of the pions more or less follow phase space. Apart from a problem with the correction (see uncorrected spectra) the data show a shift to smaller scattering angles.

Different lines show the effects from FSI (dashed), FSI &  $\sigma$ -exchange (dotted), FSI &  $\sigma$ -exchange &  $N^*$  decays according to eq. 4.19 (solid) and the latter mechanisms now including  $\Delta$  propagators according to eq. 4.20 (dashed-dotted). The shift to smaller angles in  $\theta_p^{\text{lab.}}$  is explained by the effect of  $pp$ FSI.

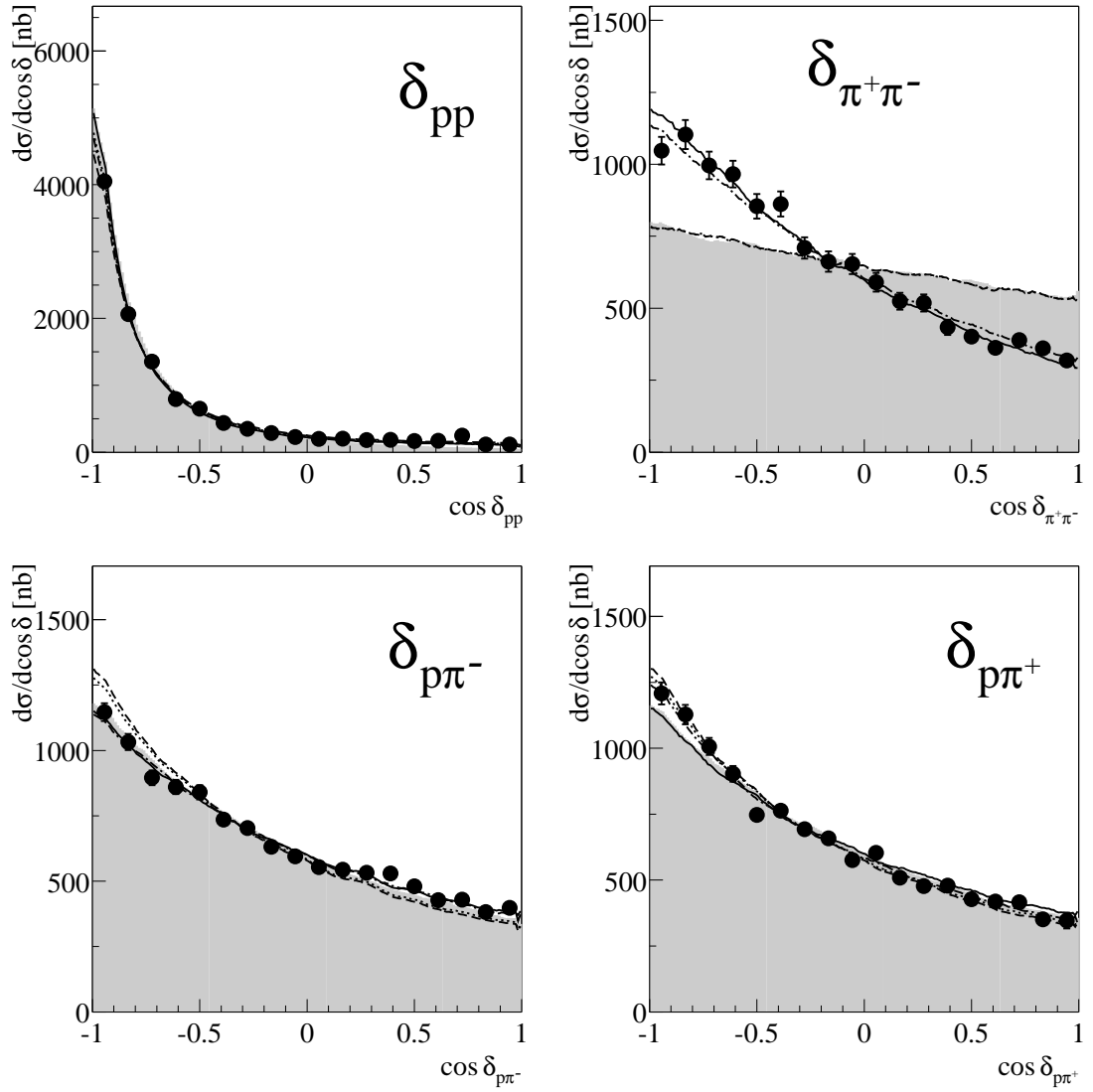


**Figure 4.18:** Opening angles in c.m. system at  $T_p = 750$  MeV. Corrected data (black points) are compared to phase space distributions (shaded area). A large difference is seen in the opening angles between the two pions. Different lines show the effects from FSI (dashed), FSI &  $\sigma$ -exchange (dotted), FSI &  $\sigma$ -exchange &  $N^*$  decays according to eq. 4.19 (solid) and the latter mechanisms now including  $\Delta$  propagators according to eq. 4.20 (dashed-dotted), which best describes the data for all observables. The effect in the  $\delta_{\pi^+\pi^-}$  spectrum is described by the interference between both  $N^*$  decay channels.

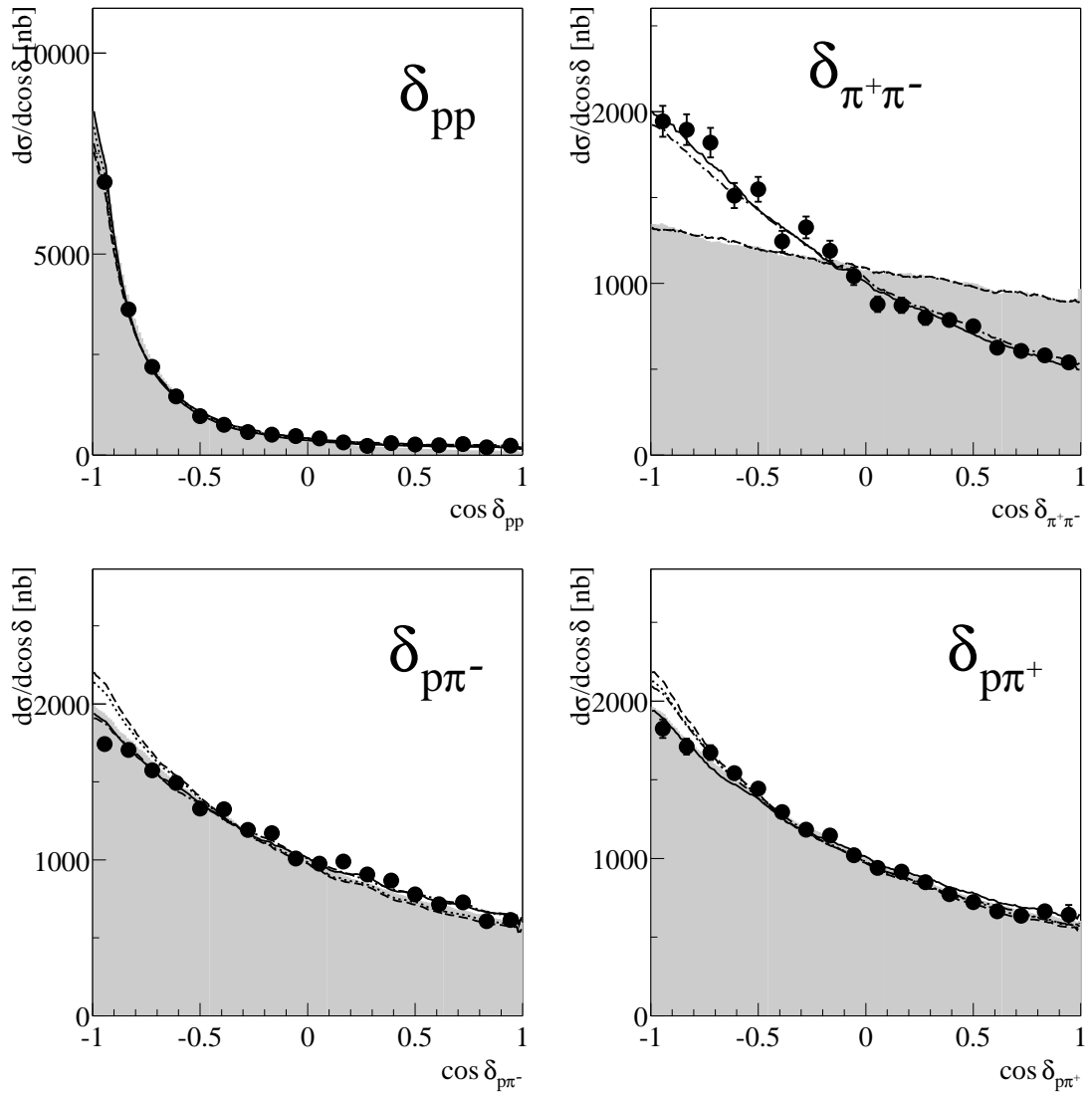


**Figure 4.19:** Opening angles in c.m. system at  $T_p = 775$  MeV. Corrected data (black points) are compared to phase space distributions (shaded area). A large difference is seen in the opening angles between the two pions. Different lines show the effects from FSI (dashed), FSI &  $\sigma$ -exchange (dotted), FSI &  $\sigma$ -exchange &  $N^*$  decays according to eq. 4.19 (solid) and the latter mechanisms now including  $\Delta$  propagators according to eq. 4.20 (dashed-dotted), which best describes the data for all observables. The effect in the  $\delta_{\pi^+\pi^-}$  spectrum is described by the interference between both  $N^*$  decay channels.

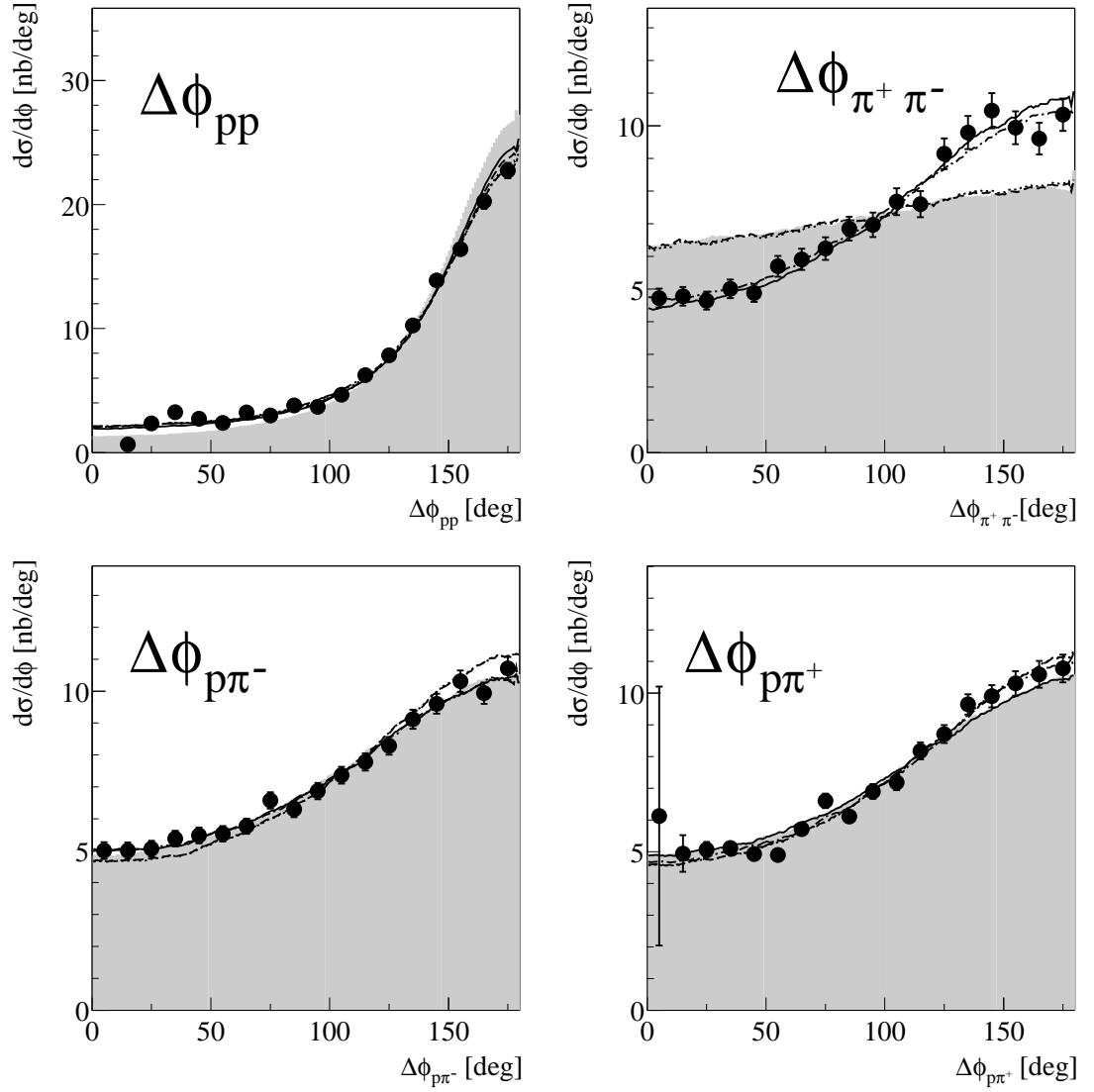


**Figure 4.20:** Planarity angles at  $T_p = 750$  MeV.

Corrected data (black points) are compared to phase space distributions (shaded area). Different lines show the effects from FSI (dashed), FSI &  $\sigma$ -exchange (dotted), FSI &  $\sigma$ -exchange &  $N^*$  decays according to eq. 4.19 (solid) and the latter mechanisms now including  $\Delta$  propagators according to eq. 4.20 (dashed-dotted), which best describes the data for all observables.

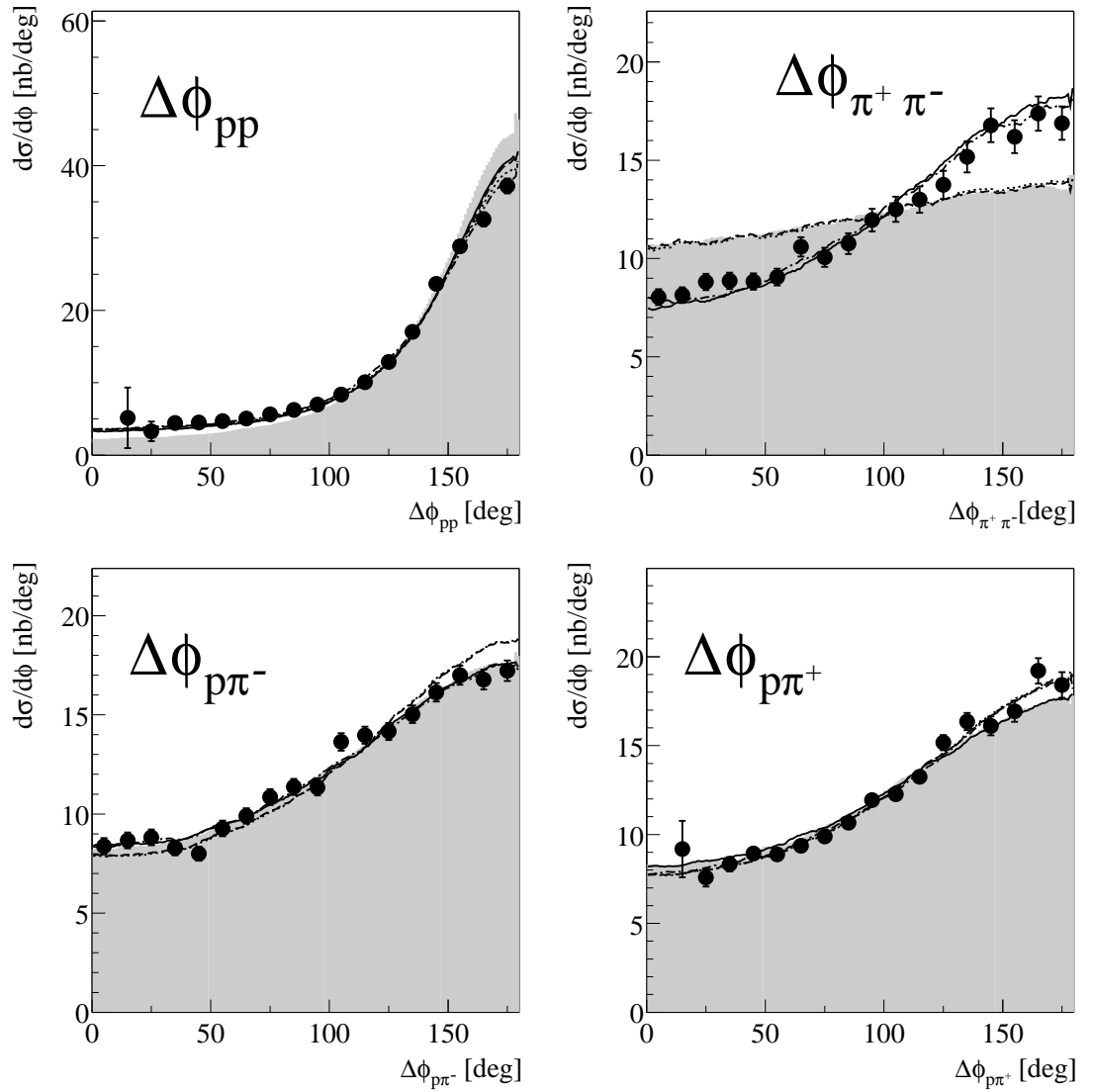


**Figure 4.21:** Planarity angles at  $T_p = 775$  MeV.

Corrected data (black points) are compared to phase space distributions (shaded area). Different lines show the effects from FSI (dashed), FSI &  $\sigma$ -exchange (dotted), FSI &  $\sigma$ -exchange &  $N^*$  decays according to eq. 4.19 (solid) and the latter mechanisms now including  $\Delta$  propagators according to eq. 4.20 (dashed-dotted), which best describes the data for all observables.

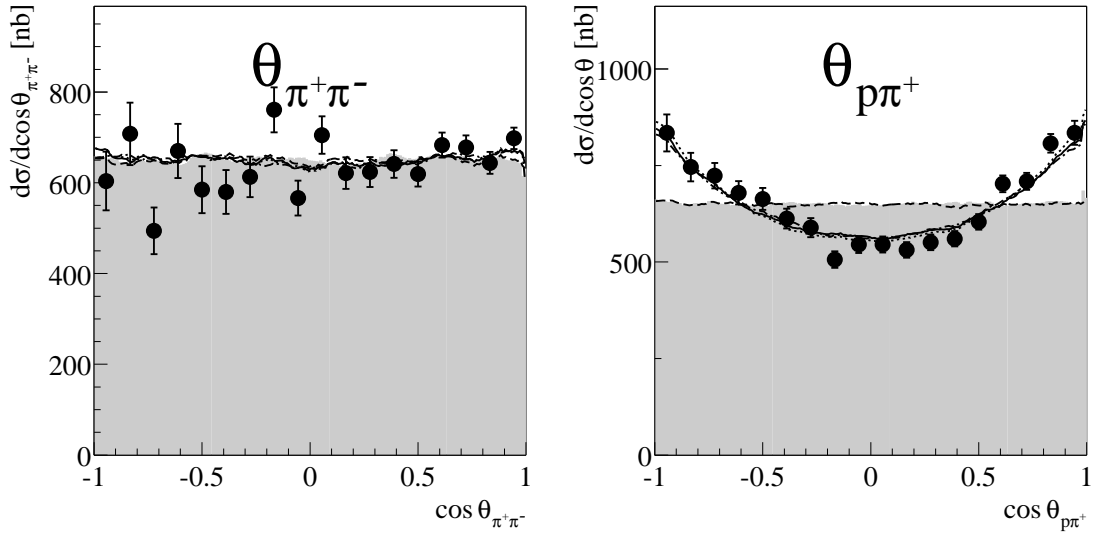


**Figure 4.22:** Scattering angle of two particles' total momentum at  $T_p = 750$  MeV. The angular distributions  $\theta_{\pi^+\pi^-}$  and  $\theta_{p\pi^+}$  are equivalent to the distributions  $\theta_{pp}$  and  $\theta_{p\pi^-}$  respectively, but with reversed signs for  $\cos\theta$ .

Corrected data (black points) are compared to phase space distributions (shaded area). Within the statistical fluctuations,  $\theta_{\pi^+\pi^-}$  follows the flat phase space distribution.  $\theta_{p\pi^+}$  shows an enhancement to forward and backward angles compared to phase space. Different lines show the effects from FSI (dashed), FSI &  $\sigma$ -exchange (dotted), FSI &  $\sigma$ -exchange &  $N^*$  decays according to eq. 4.19 (solid) and the latter mechanisms now including  $\Delta$  propagators according to eq. 4.20 (dashed-dotted). The non-flat distribution in  $\theta_{p\pi^+}$  is described by the  $\sigma$ -exchange.

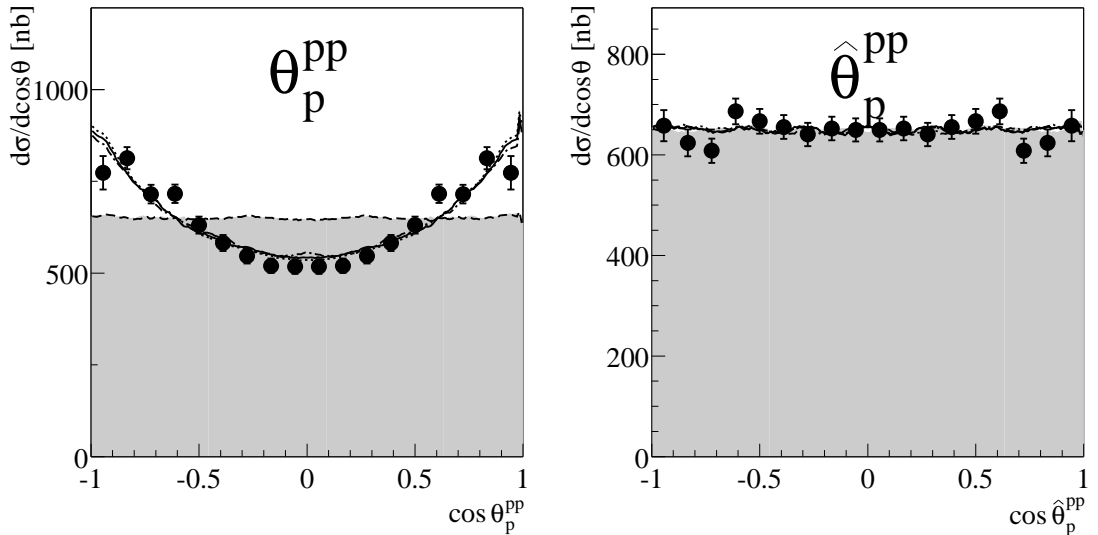


**Figure 4.23:**  $pp$  subsystem scattering angles at  $T_p = 750$  MeV.

Corrected data (black points) are compared to phase space distributions (shaded area).  $\theta_p^{pp}$  shows more events in the forward and backward angles compared to phase space.  $\hat{\theta}_p^{pp}$  has a flat distribution.

Different lines show the effects from FSI (dashed), FSI &  $\sigma$ -exchange (dotted), FSI &  $\sigma$ -exchange &  $N^*$  decays according to eq. 4.19 (solid) and the latter mechanisms now including  $\Delta$  propagators according to eq. 4.20 (dashed-dotted). The non-flat distribution in  $\theta_p^{pp}$  is described by the  $\sigma$ -exchange.

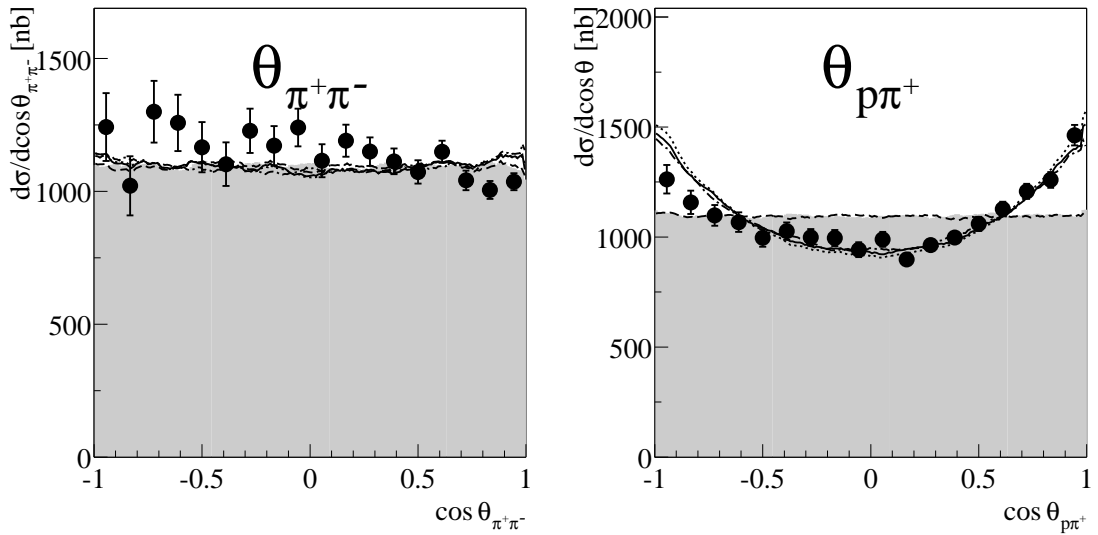


**Figure 4.24:** Scattering angle of two particles' total momentum at  $T_p = 775$  MeV. The angular distributions  $\theta_{\pi^+\pi^-}$  and  $\theta_{p\pi^+}$  are equivalent to the distributions  $\theta_{pp}$  and  $\theta_{p\pi^-}$  respectively, but with reversed signs for  $\cos\theta$ .

Corrected data (black points) are compared to phase space distributions (shaded area). Within the statistical fluctuations,  $\theta_{\pi^+\pi^-}$  follows the flat phase space distribution.  $\theta_{p\pi^+}$  shows an enhancement to forward and backward angles compared to phase space. Different lines show the effects from FSI (dashed), FSI &  $\sigma$ -exchange (dotted), FSI &  $\sigma$ -exchange &  $N^*$  decays according to eq. 4.19 (solid) and the latter mechanisms now including  $\Delta$  propagators according to eq. 4.20 (dashed-dotted). The non-flat distribution in  $\theta_{p\pi^+}$  is described by the  $\sigma$ -exchange.

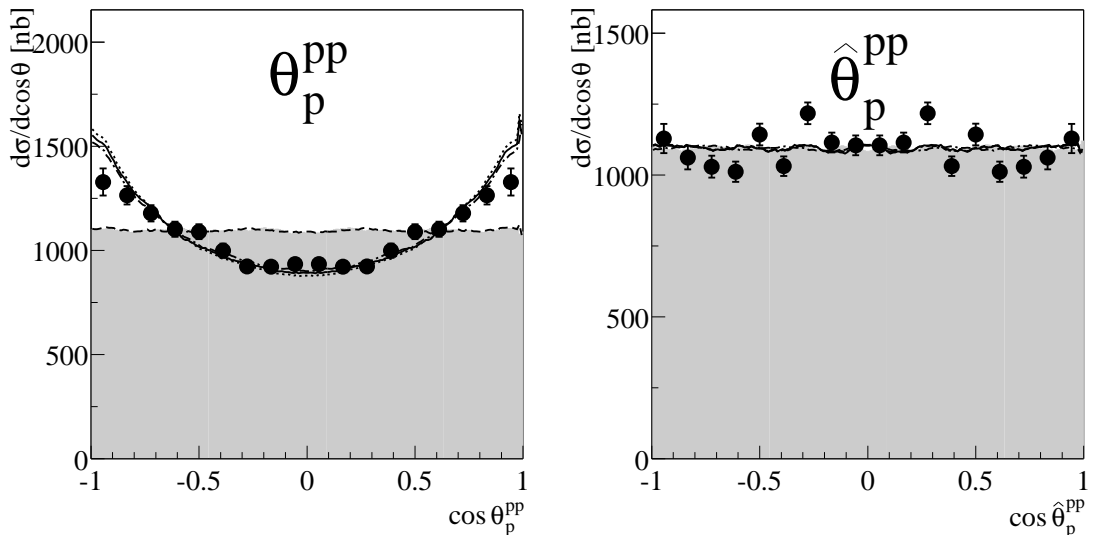


**Figure 4.25:**  $pp$  subsystem scattering angles at  $T_p = 775$  MeV.

Corrected data (black points) are compared to phase space distributions (shaded area).  $\theta_p^{pp}$  shows more events in the forward and backward angles compared to phase space.  $\hat{\theta}_p^{pp}$  has a flat distribution within some fluctuations.

Different lines show the effects from FSI (dashed), FSI &  $\sigma$ -exchange (dotted), FSI &  $\sigma$ -exchange &  $N^*$  decays according to eq. 4.19 (solid) and the latter mechanisms now including  $\Delta$  propagators according to eq. 4.20 (dashed-dotted). The non-flat distribution in  $\theta_p^{pp}$  is described by the  $\sigma$ -exchange.

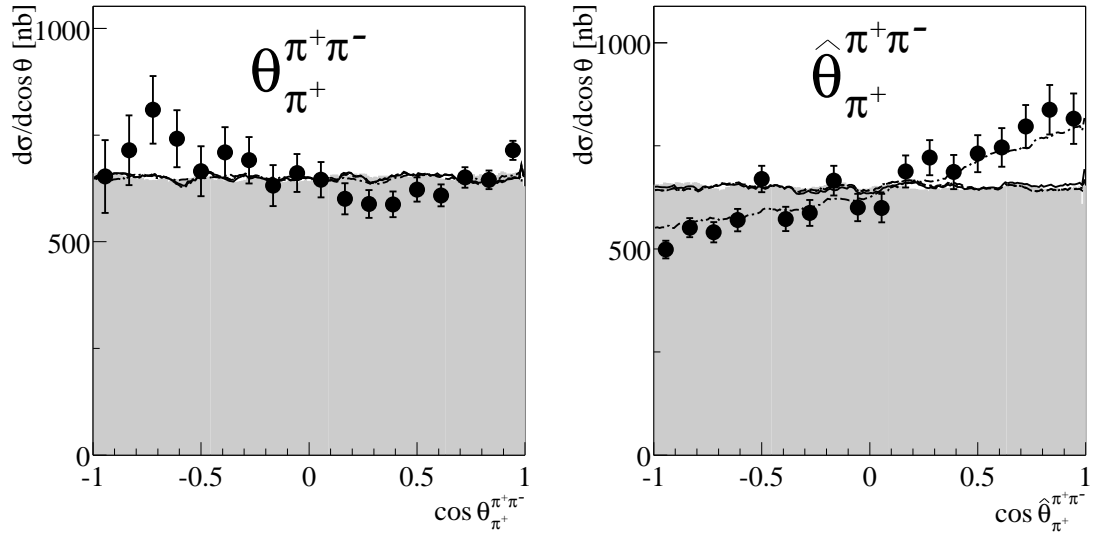


**Figure 4.26:**  $\pi^+\pi^-$  subsystem scattering angles at  $T_p = 750$  MeV.

Corrected data (black points) are compared to phase space distributions (shaded area). The pions' angular distribution with respect to the beam axis does not show a deviation within statistics with a flat distribution. But the scattering angle of the pion with respect to the two pions' summary momentum shows more events in the forward angles. Different lines show the effects from FSI (dashed), FSI &  $\sigma$ -exchange (dotted), FSI &  $\sigma$ -exchange &  $N^*$  decays according to eq. 4.19 (solid) and the latter mechanisms now including  $\Delta$  propagators according to eq. 4.20 (dashed-dotted), which best describes the data for all observables. The description of the pion scattering angle in the  $\pi\pi$  system with respect to the two pions' summary momentum axis best done with the use of the  $\Delta$  propagators multiplied to both  $N^*$  decay routes.

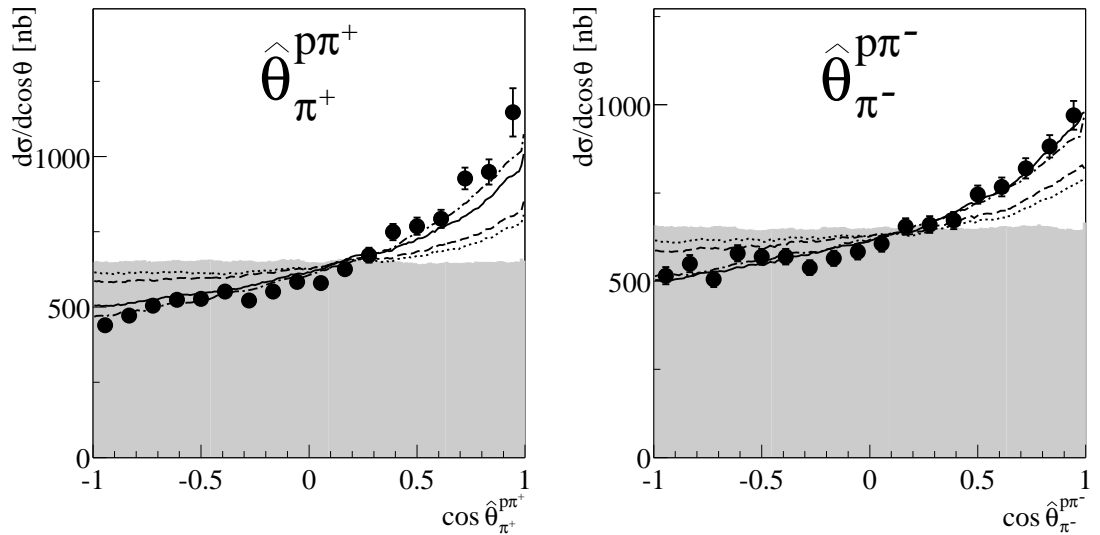


**Figure 4.27:**  $p\pi$  subsystem scattering angles at  $T_p = 750$  MeV.

Corrected data (black points) are compared to phase space distributions (shaded area). Both distributions show more events in the forward angles. Different lines show the effects from FSI (dashed), FSI &  $\sigma$ -exchange (dotted), FSI &  $\sigma$ -exchange &  $N^*$  decays according to eq. 4.19 (solid) and the latter mechanisms now including  $\Delta$  propagators according to eq. 4.20 (dashed-dotted), which best describes the data for all observables. The effect in the distribution is a dynamic effect of the model giving more events in the forward angles.



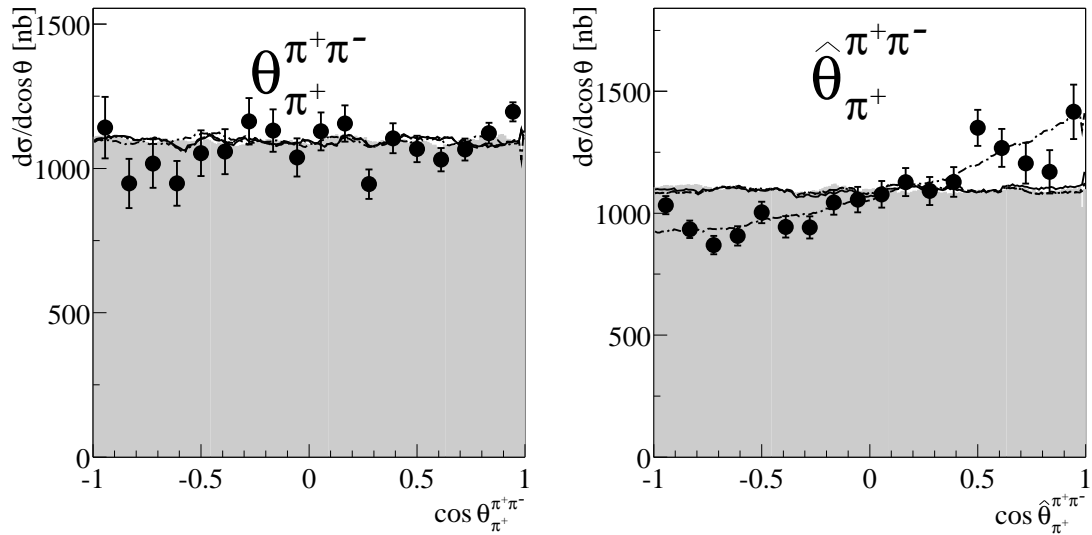


**Figure 4.28:**  $\pi^+\pi^-$  subsystem scattering angles at  $T_p = 775$  MeV.

Corrected data (black points) are compared to phase space distributions (shaded area). The pions' angular distribution with respect to the beam axis does not show a deviation within statistics with a flat distribution. But the scattering angle of the pion with respect to the two pions' summary momentum shows more events in the forward angles. Different lines show the effects from FSI (dashed), FSI &  $\sigma$ -exchange (dotted), FSI &  $\sigma$ -exchange &  $N^*$  decays according to eq. 4.19 (solid) and the latter mechanisms now including  $\Delta$  propagators according to eq. 4.20 (dashed-dotted), which best describes the data for all observables. The description of the pion scattering angle in the  $\pi\pi$  system with respect to the two pions' summary momentum axis is best done with the use of the  $\Delta$  propagators multiplied to both  $N^*$  decay routes.

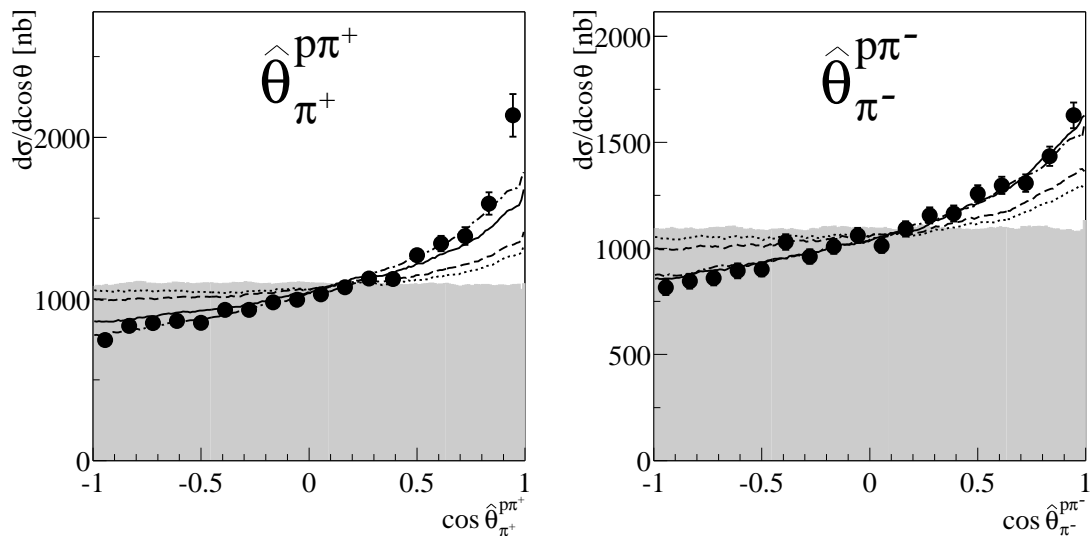


**Figure 4.29:**  $p\pi$  subsystem scattering angles at  $T_p = 775$  MeV.

Corrected data (black points) are compared to phase space distributions (shaded area). Both distributions show more events in the forward angles. Different lines show the effects from FSI (dashed), FSI &  $\sigma$ -exchange (dotted), FSI &  $\sigma$ -exchange &  $N^*$  decays according to eq. 4.19 (solid) and the latter mechanisms now including  $\Delta$  propagators according to eq. 4.20 (dashed-dotted), which best describes the data for all observables. The effect in the distribution is an dynamic effect of the model giving more events in the forward angles.

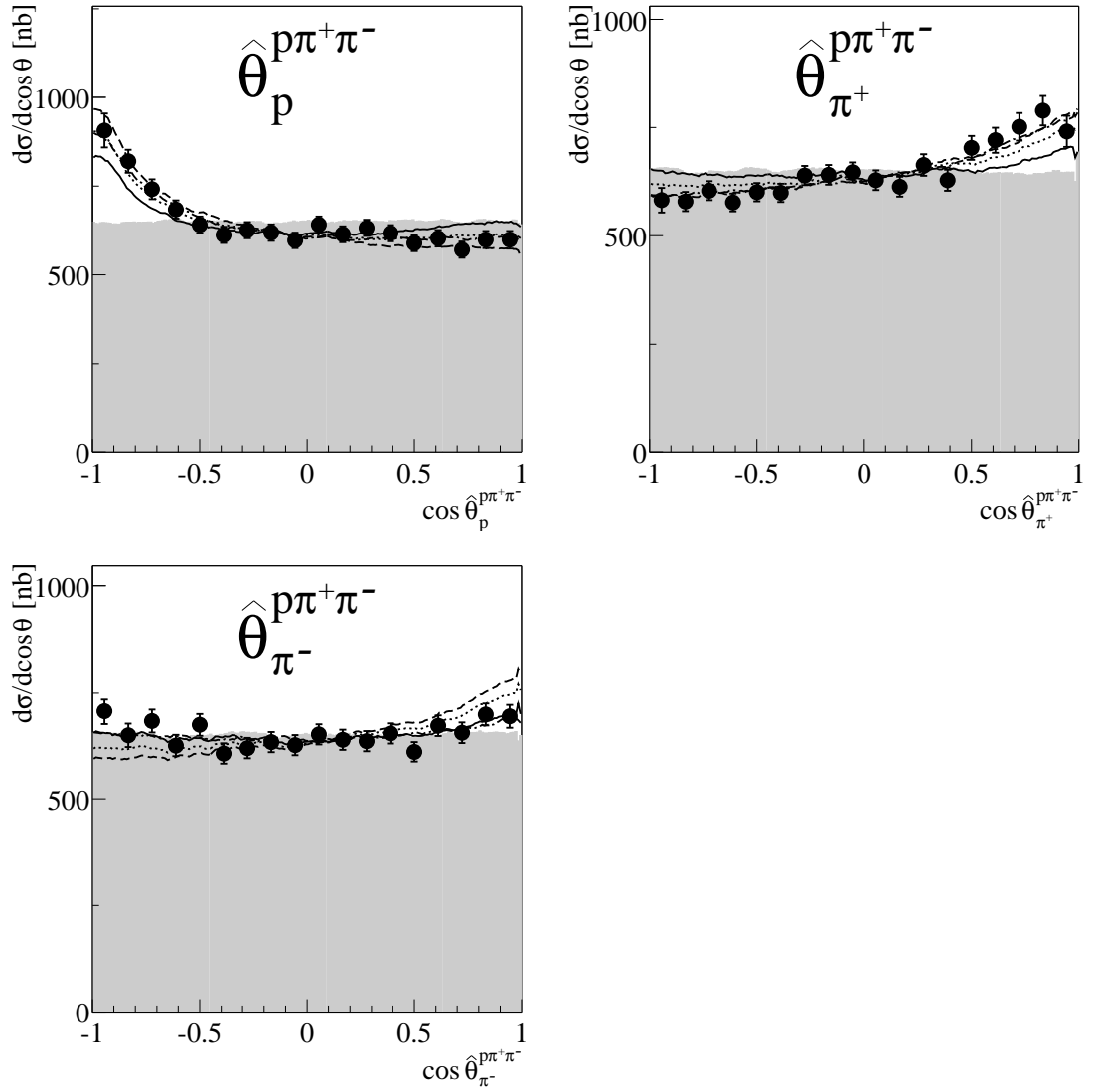


**Figure 4.30:**  $p\pi\pi$  subsystem scattering angles at  $T_p = 750$  MeV.

Corrected data (black points) are compared to phase space distributions (shaded area). Different lines show the effects from FSI (dashed), FSI &  $\sigma$ -exchange (dotted), FSI &  $\sigma$ -exchange &  $N^*$  decays according to eq. 4.19 (solid) and the latter mechanisms now including  $\Delta$  propagators according to eq. 4.20 (dashed-dotted), which best describes the data for all observables.

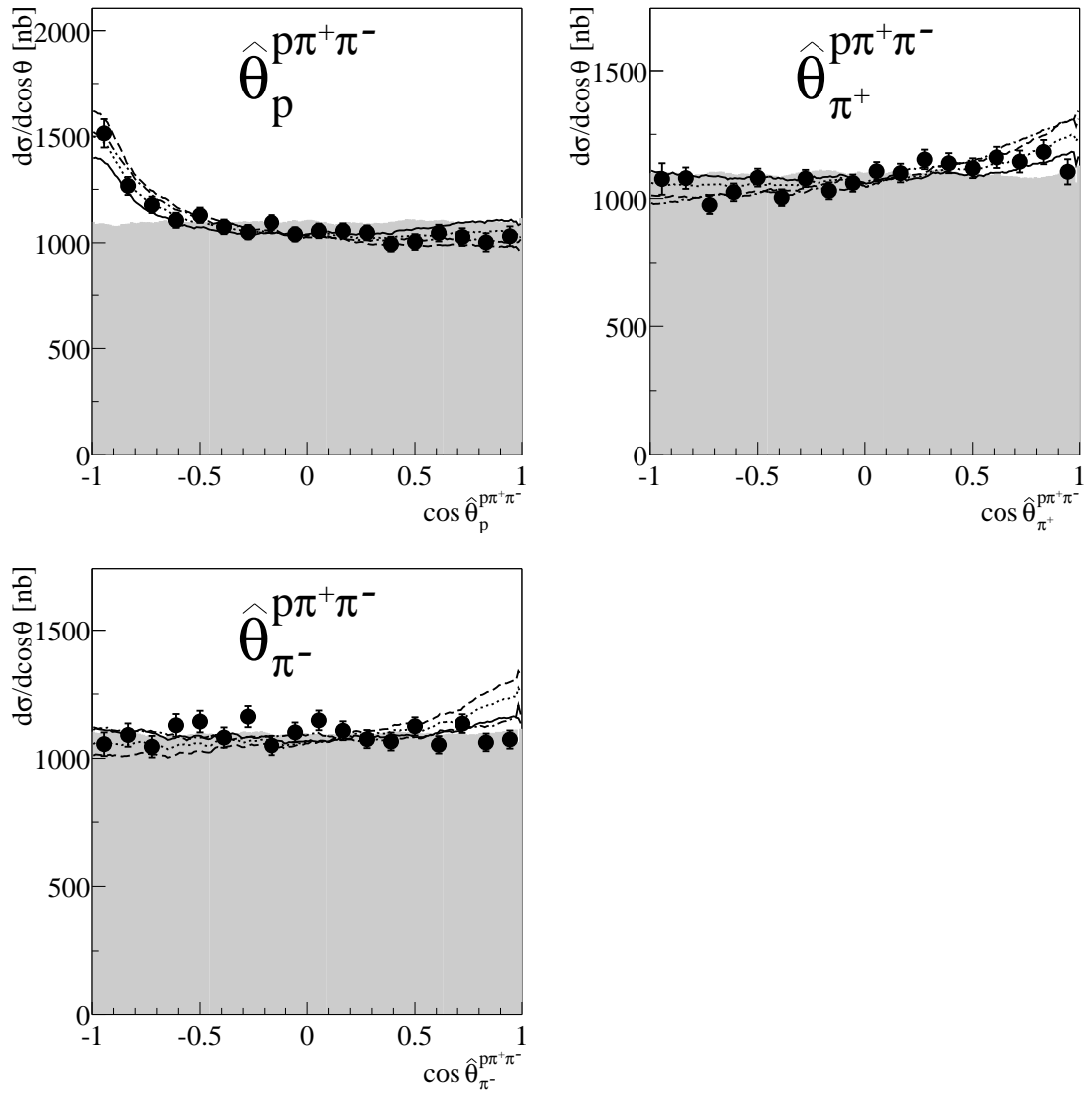


**Figure 4.31:**  $p\pi\pi$  subsystem scattering angles at  $T_p = 775$  MeV.

Corrected data (black points) are compared to phase space distributions (shaded area). Different lines show the effects from FSI (dashed), FSI &  $\sigma$ -exchange (dotted), FSI &  $\sigma$ -exchange &  $N^*$  decays according to eq. 4.19 (solid) and the latter mechanisms now including  $\Delta$  propagators according to eq. 4.20 (dashed-dotted), which best describes the data for all observables.

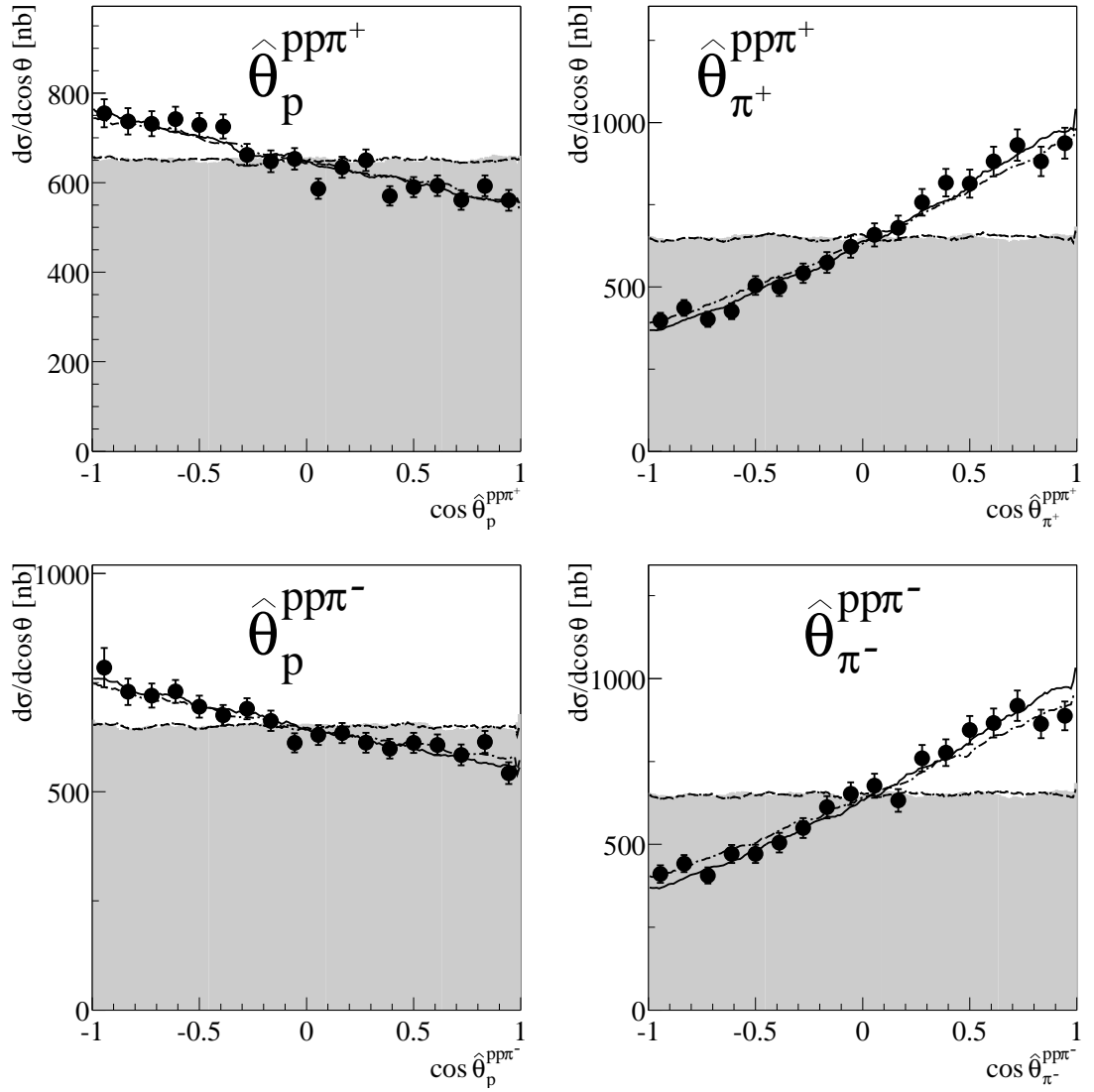


**Figure 4.32:**  $pp\pi$  subsystem scattering angles at  $T_p = 750$  MeV.

Corrected data (black points) are compared to phase space distributions (shaded area). Different lines show the effects from FSI (dashed), FSI &  $\sigma$ -exchange (dotted), FSI &  $\sigma$ -exchange &  $N^*$  decays according to eq. 4.19 (solid) and the latter mechanisms now including  $\Delta$  propagators according to eq. 4.20 (dashed-dotted), which best describes the data for all observables.

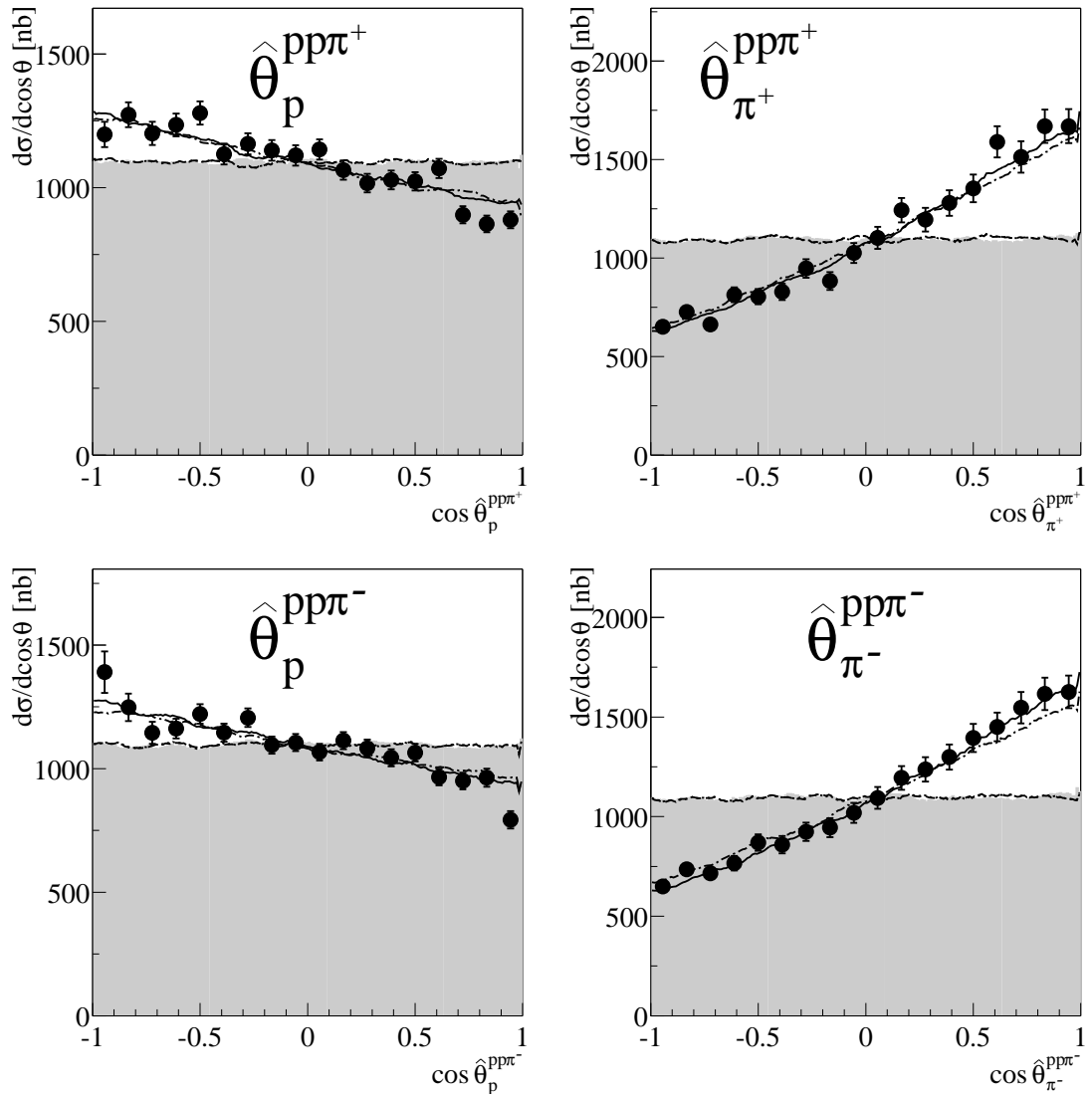


**Figure 4.33:**  $pp\pi$  subsystem, scattering angles at  $T_p = 775$  MeV.

Corrected data (black points) are compared to phase space distributions (shaded area). Different lines show the effects from FSI (dashed), FSI &  $\sigma$ -exchange (dotted), FSI &  $\sigma$ -exchange &  $N^*$  decays according to eq. 4.19 (solid) and the latter mechanisms now including  $\Delta$  propagators according to eq. 4.20 (dashed-dotted), which best describes the data for all observables.

## 4.5.3 Kinetic energy distributions

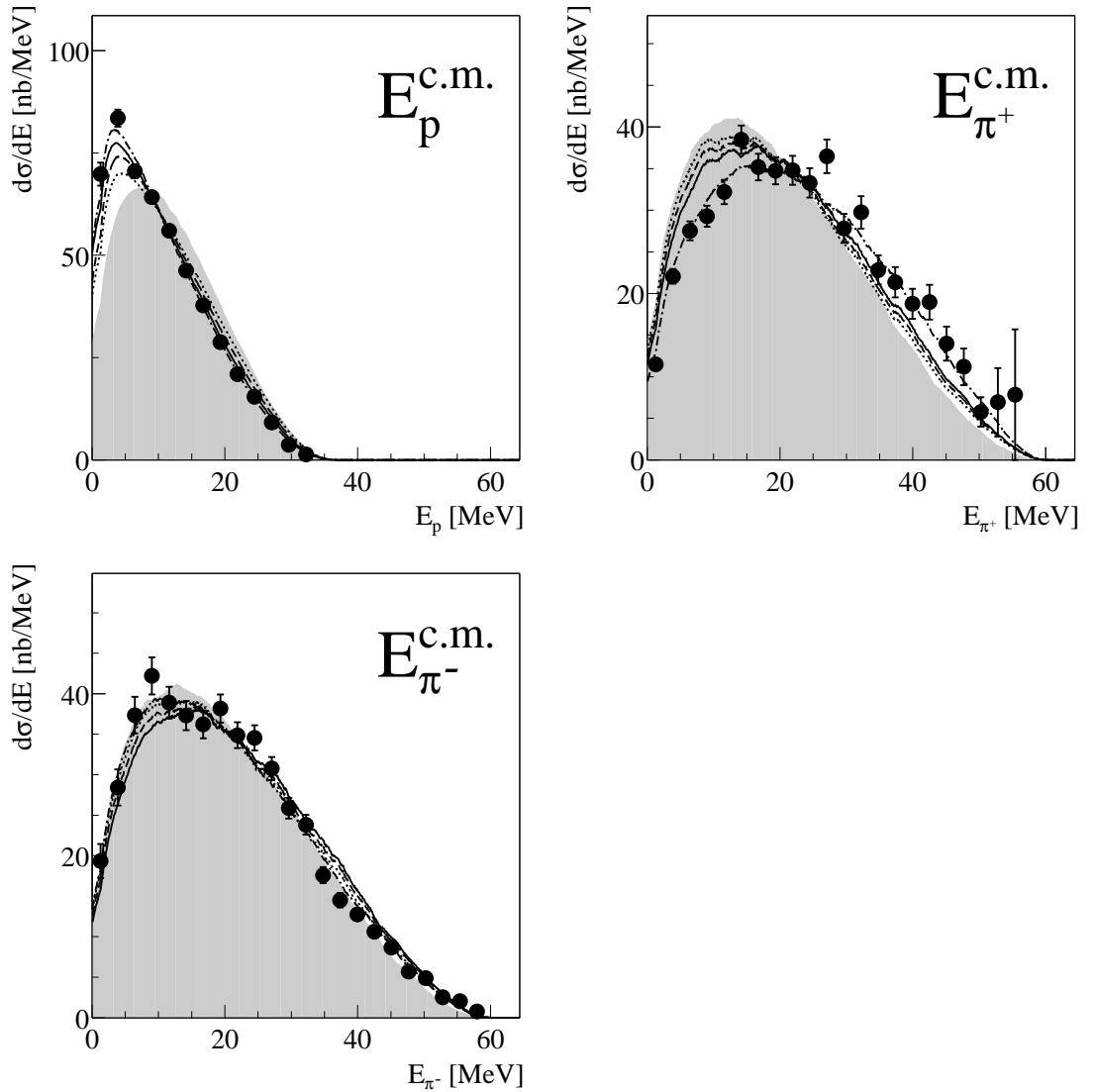


**Figure 4.34:** Kinetic energies in c.m. system at  $T_p = 750$  MeV.

Corrected data (black points) are compared to phase space distributions (shaded area).  $E_p$  is shifted to lower invariant masses, whereas the  $E_\pi$  spectra show a difference between each other.  $E_{\pi^+}$  is shifted to larger energies.

Different lines show the effects from FSI (dashed), FSI &  $\sigma$ -exchange (dotted), FSI &  $\sigma$ -exchange &  $N^*$  decays according to eq. 4.19 (solid) and the latter mechanisms now including  $\Delta$  propagators according to eq. 4.20 (dashed-dotted), which best describes the data for all observables. Already in these basic spectra of the kinetic energy of the pions the effect of the  $\Delta$  propagators is visible.

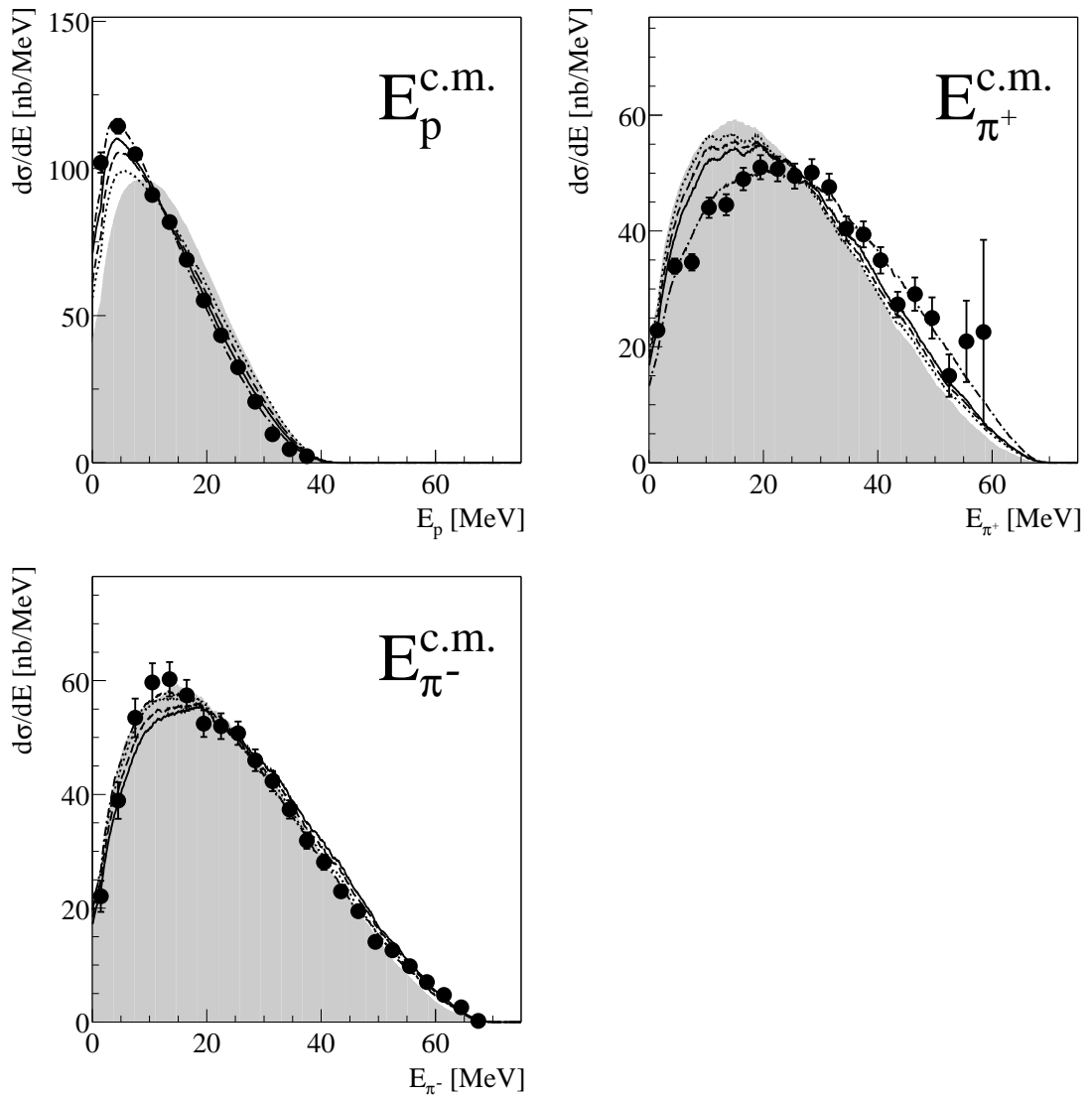


**Figure 4.35:** Kinetic energies in c.m. system at  $T_p = 775$  MeV. Corrected data (black points) are compared to phase space distributions (shaded area).  $E_p$  is shifted to lower invariant masses, whereas the  $E_\pi$  spectra show a difference between each other.  $E_{\pi^+}$  is shifted to larger energies. Different lines show the effects from FSI (dashed), FSI &  $\sigma$ -exchange (dotted), FSI &  $\sigma$ -exchange &  $N^*$  decays according to eq. 4.19 (solid) and the latter mechanisms now including  $\Delta$  propagators according to eq. 4.20 (dashed-dotted), which best describes the data for all observables. Already in these basic spectra of the kinetic energy of the pions the effect of the  $\Delta$  propagators is visible.

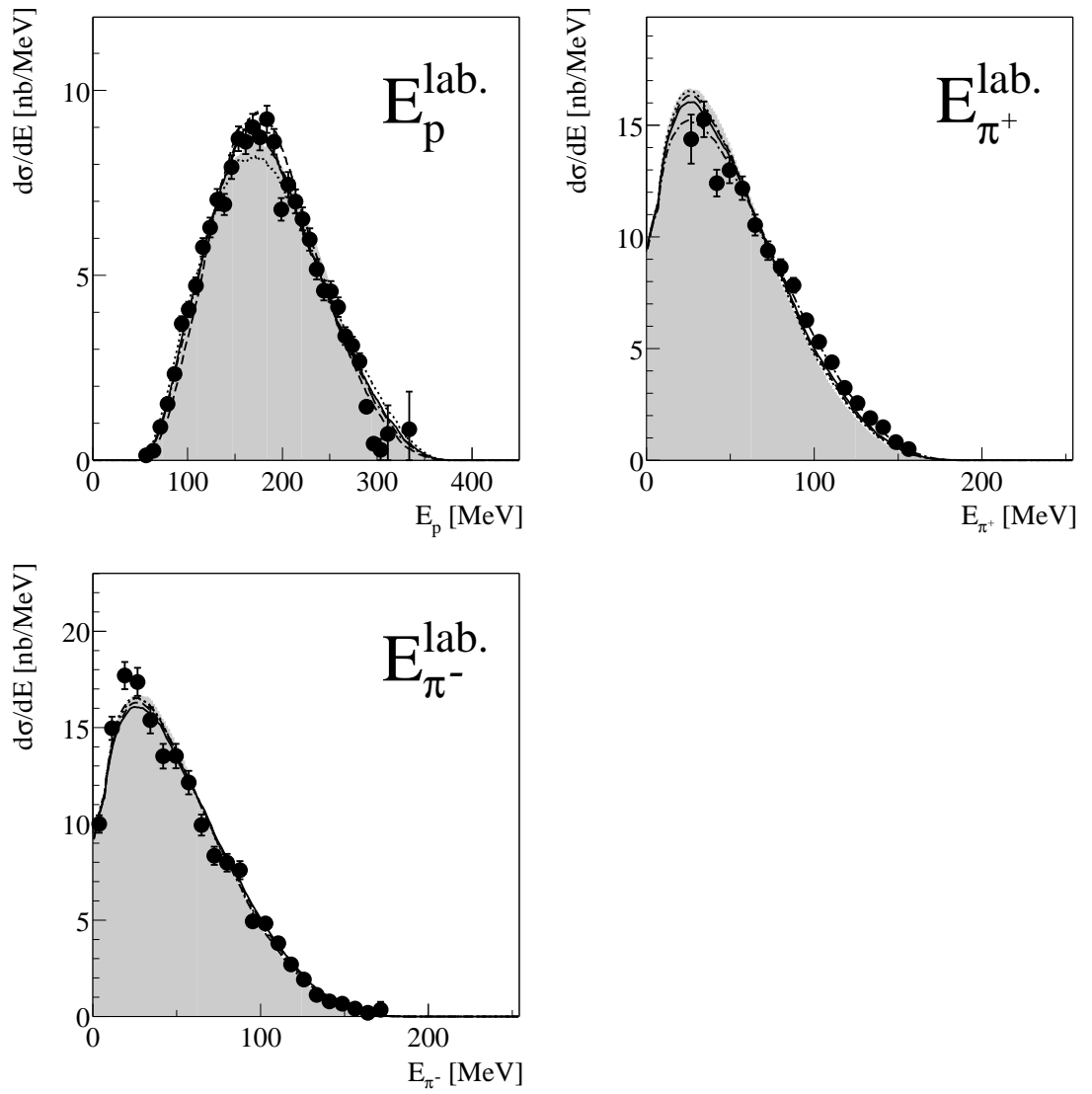


**Figure 4.36:** Kinetic energies in lab. system at  $T_p = 750$  MeV. Corrected data (black points) are compared to phase space distributions (shaded area). Different lines show the effects from FSI (dashed), FSI &  $\sigma$ -exchange (dotted), FSI &  $\sigma$ -exchange &  $N^*$  decays according to eq. 4.19 (solid) and the latter mechanisms now including  $\Delta$  propagators according to eq. 4.20 (dashed-dotted), which best describes the data for all observables.



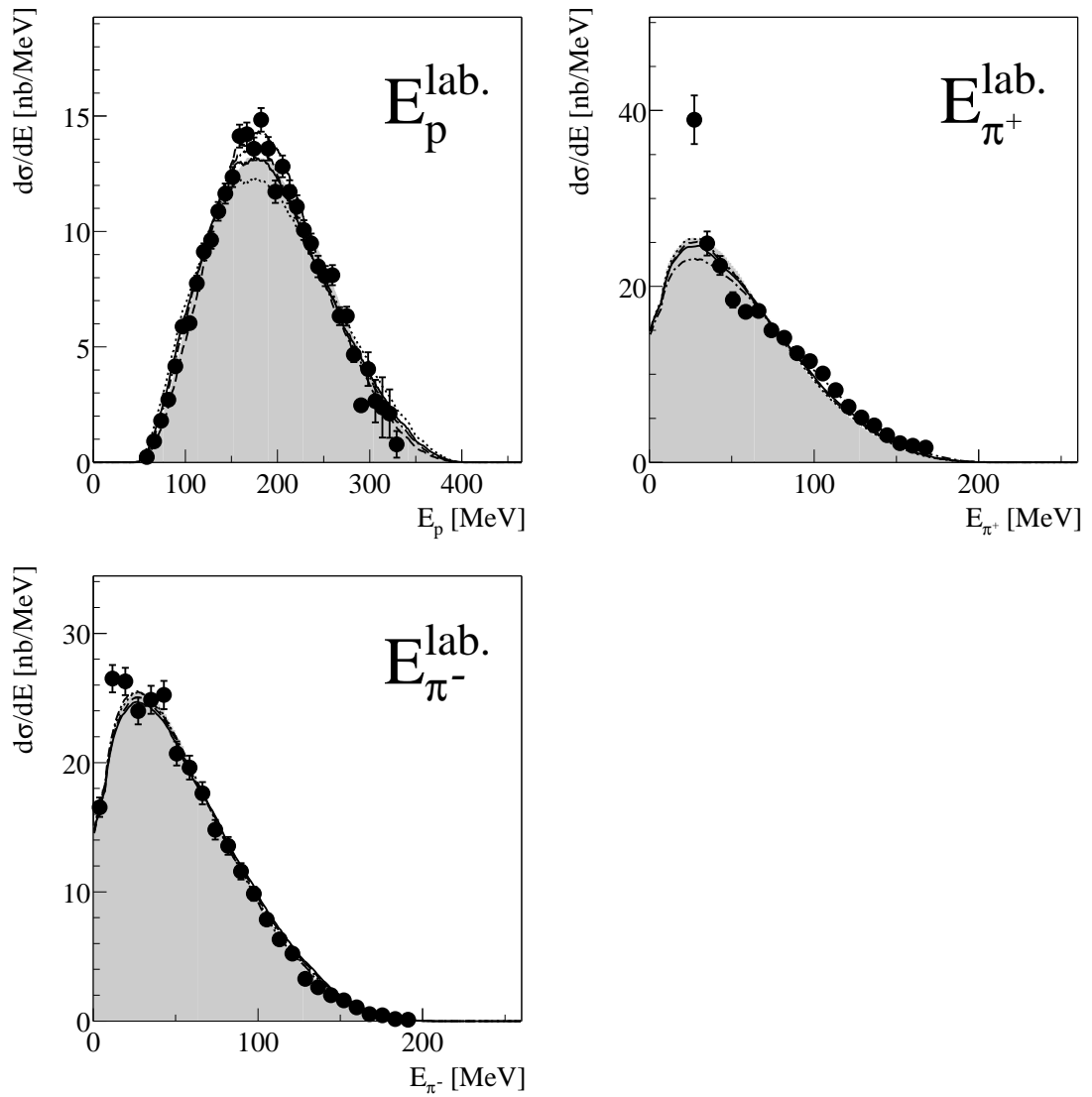


**Figure 4.37:** Kinetic energies in lab. system at  $T_p = 775$  MeV. Corrected data (black points) are compared to phase space distributions (shaded area). Different lines show the effects from FSI (dashed), FSI &  $\sigma$ -exchange (dotted), FSI &  $\sigma$ -exchange &  $N^*$  decays according to eq. 4.19 (solid) and the latter mechanisms now including  $\Delta$  propagators according to eq. 4.20 (dashed-dotted), which best describes the data for all observables.

## 4.6 Search for a narrow dibaryon resonance $d'$

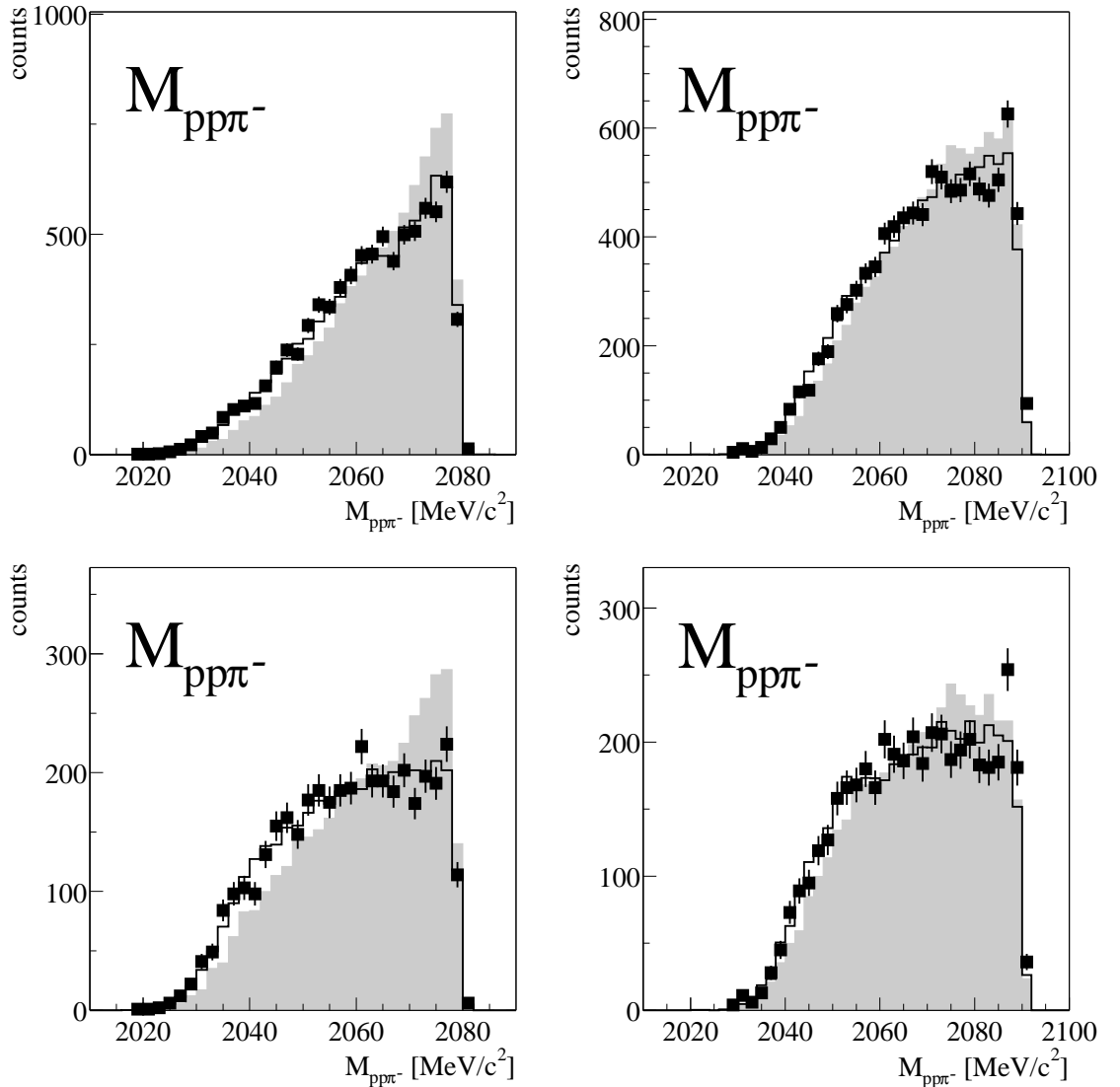


**Figure 4.38:** Spectra not corrected for efficiency and acceptance of the invariant masses of the  $pp\pi^-$  system, at the top for all events and at the bottom only for events with  $M_{pp} < 1896 \text{ MeV}/c^2$ . The left side shows the results for 750 MeV and the right one for 775 MeV. This cut should increase the sensitivity for the  $d'$  dibaryon resonance. (for details see text)

When the first experiment of two-pion production was proposed at the PROMICE/WASA detector, the main aim of the measurement was the search for a narrow dibaryon resonance in the  $NN\pi$  system called  $d'$ .

First evidence of the  $d'$  was found in DCX (double charge exchange) reactions on heavier nuclei  $^{93}\text{Nb}$ ,  $^{56}\text{Fe}$ ,  $^{40}\text{Ca}$ ,  $^{16}\text{O}$ ,  $^{12}\text{C}$ ,  $^7\text{Li}$  [Drä00]. The assumption of a  $NN\pi$  coupled dibaryon with the mass  $m_{d'} = 2065 \text{ MeV}/c^2$  and width  $\Gamma_{d'} = 5 \text{ MeV}/c^2$  has given a consistent description of the data on those nuclei. The arguments against  $d'$  were, that effects in nuclear matter make the interpretation of the DCX results on nuclei very difficult.

In order to minimise possible medium effects the DCX experiments have been extended down to the Helium isotopes  $^3\text{He}$  and  $^4\text{He}$ , where DCX measurements no longer lead to a discrete final state [Grä98]. But the results of these experiments did not prove the existence of the  $d'$ .

The  $pp$  system was identified as the simplest hadronic system, where the  $d'$  could be produced in an elementary way. The reaction would proceed according to

$$(4.21) \quad pp \rightarrow d'\pi^+ \rightarrow pp\pi^-\pi^+$$

The PROMICE/WASA detector was chosen for the experiment [Bro96]. During the further analysis of the measurements the complexity of the experiment became evident. The complicated layer structure makes it difficult to get smooth distributions due to edge effects from one layer to another. This is especially true for the  $\pi^+$  [Bro01], that is identified with the delayed pulse technique.

Events of the production of the  $d'$  should become visible in the  $pp\pi^-$  system. Fig. 4.38 shows at the top the invariant mass spectrum  $M_{pp\pi^-}$  for both energies 750 MeV from [Bro01] and the new results at  $T_p = 775$  MeV. At 750 MeV and also at 775 MeV no significant signal of the  $d'$  resonance around 2065 MeV/ $c^2$  was found [Bro02a].

A cut on smaller invariant masses was proposed to increase events containing  $d'$  decay products compared to ordinary two-pion production. The two decay protons are expected to show a substantial FSI effect, because there would be only very little kinetic energy left for the decay products.

Fig. 4.38 shows at the bottom the  $M_{pp\pi^-}$  spectra for both energies with a cut of  $M_{pp} < 1896$  MeV/ $c^2$ . In these spectra there is also no significant signature of the  $d'$  around the mass 2060 to 2070 MeV/ $c^2$ . From statistical fluctuations of single bins in the histogram, an upper limit (90% c.l.) of  $\sigma = 10 - 20$  nb for  $d'$  production can be obtained [Bro02a].

## 4.7 Summary

New measurements with the PROMICE/WASA detector have greatly improved the existing data base for the reaction  $pp \rightarrow pp\pi^+\pi^-$ . The energy excitation function of the integral cross section has been extended to a region much closer to threshold. The errors of the data are significantly smaller compared to previously published data. In the energy region where there exists an overlap with these data, the cross sections of our data are an order of magnitude smaller. Our results generally corresponds with predictions from [Alv98].

The measurements at 750 and 775 MeV are the first exclusive measurements with enough statistics to show differential cross section spectra. The spectra show significant deviations from phase space distributions. These deviations are typical for certain reaction mechanisms which we successively included in the event generator. All observables could eventually be described with these calculations.

- The concave angular distribution of the protons  $\theta_p$  give evidence of the dominance of sigma exchange between the colliding nucleons.
- Nucleon-nucleon final state interaction in the  $pp$  system leads to significant effects.  $M_{pp}$  shows a strong tendency to low invariant masses.
- The  $N^*(1440)$  excitation gives the main contribution to the reaction. The  $M_{p\pi^+\pi^-}$  spectra display the low energy tail of the  $N^*$  and for this reason it is shifted towards higher invariant masses.
- The branching ratio of the  $N^*$  decays  $N^* \rightarrow p(\pi\pi)_{l=0}$  and  $N^* \rightarrow \Delta\pi$  can be estimated from the shape of the  $M_{\pi^+\pi^-}$  spectrum and the opening angle  $\delta_{\pi^+\pi^-}$ . These spectra are strongly affected by the interference between both channels. The ratio between both channels is adjusted in the calculation to fit the experimental results. The ratio that is needed to fit the data is within the range obtained from the values of the branching ratios that are published in the particle data booklet (5 – 10% for  $N^* \rightarrow p(\pi\pi)_{l=0}$  and 20 – 30% for  $N^* \rightarrow \Delta\pi$ ).
- The remaining discrepancy in the  $p\pi$  invariant mass spectra was removed by an approach with a factor representing the  $\Delta$  propagators. The  $p\pi^+$  system is shifted to higher invariant masses, whereas the  $p\pi^-$  system is described by phase space distribution. According to the Clebsch-Gordan coefficients, the propagators  $|D_{\Delta^{++}}|^2$  and  $|D_{\Delta^0}|^2$  are added in a ratio of 9 to 1 and multiplied to both  $N^*$  decay branches.
- The angular distribution  $\theta_{\pi^-}$  is flat. So there are no signs of contributions of double  $\Delta$  processes. We conclude, that this mechanism plays at maximum a minor role in this reaction at the measured energies close to threshold.

# 5

## Outlook

In this outlook, the successor of the PROMICE/WASA detector, the CELSIUS/WASA detector, is presented. Still being in the commissioning phase, this detector is just about to start real physical measurements. Apart from measuring rare  $\eta$  and  $\pi^0$  decays, this detector is well suited to conduct exclusive two-pion production measurements, especially on reactions involving neutral particles. During the work for this thesis the forward window counter (FWC) as part of the WASA detector setup has been designed, constructed and tested here in Tübingen.

In the near future two-pion production reactions on nuclei should also be carried out to increase the knowledge on chiral restoration in dense nuclear matter, which is a very acute problem.

### 5.1 CELSIUS/WASA detector

During recent years, the CELSIUS/WASA detector setup was mounted. Parts from the old PROMICE/WASA setup are used in this new one. Notably the forward detector is essentially the same. As for the old PROMICE/WASA setup, this new one will be used for inelastic proton-nucleon reactions, in particular the production of light neutral mesons and their decays. It is capable of identifying charged particles and photons over a solid angle close to  $4\pi$  with a high measurement accuracy in energy and in track coordinates. Some  $\pi^0$  and  $\eta$  rare decay processes that are accessible with this detector setup can be used for probing the limits of the Standard Model [Cal87]. Accurate studies of such decays require a calorimeter for the energy measurement of photons and a magnet for the momentum and charge measurement of charged particles. But also further studies of two-pion production, especially of the neutral channels, require a large acceptance in the solid angle. For example in the reaction  $pp \rightarrow pp\pi^0\pi^0$  there are 2 charged proton tracks and 4 tracks from the decay photons.

### 5.1.1 Pellet target

The internal pellet target [Eks96] used with the CELSIUS/WASA detector setup creates a stream of frozen hydrogen or deuterium micro-spheres (pellets) at a rate of 50 kHz, with design diameters below  $40\ \mu\text{m}$ , crossing the CELSIUS beam at a speed of 60 m/s. Ideally there should always be only one single pellet crossing the beam. With the usual proton beam of about  $10^{10}$  protons in the ring a luminosity of about  $10^{32}\ \text{cm}^{-2}\text{s}^{-1}$  can be obtained. Around the interaction point of the beam and the pellet target is a special scattering chamber. This chamber has a 1.2 mm thin walled beryllium tube, 60 mm in diameter, to contain the CELSIUS proton beam. In forward direction (down stream) a 0.42 mm thick stainless steel window covers a polar angle of about  $18^\circ$ .

### 5.1.2 CELSIUS/WASA detector setup

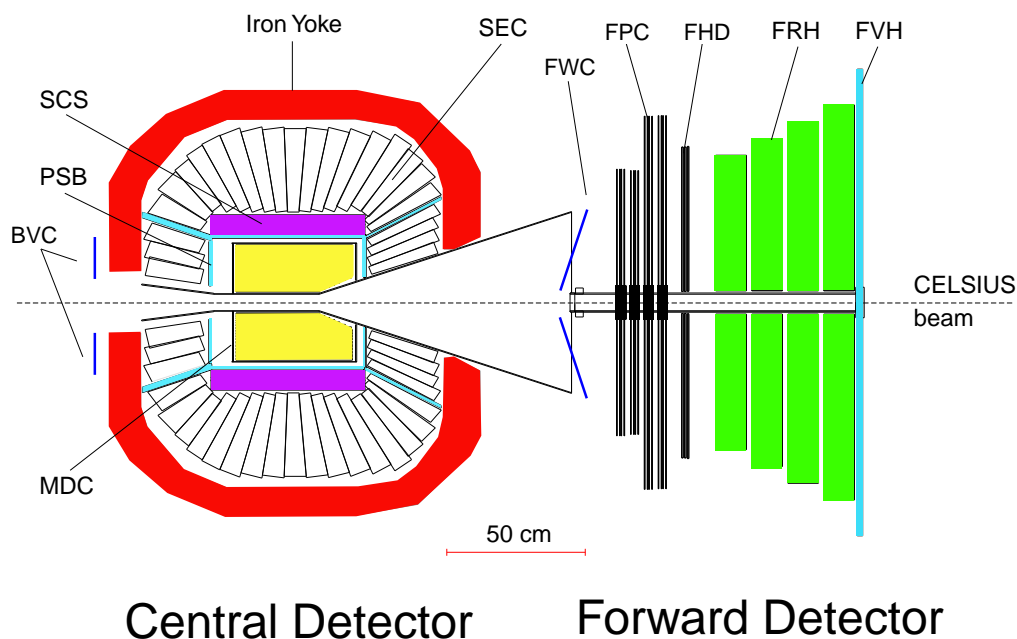


**Figure 5.1:** Schematic top view of the CELSIUS/WASA detector setup. [Rub99]

The CELSIUS/WASA detector setup shows considerable similarity to the old PROMICE/WASA setup, see Fig. 5.1 for a schematic view. Fig. 5.2 shows a side view of the detector setup in the process of cabling. Fig. 5.3 shows the Central Detector with half of the iron yoke removed. The forward detector is essentially the same, but is now mounted more downstream covering an angular range from  $3^\circ$  to  $18^\circ$ . Only the forward window counter (FWC) was a completely new design (see extra section 5.1.3 and [Mes99]).

The central detector (CD), however, is much more complex than before. If we examine first of all the inner part, the setup starts with the beryllium beam pipe already described.

The mini drift chamber (MDC) has 17 layers of individual drift tubes mounted parallel to the beam. This allows the measurement of the curvature of charged

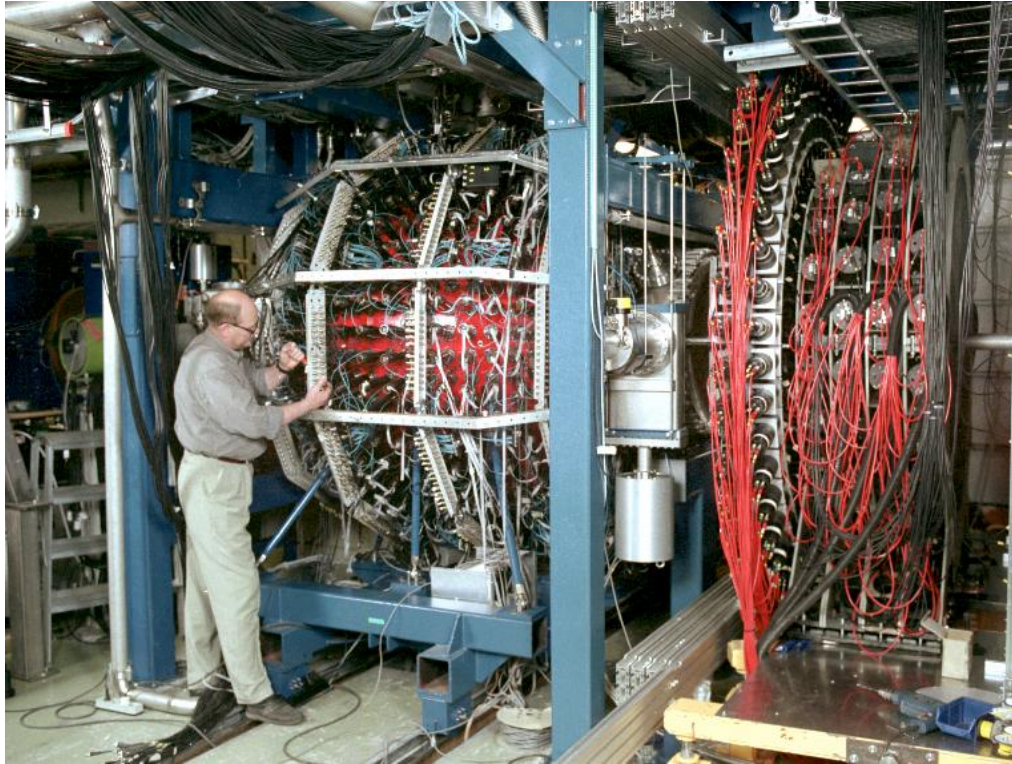


**Figure 5.2:** Side view of the CELSIUS/WASA detector. The detector is not yet completely cabled. ([TSL00], picture by Teddy Thörnlund)

particles perpendicular to the beam axis for tracks covering a polar angle between  $25^\circ$  and  $155^\circ$  with respect to the CELSIUS beam axis. Every second layer is twisted a little bit from the parallel orientation to allow measurements of this polar angle.

Inside the magnet but outside the mini drift chamber the plastic scintillator barrel (PSB) is mounted. It consists of a forward, central and backward part, each having 48 elements of plastic scintillator with a thickness of 8 mm. It is used for fast triggering purposes and as a veto for charged tracks.

The superconducting solenoid (SCS) provides the magnetic field required for the measurement of charged particles in the MDC. Its magnetic field is parallel to the beam axis. It also prevents  $\delta$ -electrons, coming from the collision of the CELSIUS beam with the hydrogen target pellets, from entering the MDC. The design of the SCS [Rub99] has been optimised for momentum measurements whilst the wall thickness has been minimised in order to reduce the probability of electromagnetic showers and to maintain accurate energy measurements in the calorimeter. The calorimeter readout electronics are shielded from the magnetic field by an iron yoke.

The 1020 elements of sodium doped CsI crystals are inside the iron yoke but read out by photo-multipliers sitting outside. The yoke has holes for the light guides for each individual CsI crystal.

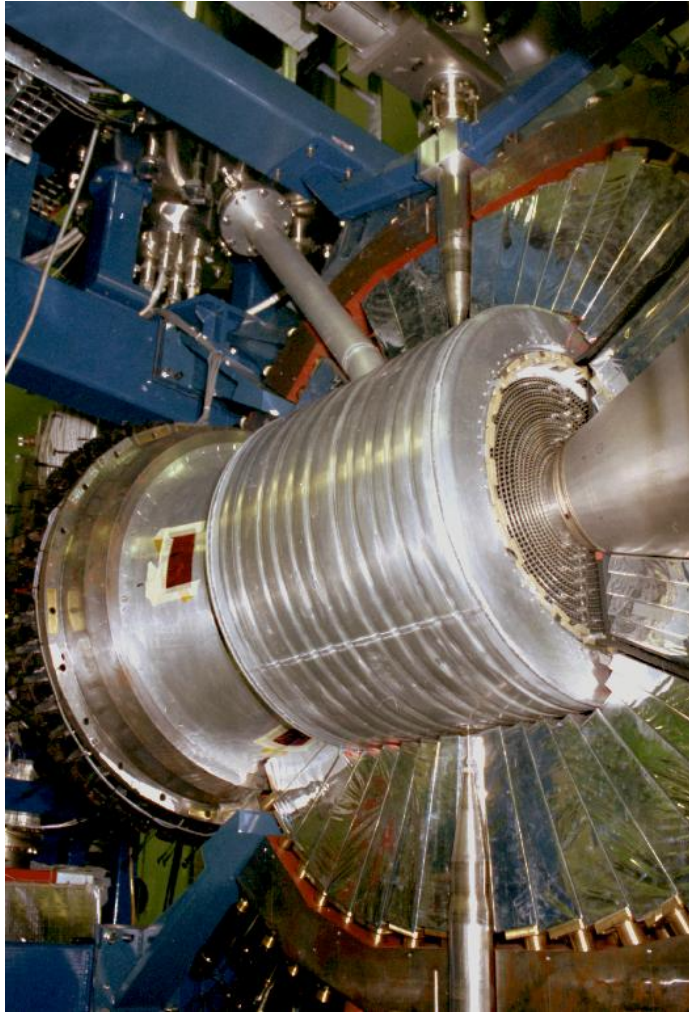


**Figure 5.3:** View of the CELSIUS/WASA detector with one half of the iron yoke removed. The CsI crystals mounted into the yoke are also removed. So the view to the crystals is open, which are covered by mylar foil in the other half. The cryostat of the superconducting solenoid is clearly seen. Inside the cryostat are the central part of the plastic scintillator barrel and the layers of the mini drift chamber. ([TSL00], picture by Teddy Thörnlund)

### 5.1.3 The new forward window counter (FWC)

A new forward window counter (FWC) was designed and constructed in Tübingen. The old one no longer fulfilled the specifications in size and shape. It improves the trigger generation for charged particles in the forward detector and is important for reducing the background caused by particles scattered in the beam pipe. It is placed downstream just behind the thin stainless steel window of the scattering chamber.

The demand for placing the detector as close as possible to the scattering chamber and the limited space for the supporting construction and the readout electronic of the new window counter, requires an elaborated design of scintillators and light guides. The detector consists of 12 radially shaped modules that are mounted separately. The elements are mounted as close as possible to each other, but there is a gap between each quadrant, where metal bars from the supporting structure of the forward window of the scattering chamber are located. The plas-



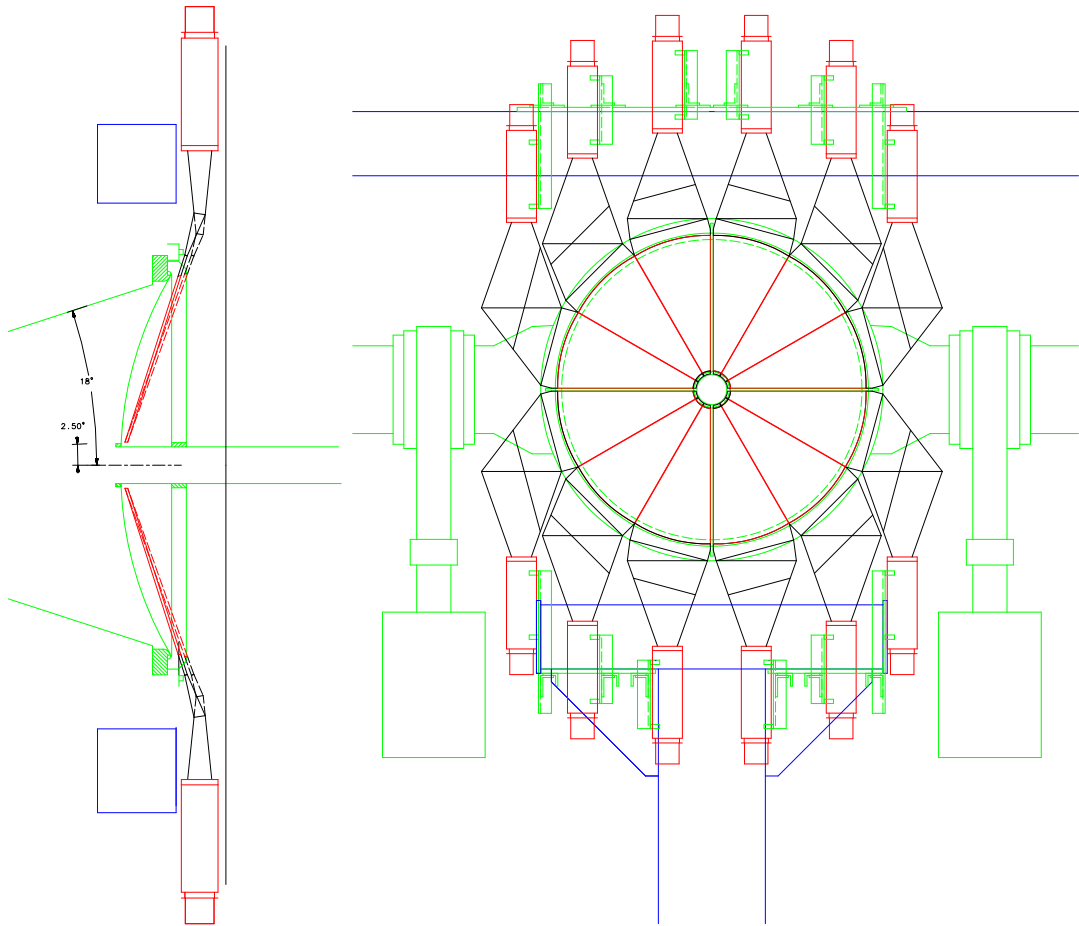


**Figure 5.4:** *FWC construction plans: side view and view from the front on the FWC. The sensitive part is tilted into the space right in front of the forward window. It shows the limited space available for the supporting construction and the readout electronic of this detector.*

tic scintillators are read out by very fast photo-multipliers and can be monitored by the light pulser system. One element always covers 4 elements of the third plane of FHD and 2 elements of FRH.

For more details on the designing and construction phase and the first tests of the FWC see [Mes99] where the details are collected.

From a recent, more realistic test run Fig. 5.5 was produced [Gre01]. It shows possible candidates for the reaction  $pp \rightarrow d\pi^+$  at a  $T_p = 400$  MeV only selected by their coplanarity. But this is also the signature for protons scattered in the beam pipe. The spectrum at the top of this figure shows the angular distribution of both particles without the condition of having at least two hits in the FWC. A large pollution of these “beam pipe events” are visible. The comb like spectrum comes from the reconstruction of the angles only by the FHD pixels, because most of those events do not hit the FPC. The lower spectrum presents the same, but with the condition that there are at least two hits in the FWC. It is free of protons scattered in the beam pipe.

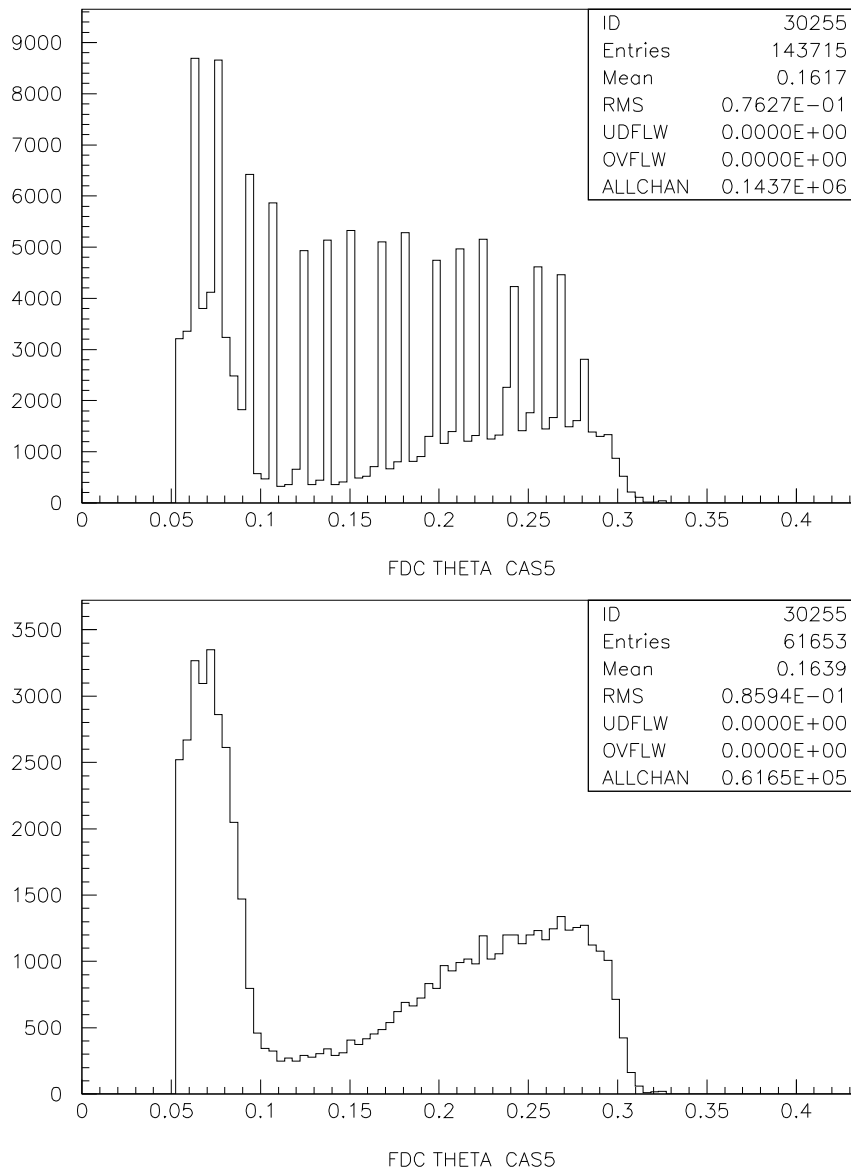


**Figure 5.5:** FWC performance: both spectra show the angular distribution of coplanar events. The upper one is without the condition of having two hits in the FWC, the lower one is with this condition. [Gre01] (for details see text)

## 5.2 Two-pion production with CELSIUS/WASA

The new CELSIUS/WASA detector offers a new opportunity for measuring two-pion production. The angular coverage of almost  $4\pi$  steradian and acceptance for neutral particles ( $\gamma$ s as well as neutrons) opens the opportunity to exclusively measure the reaction channels  $pp \rightarrow pp\pi^0\pi^0$ ,  $pp \rightarrow pn\pi^+\pi^0$  and  $pp \rightarrow nn\pi^+\pi^+$ . Measuring all four particles the reaction is well overdetermined. By applying a four constraint (4C) kinematical fit, the resolution of the detector will be improved. In addition the uncertainties from reduced acceptance, which have affected the present work will be solved. The determination of the charge of a particle — in this case the distinction of  $\pi^+$  from  $\pi^-$  — will no longer be a problem. (See sample event in Fig. 5.6.)

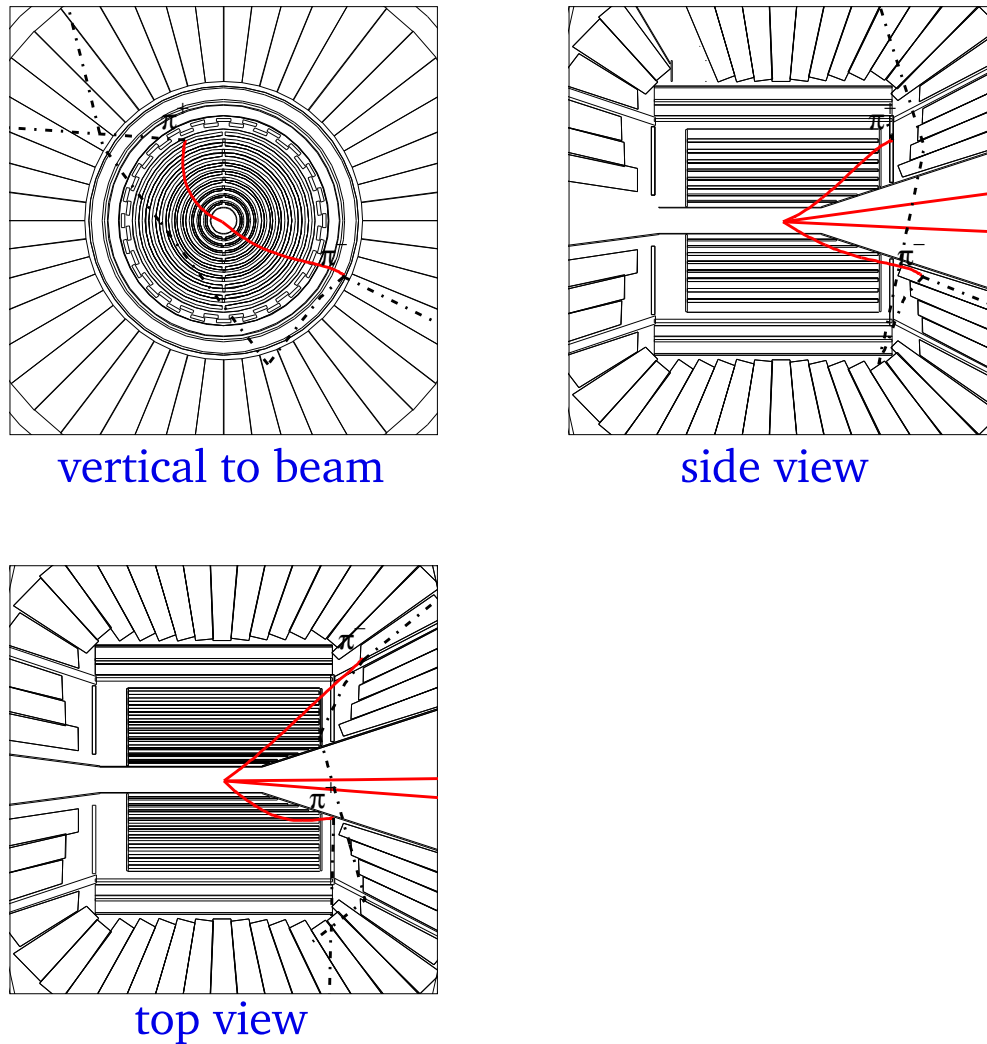


**Figure 5.6:** Illustration of a sample event in the detector simulation of the  $pp \rightarrow pp\pi^+\pi^-$  reaction at  $T_p = 750$  MeV. Shown are three different projections: perpendicular to the beam axis, side and top view. Note that in the upper left figure the proton tracks have been eliminated for clarity.

By comparing these reaction channels, one can expect to learn more about the mechanisms. For example  $pn$  or  $nn$  in the final state should experience a much stronger final state interaction, because they do not have Coulomb repulsion. In the reaction  $pp \rightarrow nn\pi^+\pi^+$  the two pions could not couple to the scalar iso-scalar channel ( $\sigma$ -channel), nor could the  $N^*(1440)$  be excited. No meson resonances are known in the  $I = 2$  channel. This is a test case for  $\Delta\Delta$  processes and non-resonant chiral terms.

## 5.3 Chiral Restoration

As pointed out in the introduction, the chiral symmetry is explicitly and spontaneously broken in nature. With increasing baryon density and/or temperature, the chiral symmetry is expected to be restored again. In experiments this effect should be observed by properties of parity partners becoming more and more

similar to each other with increasing  $\rho$  and  $T$  [Koc95]. An example for a possible partnership is the pion and the sigma meson. The predicted effects are the lowering of the sigma mass, a longer life time for the sigma meson [Lut91, Hat99] and a change of the life time of the pion [Wei01]. These effects should already happen in nuclear matter. Some hints for this effect have been found in pion induced pion production on different nuclei ( $\pi A \rightarrow \pi\pi A$ ), where different nuclear matter densities are probed. In this experiment a drastic effect in the  $\pi\pi$  systems in dependence of the matter density has been seen, but only when the two pions could couple to the sigma channel. There was no effect in the two pion systems that do not have the possibility of coupling to the sigma channel [Bon96, Bon97, Bon98, Bon99, Bon00].

This effect should also be observable in other two-pion production reactions, such as two-pion production reactions on nucleons and nuclei. Here, hadronic induced reactions are superior to photon induced ones. The latter is mainly exciting the  $N^*(1520)$  [Wol00], which could not couple to the sigma meson, whereas the hadronic induced reaction is mainly exciting the  $N^*(1440)$  [Alv98] with a large branching ratio into the sigma channel. In future two-pion production measurements on nuclei will be made with the WASA detector [Sko04] and COSY-TOF to test if this effect can also be seen in  $NN$  collisions.

# A

## Uncorrected differential cross sections

This chapter contains the raw uncorrected differential cross section spectra for 750 and 775 MeV. Direct results from the data analysis (black points) are compared to full model calculations, which are passed through a simulated detector and then are analysed in the same way as the real data. As input for the simulation, events generated according to pure phase space (shaded area) and our full model calculation including the  $\Delta$  propagators according to eq. 4.20 (solid line) have been used.

The distributions shown here for 750 MeV are the same as in [Bro01]. But they are now compared to our full model, which describes the data best for all observables. During the work for this thesis, data measured at  $T_p = 775$  MeV were analysed. The direct results from this analysis are presented in this chapter.

## A.1 Invariant masses

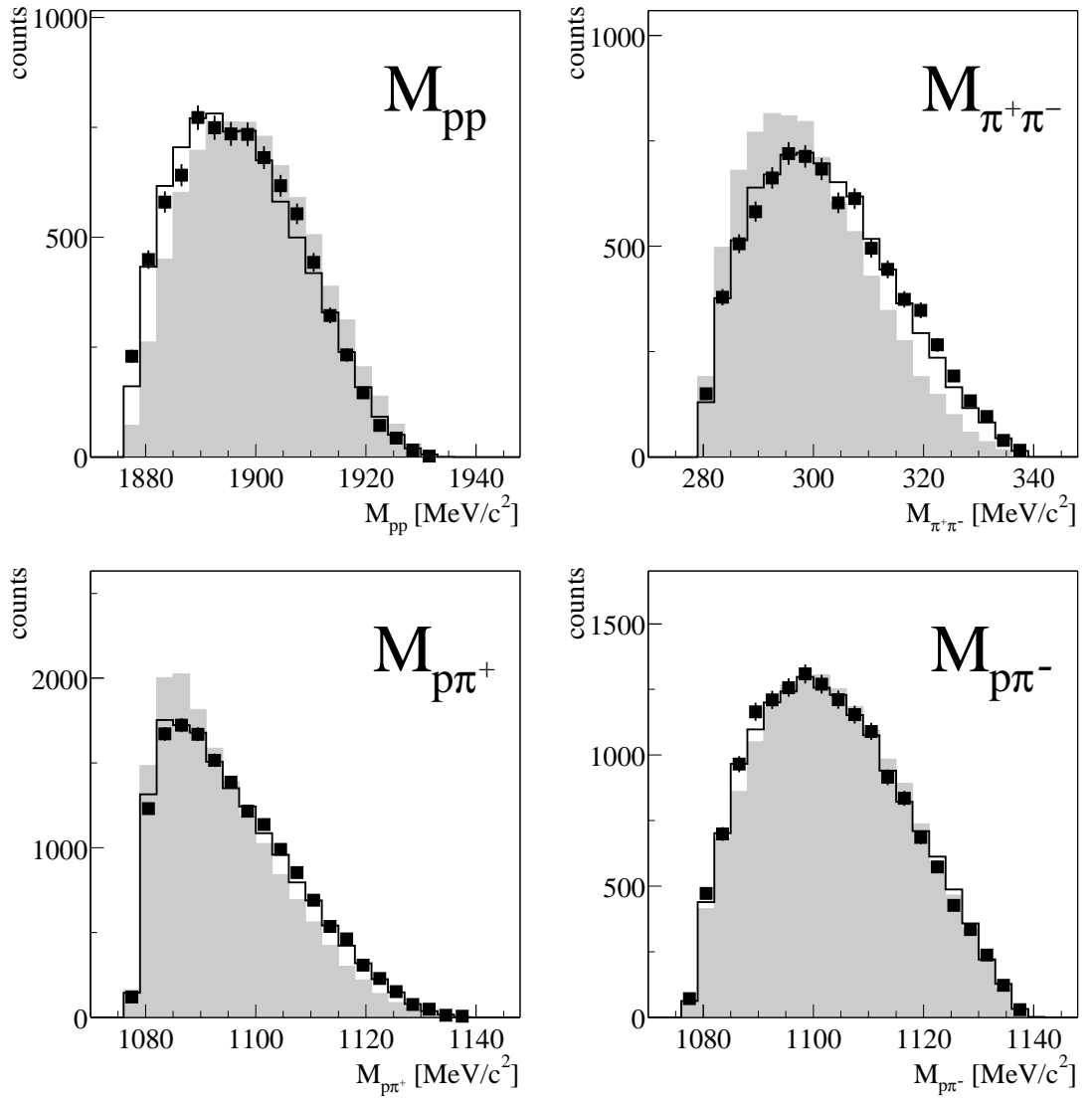


**Figure A.1:** Invariant masses of two particle systems at  $T_p = 750$  MeV.

Uncorrected data (black points) are compared to phase space distributions (shaded area) and the distributions of the model calculation including the  $\Delta$  propagators according to eq. 4.20 (solid line).

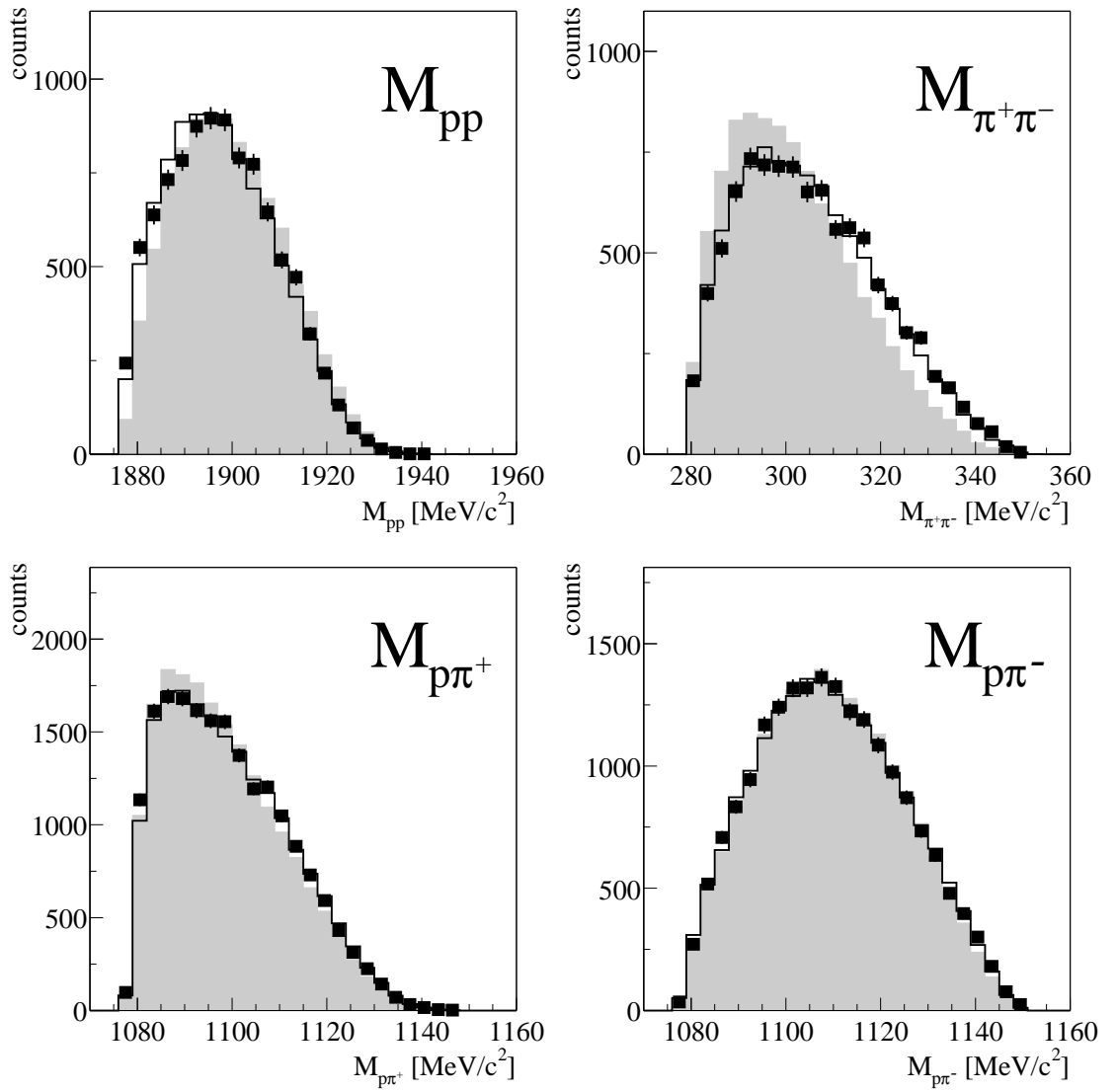


**Figure A.2:** Invariant masses of two particle systems at  $T_p = 775$  MeV.

Uncorrected data (black points) are compared to phase space distributions (shaded area) and the distributions of the model calculation including the  $\Delta$  propagators according to eq. 4.20 (solid line).

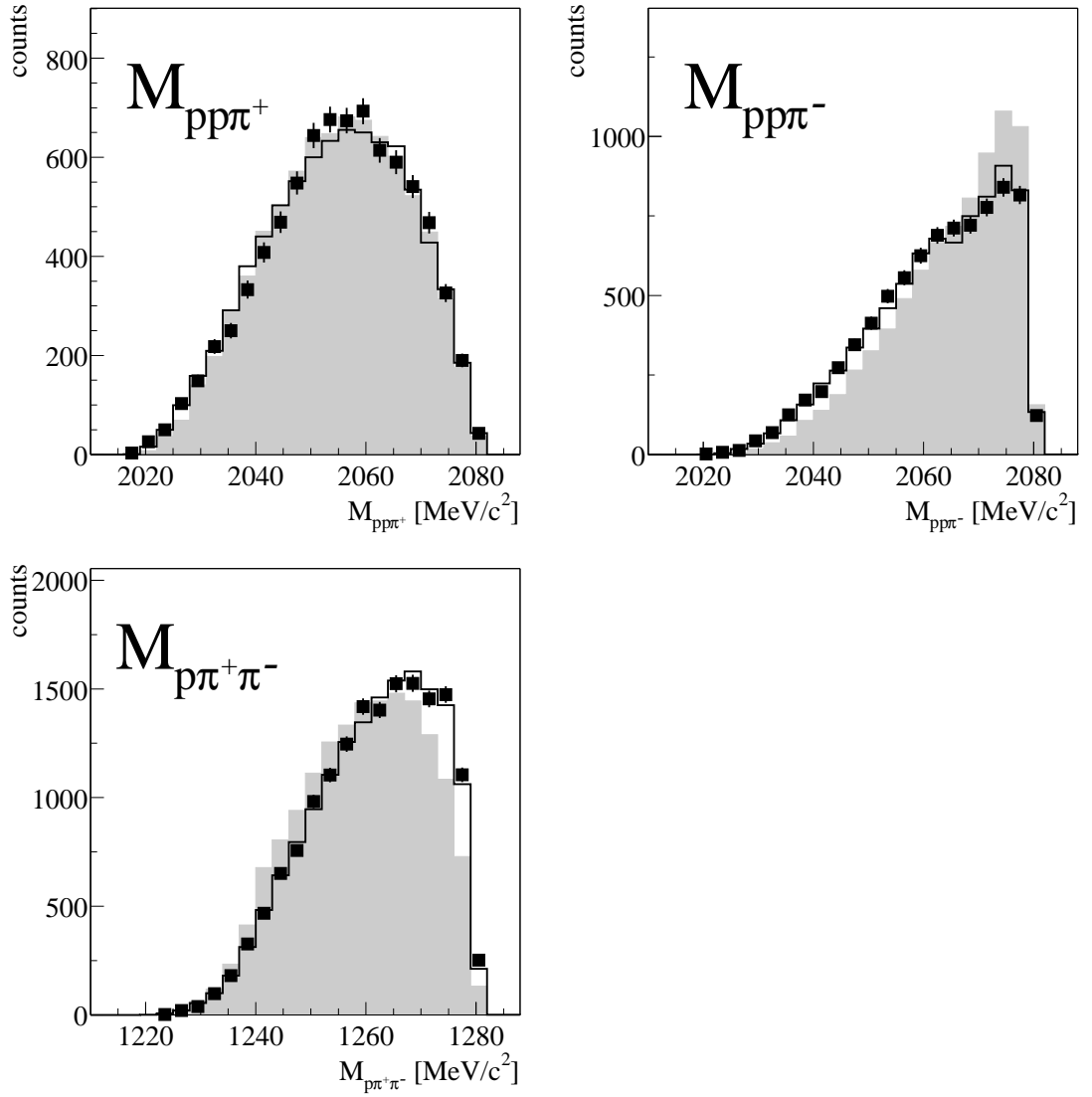


**Figure A.3:** Invariant masses of three particle systems at  $T_p = 750$  MeV. Uncorrected data (black points) are compared to phase space distributions (shaded area) and the distributions of the model calculation including the  $\Delta$  propagators according to eq. 4.20 (solid line).



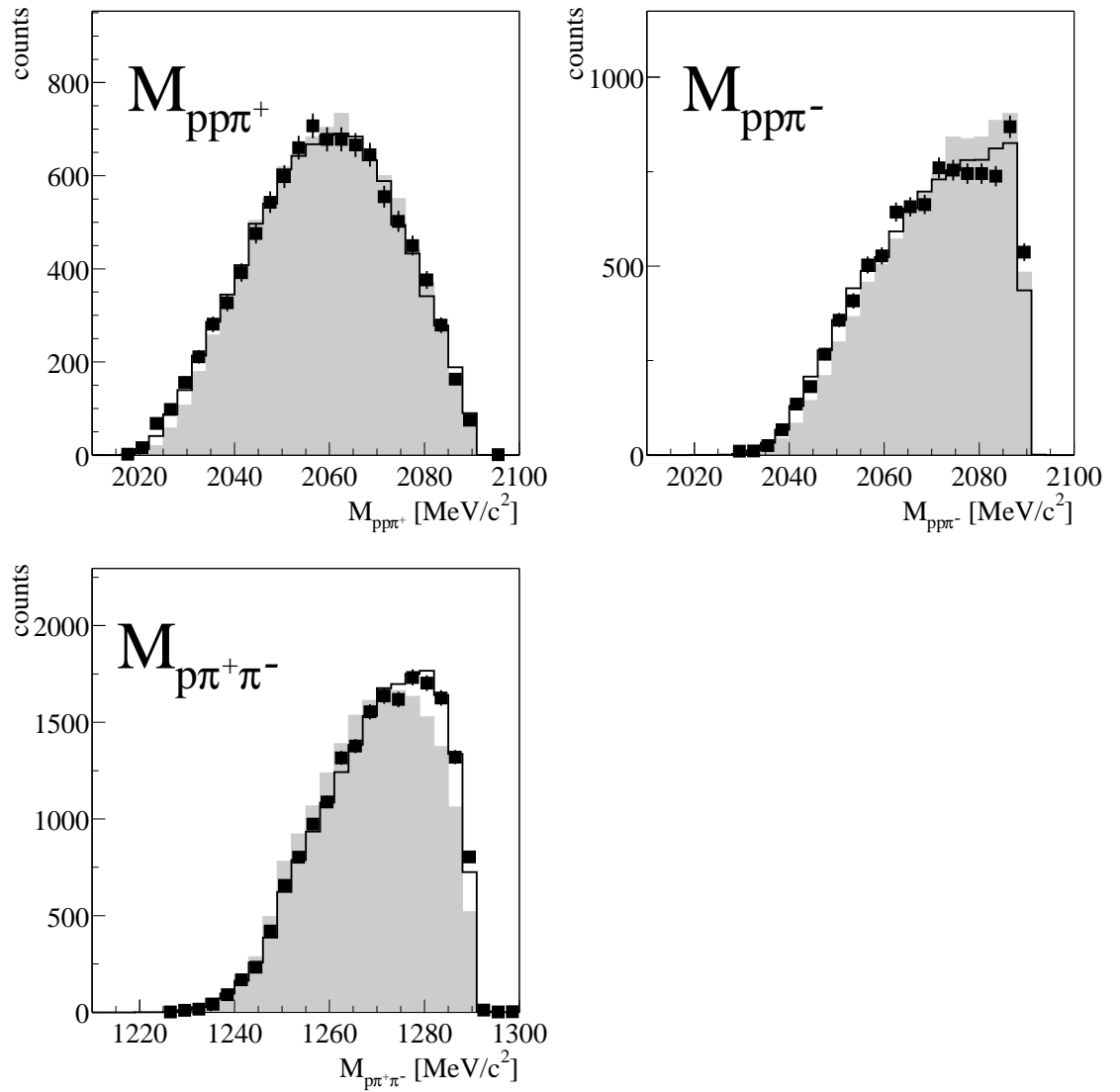


**Figure A.4:** Invariant masses of three particle systems at  $T_p = 775$  MeV. Uncorrected data (black points) are compared to phase space distributions (shaded area) and the distributions of the model calculation including the  $\Delta$  propagators according to eq. 4.20 (solid line).

## A.2 Angular distributions

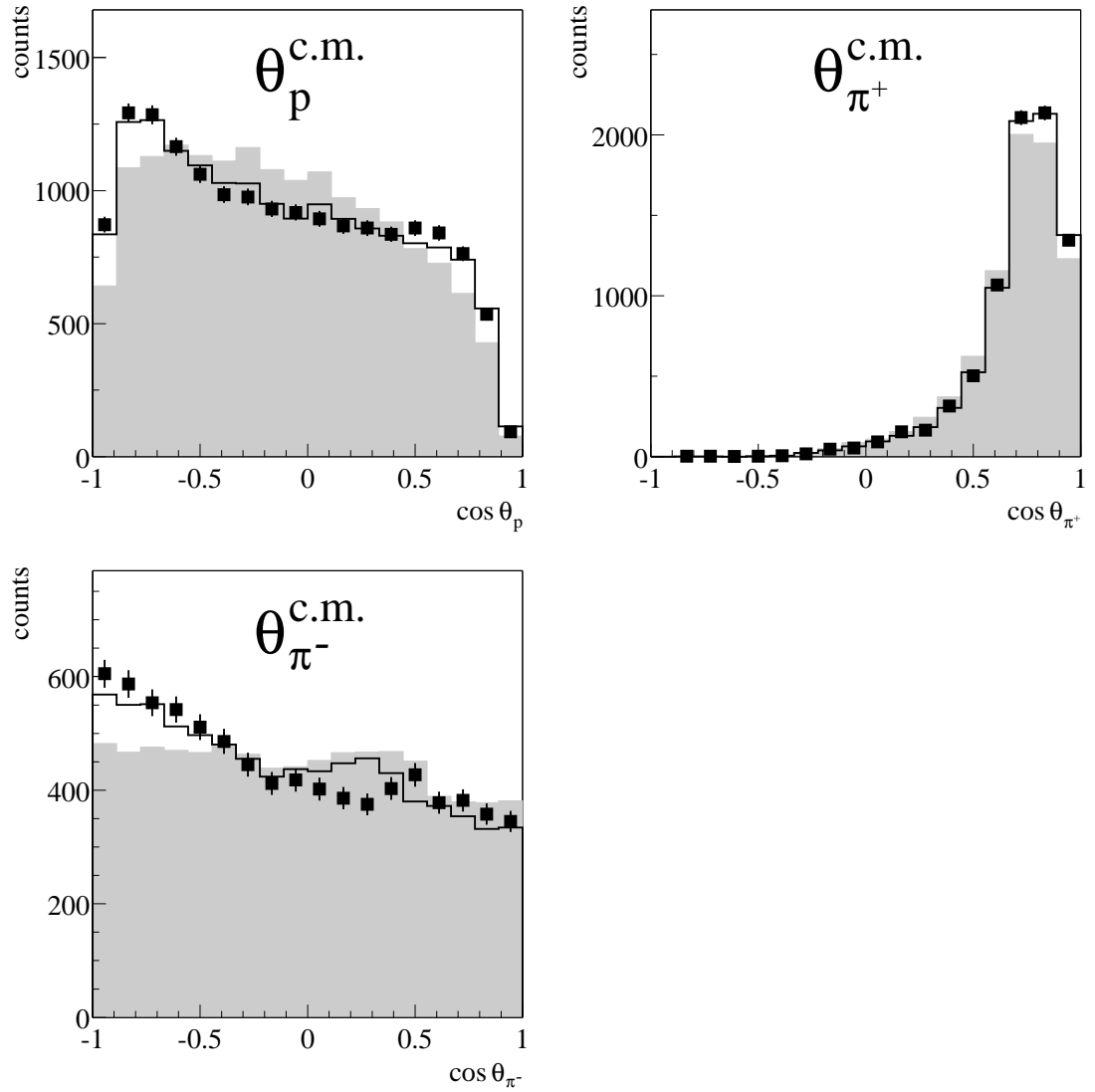


**Figure A.5:** Scattering angles in c.m. system at  $T_p = 750$  MeV. Uncorrected data (black points) are compared to phase space distributions (shaded area) and the distributions of the model calculation including the  $\Delta$  propagators according to eq. 4.20 (solid line).

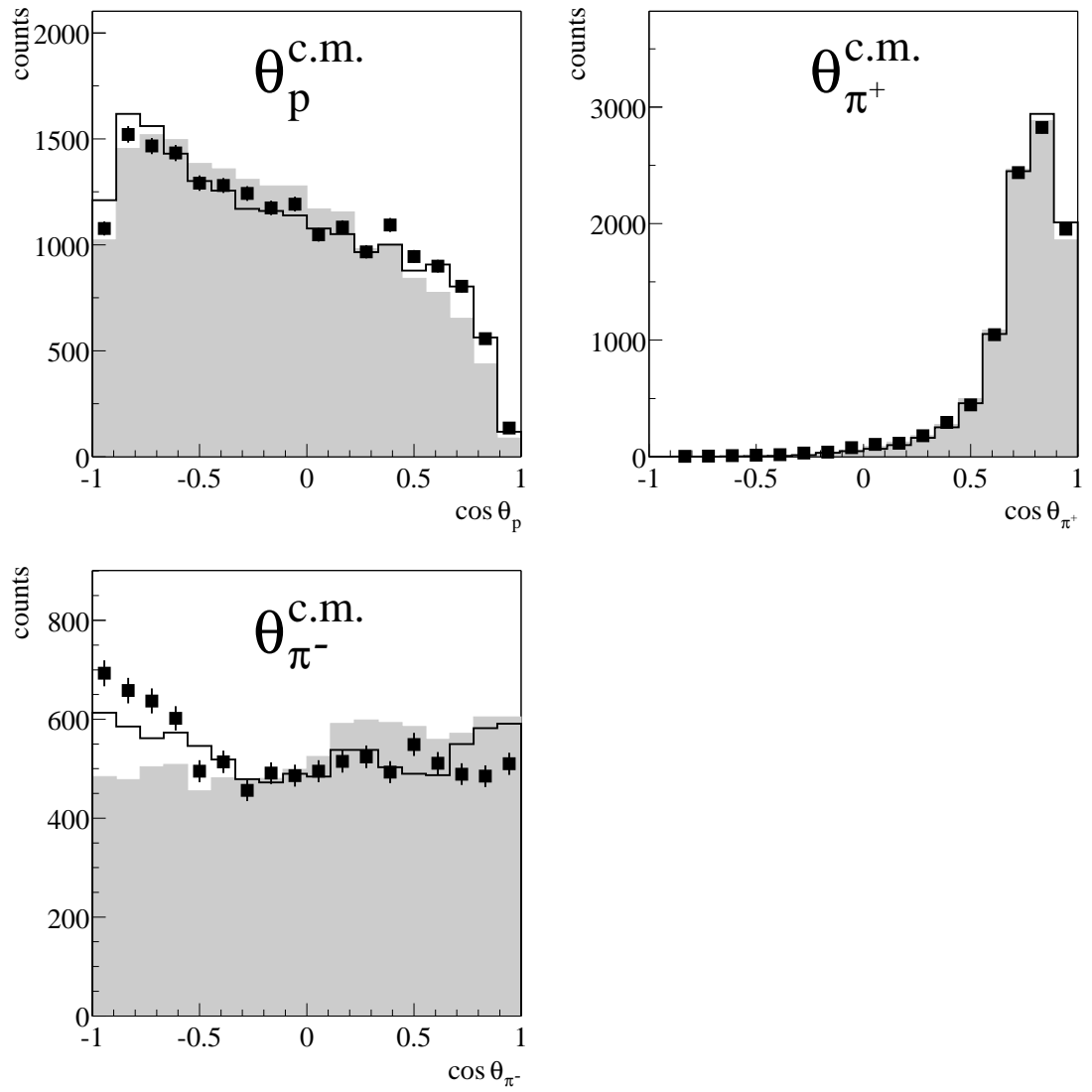


**Figure A.6:** Scattering angles in c.m. system at  $T_p = 775$  MeV.

Uncorrected data (black points) are compared to phase space distributions (shaded area) and the distributions of the model calculation including the  $\Delta$  propagators according to eq. 4.20 (solid line).

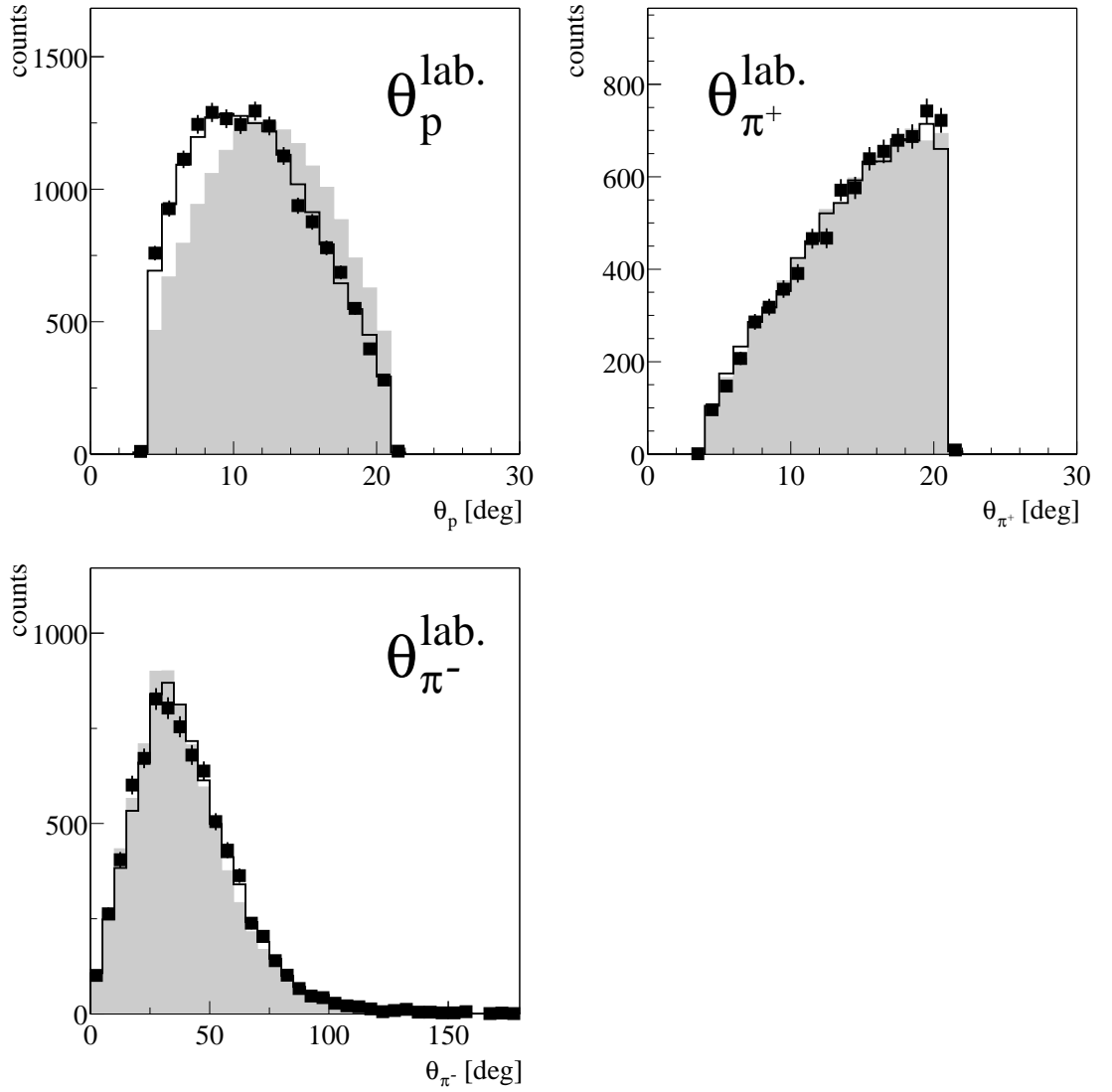


**Figure A.7:** Scattering angles in lab. system at  $T_p = 750$  MeV.

Uncorrected data (black points) are compared to phase space distributions (shaded area) and the distributions of the model calculation including the  $\Delta$  propagators according to eq. 4.20 (solid line).

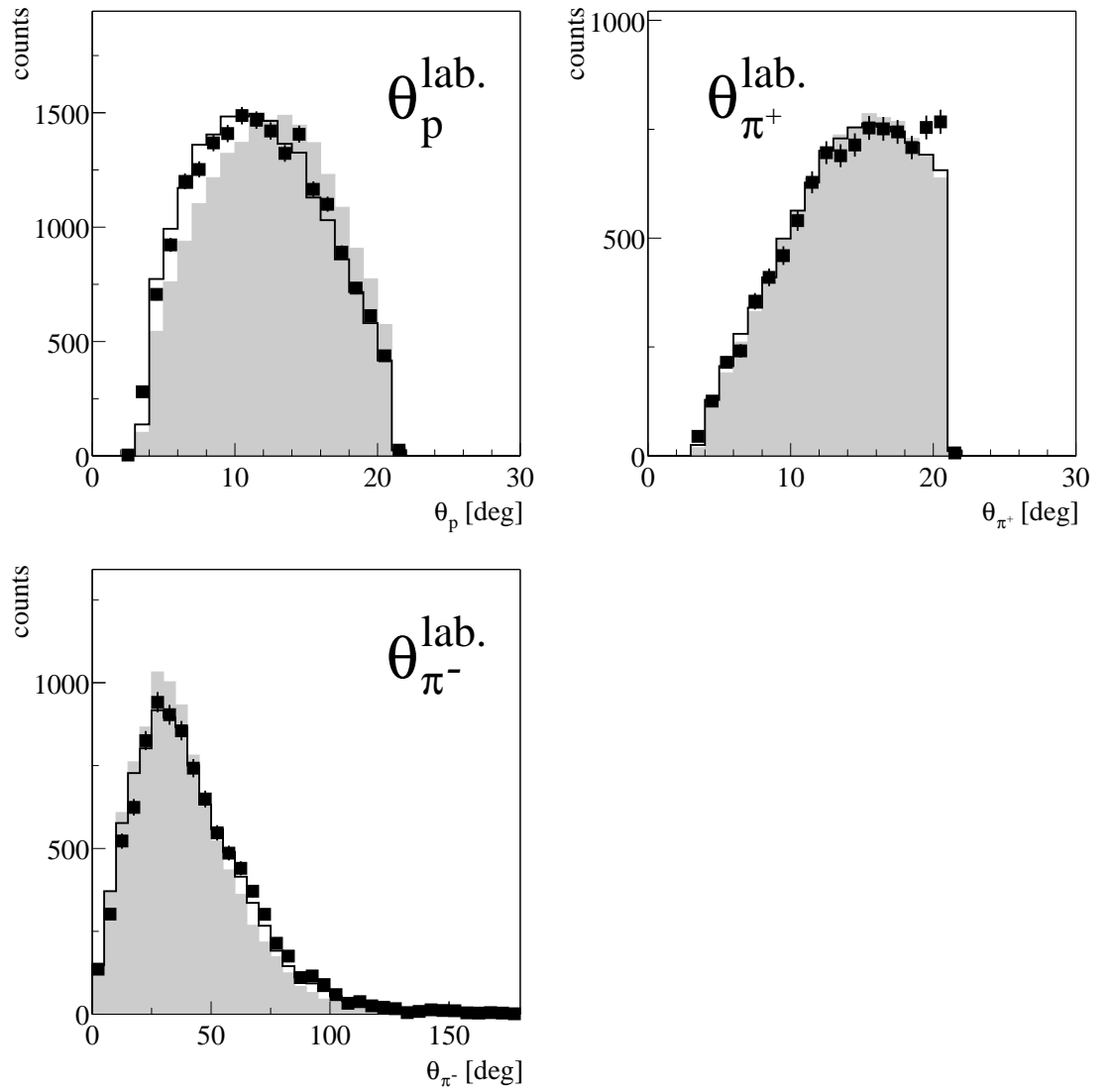


**Figure A.8:** Scattering angles in lab. system at  $T_p = 775$  MeV. Uncorrected data (black points) are compared to phase space distributions (shaded area) and the distributions of the model calculation including the  $\Delta$  propagators according to eq. 4.20 (solid line).

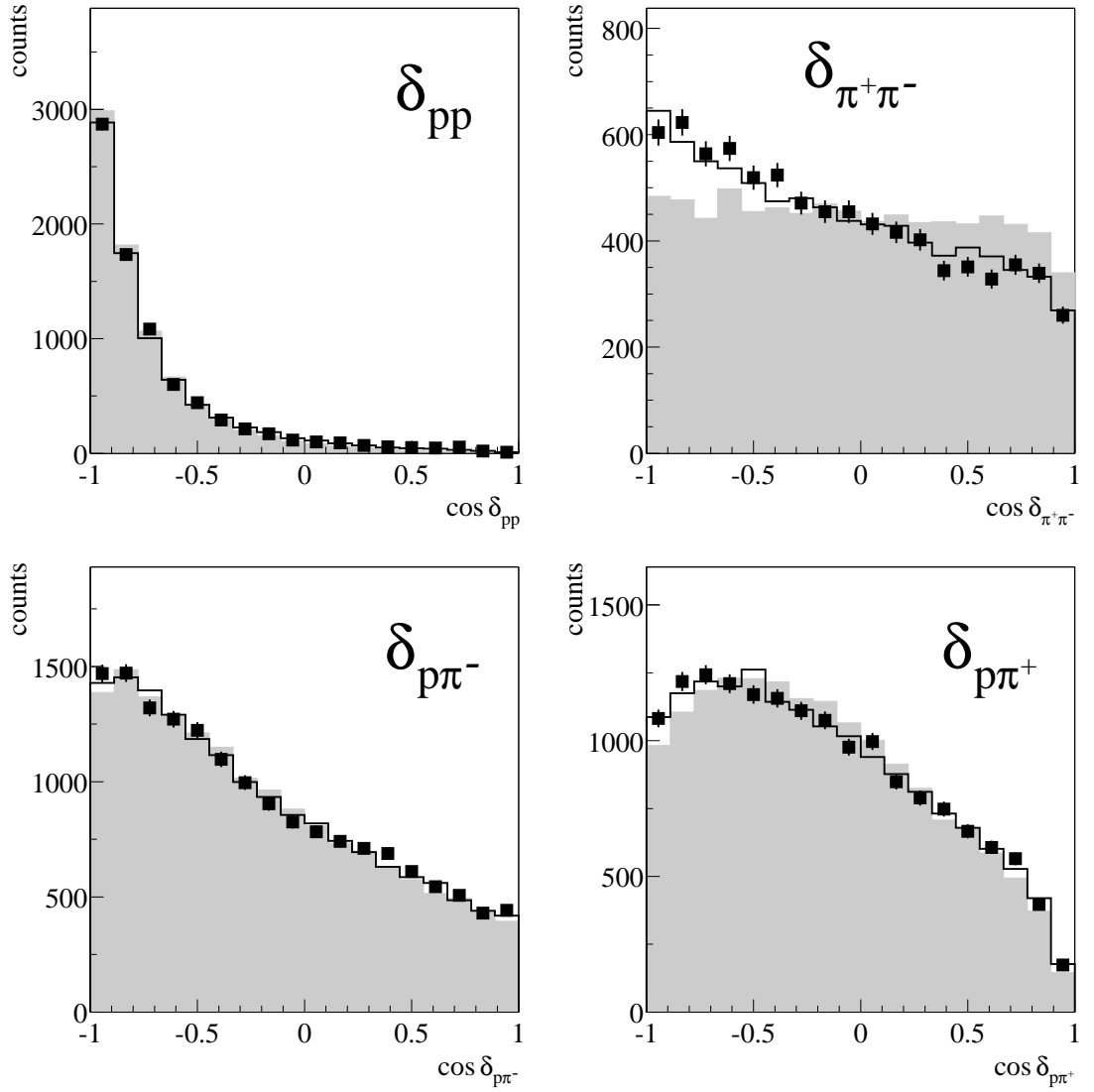


**Figure A.9:** Opening angles in c.m. system at  $T_p = 750$  MeV. Uncorrected data (black points) are compared to phase space distributions (shaded area) and the distributions of the model calculation including the  $\Delta$  propagators according to eq. 4.20 (solid line).

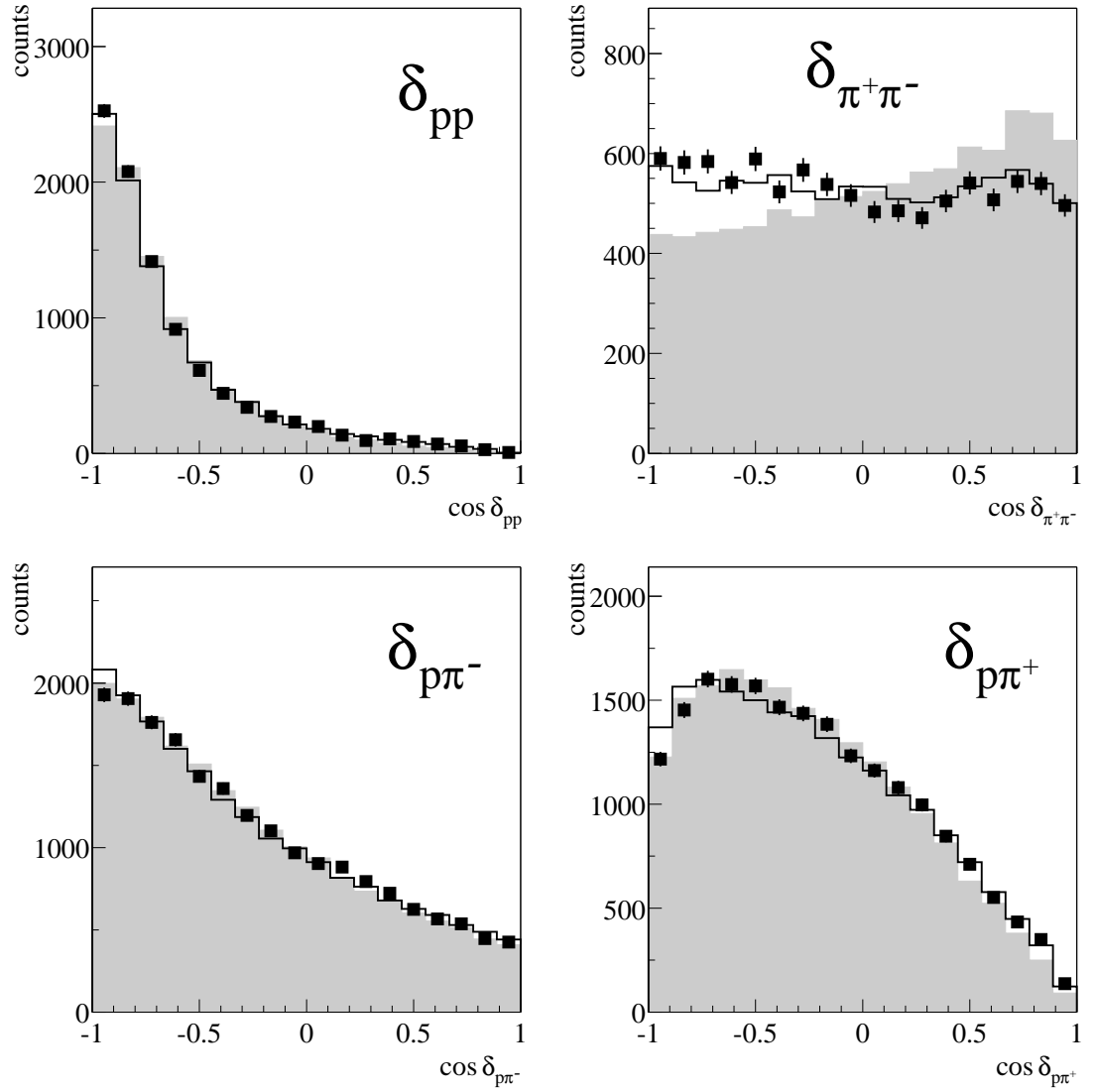


**Figure A.10:** Opening angles in c.m. system at  $T_p = 775$  MeV. Uncorrected data (black points) are compared to phase space distributions (shaded area) and the distributions of the model calculation including the  $\Delta$  propagators according to eq. 4.20 (solid line).

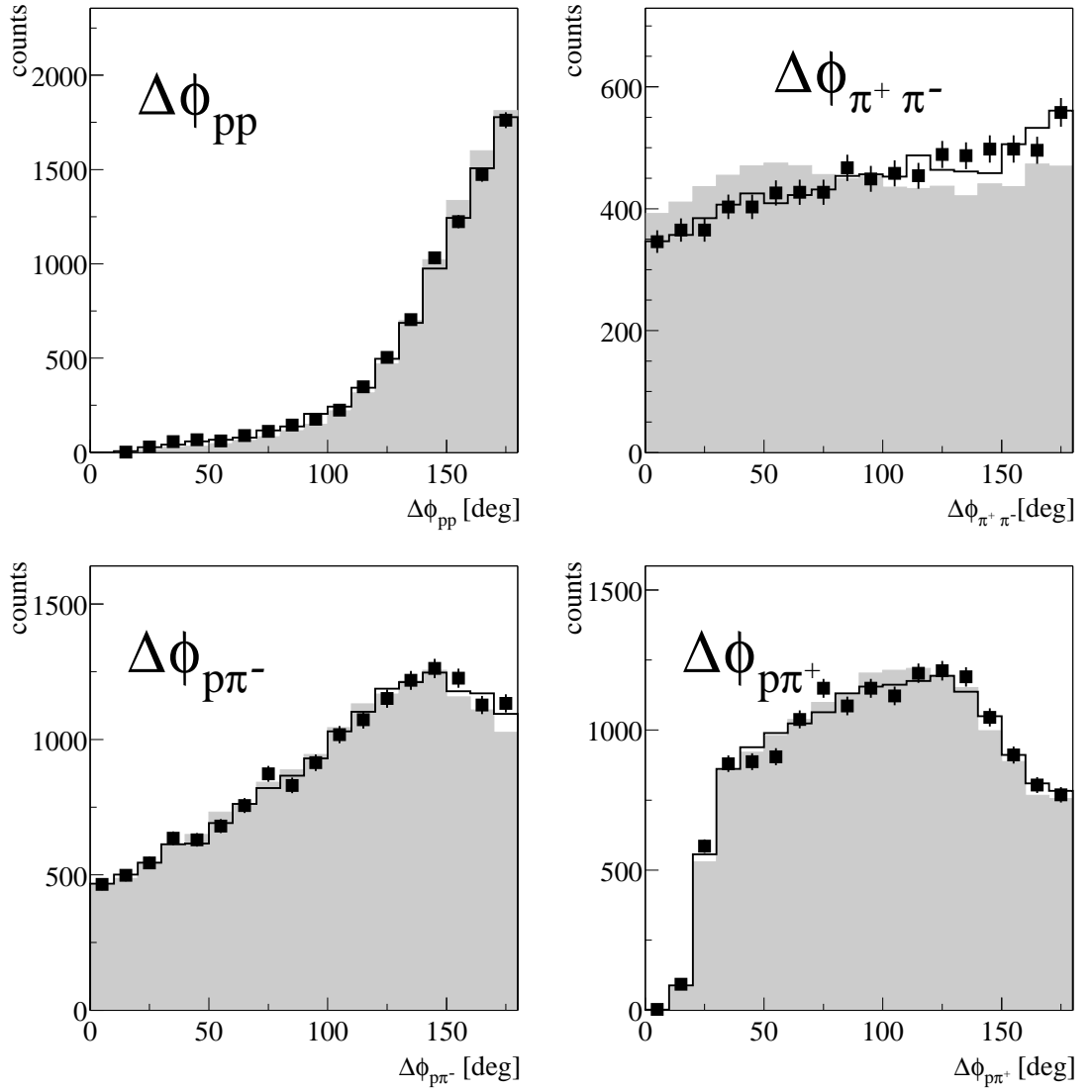


**Figure A.11:** Planarity angles at  $T_p = 750$  MeV.

Uncorrected data (black points) are compared to phase space distributions (shaded area) and the distributions of the model calculation including the  $\Delta$  propagators according to eq. 4.20 (solid line).



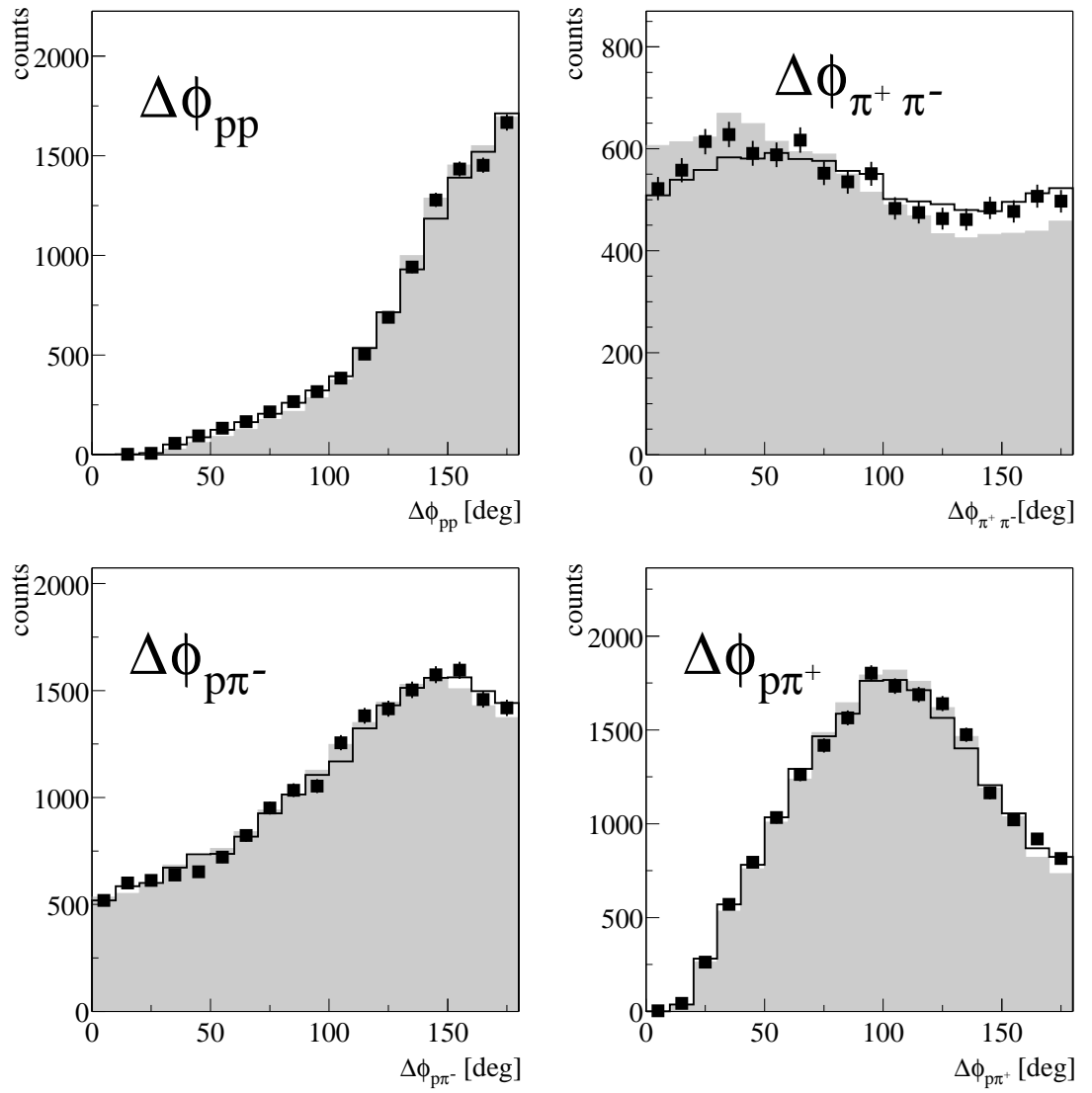


**Figure A.12:** Planarity angles at  $T_p = 775$  MeV.

Uncorrected data (black points) are compared to phase space distributions (shaded area) and the distributions of the model calculation including the  $\Delta$  propagators according to eq. 4.20 (solid line).

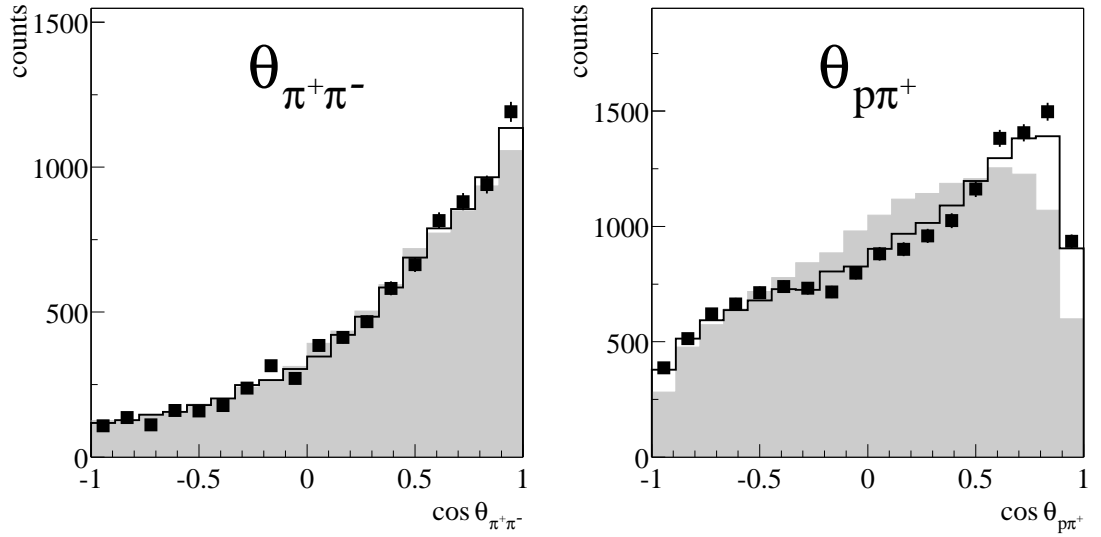


**Figure A.13:** Two particle summary scattering angles at  $T_p = 750$  MeV.

The angular distributions  $\theta_{\pi^+\pi^-}$  and  $\theta_{p\pi^+}$  are equivalent to the distributions of  $\theta_{pp}$  and  $\theta_{p\pi^-}$  respectively, but with reversed signs for  $\cos\theta$ . Uncorrected data (black points) are compared to phase space distributions (shaded area) and the distributions of the model calculation including the  $\Delta$  propagators according to eq. 4.20 (solid line).

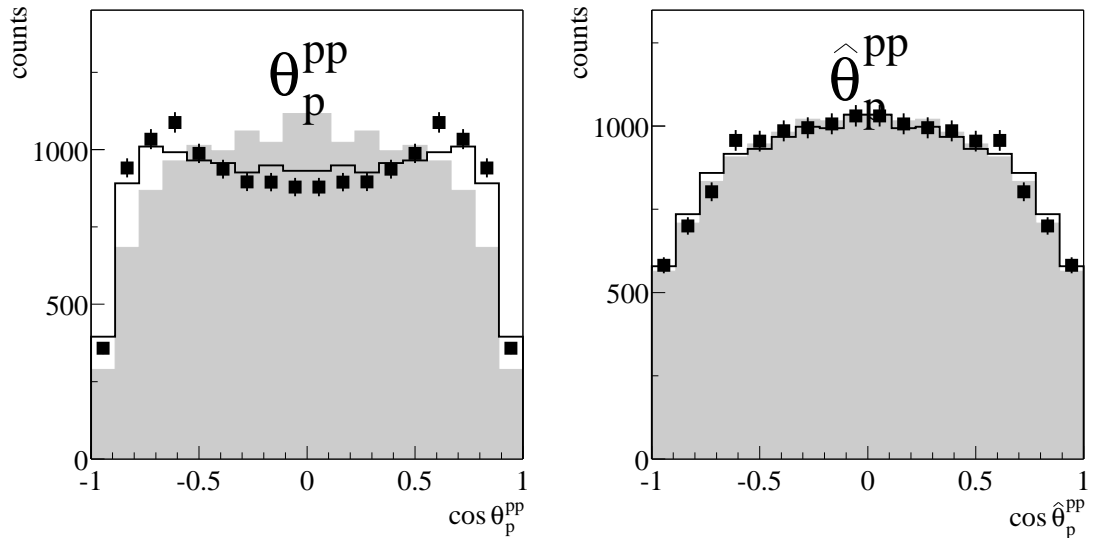


**Figure A.14:**  $pp$  subsystem scattering angles at  $T_p = 750$  MeV.

Uncorrected data (black points) are compared to phase space distributions (shaded area) and the distributions of the model calculation including the  $\Delta$  propagators according to eq. 4.20 (solid line).

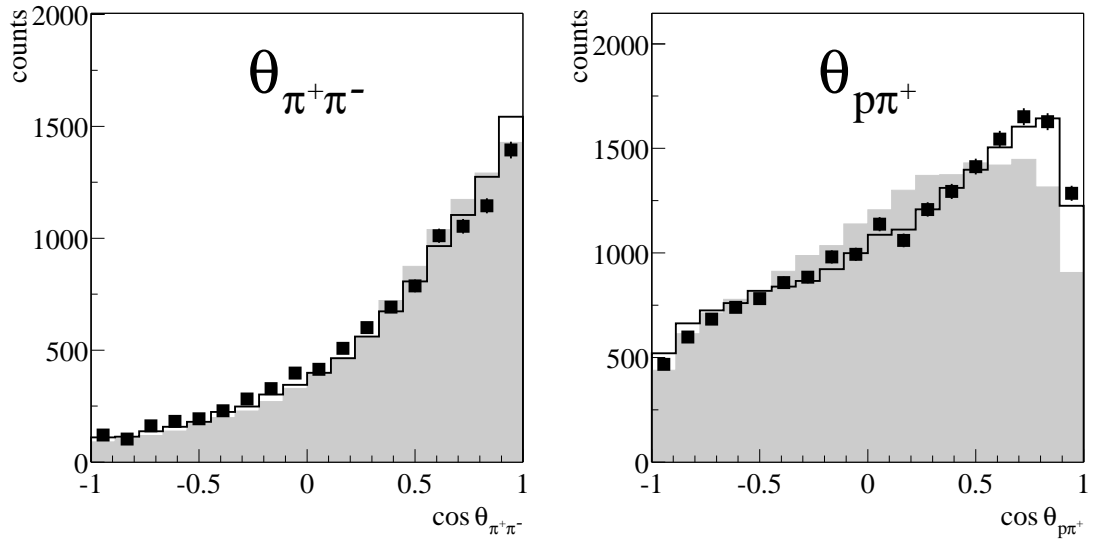


**Figure A.15:** Two particle summary scattering angles at  $T_p = 775$  MeV.

The angular distributions  $\theta_{\pi^+\pi^-}$  and  $\theta_{p\pi^+}$  are equivalent to the distributions of  $\theta_{pp}$  and  $\theta_{p\pi^-}$  respectively, but with reversed signs for  $\cos\theta$ . Uncorrected data (black points) are compared to phase space distributions (shaded area) and the distributions of the model calculation including the  $\Delta$  propagators according to eq. 4.20 (solid line).

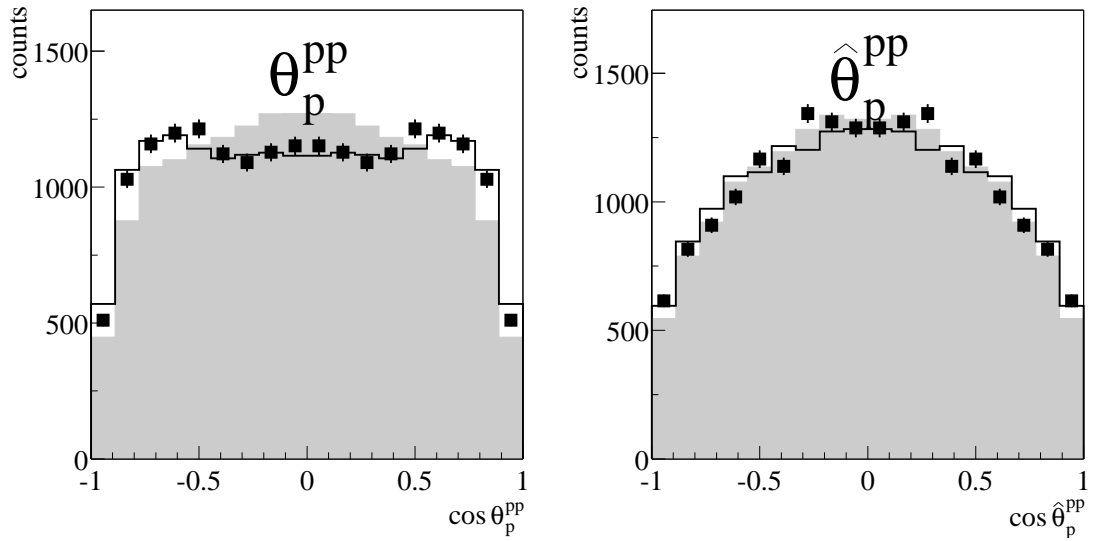


**Figure A.16:**  $pp$  subsystem scattering angles at  $T_p = 775$  MeV.

Uncorrected data (black points) are compared to phase space distributions (shaded area) and the distributions of the model calculation including the  $\Delta$  propagators according to eq. 4.20 (solid line).

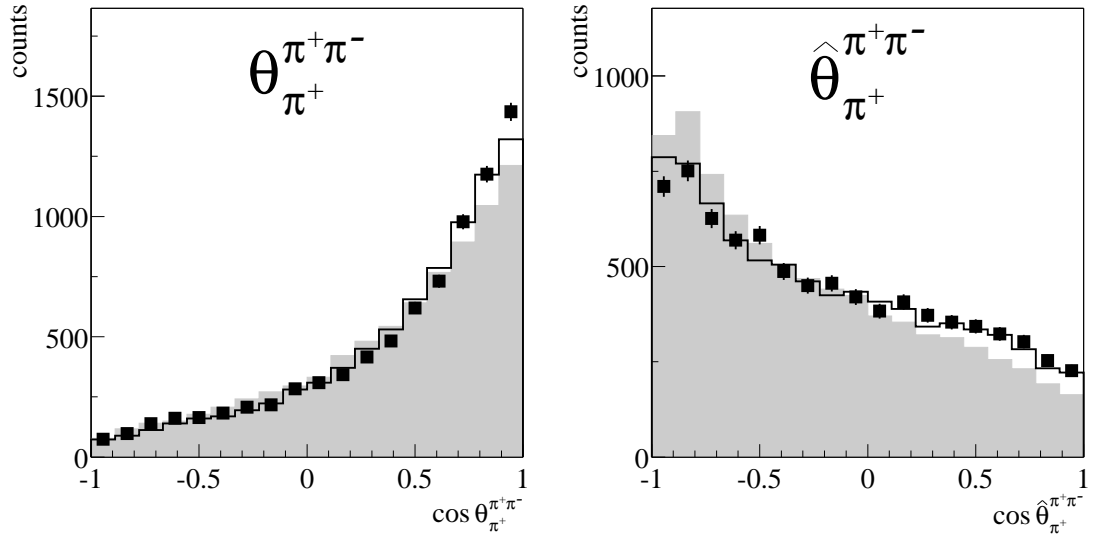


**Figure A.17:**  $\pi^+\pi^-$  subsystem scattering angles at  $T_p = 750$  MeV. Uncorrected data (black points) are compared to phase space distributions (shaded area) and the distributions of the model calculation including the  $\Delta$  propagators according to eq. 4.20 (solid line).

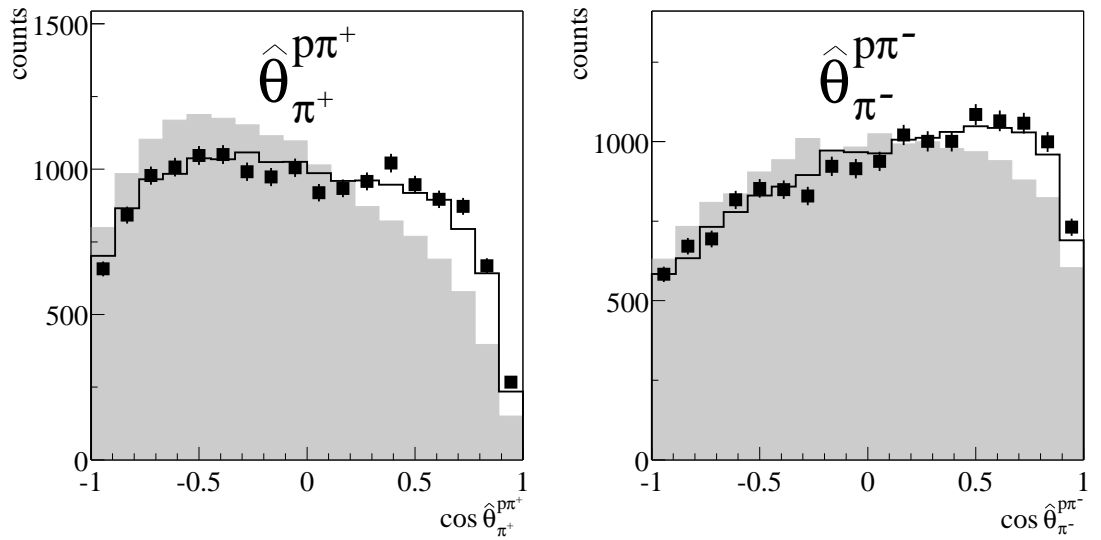


**Figure A.18:**  $p\pi$  subsystem scattering angles at  $T_p = 750$  MeV. Uncorrected data (black points) are compared to phase space distributions (shaded area) and the distributions of the model calculation including the  $\Delta$  propagators according to eq. 4.20 (solid line).

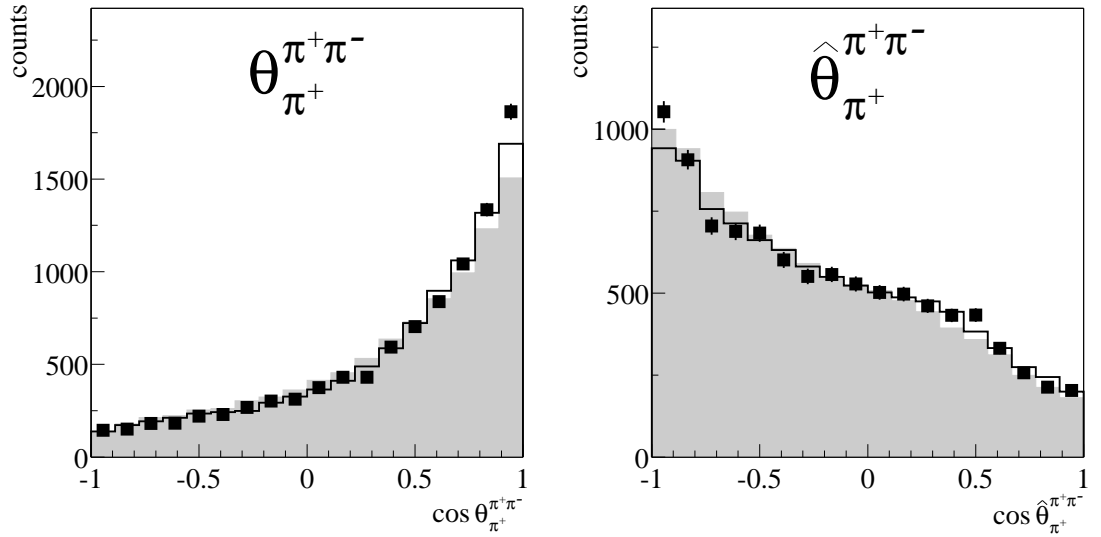


**Figure A.19:**  $\pi^+\pi^-$  subsystem scattering angles at  $T_p = 775$  MeV. Uncorrected data (black points) are compared to phase space distributions (shaded area) and the distributions of the model calculation including the  $\Delta$  propagators according to eq. 4.20 (solid line).

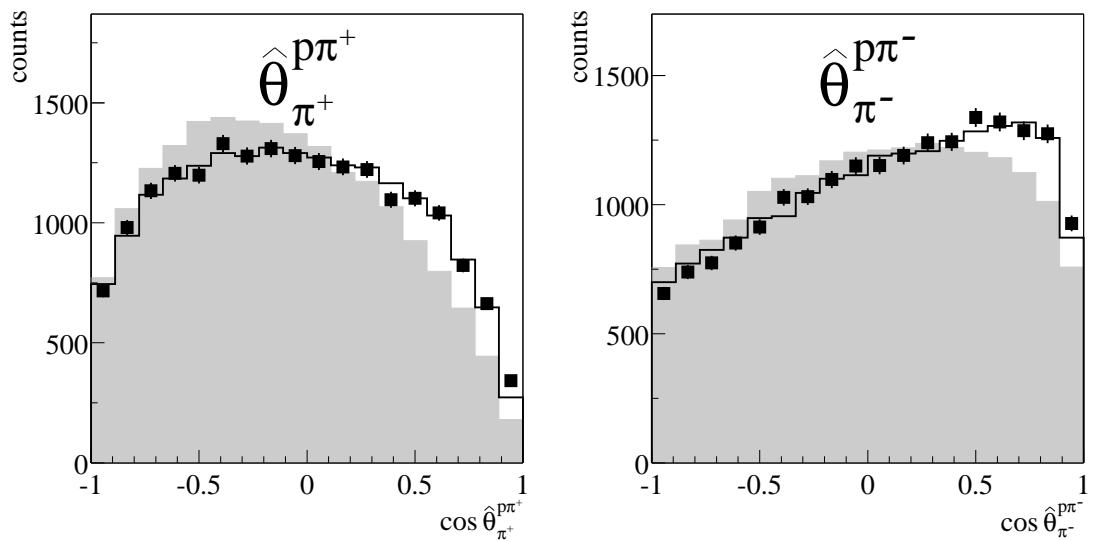


**Figure A.20:**  $p\pi$  subsystem scattering angles at  $T_p = 775$  MeV. Uncorrected data (black points) are compared to phase space distributions (shaded area) and the distributions of the model calculation including the  $\Delta$  propagators according to eq. 4.20 (solid line).

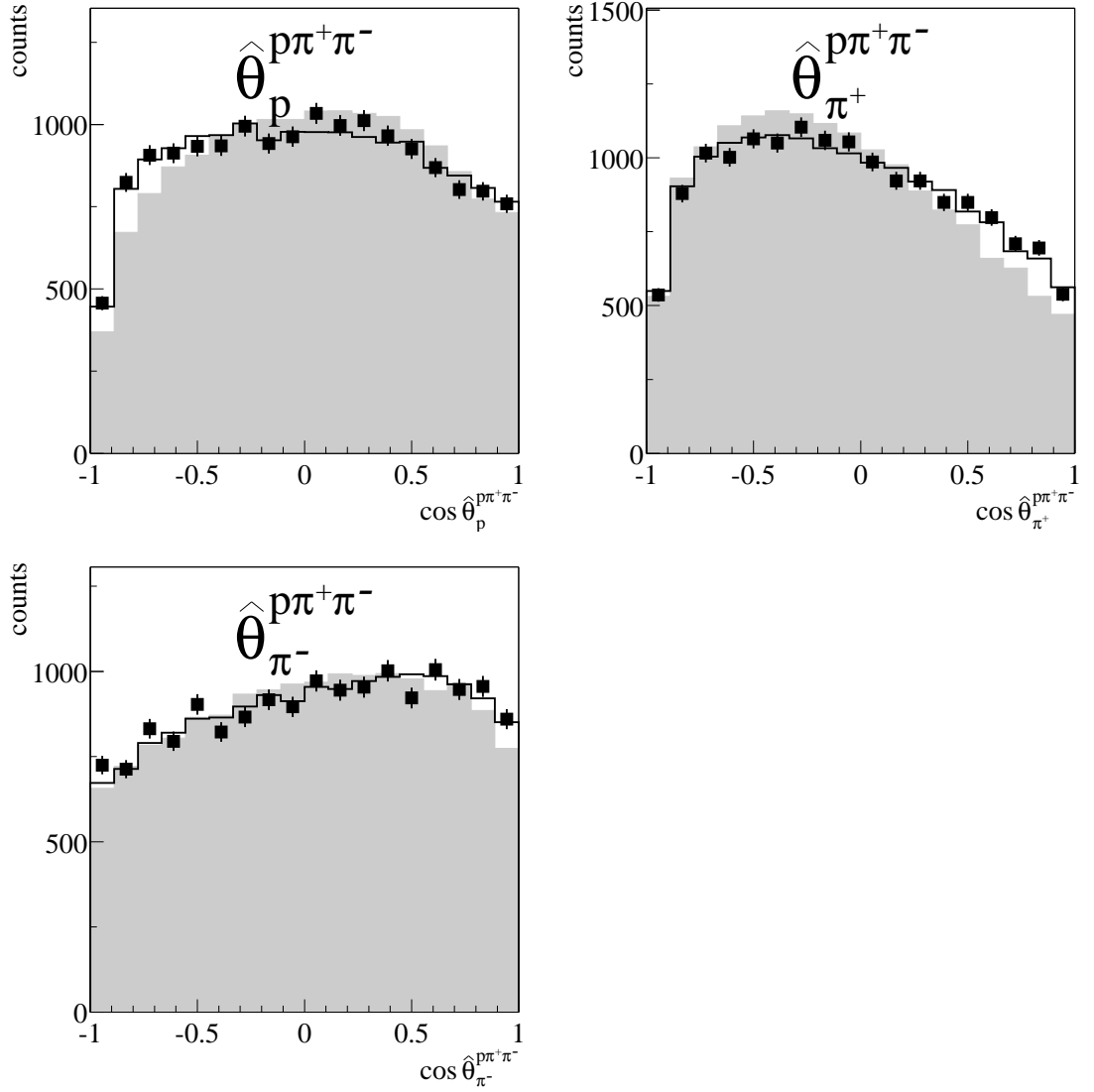


**Figure A.21:**  $p\pi\pi$  subsystem scattering angles at  $T_p = 750$  MeV.

Uncorrected data (black points) are compared to phase space distributions (shaded area) and the distributions of the model calculation including the  $\Delta$  propagators according to eq. 4.20 (solid line).

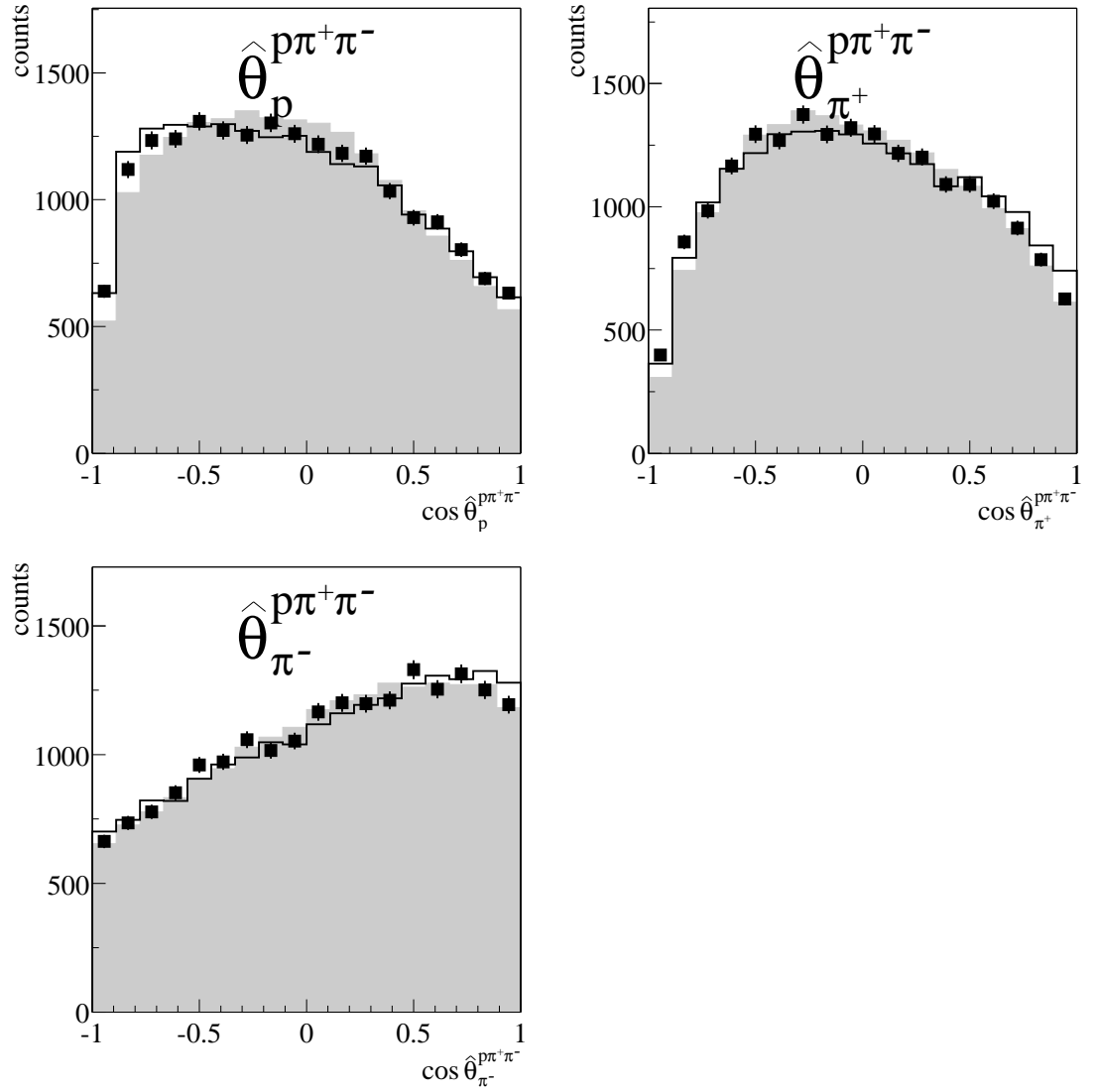


**Figure A.22:**  $p\pi\pi$  subsystem scattering angles at  $T_p = 775$  MeV.

Uncorrected data (black points) are compared to phase space distributions (shaded area) and the distributions of the model calculation including the  $\Delta$  propagators according to eq. 4.20 (solid line).

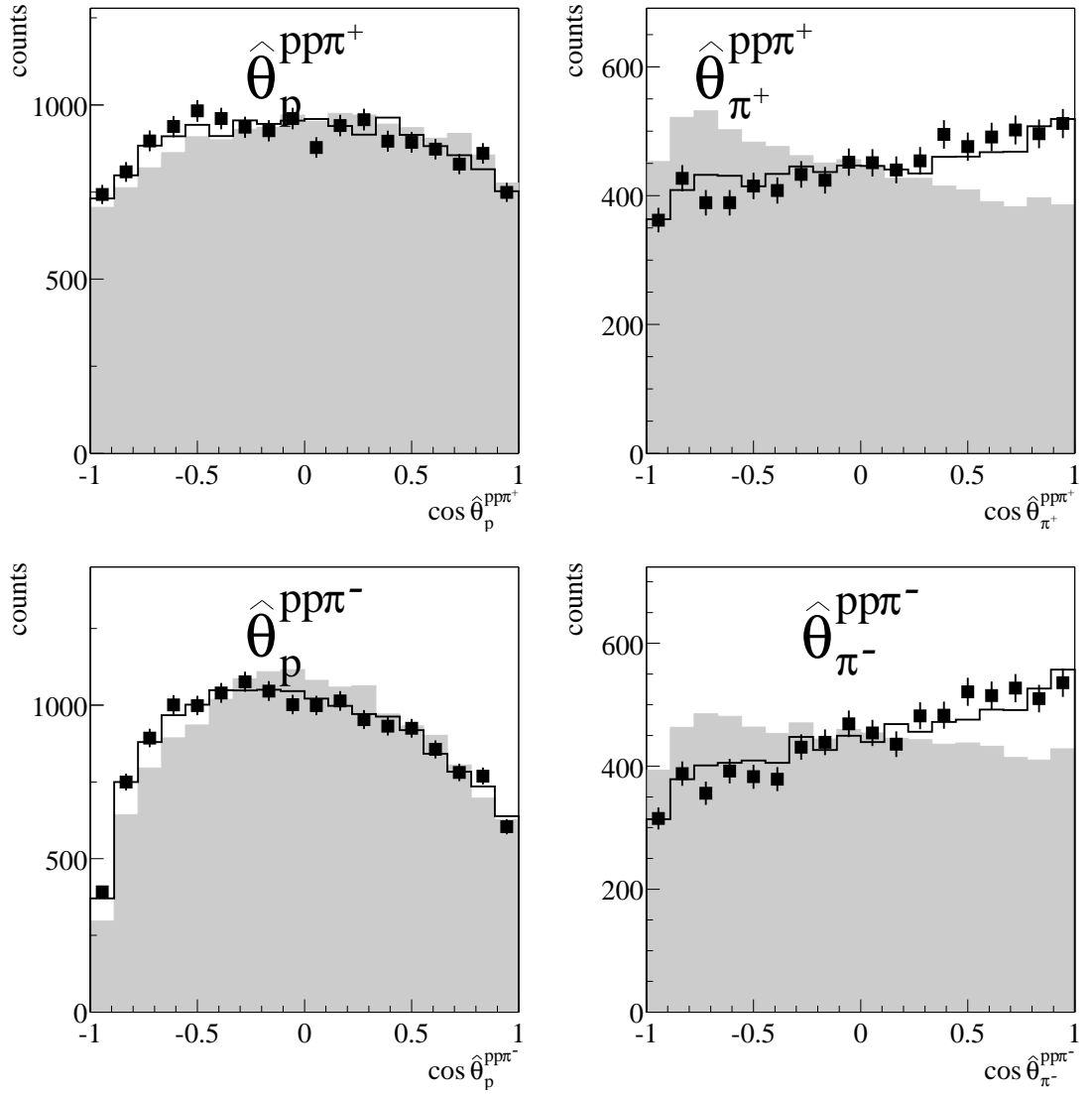


**Figure A.23:**  $pp\pi$  subsystem scattering angles at  $T_p = 750$  MeV.

Uncorrected data (black points) are compared to phase space distributions (shaded area) and the distributions of the model calculation including the  $\Delta$  propagators according to eq. 4.20 (solid line).



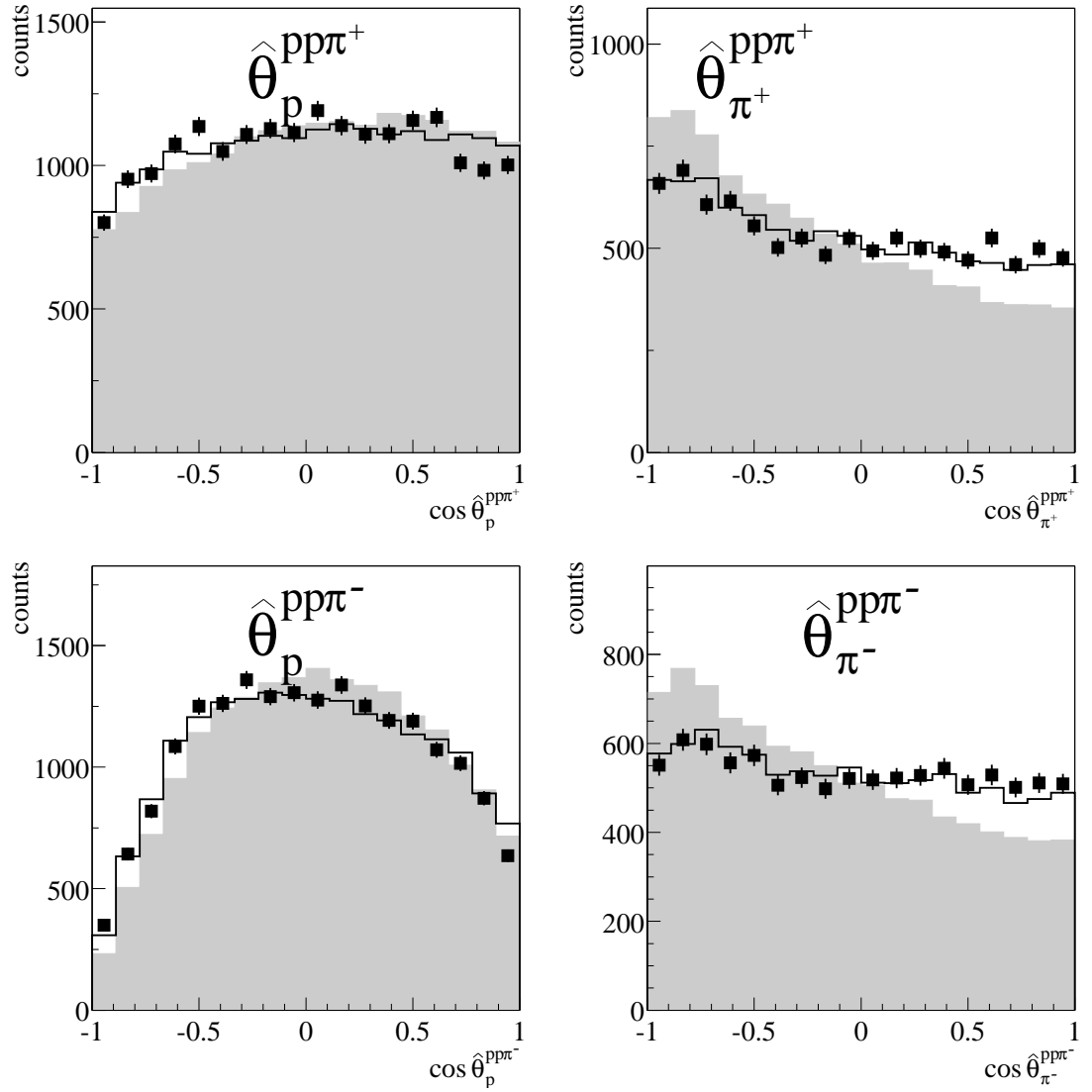


**Figure A.24:**  $pp\pi$  subsystem scattering angles at  $T_p = 775$  MeV.

Uncorrected data (black points) are compared to phase space distributions (shaded area) and the distributions of the model calculation including the  $\Delta$  propagators according to eq. 4.20 (solid line).

### A.3 Kinetic energy distributions

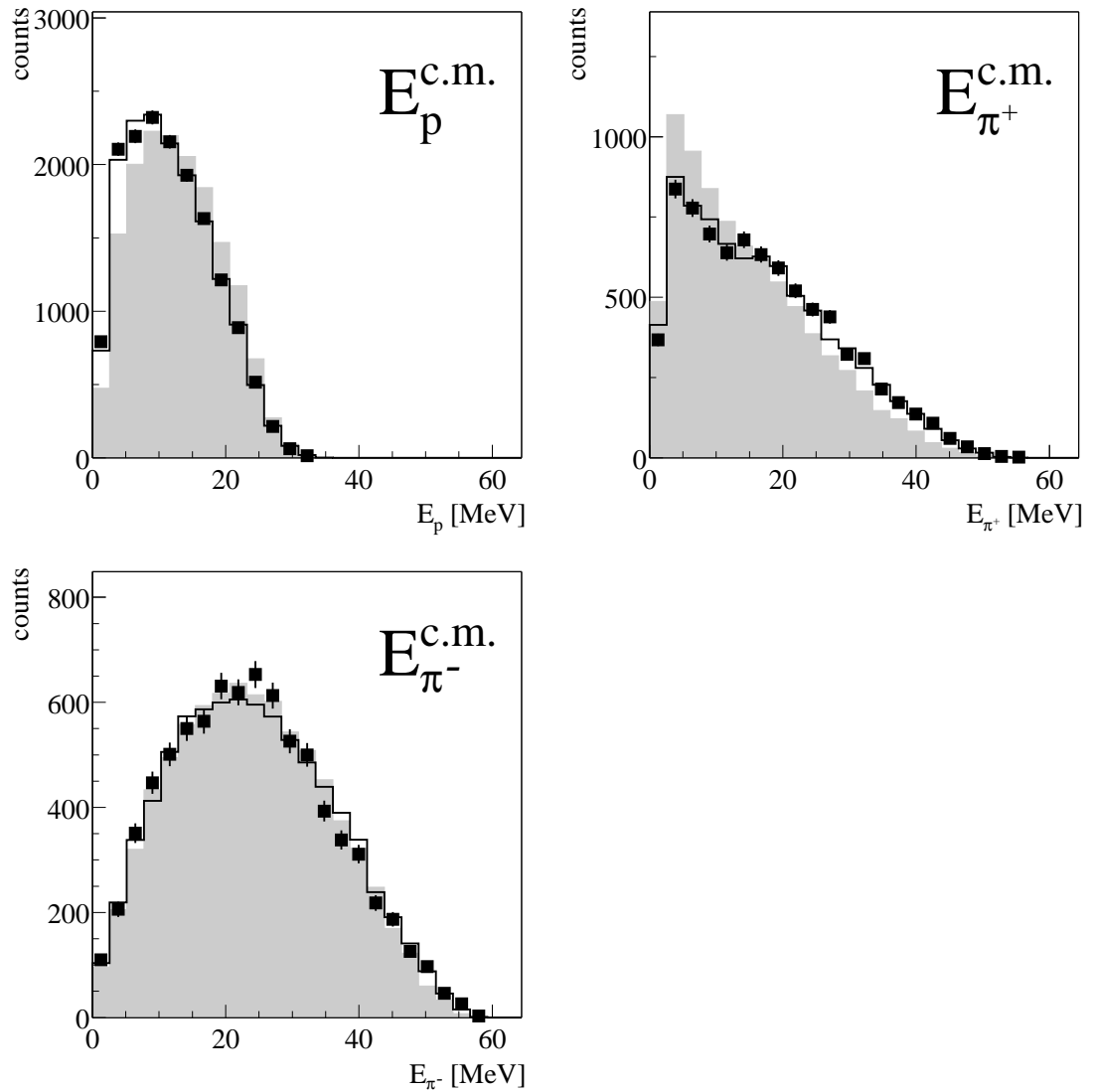


**Figure A.25:** Kinetic energies in c.m. system at  $T_p = 750$  MeV. Uncorrected data (black points) are compared to phase space distributions (shaded area) and the distributions of the model calculation including the  $\Delta$  propagators according to eq. 4.20 (solid line).

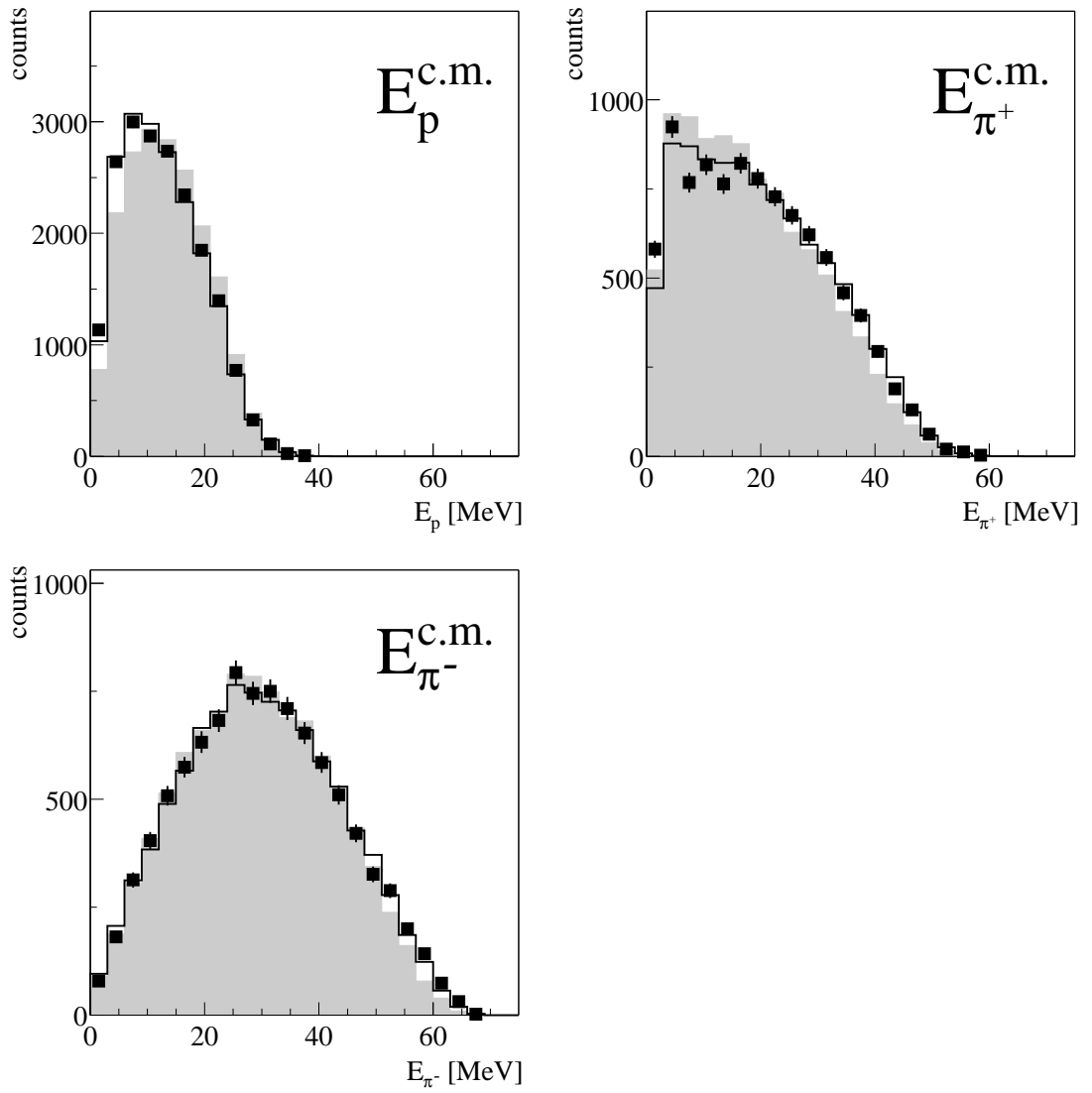


**Figure A.26:** Kinetic energies in c.m. system at  $T_p = 775$  MeV. Uncorrected data (black points) are compared to phase space distributions (shaded area) and the distributions of the model calculation including the  $\Delta$  propagators according to eq. 4.20 (solid line).

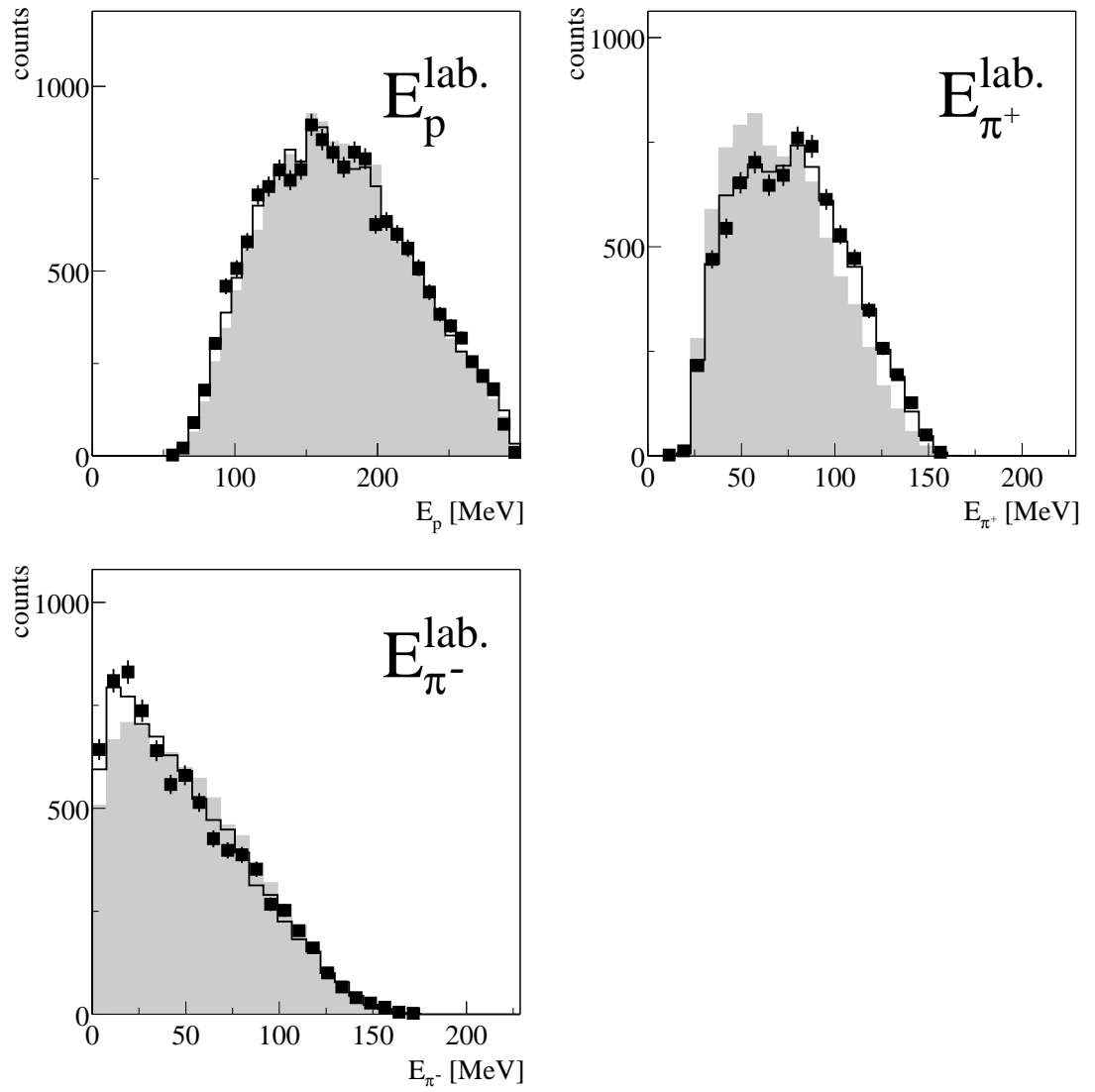


**Figure A.27:** Kinetic energies in lab. system at  $T_p = 750$  MeV. Uncorrected data (black points) are compared to phase space distributions (shaded area) and the distributions of the model calculation including the  $\Delta$  propagators according to eq. 4.20 (solid line).

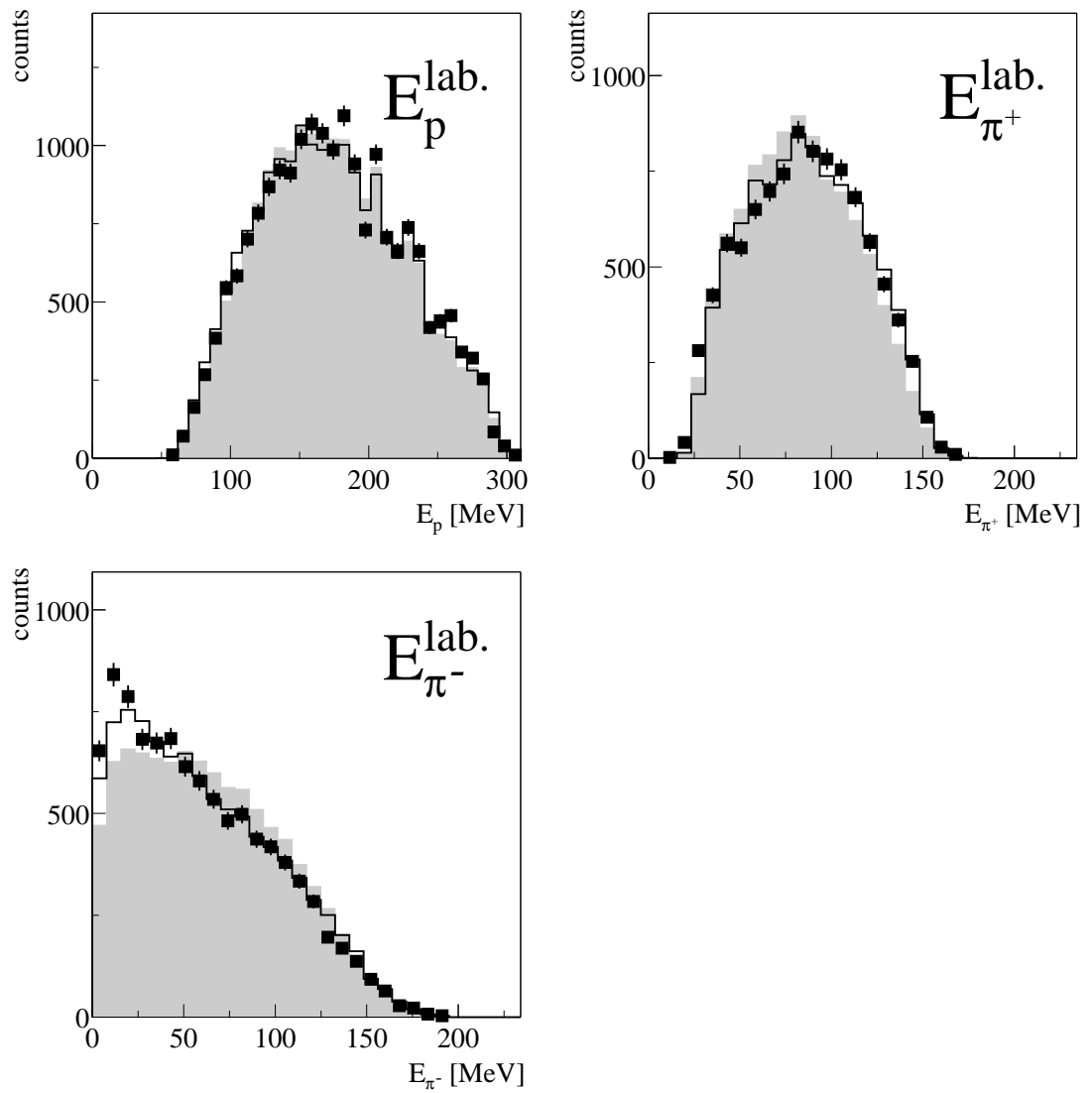


**Figure A.28:** Kinetic energies in lab. system at  $T_p = 775$  MeV. Uncorrected data (black points) are compared to phase space distributions (shaded area) and the distributions of the model calculation including the  $\Delta$  propagators according to eq. 4.20 (solid line).

# B

## Acceptance and efficiency

The figures on the following pages show the efficiency and acceptance obtained from the detector simulation for all measured observables. According to Fig. 3.12 it is

$$(B.1) \quad \frac{\text{histogram}(\text{simulation})}{\text{histogram}(\text{model})}$$

or in other words the reciprocal of the efficiency and acceptance correction histogram.

## B.1 Invariant masses

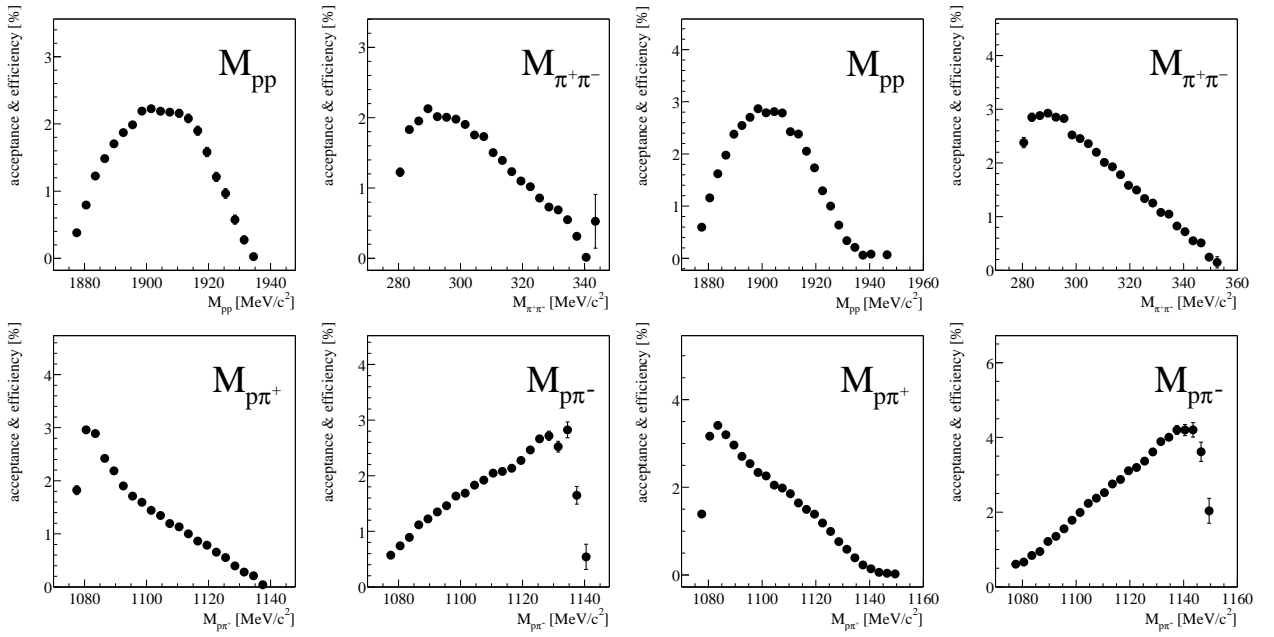


**Figure B.1:** Acceptance and efficiency of the invariant masses of two particle systems at  $T_p = 750$  MeV (left) and 775 MeV (right).

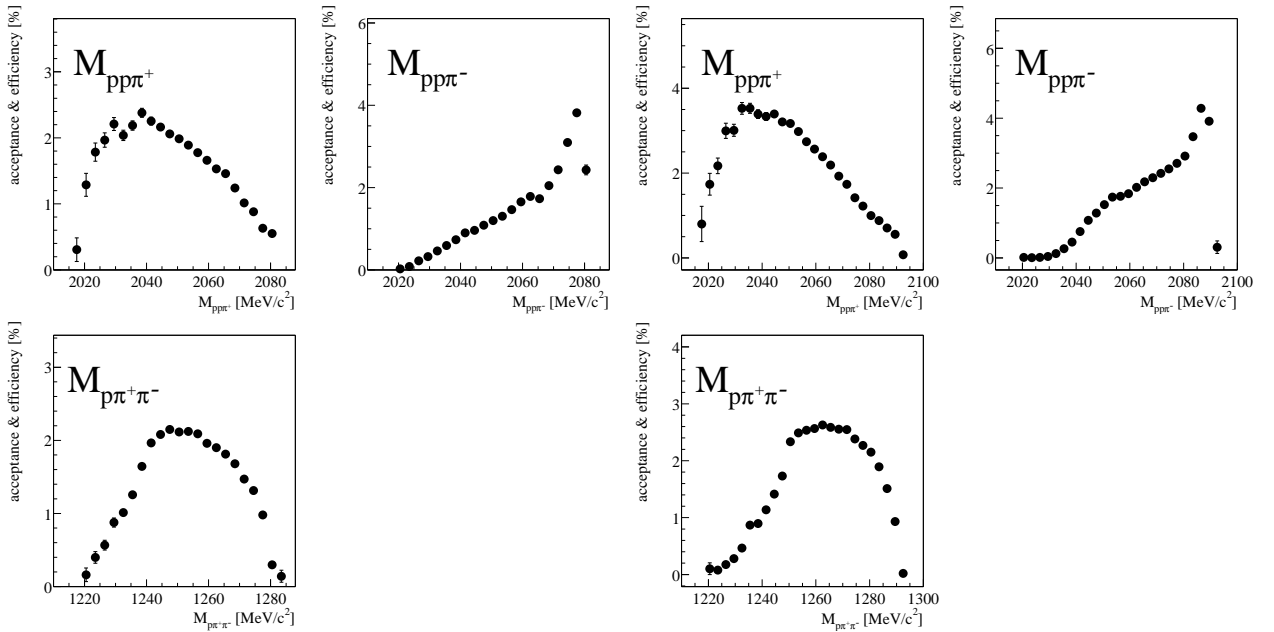


**Figure B.2:** Acceptance and efficiency of the invariant masses of three particle systems at  $T_p = 750$  MeV (left) and 775 MeV (right).

## B.2 Angular distributions

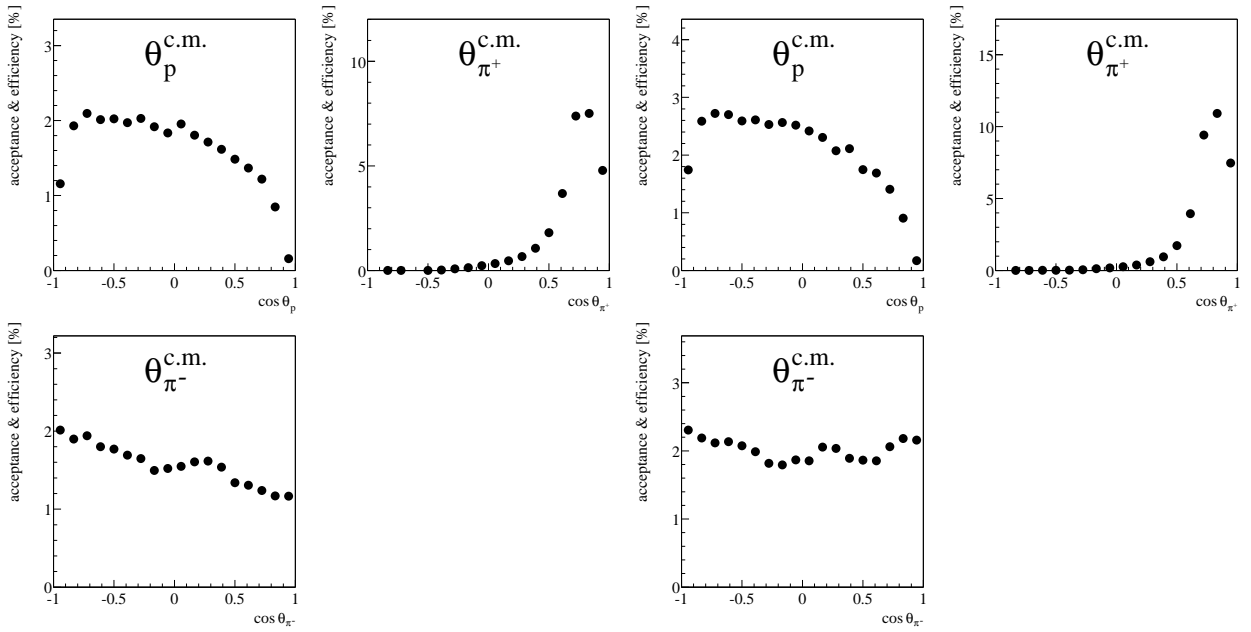


**Figure B.3:** Acceptance and efficiency of the scattering angles in c.m. system at  $T_p = 750$  MeV (left) and 775 MeV (right).

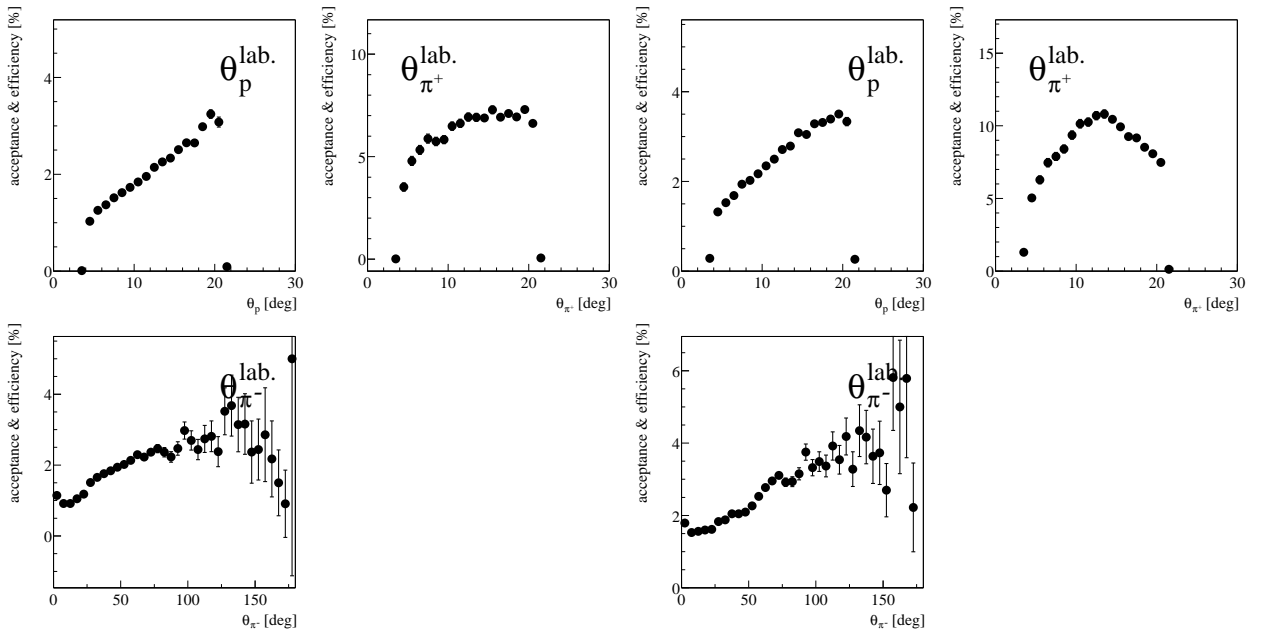


**Figure B.4:** Acceptance and efficiency of the scattering angles in lab. system at  $T_p = 750$  MeV (left) and 775 MeV (right).



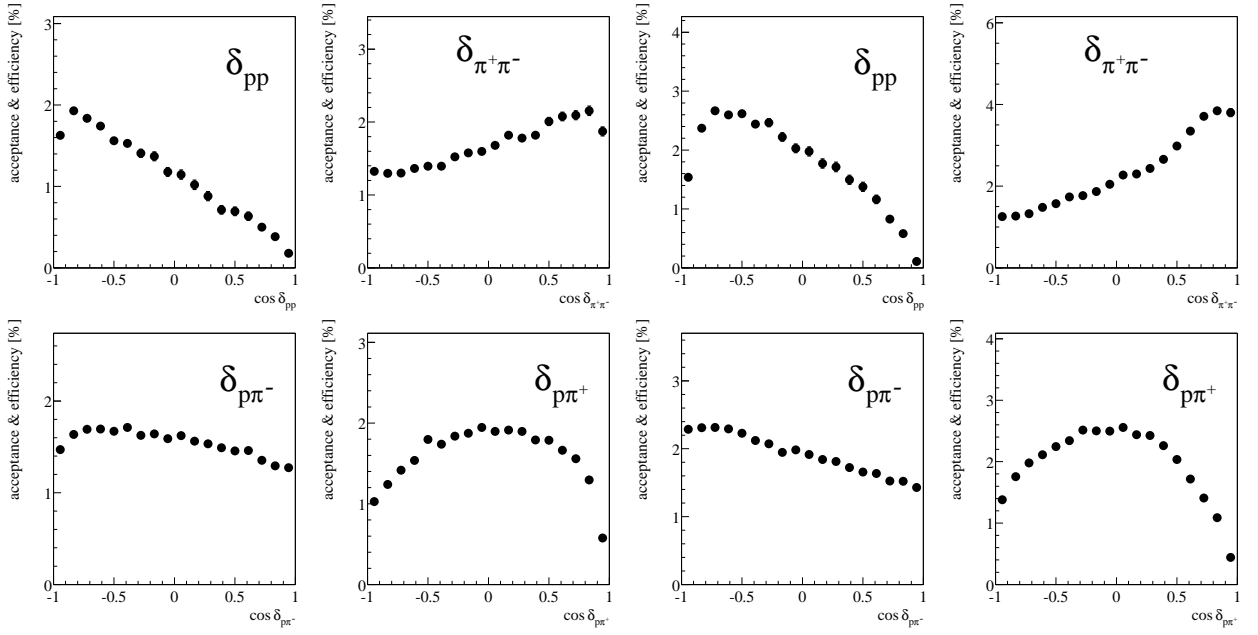


**Figure B.5:** Acceptance and efficiency of the opening angles in c.m. system at  $T_p = 750$  MeV (left) and 775 MeV (right).

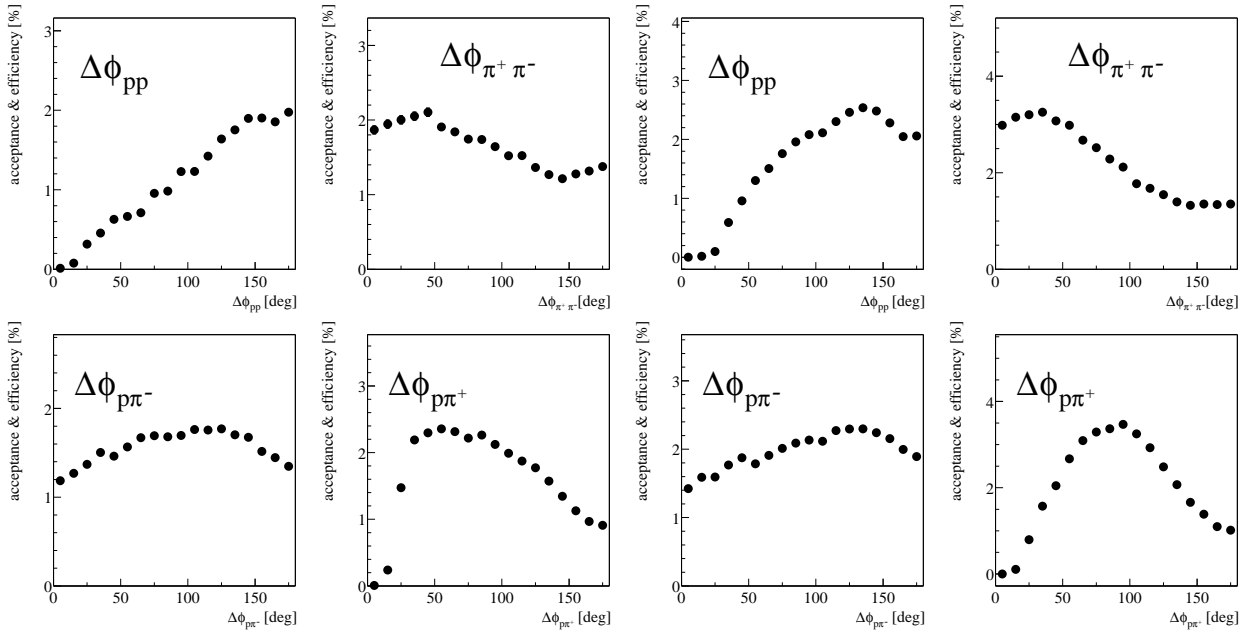


**Figure B.6:** Acceptance and efficiency of the planarity angles at  $T_p = 750$  MeV (left) and 775 MeV (right).

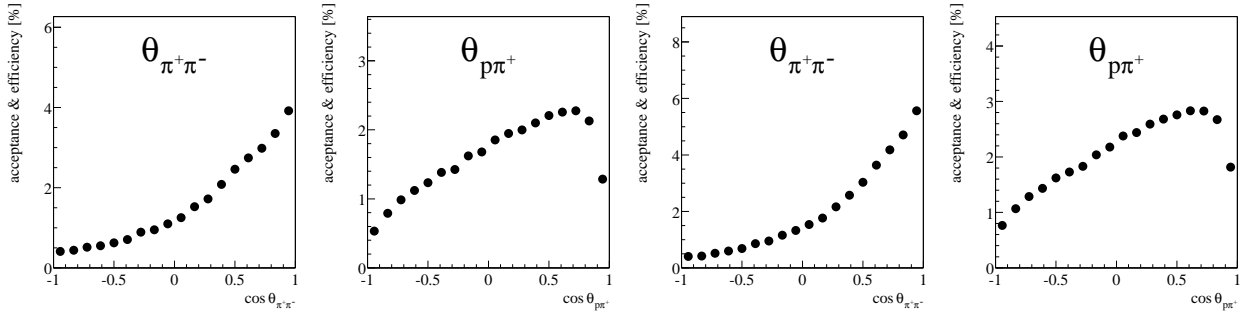


**Figure B.7:** Acceptance and efficiency of the two particle summary scattering angles at  $T_p = 750$  MeV (left) and 775 MeV (right).

The angular distributions  $\theta_{\pi^+\pi^-}$  and  $\theta_{p\pi^+}$  are equivalent to the distributions of  $\theta_{pp}$  and  $\theta_{p\pi^-}$  respectively, but with reversed signs for  $\cos$ .

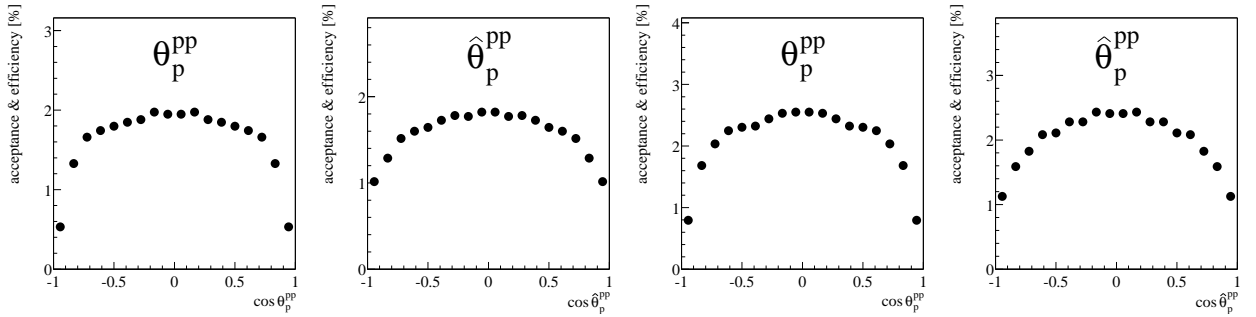


**Figure B.8:** Acceptance and efficiency of the  $pp$  subsystem scattering angles at  $T_p = 750$  MeV (left) and 775 MeV (right).

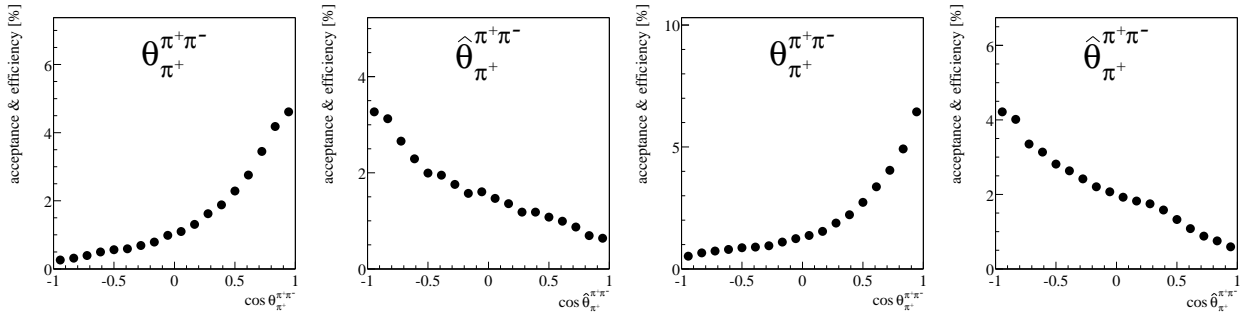


**Figure B.9:** Acceptance and efficiency of the  $\pi^+\pi^-$  subsystem scattering angles at  $T_p = 750$  MeV (left) and 775 MeV (right).

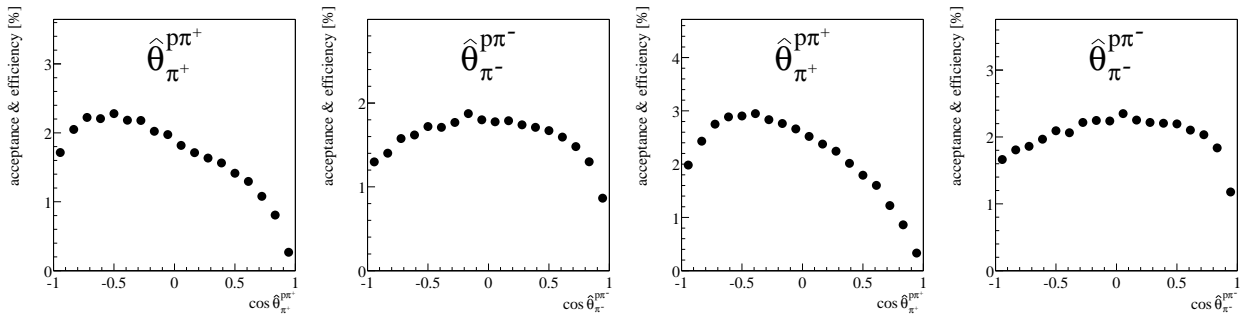


**Figure B.10:** Acceptance and efficiency of the  $p\pi$  subsystem scattering angles at  $T_p = 750$  MeV (left) and 775 MeV (right).

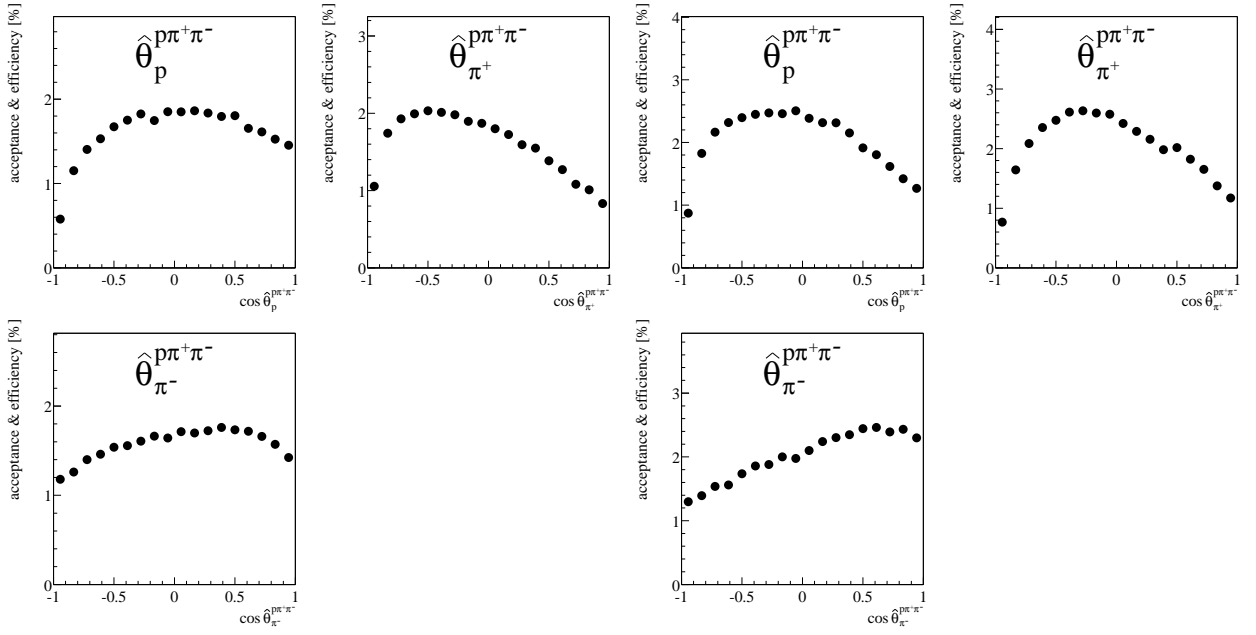


**Figure B.11:** Acceptance and efficiency of the  $\rho\pi\pi$  subsystem scattering angles at  $T_p = 750$  MeV (left) and 775 MeV (right).

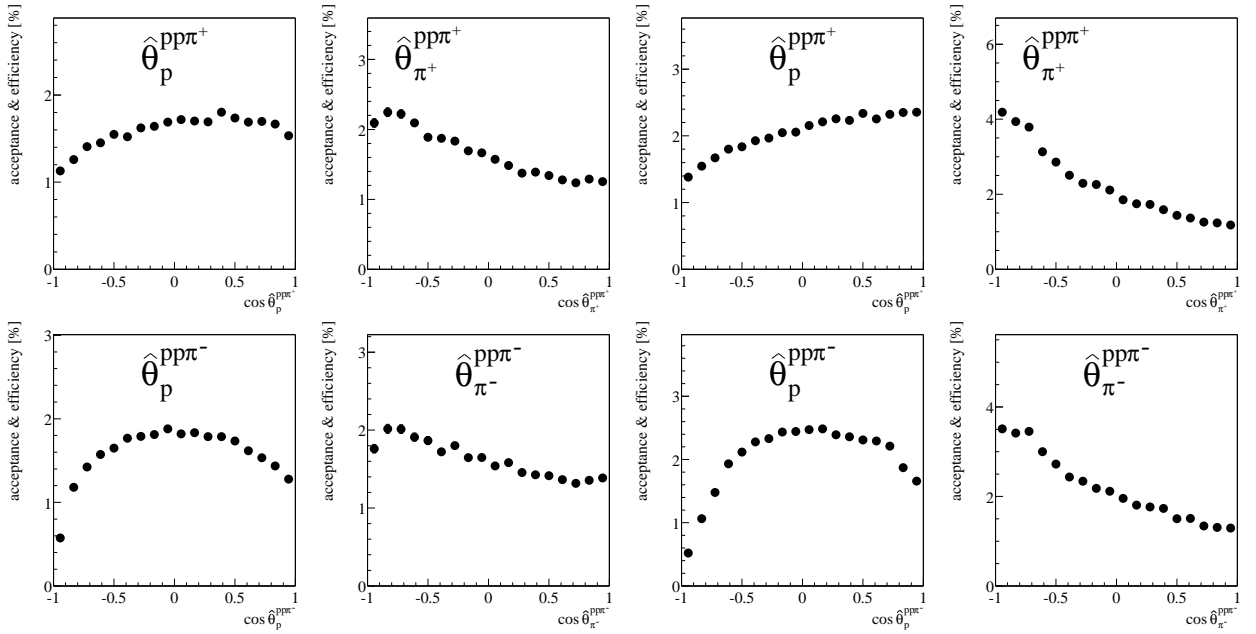


**Figure B.12:** Acceptance and efficiency of the  $\rho\rho\pi$  subsystem scattering angles at  $T_p = 750$  MeV (left) and 775 MeV (right).

## B.3 Kinetic energy distributions

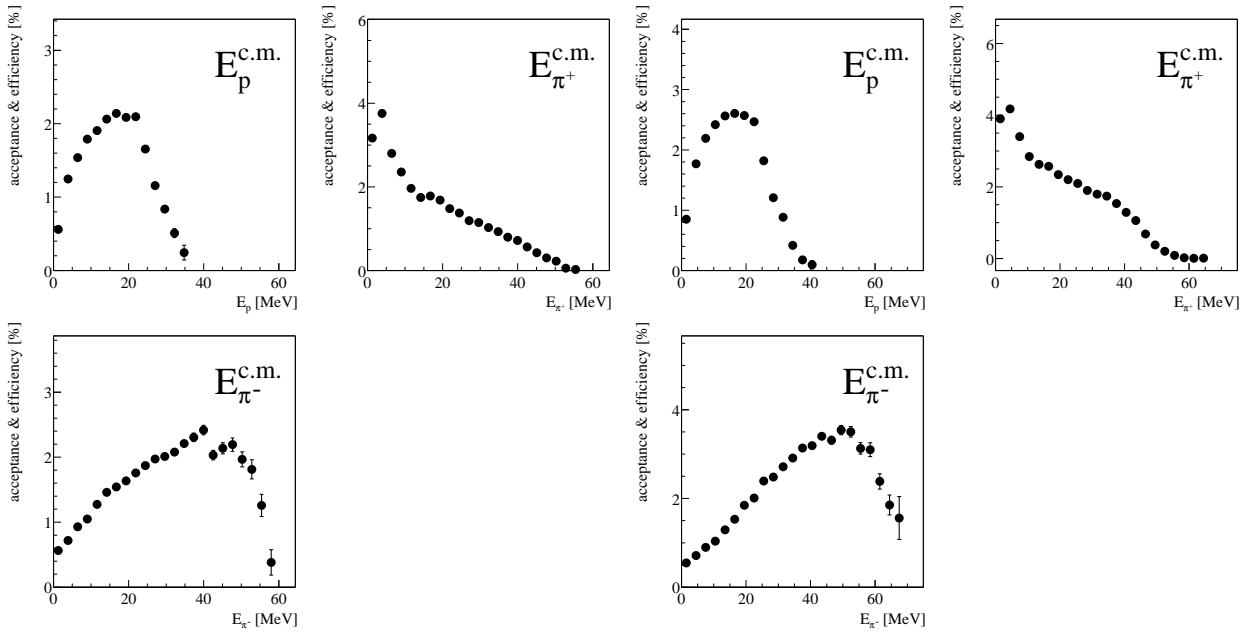


**Figure B.13:** Acceptance and efficiency of the kinetic energies in c.m. system at  $T_p = 750$  MeV (left) and 775 MeV (right).

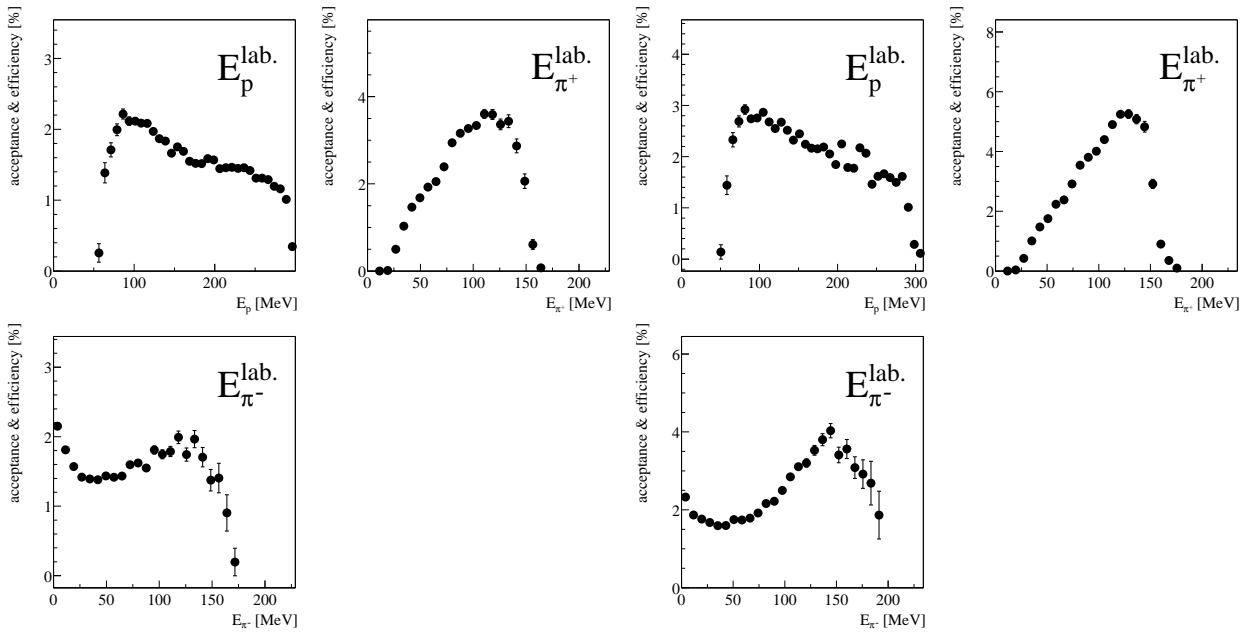


**Figure B.14:** Acceptance and efficiency of the kinetic energies in lab. system at  $T_p = 750$  MeV (left) and 775 MeV (right).

# C

## Acronyms

<b>ADC</b>	Analog to Digital Converter
<b>BVC</b>	Backward Veto Counter
<b>CD</b>	Central Detector
<b>CEC</b>	Central Electromagnetic Calorimeter
<b>CELSIUS</b>	Cooling with Electrons and Storing of Ions from the Uppsala Synchro-cyclotron
<b>CERN</b>	Centre Européen pour la Recherche Nucléaire
<b>CFB</b>	Central FiBre detector
<b>COSY</b>	COoler SYncrotron
<b>DAQ</b>	Data AQuisition
<b>FD</b>	Forward Detector
<b>FHD</b>	Forward trigger HoDoscope
<b>FPC</b>	Forward Proportional Counter
<b>FRH</b>	Forward Range Hodoscope
<b>FSI</b>	Final State Interaction
<b>FVH</b>	Forward Veto Hodoskope
<b>FWC</b>	Forward Window Counter
<b>GEANT</b>	GEometry ANd Tracking
<b>LRTDC</b>	Long Range Time to Digital Converter
<b>MDC</b>	Mini Drift Chamber

<b>PROMICE</b>	PRoduction Of Mesons In CElsius
<b>PSB</b>	Plastic Scintillator Barrel
<b>QCD</b>	Quantum Chromo Dynamics
<b>QDC</b>	charge (Q) to Digital Converter
<b>SCS</b>	Super Conducting Solenoid
<b>SEC</b>	Scintillating Electromagnetic Calorimeter
<b>TDC</b>	Time to Digital Converter
<b>TRIUMF</b>	TRI University Meson Facility
<b>TSL</b>	Theodor Svedberg Laboratory
<b>WASA</b>	Wide Angle Shower Apparatus

# D

## Nomenclature

<b>c.m.</b>	centre of mass (system)
$\Delta$	excitation of the nucleon with spin $s = \frac{3}{2}$ , here: the first $\Delta$ excitation, the $\Delta(1232)$ with a mass of $m_\Delta = 1232 \text{ MeV}/c^2$ and a width of $\Gamma_\Delta = 120 \text{ MeV}/c^2$
$\Delta E$	partial energy deposition in a thin detector
$E$	kinetic energy
$I$	isospin
$l$	angular momentum
<b>lab.</b>	laboratory (system)
$M$	invariant mass
$MM$	missing mass
$N^*$	general: excitation of the nucleon with spin $s = \frac{1}{2}$ ; here: synonym for $N^*(1440)$
$N^*(1440)$	first $N^*$ excitation of the nucleon, with a mass of $m_{N^*} = 1440 \text{ MeV}/c^2$ and a width of $\Gamma_{N^*} = 350 \text{ MeV}/c^2$ .
$\phi$	azimuthal (scattering) angle
$\pi$	$\pi$ -meson, pion, lightest meson
$p$	proton
$\sigma$	$\sigma$ -meson, sigma, also denoted as correlated $\pi\pi$ -pair in $l = I = 0$ (scalar, iso-scalar) state
$\tau$	mean life time
$T_p$	kinetic energy of the proton beam
$\theta$	(polar) scattering angle

# E

## Software

### E.1 Programs

#### E.1.1 `cvs`

The program code is managed with the source code management tool `cvs`. This tool allows to manage the simultaneous development of the code by several developers. This tool keeps track of changes in the source code files, so the history of changes can be replayed. When and which changes have been carried out can be analysed.

(see <http://www.gnu.org/software/cvs/cvs.html>)

#### E.1.2 `gmake`

The creation of executable programs from the code is lead by `gmake`. In `gmake` target files are defined. They are usually object files or executable files. For each of these files commands are defined, which specify how they should be created. In addition dependencies for each target are given. Usually they are a list of files from which the targets are created. During the run of `gmake`, the individual target files are always updated when they are out of date. This means a target file is always updated when a target file is older than one of the files it depends on. The "Makefile" in this project is written to include automatically new source files into the project. Also automatically generated dependency files are used.

(see <http://www.gnu.org/software/make/make.html>)

#### E.1.3 `root`

`root` has been developed (and is still evolving) within the NA49 collaboration. In the context of the development presented here it replaces `paw` and `hbook` from the CERNLIB.

(see <http://root.cern.ch>)



### E.1.4 **clhep & GEANT4**

GEANT4 is replacing the old detector simulation program GEANT3. Founded on the `clhep` class library, the structure of the program is nearly self documented. This makes it easy for physicists to understand the underlying physical models that are used inside the program. The core development for this program was finished in the end of 1998, when its first release (4.0.0) was published. (see <http://wwwinfo.cern.ch/asd/geant4/>)

### E.1.5 **gcc**

The developed code was written in C++. For the compilation the GNU compiler collection (`gcc`) has been used. `gcc` is available for different operating systems and architectures. The code developed to conduct the analysis presented here, should run on all target machines of `gcc`. (see <http://gcc.gnu.org>)

## E.2 **GIN format**

At some stages in the analysis, information about events must be exchanged via a file. It is used for in- and output of the event generation, for input of the detector simulation and for the output of the selected events in the data analysis. Here the definition of this file format is given:

Each file has two lines of header, afterwards the events each come with one header line and a line for each particle.

<b>header first line</b>	reaction number, cross section, beam momentum in GeV/c, three free parameters, number of events
<b>header second line</b>	comment text
<b>event header</b>	event number, reaction number, number of particle, beam momentum in GeV/c, weight of event
<b>particle line</b>	particle number, momentum vector $p_x, p_y, p_z$ in lab. in GeV/c, GEANT particle type

The Fortran format statement and the c-function printf format strings:

<b>event header</b>	FORMAT (1x,3I10,F10.4,E10.3) " %10d%10d%10d%10.4f%10.3e\n"
<b>particle line</b>	FORMAT (1x,I3,3F10.4,I3) " %3d%10.4f%10.4f%10.4f%3d\n"

(It is the same format as used in the Fortran code used by other analysis [[Cal97](#)].)

## E.3 Analysis abstraction

Part of the data analysis tool is rather independent of experiments. That is the abstraction of the data acquisition system into: *crate, slot, channel and device (ADC/TDC/LRTDC/SCALER)*, and the abstraction of the detector into *detector, plane, element, kind of information (Energy, Time, Delayed Time, Scaler)*. So parts of the code developed here could be in principle directly taken for all kinds of medium sized nuclear and particle physics experiments. A powerful abstract interface for manipulating the data is included. It is used, for example, in applying calibration constants to ADC values.

The reconstruction itself is rather experiment dependent. Here the developed interfaces should be used to implement your own experiment dependent reconstruction code.

The whole analysis is leading back to events in the same format as used in the computer simulation of the physical models. With this approach a consistent and complete tool can be used for physical analysis of the measured data and for efficiency and acceptance correction.

## Acknowledgments

During the work for my thesis I have met a lot of people. It is not possible to mention all of them here. So this is to you all: thank you! It has been a great time working with you in experimental particle physics.

Such a big experiment can only be done within a big group. I would like to thank the staff at TSL. Here I want to especially mention Dag Reistad and Carl-Johan Fridén. All of you were always helpful during the experiment as well as during the setup of the FWC. Birgitta Holmgren and Catharina Åsbjörk, thank you for always organising accommodation for me during my visits to Uppsala.

The people in the workshop in Tübingen have done a great job in cutting out the most complicated structures of plexiglass one can imagine. I would like to especially thank Günther Brodbeck, Norbert Stockmaier and Wolfgang Helle.

I would like to thank Mareike Khalil, Brunhilde Eiskant and Heinrich Lindel in our office. You have always been very helpful in all the questions concerning administration and have saved me of a lot of administrative work.

The computer system essential for our work have been kept in good condition: In Uppsala by Ib Koersner, Stefan Pomp and Roger Ruber. In Tübingen by Uwe Siodlacek, Peter Jesinger and Arthur Erhardt. Thank you for your support and if there was a problem for your quick help. (Do we ever have problems with computers?)

Thank you Wolfram Brodowski and Jochen Kreß sharing the same room, we have been a great team and we have had good times together, not only with physics!

I would like to thank my colleagues (also PhD students as I was), who are carrying out and have carried out experiments with WASA and PROMICE/WASA and are struggling with the same and similar problems and suffering from delays: Levent Demiroers, Jan Greiff, Jan Johanson, Marek Jacewicz, Inken Koch, and Tatiana Skorodko. For you, who are still working on your thesis, I wish you good luck with your work.

I would like to thank the other PhD students and students in Tübingen: Axel Betsch, Johannes Breitschopf, Margit Cröni, Holger Denz, Evgueni Dorochkevitch, Jan Dräger, Jan Gräter, Rüdiger Großmann, Mirjam Wißkirchen and Florian von Wochrem for your good friendship. I will always remember our extensive coffee breaks after lunch.

I would especially like to mention Oliver Messner. We had a great time mounting the FWC during Vålborg.

“Atlas” Ait-Salem, I had interesting discussions with you about recent middle east history.

Ralph Bilger, you were a great support for me during the work for my thesis, thank you for reading the proofs on my thesis.

Thanks Rudi. Rudolf Meier, you have offered me a lot of help, I could greatly benefit from your experience in all we need in middle energy physics, from the conduction of an experiment until the analysis of the physical results, there is no question you cannot answer.

Thank you, Hans Calén and Andrzej Kupść, Jozef Zlomanczuk and Kjell Fransson, we have been a good team during the experiments.

Mischa Schepkin, I would like to thank you for the discussion and calculation of models.

Thank you, Luis Alvarez-Ruso, for the productive collaboration on trying to understand the reaction mechanism by exchanging simulated events of your model and the discussions.

I would like to thank my supervisors in Uppsala Bo Höistad and Sven Kullander.

I would like to thank my supervisor Heinz Clement for the essential support of my work and for fruitful discussions, when there was a need for new ideas.

I would like to thank my second supervisor, the Dean of our faculty and until recently the director of our department Gerhard Wagner.

Additionally I would like to thank the people all over the world developing all those nice and useful computer programs licensed under the GPL (Gnu Public License and similar licenses) [GNU]. They provide the Freedom we need in science. Without them one must always fear to have one foot in jail. Please take a look at my program via anonymous cvs (you might find it useful :-):

```
setenv CVSROOT :pserver:CWanalysis@pit.physik.uni-tuebingen.de:/cvs/CWanalysis
cvs login (Password: CWanalysis)
cvs checkout CWanalysis
```

as long as the repository will be maintained on this server.

I am grateful to Svenja and Milan.

# List of Publications

## Journals

- W. Brodowski, J. Pätzold et al., *Search for Narrow  $NN\pi$  Resonances in Exclusive  $pp \rightarrow pp\pi^+\pi^-$  Measurements*, submitted to be published in Phys. Lett. B (arxiv:nucl-ex/0206020)
- W. Brodowski, J. Pätzold et al., *Exclusive Measurements of the  $pp \rightarrow pp\pi^+\pi^-$  Reaction Near Threshold*, Phys. Rev. Lett. **88**, 192301 (2002)
- U. Schiefer, J. Pätzold et al., *Evaluation of glaucomatous visual field loss with locally condensed grids using fundus orientated perimetry (FOP)*, European Journal of Ophthalmology, Vol. 11, Suppl. 2 2001, pp. S57 – S62
- U. Schiefer, J. Pätzold et al., *Evaluation of extensive visual field defects with computer-assisted kinetic perimetry*, Klinische Monatsblätter für Augenheilkunde 218(1) (2001) 13
- J. Dräger, J. Pätzold et al., *Systematics of the low-energy pionic double charge exchange in nuclei*, Phys. Rev. **C 62** (2000) 064615
- J. Gräter, J. Pätzold et al., *Inclusive measurements of pionic double charge exchange on  $^3\text{He}$  at low energies*, Phys. Lett. B 471 (1999) 113
- E. Fragiaco, J. Pätzold et al., *A low-energy  $\pi / \mu$  identifier*, Nucl. Inst. Meth. A 439 (2000) 45
- R. Bilger, J. Pätzold et al., *Search for exotic muon decays*, Phys. Lett. B 446 (1999) 363
- A. Betsch, J. Pätzold et al., *Observation of strong final-state effects in  $\pi^+$  production in  $pp$  collisions at 400 MeV*, Phys. Lett. B 446 (1999) 179
- J. Pätzold et al., *The reaction  $^7\text{Li}(\pi^+, \pi^-)^7\text{B}$  and its implications for  $^7\text{B}$* , Phys. Lett. B 443 (1998) 77
- J. Pätzold et al., *Pionic double charge exchange on  $^{93}\text{Nb}$  at low energies*, Phys. Lett. B 428 (1998) 18
- J. Gräter, J. Pätzold et al., *Search for a bound trineutron with the  $^3\text{He}(\pi^-, \pi^+)nnn$  reaction*, Europ. Phys. Jour. A 4/1 (1999) 5
- K. Föhl, J. Pätzold et al., *Pionic double charge exchange on  $N=Z$  doubly closed shell nuclei*, Phys. Rev. Lett. 79 (1997) 3849

## Conference proceedings

- J. Pätzold et al., *A Computer Application for Training Kinetic Perimetry*, to be published in *Perimetry Update 2001/2002*, Kugler Publications Amsterdam/New York (2002)
- U. Schiefer, J. Pätzold et al., *Realisation of Semi-automated Kinetic Perimetry (SKP) with the Interzeag 101 Instrument*, to be published in *Perimetry Update 2001/2002*, Kugler Publications Amsterdam/New York (2002)
- J. Schiller, J. Pätzold et al., *Evaluation of Stato-kinetic Dissociation using (Examiner-independent) Automated Perimetric Techniques*, to be published in *Perimetry Update 2001/2002*, Kugler Publications Amsterdam/New York (2002)
- E. Dorochkevich, J. Pätzold et al., *Status on the Search for the NN-decoupled NN $\pi$  Resonance  $d'$* , MESON2002, to be published in *Acta Phys. Pol. B* (2002)
- J. Pätzold et al., *Exclusive measurements of the  $pp \rightarrow pp\pi^+\pi^-$  reaction*,  $\pi N$  Newsletter **16** (2001) 370 – 372
- W. Brodowski, J. Pätzold et al., *Exclusive Measurement of the  $pp \rightarrow pp\pi^+\pi^-$  Reaction Close to Threshold*, AIP Conf. Proc. no. 603, 2001, p. 503 – 506
- U. Schiefer, J. Pätzold et al., *Evaluation of advanced visual field loss with computer-assisted kinetic perimetry*, *Perimetry Update 2000/2001*, Kugler Publications Amsterdam/New York, 131 – 136 (2001)
- R. Schwabe, J. Pätzold, et al., *Modeling the hill of vision*, *Perimetry Update 2000/2001*, Kugler Publications Amsterdam/New York, 71 – 79 (2001)
- W. Brodowski, J. Pätzold et al., *Exclusive measurement of  $pp \rightarrow pp\pi^+\pi^-$  at CELSIUS*, MESON2000, *Acta Phys. Pol. B* vol. 31 (2000) 2295
- C. Bargholtz, J. Pätzold et al., *The CELSIUS/WASA 4 $\pi$  detector facility*, MESON2000, *Acta Phys. Pol. B* vol. 31 (2000) 2249
- H. Calen, J. Pätzold et al., *WASA detector: towards rare pion and eta decays*, STORI99, AIP Conf. Proc. no. 512 (2000) 229
- R. Bilger, J. Pätzold et al., *The WASA detector at CELSIUS*, PANIC99, *Nucl. Phys. A* 663 – 664 (2000) 1073c
- R. Bilger, J. Pätzold et al., *Search for exotic muon decays*, PANIC99, *Nucl. Phys. A* 663 – 664 (2000) 829c
- R. Bilger, J. Pätzold et al., *2  $\pi$  Production in  $pp$  Collisions Close to Threshold*, PANIC99, *Nucl. Phys. A* 663–664 (2000) 469c
- R. Bilger, J. Pätzold et al., *The CELSIUS/WASA facility*, *Acta Phys. Pol. B* vol. 31 (2000) 77
- R. Meier, J. Pätzold et al., *Measurement of  $\pi^+p$  analyzing powers at low energy at PSI*, MENU1999,  $\pi N$  Newsl. no. 15 (1999) 43
- H. Clement, J. Pätzold et al., *Pionic double charge exchange*, MESON98, *Acta Phys. Pol. B* vol. 29 (1998) 2999
- G. J. Wagner, J. Pätzold et al., *Hunting the dibaryon  $d'(2065)$* , MESON98, *Acta Phys. Pol. B* vol. 29 (1998) 2415

J. Pätzold et al., *Discrete strategies in perimetry*, M. Wall, A. Heijl (editors) Perimetry Update 1996/1997, Kugler Publications Amsterdam/New York, 99 (1997)

## Conference contributions

*A Computer Application for Training Kinetic Perimetry*, IPS-meeting 2002 in Stratford-upon-Avon, contributed poster

*Nukleon-induzierte Zwei-Pionen-Produktion nahe der Schwelle*, Arbeitstreffen "Hadronen und Kerne" 2001 Schloss Pommersfelden, invited talk

*Exclusive Measurements of the  $pp \rightarrow pp\pi^+\pi^-$  Reaction Close to Threshold*, INPC2001 in Berkley, contributed poster

*Exclusive Measurements of the  $pp \rightarrow pp\pi^+\pi^-$  Reaction*, MENU2001 in Washington DC, contributed talk

*Exklusive Messungen der Zwei-Pion-Produktion im Proton-Proton-Stoß nahe der Schwelle*, DPG Frühjahrstagung 2001 in Erlangen, contributed talk

*Exclusive measurement of  $pp \rightarrow pp\pi^+\pi^-$  at CELSIUS*, MESON2000, contributed talk

*Exklusive Messungen zur  $1\pi$ -Produktion im NN-Stoß an CELSIUS mit dem PROMICE/WASA-Detektor*, DPG Frühjahrstagung 1999 in Freiburg, contributed talk

*Systematics of the Low-Energy Pionic Double Charge Exchange and its Bumpy Structure*, DPG Frühjahrstagung 1998 in Bochum, contributed talk

## Shortcuts for conference names

<b>DPG</b>	Deutsche Physikalische Gesellschaft
<b>MESON</b>	International Workshop on Production, Properties and Interaction of Mesons or International Workshop on the Structure of Mesons, Baryons and Nuclei
<b>MENU</b>	International Symposium on Meson-Nucleon Physics and the Structure of the Nucleon
<b>INPC</b>	International Nuclear Physics Conference
<b>IPS</b>	International Perimetric Society
<b>STORI</b>	Nuclear Physics at Storage Rings

## Bibliography

- [Aba60] A. Abashian et al., Phys. Rev. Lett. **5**, 258 (1960)
- [Aba61] A. Abashian et al., Phys. Rev. Lett. **7**, 35 (1961)
- [Alv98] L. Alvarez-Ruso, E. Oset, E. Hernández, *Theoretical study of the  $NN \rightarrow NN\pi\pi$  reaction*, Nucl. Phys. A **633** (1998) 519 – 543
- [Alv99] L. Alvarez-Ruso, *The role of the Roper resonance in  $np \rightarrow d(\pi\pi)^0$* , Phys. Lett. B **452** (1999) 207 – 213
- [Alv99a] L. Alvarez-Ruso, *Excitation of Baryonic Resonances Induced by Nucleons and Leptons*, PhD thesis, University of Valencia, 1999
- [Alv00] L. Alvarez-Ruso, *private communication*, 2000
- [Alv01] L. Alvarez-Ruso, *private communication*, 2001
- [Bel99] F. Bellemann et al., Phys. Rev. **C 60**, 061002 (1999)
- [Bil98] R. Bilger et al.,  *$2\pi$ -Production and  $d'$  Search in  $pp$ -Collisions*, Proceedings of the 8<sup>th</sup> International Conference on the Structure of Baryons, Bonn 22 - 26 September 1998, World Scientific 601 (1998)
- [Bir51] J. B. Birks, Proc. Phys. Soc. **A 64**, 874 (1951)
- [Boc94] Grady Booch, *Object-Oriented Analysis and Design with Applications*, Addison-Wesley, 1994
- [Bro95] Wolfram Brodowski, *Design und Aufbau einer Vetowand für den WASA/PROMICE-Detector am CELSIUS-Speicherring und erste Messungen der Reaktion  $pp \rightarrow pp\pi^+\pi^-$* , Diplomarbeit, University of Tübingen, 1995
- [Bro96] W. Brodowski et al., *A Signal of a Narrow  $\pi NN$ -Resonance in  $pp \rightarrow pp\pi^+\pi^-$* , Z. Phys. **A 355**, 5 (1996)
- [Bro01] Wolfram Brodowski, *Exclusive Measurement of the Reaction  $pp \rightarrow pp\pi^+\pi^-$  at CELSIUS and the Search for  $d'$* , PhD thesis, University of Tübingen, 2001
- [Bro02] W. Brodowski et al., *Exclusive Measurements of the  $pp \rightarrow pp\pi^+\pi^-$  Reaction Near Threshold*, Phys. Rev. Lett. **88**, 192301 (2002)
- [Bro02a] W. Brodowski et al., *Search for Narrow  $NN\pi$  Resonances in Exclusive  $pp \rightarrow pp\pi^+\pi^-$  Measurements*, submitted to be published in Phys. Lett. B (arxiv:nucl-ex/0206020)



- [Brü69] H. Brückmann, W. Kluge, H. Matthäy, L. Schänzler, K. Wick, *Proton-Proton Final State Interaction in the Three Nucleon Reaction  $p + d \rightarrow p + p + n$* , Phys. Lett. B **30** 460 (1969)
- [Bru69] D. C. Brunt et al., *Inelastic Reactions in Proton-Deuteron Scattering at 1.825 and 2.11 GeV/c*, Phys. Rev. **187**, 1856 (1969)
- [Bon96] F. Bonutti et al, Phys. Rev. Lett. **77**, 603 (1996)
- [Bon97] F. Bonutti et al, Phys. Rev. C **55**, 2998 (1997)
- [Bon98] F. Bonutti et al, Nucl. Phys. A **638**, 729 (1998)
- [Bon99] F. Bonutti et al, Phys. Rev. C **60**, 18201 (1999)
- [Bon00] F. Bonutti et al, Nucl. Phys. A **677**, 213 (2000)
- [Bys87] J. Bystricky et al., J. Physique **48**, 1901 (1987)
- [Cal87] H. Calen et al., *Proposal for elementary particle physics using WASA*, PAC Proposal, Theodor Svedberg Laboratory, Box 533, S-75121 Uppsala, Sweden (1987)
- [Cal96] H. Calen et al., *Detector setup for a storage ring with an internal target*, Nucl. Inst. and Meth. A **379** (1996) 57
- [Cal97] H. Calen, *Overview of the WASA-PROMICE Offline Programs*, WASA Program Library 1992, Last updated 1997
- [cern] CERN Program Library Long Writeups, CERN Program Library Office, CERN-CH Division, CH-1211 Geneva 23, Switzerland
- [Coc72] D. R. F. Cochran et al., *Production of Charged Pions by 730-MeV Protons from Hydrogen and Selected Nuclei*, Phys. Rev. **D 6**, 3085 (1972)
- [Cve81] F. H. Cverna et al., *Single and double pion production from 800 MeV proton-proton collisions*, Phys. Rev. **C23**, 1698 (1981)
- [Dak83] L. G. Dakhno et al., Sov. J. Nucl. Phys. **37**, 540 (1983)
- [Drä00] J. Dräger et al., *Systematics of the low-energy pionic double charge exchange in nuclei*, Phys. Rev. C **62** (2000) 064615
- [Dyr97] J. M. Dyring, *Detailed studies of the Reaction  $pp \rightarrow pp\eta$  using a Straw Chamber Tracking Device*, PhD thesis, University of Uppsala, 1997
- [Eks96] C. Ekström et al., , Nucl. Inst. and Meth. A **371** (1996) 572
- [Eks97] C. Ekström et al., *Internal targets for storage rings*, Nucl. Phys. A **626** (1997) 405
- [Ehr03] Arthur Erhardt, PhD thesis (in preparation), University of Tübingen, 2003
- [Fis90] H. Fischer, H. Kaul, *Mathematik für Physiker 1*, Teubner, 1990
- [geant3] GEANT (GEometry ANd Tracking), *Detector Description and Simulation Tool*, CERN Program Library Long Write Up W5013 (1993)

- [geant4] GEANT4 (GEometry ANd Tracking),  
<http://wwwinfo.cern.ch/asd/geant4/>
- [GNU] GNU, Gnu is Not Unix, <http://www.gnu.org>
- [Grä98] Jan Gräter, *Inclusive Pionic Double Charge Exchange Reactions on  $^3\text{He}$  and  $^4\text{He}$* , PhD thesis, University of Tübingen, 1998
- [Gre01] Jan Greiff, *private communication*, 2001
- [Gro97] R. Großmann, *Suche nach einer schmalen Dibaryon-Resonanz an Cosy-11*, Diplomarbeit, Universität Tübingen, 1997
- [Hat99] T. Hatsuda et al., *Phys. Rev. Lett.* **82**, 2840 (1999)
- [Jan01] S. Janssen, *Doppel- $\pi^0$ -Photoproduktion an Kernen*, Verhandlungen der Deutschen Physikalischen Gesellschaft Erlangen (2001)
- [Joh00] Jan Johanson, *Two-Pion Production in Proton-Proton Collisions Near Threshold*, PhD thesis, University of Uppsala, 2000
- [Joh02] J. Johanson et al., *Two-pion production in proton-proton collisions near threshold*, in preparation to be published (2002)
- [Knu86] Donald E. Knuth, *The T<sub>E</sub>Xbook*, Addison-Wesley, 1986
- [Koc95] V. Koch, *Introduction to Chiral Symmetry*, LBNL-Report 38000, arXiv:nucl-th/9512029 (1995)
- [Kop95] Helmut Kopka, *A Guide to L<sup>A</sup>T<sub>E</sub>X 2<sub>ε</sub>*, Addison-Wesley, 1995
- [Kre97] Jochen Kreß, *Aufbau und Test von Szintillatormodulen für ein Zentralkalorimeter am Flugzeitspektrometer COSY-TOF*, Diplomarbeit, University of Tübingen, 1997
- [Kre02] Jochen Kreß, PhD thesis (in preparation), University of Tübingen, 2002
- [Kup95] A. Kupsc, *Note on kinematical fit*, private communication, 1995
- [Leo94] W. R. Leo, *Techniques for Nuclear and Particle Physics Experiments*, Springer Verlag, 1992
- [Lip98] Stanley B. Lippman, Josée Lajoie, *C++ Primer*, Addison-Wesley, 1998
- [Lut91] M. Lutz, S. Klimt, W. Weise, *Nucl. Phys. A* **542**, 521 (1991)
- [Mes99] Oliver Messner, *Design and Setup of the Window Hodoscope for the new WASA 4 $\pi$ -Detector at CELSIUS*, Diploma Thesis, University of Tübingen, 1999
- [midas] MIDAS, <http://midas.psi.ch/>
- [Nef00] B. M. K. Nefkens et al., *Acta Phys. Pol.* **B 31** 10-11 pp. 2669 – 2681 (2000)
- [PDG00] Particle Data Group, D. E. Groom, *Review of Particle Physics*, *Europ. Phys. Jour.* **C 15** (2000) 1

- 
- [Per87] D. H. Perkins, *Introduction to High Energy Physics*, Addison-Wesley, 1987
- [root] ROOT — An Object-Orientated Analysis Framework,  
<http://root.cern.ch/>
- [Roz88] F. M. Rozon, N. Grino, R. Rui, *Nucl. Instr. Methods A* **267**, 101 (1988)
- [Rub99] R. J. M. Y. Ruber, *An Ultra-thin-walled Superconducting Solenoid for Meson-decay Physics*, PhD thesis, University of Uppsala, 1999
- [SAID] SAID data base, start request:  
`ssh -l said fphws01.physik.uni-karlsruhe.de`
- [Sch98] M. Schepkin, *private communication*, 1998
- [Sch00] M. Schepkin, *private communication*, 2000
- [Shi82] F. Shimizu et al., *Nucl. Phys. A* **386**, 571 (1982)
- [Sio96] Uwe Siodlaczek, *Simulation von Pionproduktionsexperimenten für den WASA/PROMICE-Detector am CELSIUS-Speicherring*, Diplomarbeit, University of Tübingen, 1996
- [Sko04] Tatiana Skorodko, PhD thesis (in preparation), University of Tübingen, 2004
- [Str99] Bjarne Stroustrup, *The C++ Programming Language*, Addison-Wesley, 1999
- [TSL92] Theodor Svedberg Laboratory, *TSL Progress Report 1987 – 1991*, Uppsala, Sweden, February 1992
- [TSL94] Theodor Svedberg Laboratory, *TSL Progress Report 1992 – 1993*, Uppsala, Sweden, February 1994
- [TSL96] Theodor Svedberg Laboratory, *TSL Progress Report 1994 – 1995*, Uppsala, Sweden, March 1996
- [TSL98] Theodor Svedberg Laboratory, *TSL Progress Report 1996 – 1997*, Uppsala, Sweden, March 1998
- [TSL99] The Theodor Svedberg Laboratory, leaflet, Uppsala, May 1999
- [TSL00] Theodor Svedberg Laboratory, *TSL Progress Report 1998 – 1999*, Uppsala, Sweden, March 2000
- [Wat94] M. Waters, *The Reaction  $pd \rightarrow {}^3\text{He} \eta$  at 200 MeV Excess Energy*, Doktorarbeit, Forschungszentrum Jülich 1994
- [Wei01] W. Weise, *Nucl. Phys. A* **690**, 98 (2001)
- [Wol00] M. Wolf et al., *Eur. Phys. J. A* **9**, 5 (2000)
- [Zab94] J. Zabierowski, *High power LED pulser for gain monitoring in a multiscounter experiment*, *Nucl. Inst. and Meth. B* **338** (1994) 577

# Lebens- und Bildungsgang

## Persönliche Daten:

Name	Jens Pätzold
Geburtstag	4. Februar 1972
Geburtsort	Ebingen

## Schulischer Werdegang:

1978 – 1980	Grundschule in Albstadt-Tailfingen
1980 – 1982	Grundschule in Dotternhausen
1982 – 1991	Gymnasium in Balingen
26.6.1991	Allgemeine Hochschulreife

## Studium und Promotion:

10.1992 – 12.1997	Studium an der Universität Tübingen, eingeschrieben im Fach Physik (Diplom)
14.10.1994	Vordiplom in Physik
24.12.1997	Diplom in Physik
1.1998 – 3.1998	Stipendiat im Graduiertenkolleg „Hadronen und Kerne“ an der Universität Tübingen
1.1998 – 4.2002	Anfertigung einer Doktorarbeit auf dem Gebiet der Mittlereenergiephysik zum Thema <i>Exclusive Measurements of the <math>pp \rightarrow pp\pi^+\pi^-</math> Reaction Close to Threshold</i> unter der Betreuung von Prof. Dr. Clement.

## Bisherige Tätigkeiten:

1.7.1991 – 30.9.1992	Zivildienst am Paracelsus Krankenhaus in Bad Liebenzell
11.1995 – 5.1997	Wissenschaftliche Hilfskraft am Universitätsklinikum Tübingen, Augenklinik Abt. II und Institut für medizinische Biometrie
10.1997 – 3.1998	Wissenschaftliche Hilfskraft am Physikalischen Institut der Universität Tübingen
4.1998 – 12.2001	wissenschaftlicher Angestellter am Physikalischen Institut der Universität Tübingen
seit 1.2002	wissenschaftlicher Angestellter im Universitätsklinikum Tübingen, Augenklinik Abt. II

## Meine akademischen Lehrer waren die Professoren und Privatdozenten:

M. Baumann, R. Bilger, A. Buchmann, H. Clement, W. Dittrich, H. Fischer, K.-H. Gaukler, P. Grabmayr, W. Hartmann, F. Hoyler, R. Hübner, H. Kaul, H. Klaeren, D. Kern, E. Lindner, O. Lutz, R. Meier, G. Mertens, H. Pfister, E. Plies, K. W. Schmid, H. Reinhardt, R. Schief, U. Schiefer, A. Schwenk, G. Staudt, G. J. Wagner